INFORMATION TO USERS

This manuscript has been reproduced from the microfilm master. UMI films the text directly from the original or copy submitted. Thus, some thesis and dissertation copies are in typewriter face, while others may be from any type of computer printer.

The quality of this reproduction is dependent upon the quality of the copy submitted. Broken or indistinct print, colored or poor quality illustrations and photographs, print bleedthrough, substandard margins, and improper alignment can adversely affect reproduction.

In the unlikely event that the author did not send UMI a complete manuscript and there are missing pages, these will be noted. Also, if unauthorized copyright material had to be removed, a note will indicate the deletion.

Oversize materials (e.g., maps, drawings, charts) are reproduced by sectioning the original, beginning at the upper left-hand corner and continuing from left to right in equal sections with small overlaps.

Photographs included in the original manuscript have been reproduced xerographically in this copy. Higher quality 6" x 9" black and white photographic prints are available for any photographs or illustrations appearing in this copy for an additional charge. Contact UMI directly to order.

Bell & Howell Information and Learning
300 North Zeeb Road, Ann Arbor, MI 48106-1346 USA
800-521-0600

STRUCTURAL AND PHYSICAL PROPERTIES OF THE VACANCY DOPED SYSTEMS $R_{(1-x)}TiO_3$ (R = Nd for $0.00 \leq x \leq 0.33$ and Sm for $0.00 \leq x \leq 0.17$): AN INVESTIGATION OF METAL-INSULATOR TRANSITIONS.

By

GISELE AMOW

A Thesis

Submitted to the School of Graduate Studies

in Partial Fulfilment of the Requirements

for the Degree

Doctor of Philosophy

McMaster University

STRUCTURAL AND PHYSICAL PROPERTIES OF THE VACANCY DOPED SYSTEMS $R_{(1-x)}TiO_3$ (R = Nd for $0.00 \leq x \leq 0.33$ and Sm for $0.00 \leq x \leq 0.17$): AN INVESTIGATION OF METAL-INSULATOR TRANSITIONS.

DOCTOR OF PHILOSOPHY (1999) McMaster University

(Chemistry) Hamilton, Ontario

TITLE: Structural and Physical Properties of the Vacancy Doped Systems, $R_{(1-x)}TiO_3$ (R = Nd for $0.00 \leq x \leq 0.33$ and Sm for $0.00 \leq x \leq 0.17$): An Investigation of Metal-Insulator Transitions.

AUTHOR: Gisele Amow, B.Sc. (McMaster University)

SUPERVISOR: Dr. John E. Greedan

NUMBER OF PAGES: xix, 237

ABSTRACT

Members of the solid solutions, $R_{(1-x)}TiO_3$ (R = Nd, Sm) have been prepared for $0.00 \leq x \leq 0.33$ and $0.00 \leq x \leq 0.17$ for R = Nd and Sm respectively. Three structural types have been identified for the R=Nd system: *Pnma* ($0.00 \leq x \leq 0.17$), *Pban* ($0.25 \leq x \leq 0.30$) and *P4/mmm* ($x = 0.33$). For the R = Sm system, only the *Pnma* structure type has been identified by x-ray powder diffraction. D.c. susceptibility measurements reveal canted antiferromagnetic behaviour for the nominal x = 0.00 and 0.05 compositions in both systems. The observed Néel temperatures are 100K and 75K respectively for x = 0.00 and 0.05 in the $Nd_{(1-x)}TiO_3$ system and 50K and 42K for the x = 0.00 and 0.05 compositions in the $Sm_{(1-x)}TiO_3$ system. The magnetic structures of these phases have been determined using neutron diffraction methods. Paramagnetic behaviour is observed for $x \geq 0.10$ in both systems. Four probe van der Pauw measurements reveal two metal-insulator transitions in the $Nd_{(1-x)}TiO_3$ system at x = 0.10 and x = 0.25 and only one for the $Sm_{(1-x)}TiO_3$ system at x = 0.10. In the metallic regime, the resistivity behaviour indicates these compounds are poor metals with highly correlated behaviour possibly associated with the Kondo effect and Fermi liquid character. Further investigation of these "metallic" phases by specific heat measurements reveal a divergence of the carrier mass as the Mott transition is approached from the itinerant side in accordance with the Brinkmann-Rice model. Thermopower measurements in both systems reveal the presence of p-type conduction in the Mott insulator phases, while n-type conduction is observed for $x \geq 0.10$. The thermopower behaviour of the "metallic" phases can be described using Mott's law for metals.

ACKNOWLEDGMENTS

During my stay at McMaster University I have had the immense pleasure and fortitude to work with some very talented and experienced individuals. Foremost, I thank my supervisor, Dr. John E. Greedan, for the opportunity to be a part of his group and for providing me with interesting research challenges and the resources to pursue them. His guidance and invaluable contributions to this work are deeply appreciated. I also owe a great deal of gratitude to the thermopower team: Bruce Collier, for his attention to detail and commitment to getting the best measurement possible. Jim Garret for always helping me out when I seemed to need it the most, for *small* things like making crucibles to *big* things like machining parts for the thermopower apparatus. I also thank Dr. Anton Dabkowksi for his enthusiasm and the many hours he devoted to write the software program for the thermopower project and Dr. Timusk for his supervisory role on this project as well as being a committee member.

I have also had the pleasure to work with Dr. Hania Dabkowska who introduced me to the flux growth method. I am thankful for her patience and enthusiasm in teaching me the finer points of this technique. Gratitude is also owed to Dr. R.P. Nandyala for his many discussions on a variety of topics and for his significant contributions to the specific heat measurements, Dr. James Britten for single crystal x-ray diffraction data collections, Mr. Frank Gibbs for thermogravimetric analyses and W.E. Gong for performing x-ray powder diffraction data collections. I also thank Dr. J. Barbier, also a committee member, for being

a willing participant in performing the TEM measurements and for his many insights into solving crystal structures. I also thank Dr. A.P. Hitchcock for being a committee member.

I have had the opportunity to work with other scientists outside McMaster University to whom I am also grateful for their advice and assistance. These include Dr. Thom Mason and Dr. Carl Adams (formerly at the University of Toronto) for specific heat measurements and Dr. Clemens Ritter at the Institut Laue-Langevin, Grenoble, France with regard to the single crystal neutron diffraction study on $Sm_{0.97}TiO_3$. I also thank Christopher Jones at Cornell University for discussions regarding thermopower and for the preparation and measurement of the $CePd_3$ standard.

TABLE OF CONTENTS

LIST OF TABLES

LIST OF FIGURES

CHAPTER 1

INTRODUCTION

Fifty years ago Mott considered the problem of how a transition from a localized magnetic insulating state to an itinerant metallic state (also known as the Mott transition) can proceed. The question grew out of a need to explain the insulating nature of NiO which, as first pointed out by deBoer and Verwey (deBoer and Verwey, 1937), should be metallic according to the then successful band theory developed by Bloch and Wilson (Bloch, 1929; Wilson, 1931). To explain this conundrum, it was first pointed out by Peierls, that one must consider the importance of Coulombic electron interactions (Mott, 1990). It was later shown by Mott and Hubbard, that the one electron model fails if the energy needed to place two electrons on the same site, U, is greater than or equal to the one electron bandwidth, W (Hubbard, 1963; Hubbard, 1964; Mott, 1949)

Following the discovery of high T_c cuprate superconductors, there has been renewed interest in the investigation of narrow band systems which undergo metal-insulator (M-I) transitions (Imada et al., 1998; Mott, 1990). It has long been established that a close relationship exists between antiferromagnetism and superconductivity. In systems such as $La_{(2-x)}Sr_xCuO_4$, the parent compounds are antiferromagnetic insulators (also known as Mott insulators) which, when doped with holes, become superconducting. Thus, it is believed that one can treat antiferromagnetism, superconductivity and M-I transitions within the same theoretical framework of correlated electrons in narrow band systems, that is, those in which strong electron-electron interactions

are significant. The vacancy doped perovksite systems, $R_{(1-x)}TiO_3$(R =Nd, Sm), which are expected to show effects of strong electron correlation are the focus of this thesis.

1.1. THEORETICAL MODELS:

In this section, the development of the theories pertinent to the field of M-I transitions in narrow *d* band systems is presented. Generally, three approaches have been taken in order to understand the Mott transition. The first being developed by Mott and is briefly described in Section 1.1.a. The second approach was taken by Hubbard who placed Mott's model on a quantitative footing that included short range Coulomb interactions. The third approach was developed by Brinkman and Rice (Brinkman and Rice, 1970; Brinkman and Rice, 1970) based on a variational method by Gutzwiller (Gutzwiller, 1965), to include long range Coulomb interactions.

1.1.a. Mott-Hubbard theory: To explain the M-I transition, Mott proposed the idea of minimum metallic conductivity. He imagined a crystalline array of hydrogen-like atoms with a lattice constant, *a*, which could be varied. For large values of *a* the material was expected to be insulating while for smaller values it would be metallic. The value at which the M-I transition would occur was determined to be,

$$n^{1/3}a_H = 0.2 \qquad (1)$$

where n is the number of electrons per unit volume and a_H is the hydrogenic radius. Furthermore, the M-I transition was reasoned to be discontinuous where all the electrons go from being

trapped in the localized state to being free in the metallic state.

Hubbard treated the correlation problem in terms of the parameter U which is the energy penalty for putting two electrons onto the same site as described by,

$$d_i^n d_j^n \rightarrow d_i^{n-1} d_j^{n+1} \qquad (2)$$

The energy required to do this is essentially equal to the energy needed to transfer an electron from one atom to another (i.e. ionization energy, I), and the energy to recover this electron, the electron affinity, A, thus U = I-A. In narrow band systems, the M-I transition can be regarded as a competition between the kinetic energy favouring delocalization which inevitably leads to metallic behaviour, and the potential energy favouring localization to give the insulating state.

The M-I transition can be understood using Fig.1.1. If U ≥ W, the *d* bands of the transition metal are split into upper and lower Hubbard bands which creates a band gap. In this limit, for a half filled band, the model is clearly insulating, while in the small U≤ W limit it is metallic. A measure of the correlation strength is generally regarded as the ratio, U/W.

1.1.b. The Zaanen Sawatsky Allen framework:

Despite the apparent success of the Hubbard model, particularly for the early transition metals (Ti-V), there was growing experimental evidence to suggest that it was not applicable for the late transition metal compounds (Mn-Cu). Zaanen, Sawatsky and Allen (Zaanen et al., 1985; Zaanen et al., 1986) considered the nature of the band gap in such systems and showed

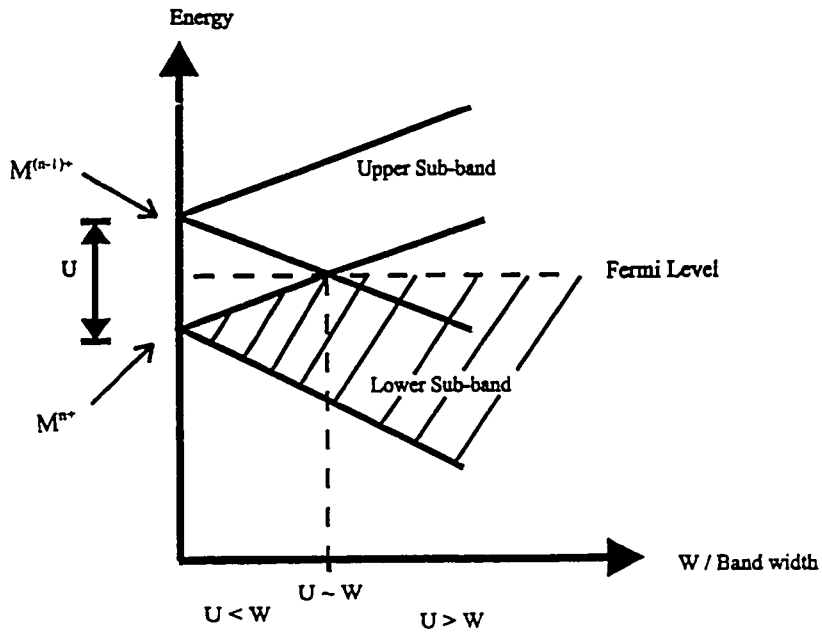

Fig. 1.1. The Hubbard model showing the variation of U with the bandwidth, W.

that a third energy must also be considered, the charge transfer energy, Δ. This is the energy gap between the p-bands of the ligand anions and the unoccupied upper Hubbard band of the transition metal, see Fig. 1.2b.

The ZSA framework has become a useful scheme for classifying correlated insulators. In this scheme, insulating transition metal compounds can be classified into two groups depending on the relative energies, U, W and Δ. The first group is the Mott Hubbard insulator in which, as shown before, the d-bands of the transition metal are split into upper and lower Hubbard bands creating a band gap between the two bands, shown in Fig. 1.2d. The other group is a charge transfer insulator which has an energy gap, Δ, as described above. Metallic conductivity will be attained if either of these two gaps (U or Δ) becomes smaller than the bandwidth, W, as shown in Figs. 1.2a and 1.2e. Early transition metal perovksites ($RTiO_3$, RVO_3) generally fall in the Mott-Hubbard class while the heavier transition metal oxides, in which the high T_c superconductors are found, are placed in the charge transfer class. It is to be noted that the ZSA framework has also been modified to include transition metal oxides which have strong covalent bonds, thus leading to a third category of insulators, that is, the covalent insulator (Sarma, 1990).

1.1.c. Brinkmann-Rice theory:

An alternative approach in understanding the M-I transition was developed by Brinkman and Rice. They approached the M-I transition using Gutzwiller's variational method and considered the case of one electron per atom. Starting with the Hubbard Hamiltonian, Gutzwiller derived

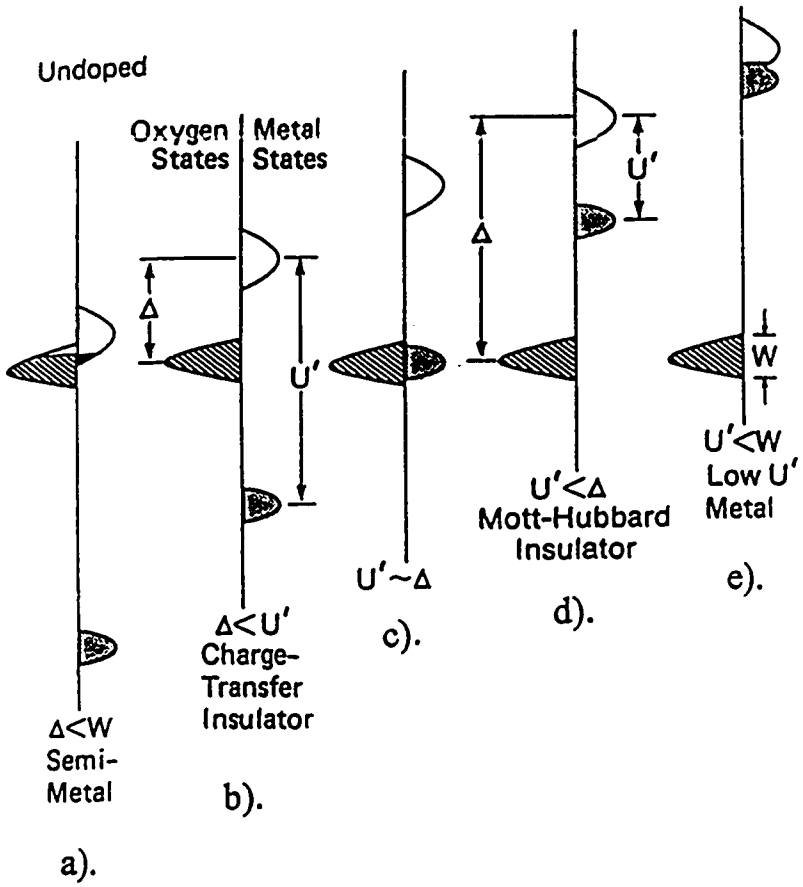

Fig. 1.2. The Zaanen-Sawatsky-Allen-Framework.

the general relationships between a variational parameter, η, the discontinuity in the single particle occupation number at the Fermi surface, q, and the fraction of doubly occupied sites, v. By minimizing the energy of the system in terms of these parameters, they were able to derive the properties of a trial wave function on the metallic side of the transition. This led to the important result that near the Mott transition, a mass enhancement of the carriers is expected which is described by,

$$\frac{m^*}{m} = \left[1 - \left(\frac{U}{U_0}\right)^2\right]^{-1} \qquad (3)$$

where U_0 is the critical interaction strength above which the fraction of doubly occupied sites goes to zero thus producing the insulating state. Furthermore it was shown that the Pauli susceptibility, χ, is described by,

$$\frac{1}{\chi} = \frac{1-(U/U_0)^2}{\rho(\varepsilon_F)}\left[1 - [U\rho(\varepsilon_F)]\left(\frac{1+(U/2U_0)}{[1+(U/U_0)]^2}\right)\right] \qquad (4)$$

where $\rho(\epsilon_F)$ is the band structure density of states at the Fermi energy. Thus as $U \rightarrow U_0$, i.e. as the M-I boundary is approached, both the effective mass and susceptibility diverge in proportion to $[1-(U/U_0]^2]^{-1}$.

1.2. Perovskite Titanate Systems and the M-I Transition:

1.2.a. $RTiO_3$ systems: The perovskite family of compounds are represented by the general formula, ABX_3, where A and B are cations and X, anions. Due to the large number of different ions that can be substituted for A, B or X, compounds of this type have been of

significant interest for their potentially wide variety of structural and physical properties. One such class of compounds that has been studied are the rare earth titanates, where A = rare earth ion, B = titanium and X = oxygen.

The ideal cubic perovksite, $SrTiO_3$, can be described as the A site cation (Sr^{2+}) occupying the body centre of the unit cell, the B cations (Ti^{4+}) at the corners of the cube, and the X anions (O^{2-}) at the edge centres, with cell parameter, a_p ~3.8Å, see Fig. 1.3a. Substitution of a smaller rare earth cation on the A-site causes the structure to distort so as to maximize the R-X bonding. This results in the orthorhombically distorted $GdFeO_3$ structure in which the TiO_6 framework is tilted where the new unit cell is related to the cubic cell by the relationship, $a \sim \sqrt{2}a_p$, $b \sim \sqrt{2}a_p$ *and* $c \sim 2a_p$, see Fig. 1.3b. It has been determined that there is an almost linear decrease of the Ti-O-Ti bond angle as the size of the rare earth cation is decreased from R = La to Lu, see Fig. 1.4. Since the exchange and conduction pathways are controlled by the overlap of the Ti3*d* t_{2g} and O2*p*π orbitals, a decrease of the Ti-O-Ti bond angle alters the conduction bandwidth, posing some significant implications for the physical properties of these compounds. The rare earth titanates all are semiconducting with activation energies that increase by an order of magnitude from 0.01 eV in Pr, Nd to 0.1eV for R = Gd, Y. Magnetically, these compounds show a remarkable variation ranging from antiferromagnetic behaviour observed for R = La to Sm to ferro- and ferri-magnetic behaviour for R =Gd toTm. Torrance and Lacorre have predicted that the $RTiO_3$ members should be Mott insulators based on estimated values of U and Δ using a simple ionic model (Torrance and Lacorre, 1991). This was subsequently confirmed with reflectance spectroscopy results which showed evidence of a Hubbard gap (Crandles et al., 1992).

a).

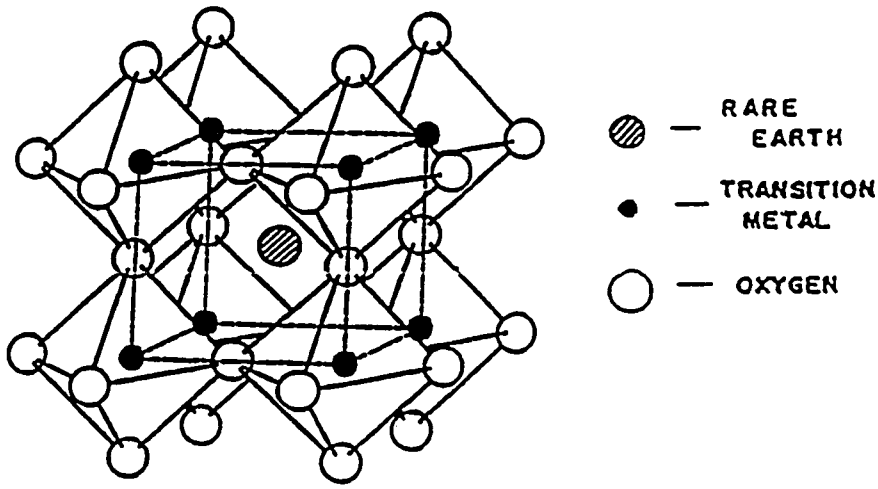

b).

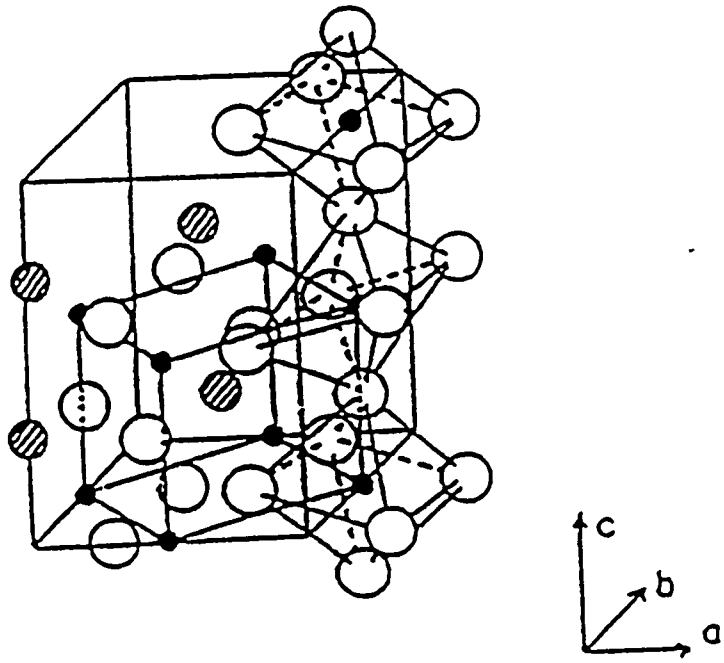

Fig. 1.3. a). The ideal cubic perovskite and b). The orthorhombically distorted $GdFeO_3$ perovskite.

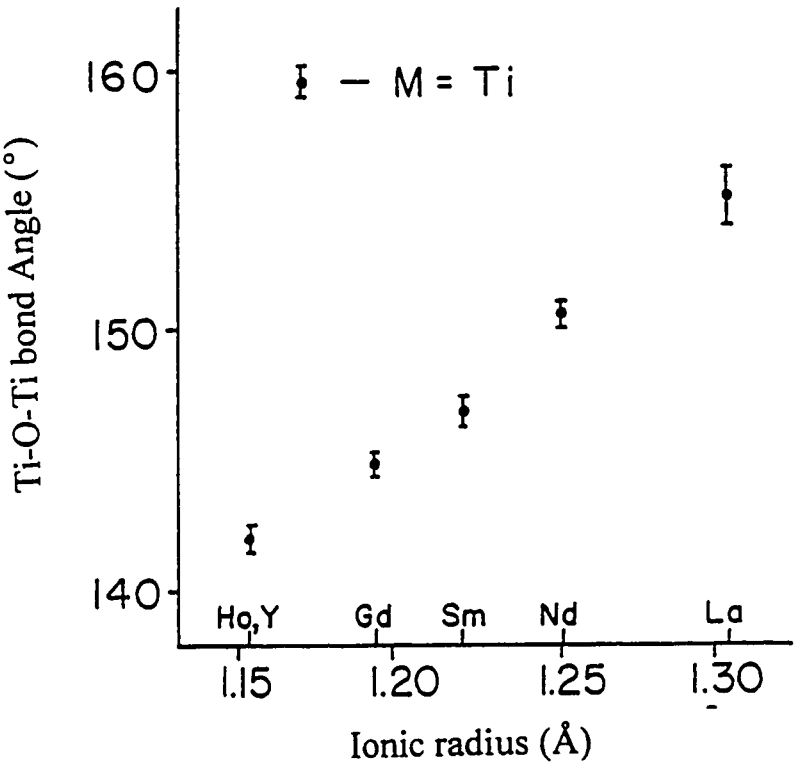

Fig. 1.4. Average Ti-O-Ti bond angle vs. rare earth ionic radius.

1.2.b. $R_{(1-x)}A_xTiO_3$ systems: The alkali earth doped system, $La_{(1-x)}Sr_xTiO_3$, has been the main focus of investigation of the M-I transition. It is easily seen that introduction of divalent alkali earth metals onto the A-sites of the perovskite structure introduces holes into the conduction band thereby inducing a mixed valent Ti^{3+} (d^1) / Ti^{4+} (d^0) system. Consequently, the band filling can be controlled with the doping content thus allowing for systematic studies into the physical properties of such systems. At the same time, the band width, W, is also changed with the incorporation of the alkali earth ions on the A-site. From the specific heat, Pauli susceptibility and optical measurements it has been determined that the M-I transition in $La_{(1-x)}Sr_xTiO_3$ is driven by the enhancement of the renormalised electron mass due to electron correlation and not by a decrease of the carrier density (Fujimori et al., 1992; Kumagai et al., 1993). This is reflected by the parallel increase in the effective mass (specific heat) and Pauli susceptibility as predicted by the Brinkman-Rice theory presented earlier. Since then, investigations have been extended to include other $R_{(1-x)}A_xTiO_3$ systems where R = Nd, A = Ca, Sr, Ba and $R_{(1-x)}R'_xTiO_3$ (R = La, Nd; R' = Nd, Sm) (Eylem et al., 1992; Eylem et al., 1995; Ju et al., 1994; Yoshii and Nakamura, 1997).

1.2.c. $R_{(1-x)}TiO_3$ systems: Alternatively, one can introduce vacancies on the A-sites to bring about a change in the electronic structure and thus induce an M-I transition. As the end members (x = 0.00 and x = 0.33) are both insulators, two M-I transitions are anticipated in these types of systems. Most recently, the $La_{(1-x)}TiO_3$ system has been investigated (Crandles et al., 1994; MacEachern et al., 1994). Magnetic susceptibility and resistivity measurements indicated the correlation strength is larger for $La_{(1-x)}TiO_3$ than in the $La_{(1-x)}Sr_xTiO_3$ system. In

addition, three structural phase transitions have been determined. The M-I transitions reveal the effect of decreasing the bandwidth in these systems as well as the increased disorder in this system. On the antiferromagnetically insulating end of the system (x = 0.00) the M-I transition involves a change to paramagnetism with the simultaneous onset of metallic behaviour at x = 0.08. From the other end, (x = 0.33), the M-I transition is associated with the presence of a high carrier level (%Ti^{3+}) and the criteria of eqn. (1) applies. Anderson localization may become important as a higher concentration of vacancies is involved. This concept will be described in some detail in Chapter 5, Section 5.1.a.

1.4. Purpose of the thesis.

The purpose of the research undertaken in this thesis is to investigate the structural and physical properties of the correlated systems $Nd_{(1-x)}TiO_3$ and $Sm_{(1-x)}TiO_3$ with an emphasis on M-I transitions. Based on the Ti-O-Ti bond angles observed in the parent titanates, $RTiO_3$, it is anticipated that the correlation strength will increase as with the decrease of the rare earth ionic size, the band width, W, decreases. Furthermore, with the progressive introduction of vacancies as one goes from x = 0.00 to x = 0.33 a higher hole (Ti^{4+}) concentration per rare earth ion is involved. This is expected to result in strong disorder, possibly leading to Anderson localization within these systems. Structural characterization is achieved by neutron and x-ray diffraction methods, while the physical properties are probed with magnetic susceptibility, resistivity, specific heat and thermopower measurements. The results from the present study are compared with those of the $R_{(1-x)}A_xTiO_3$ systems, notably $La_{(1-x)}Sr_xTiO_3$ and the vacancy

doped $La_{(1-x)}TiO_3$ system.

The plan for the remainder of the thesis is as follows: Chapter 2 presents the experimental details which describes sample preparation and a description of the instruments and techniques used to characterize the compounds of interest. Structural characterizations are presented in Chapter 3. The results of the magnetic studies are presented in Chapter 4 followed by the transport properties in Chapter 5. Within Chapters 2 to 5, a summary of previous results obtained for the related $R_{(1-x)}A_xTiO_3$ and $La_{(1-x)}TiO_3$ systems are presented. Finally, a summary and conclusions drawn from the present study as well as potential avenues for future research involving these systems are presented in Chapter 6.

CHAPTER 2

EXPERIMENTAL PROCEDURES

2.1. Sample Preparation

2.1.1 $Nd_{(1-x)}TiO_3$ system.

2.1.1.a. ***$NdTiO_3$:*** Polycrystalline neodymium titanate was prepared by arc-melting together pellets composed of stoichiometric amounts of neodymium oxide, Nd_2O_3(Research Chemicals, 99.99%) and titanium (IV) oxide, TiO_2 (Fisher Scientific, 99.97%) with titanium metal (99.9%) according to the equation:

$$Nd_2O_3 + 3/2\ TiO_2 + 1/2Ti \rightarrow 2\ NdTiO_3$$

The oxides were pre-dried previously overnight at 950°C to remove unwanted hydroxides and carbonates. They were then ground together in acetone and pressed into 3/8" pellets. The reaction was carried out on a water cooled copper hearth under 0.5atm of prepurified argon gas (99.998%). The product obtained was black in colour. Approximately, 5gms of material were prepared by this method.

2.1.1.b. ***Doped compositions:*** For the remaining compositions, x = 0.05, 0.10, 0.15, 0.17, 0.20, 0.25 and 0.30, the reactions were carried out under vacuum in a sealed molybdenum crucible placed in an induction furnace. This method has the advantage of a higher degree of control in arriving at the desired nominal composition. Stoichiometric amounts of titanium sesquioxide, "Ti_2O_3" (Cerac, 99.9%) and the pre-dried oxides, Nd_2O_3 and TiO_2, were weighed out according to,

$$(1-x)/2\ Nd_2O_3 + yTiO_2 + (1-y)/2\ Ti_2O_3 \rightarrow Nd_{(1-x)}TiO_3$$

The oxygen content of Ti_2O_3 was checked by thermogravimetric analysis (TGA) and was shown to be non-stoichiometric in oxygen, see TABLE 2.1. Furthermore, it was previously found that the residual oxygen in the reaction chamber results in a slightly more enriched oxygen product than desired. To compensate for this an excess of Ti_2O_3 was added. The molar amounts used for the preparation of each composition are found in TABLE 2.1. The oxides, approximately 5 grams in total, were ground together in acetone, made into 3/8" pellets and then sealed in a 5/8" molybdenum crucible. The crucible was placed into a graphite susceptor housed in a boron nitride shield. This assembly was then placed in a radio frequency induction furnace. The reaction conditions used for the preparations were typically ~1400°C in a vacuum of ~3 x 10^{-4} Torr or better for several hours. The temperature was monitored using an optical pyrometer with a tolerance of ±50°C. To achieve phase purity it was often necessary to grind the samples after the initial reaction and refire under the same conditions as before. Phase purity determination was carried out by X-ray powder diffraction using a Guinier Hägg camera. With the exception of the grey colour observed for the x = 0.25 and 0.30 compositions, the remaining compositions were black.

2.1.1.c. ***$Nd_{2/3}TiO_3$ and $K_2Nd_2Ti_3O_{10}$:*** Initial attempts to prepare this phase by firing stoichiometric amounts of the Nd_2O_3 and TiO_2 oxides in air according to,

$$1/3Nd_2O_3 + TiO_2 \rightarrow Nd_{2/3}TiO_3$$

resulted in the formation of $Nd_2Ti_2O_7$ and TiO_2. Subsequent attempts to perform the reaction in a sealed crucible using the induction furnace produced an impure product which included

TABLE 2.1: Molar quantities used for sample preparations.

Compound	Nd_2O_3	TiO_2	"Ti_2O_3"
$Nd_{0.95}TiO_3$	0.475	0.0614	0.4693[a]
$Nd_{0.90}TiO_3$	0.450	0.2559	0.3720[a]
$Nd_{0.85}TiO_3$	0.425	0.3756	0.3122[a]
$Nd_{0.83}TiO_3$	0.415	0.4438	0.2781[a]
$Nd_{0.80}TiO_3$	0.400	0.5459	0.2270[a]
$Nd_{0.75}TiO_3$	0.375	0.7033	0.1484[a]
$Nd_{0.70}TiO_3$	0.350	0.8657	0.0672[a]
Compound	Sm_2O_3	TiO_2	"Ti_2O_3"
$Sm_{0.95}TiO_3$	0.4750	0.0614	0.4693[a]
$Sm_{0.90}TiO_3$	0.4500	0.2667	0.3666[b]
$Sm_{0.87}TiO_3$	0.4350	0.3610	0.3195[b]
$Sm_{0.85}TiO_3$	0.4250	0.3643	0.3179[b]
$Sm_{0.83}TiO_3$	0.4150	0.4866	0.2567[a]

[a] $Ti_2O_{3.031}$; [b] $Ti_2O_{2.998}$

the $Nd_2Ti_2O_7$ phase as identified by x-ray powder analysis.

Consequently, an attempt to prepare this phase as single crystals was made using the flux method. Initially, predried Nd_2O_3 (0.989 g) and TiO_2 (1.124g) were mixed with a KF (8.711g,CERAC, 99.999%) / NaB_4O_7 (1.662g, Fisher Scientific 99.99%) flux in an inert atmosphere to avoid absorption of moisture by KF. The mixture was placed into a 20ml platinum crucible with a tightly fitting lid. The growth conditions involved heating the crucible to 1100°C, soaking at this temperature for 2 hours, then cooling down to 1000°C at 1°C/hr. The crucible was then quenched at 1000°C to RT and hot poured in order to isolate the crystals from the flux. The evaporation losses were high at ~59%. The product crystallized as transparent light purple blocks varying from ~ 0.25 to 0.75 mm^2, each consisting of very thin plates several microns thick. Elemental analysis by EDX revealed the presence of Nd, Ti and K, strongly suggesting incorporation of K into the perovksite structure. Determination of the cell constants of this phase by x-ray powder diffraction was not possible due to the strong preferred orientation of the plate-like habit of the crystals which was seen to persist even at the microscopic level as shown by TEM. Subsequent analysis by single crystal x-ray diffraction revealed that the compound is a layered compound of the formula $K_2Nd_2Ti_3O_{10}$.

As it became apparent that KF is an inappropriate choice as a flux reagent, CsF was tried instead as it was expected that the larger Cs ion would not be incorporated into the layered structure. Consequently, 0.7872 g of Nd_2O_3, 1.1161 g TiO_2 , 15.039 g CsF and 0.993 g NaB_4O_7 were ground together in an inert atmosphere and similar growth conditions were

used as before. The crystals that formed were transparent purple-brown in colour and rectangular in shape with dimensions of ~1 mm x 1.5 mm x 0.5 mm. The evaporation loss was extremely high at ~73%. Energy dispersive x-ray spectroscopy (EDX) analysis revealed Nd and Ti as the only metal ions present.

2.1.2. $Sm_{(1-x)}TiO_3$ system.

2.1.2.a. ***$SmTiO_3$ single crystals:*** A polycrystalline sample of $SmTiO_3$ was prepared using the induction furnace as described above, following the equation,

$$0.5\ Sm_2O_3 + 0.5662\ TiO_{1.046} + 0.4338\ TiO_2 \rightarrow SmTiO_3$$

Single crystals of the nominal phase, x = 0.00 were obtained by firing the polycrystalline sample to just above its melting point (~1800°C) in a sealed molybdenum crucible in the induction furnace with subsequent quenching to room temperature. The crystals formed as shiny black blocks with very well defined faces having an average dimension of ~1.5mm × 1.5mm × 1mm.

2.1.2.b. ***Doped compositions:*** The doped compositions x = 0.05, 0.10, 0.13, 0.15 and 0.17 were prepared using the induction furnace as described previously for $Nd_{(1-x)}TiO_3$, using instead samarium oxide, Sm_2O_3 (Rhone Poulenc, 99.99%).The molar quantities used can also be found in TABLE 2.1.

2.2. INSTRUMENTATION:

2.2.1. Thermogravimetric analysis (TGA):

The oxygen content of the nominally prepared compositions was determined by thermogravimetric analysis using a Netzch STA 409 Thermal Analyser. The method is based on the weight change observed as a function of temperature or time. In our particular situation the samples were heated under flowing air at 1000°C so that complete oxidation to the $Nd_2Ti_2O_7$ phase was obtained. The weight change associated with this oxidation was then used to determine the amount of oxygen present per formula unit assuming the nominal rare earth and titanium content. The error in the experimental weight gain is ± 0.05%.

2.2.2. Energy Dispersive X-ray Spectroscopy (EDX):

Analysis of the metal ions in the single crystals of $K_2Nd_2Ti_3O_{10}$ and $Nd_{2/3}TiO_3$ were carried out with this method using a Philips 515 Scanning Electron Microscope with a LaB6 Cathode equipped with a Link QX2000 energy dispersive x-ray analyser at McMaster University. The basis of the technique lies in the ionization of the atoms when the sample is exposed to a high energy electron beam. The atoms are ionized ejecting an inner shell electron. This results in an energetic atom with a vacant electron state. In order to relax to its ground energy state, an electron from an upper shell falls down to fill this vacancy and in the process releases an x-ray photon. Consequently, by collecting and analyzing the energy of these x-rays the constituent elements of the sample can be identified.

2.2.3. Transmission Electron Microscopy (TEM):

A Philips CM12 transmission electron microscope operating at 120 kV was used for the electron diffraction study of $Nd_{2/3}TiO_3$ in the SAED (selected area electron diffraction) mode, which allows one to obtain a diffraction pattern from a specific region of the sample under investigation. From the diffraction pattern, d-spacings can be calculated from,

$$d = \lambda L/R \quad (1)$$

where λ is the wavelength used, L is the camera length and R is the distance between the transmitted spot to the diffracted spot. To prepare the $Nd_{2/3}TiO_3$ composition for analysis, several crystals were finely ground and suspended in butanol. Several droplets of this suspension were then placed onto the sample holder which consisted of a holey carbon film supported by a copper grid.

2.2.4. Precession Photography:

Single crystal precession photographs were taken using a Charles Supper Company precession camera (Model 3310) with Mo Kα radiation (λ= 0.71069 Å). The crystal was mounted on a glass fibre with epoxy which was subsequently mounted on a goniometer. The crystal was aligned on the camera such that a major cell axis was parallel to the incident x-ray beam. The axis was then offset by an angle μ and allowed to precess about the beam. By keeping a piece of film tangential to the sphere of reflection of the moving crystal, the precession camera allows undistorted images of the reciprocal lattice to be obtained.

2.2.5. Guinier Hägg X-Ray Powder Diffraction:

A Guinier-Hägg camera (IRDAB Model XDC700) with Cu $K\alpha_1$ radiation was used for phase identification and cell parameter determination. The camera utilizes a curved quartz crystal as a monochromator to produce a highly monochromatic, intense and convergent x-ray beam. The basis of operation of the Guinier camera makes use of the theory of a circle, illustrated in Fig. 2.1. The quartz crystal is oriented such that an incident, divergent beam of x-ray radiation is monochromated to yield pure Cu $K\alpha_1$ radiation (λ= 1.5406Å). The monochromated, convergent beam then passes through the sample, denoted by point X. Any radiation that is not diffracted on passing through the sample comes to a focus at point A on the circle and represents the undiffracted beam at $2\theta = 0°$ which is used as a reference point. This reference point is obtained by opening the beam stop for a fraction of a second while the x-rays are turned on. Similarly, diffracted beams are focussed at various points along the circumference of the circle, at B, C etc. The diffraction pattern can thus be recorded by placing a length of film along that part of the circle defined by A, B, C etc. Since the distance between the reference point A and any other point on the circle, B, C, scales linearly with 2θ, the d-spacings of the diffracted lines can thus be obtained easily.

The samples for Guinier analysis (<1 mg) were prepared by grinding and mixing with high purity silicon, which is used as an internal standard. The internal standard serves to correct for film shrinkage and stretching during processing of the film. The intensities and positions of the diffraction lines on the film were digitized using a KEJ Instruments Model LS20 line scanner. The digitized information was subsequently converted to accurate d-

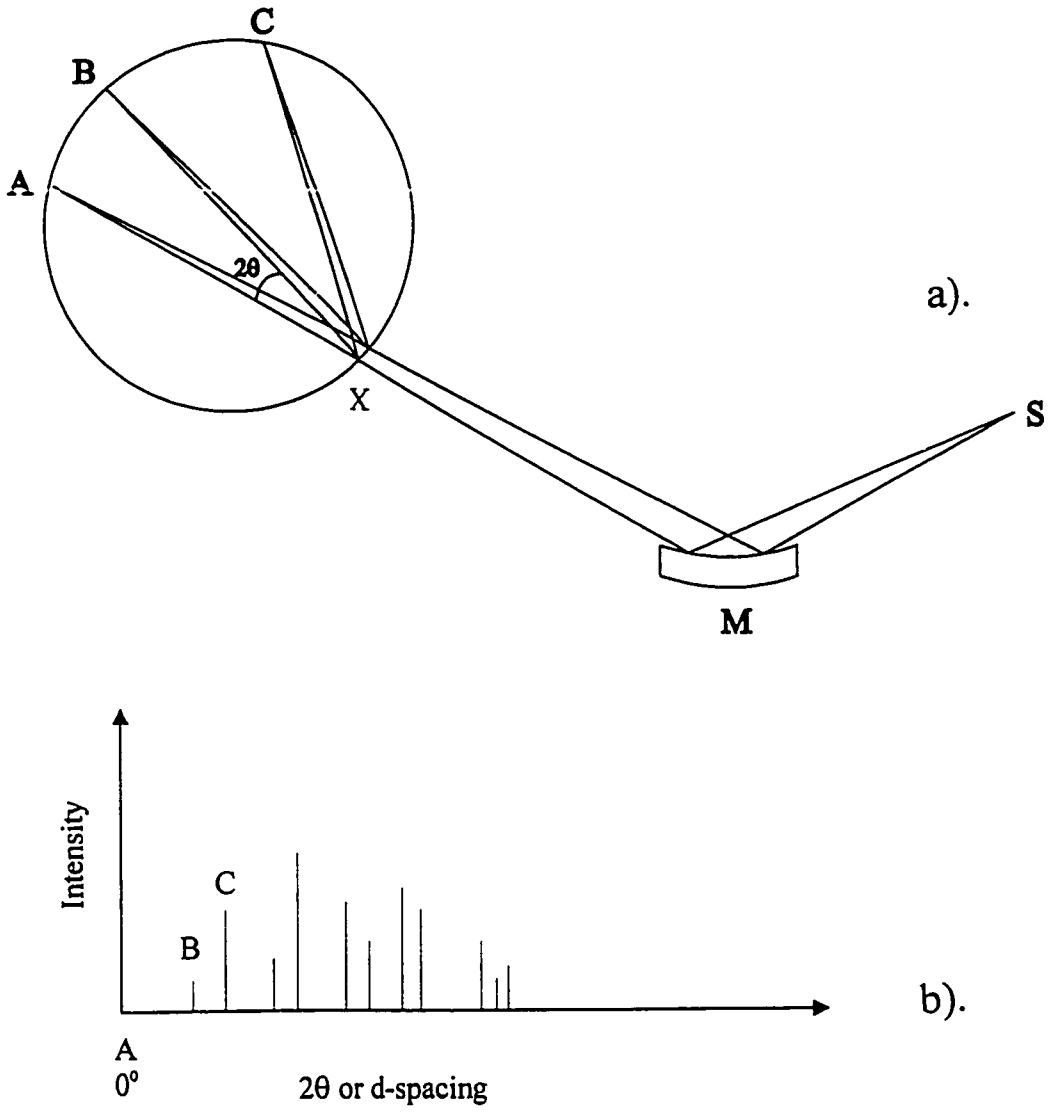

Fig. 2.1. a). Arrangement of the crystal monochromator (M), source (S) and sample (X) in a focusing camera. b). Powder diffraction profile. Adapted from (West, 1984)

spacings using the program SCANPI. The unit cell constants were extracted from this data using the least squares refinement program LSUDF.

2.2.6. X-Ray Powder Diffraction:

Data were collected for the samarium samples for structural refinement using a Nicolet I2 automated powder diffractometer with Cu Kα radiation. The data were collected over the 2θ range of 10° to 90° with a 0.03° step size. Structural refinements were carried out using the Rietveld analysis program DBWS-9006 on a 486DX-66MHz IBM compatible computer.

2.2.7. Neutron Powder Diffraction:

Neutron powder data, for the purposes of chemical and magnetic structural determinations, were obtained at the McMaster Nuclear Reactor. A beam with wavelength 1.3920Å was obtained by reflection from a (200) copper monochromator. A position sensitive detector (PSD) was used to collect the data. Typically, the data were collected over a 2θ range of 25° for a single detector setting so that several settings were required before a full dataset was obtained. Once obtained, the raw data were corrected for the geometry of the instrument. The corrected data were then refined using the Rietveld analysis program DBWS-9006.

For structural characterizations, the samples (typically 4-5 grams) were placed into a thin walled vanadium can. Data were typically collected over a 2θ range of 10° to 120° at

room temperature. For the purposes of collecting data at low temperatures for magnetic structural determinations, a thin walled aluminum can filled with He exchange gas and sealed with an indium gasket was used. Refrigeration control was maintained using a CTI Inc. Model 21 closed cycle refrigerator with a Cryogenics Inc. Model DRC 80C temperature controller. Measurements were made over a 2θ range of 10° to 40° for a series of temperatures from room temperature to 20K. An extended data set ranging from 10° to 78° was collected at 10K for a full magnetic structure refinement.

2.2.8. Single Crystal X-Ray Diffraction:

Data for the nominal $SmTiO_3$ was acquired using a Siemens P3 four circle diffractometer using Ag-Kα radiation (λ = 0.56086Å). An ω-2θ scan was used and the semi-empirical ψ scan method was used for absorption correction to the data.

In the case of the $K_2Nd_2Ti_3O_{10}$ and $Nd_{2/3}TiO_3$ data were collected with a P4 Siemens diffractometer equipped with a Siemens SMART 1K Charge Coupled Device (CCD) Area detector and a rotating anode using graphite monochromated Mo-Kα radiation (λ = 0.71073Å). Due to the plate like habit of both compounds, face indexed absorption corrections were applied to the datasets. Structural refinements of all datasets were carried out with the SHELXTL93 software package (Sheldrick, 1993).

2.2.9. Single Crystal Neutron Diffraction:

Neutron data for nominal $SmTiO_3$ were collected using the D9 four circle single

crystal diffractometer at the Institut Laue-Langevin, Grenoble, France. The diffractometer is equipped with a two dimensional position sensitive detector (PSD) and a wavelength of ~0.4710Å, obtained by reflection from a Cu(220) single crystal monochromator, was used. A Displex cryostat was used for temperature control down to 15K. At 15K, several key magnetic reflections at low angle were scanned for ~6 hours each using an ω-scan. A full dataset (2θ = 5°-35.93°) was also collected at this temperature for the purposes of a structural refinement. Due to time constraints on the experiment, it was not possible to do this at room temperature. The integrated intensities were extracted from the raw data using the program RACER and structural refinement of the dataset collected at 15K was carried out using the SHELXTL93 software package (Sheldrick, 1993).

2.2.10. Magnetic Susceptibility Measurements:

A Quantum Design SQUID (Superconducting Quantum Interference Device) magnetometer was used to measure the d.c. susceptibility as a function of temperature in the range of 5K-300K. In a typical experiment the sample was cooled to 5K in zero field (ZFC). Data were then collected from 5K to 300K with an applied field of ~50 or 100 Oe. The sample was subsequently cooled in an applied field (FC) of ~50 or 100 Oe and the measurements were repeated in the same manner as before from 5K to 300K. The samples used were sintered pellets having typical masses of ~50-100mg.

2.2.11. Resistivity Measurements:

The temperature dependence of the resistivity was measured using the van der Pauw four probe method (van der Pauw, 1958). The samples were mounted on the probe using GE varnish with four Au-0.07%Fe measurement wires attached to the sample using silver paste. The probe is inserted into a helium Dewar in order to perform the measurements from room temperature down to 5K. The samples used were sintered, polycrystalline blocks ~4mm × ~4mm × 2 mm thick.

2.2.12. Specific Heat Measurements:

The specific heats of the samples were measured using an adiabatic heat pulse method. In this method the sample temperature, T_1, is monitored for a predefined period of time, t_1 (seconds), after which a heat pulse of known power, P (typically in μW), is applied for t_0 seconds. After a decay period, t_2 (seconds), to allow for internal thermal equilibration of the sample, the temperature is again monitored. The heat capacity is then obtained from the relationship,

$$C = \lim_{\Delta T \to 0} P.t_o / \Delta T \quad (2)$$

where t_o is the duration of the heat pulse and ΔT is the temperature difference before (T_1) and after (T_2) the heat pulse is applied.

The apparatus consisted of an Oxford Instruments Heliox insert which is equipped with a sorption pumped ^{3}He refrigerator capable of reaching temperatures below 1K. An Oxford Instruments ITC503 temperature controller was used for temperature monitoring and

variation. The sample is mounted onto a sapphire plate affixed to the Heliox insert and on this plate are also attached a RuO_2 temperature sensor and strain gauge heater. The measurements were carried out on polycrystalline samples that exhibited metallic behaviour. Typical sample sizes varied from ~125-200 mg and were ~ 1.5-2mm thick. The experiments were performed at the University of Toronto.

2.2.13. Thermopower Measurements:

In the determination of Seebeck coefficients two fundamental quantities must be measured, the temperature gradient across the sample, ΔT, and the corresponding voltage, E_s, that results. The equipment used for measuring this physical property was built at McMaster University. As measurements from this instrument are being reported for the first time in this body of work some detail is warranted in its description. Typically, for low temperature thermopower measurements, helium dewars are often used into which a sample probe is inserted. However in the design described here, a CTI Inc. Model 21C closed cycle refrigerator is used. The advantages of using this type of cooling system lies in the complete automation of the experiment, zero liquid helium consumption and the provision of a static environment (vacuum) for measurement conditions. A schematic diagram of the sample holder is shown in Fig. 2.2. The sample is sandwiched between two copper heads **A** and **B** which are in thermal contact (but electrically isolated) with base stage **C**, itself being affixed to the 10K cold stage on the refrigerator. A 6Ω ceramic resistor is housed in each of the copper heads, **A** and **B**, which serves as heaters, while the base stage **C** has a wire wound Ni-

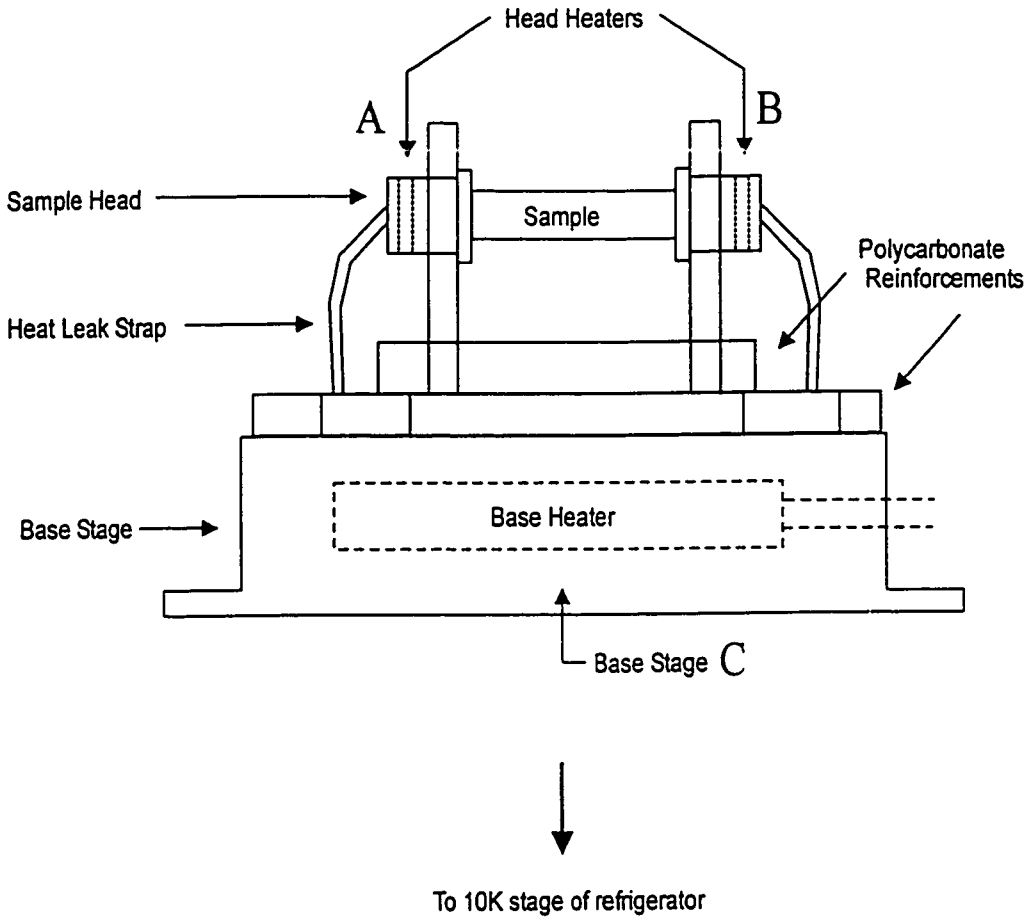

Fig. 2.2. Schematic diagram of the sample holder for thermopower measurement.

Cr 25 Watt cartridge heater. The purpose of the base heater is to allow the copper heads to achieve higher temperatures. In this manner the temperature gradient across the sample can be controlled by varying the power to the heaters in heads **A** and **B** while keeping the temperature of the base stage **C** constant. The temperature gradient can thus be reversed across the sample between **A** and **B**. The advantage of doing this is to reduce any systematic errors presented by the asymmetry of the two copper heads during fabrication.

The temperature gradient of the sample is measured using two chromel vs. Au-0.07% Fe thermocouples attached to the sample with silver paste. The reference junction of each thermocouple is placed in an electric ice-point bath. Similarly, the Seebeck voltage is measured from two copper wires attached to the sample using silver paste. Care must be taken to ensure that the copper wires are placed at the same points as the thermocouples on the sample as shown in Fig. 2.3.

The three heaters on the sample holder are controlled by individual Lakeshore Model 321 autotuning silicon diode temperature controllers, while the voltages generated are measured with a Keithly Model 2000 digital multimeter equipped with a Model 2000 scanner card. For complete automation of the data collection process each instrument is controlled via a standard RS232 serial interface using a 486-66 MHz IBM compatible computer. A brief description of the methodology for the collection and extraction of data is given below.

In order to determine the Seebeck coefficients at various temperatures the sample is allowed to equilibrate at each temperature of interest. At each of these temperatures the base stage **C** is held at a constant temperature difference below the two heads A and B. One end

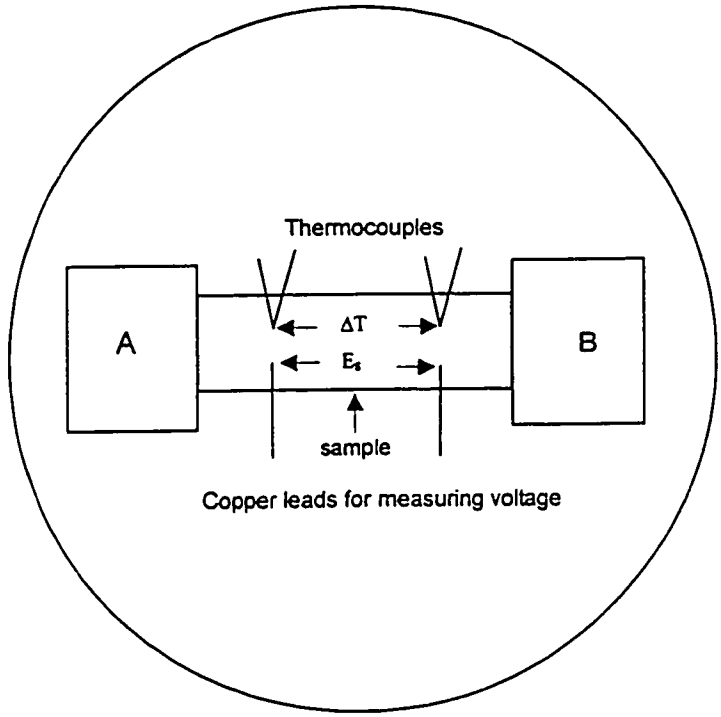

Fig. 2.3. Top view of sample holder showing the arrangement of electrical contacts. The copper heads are labelled A and B for easy reference.

of the sample is held at a constant temperature, $\mathbf{T_1}$, while the other end, $\mathbf{T_2}$ is allowed to vary in the range of $\mathbf{T_1}$±5K in δT (2K) steps. This effectively reverses the temperature gradient across the sample and Fig.2.4 illustrates this more clearly. At each δT step in the temperature profile, the sample is allowed to reach equilibrium at which point the temperature difference, ΔT, across the sample and the resulting voltage, E_s, are measured several times for statistical averaging. Once the temperature profile (T_1 ±5K, δT) has been swept, the sample is heated to the next temperature of interest and the measurement process is repeated. The Seebeck coefficient, **S'**, at each temperature of interest, is then extracted from the gradient of the averaged voltage (E_s) vs. the averaged temperature difference (ΔT) obtained at each δT step, see Fig. 2.5. This method of obtaining the Seebeck coefficient compensates for any systematic errors present in the experiment such as d.c. offsets. From this value the absolute thermopower of the sample may be determined by compensating for contributions to the thermopower by the silver paste and the copper wires , thus leading to the expression,

$$S_{sample} = S^{'} + S_{Ag} + S_{cu} \quad (3)$$

The integrity of the data obtained from this instrument was tested using two standards measured at Cornell University. The chosen standards were $CePd_3$ (provided by Cornell University) and $Nd_{0.85}TiO_3$. Very good agreement can be seen for both standards in Figs. 2.6 and 2.7 with no more than 10% variation being observed in the data. Furthermore, reproducibility of the data for the $Nd_{0.85}TiO_3$ sample after a separate mounting attests to the reliability of the instrument, see Fig. 2.7. The measurements were carried out under vacuum (~10^{-5} Torr) using sintered polycrystalline samples which were generally between 5-8mm in

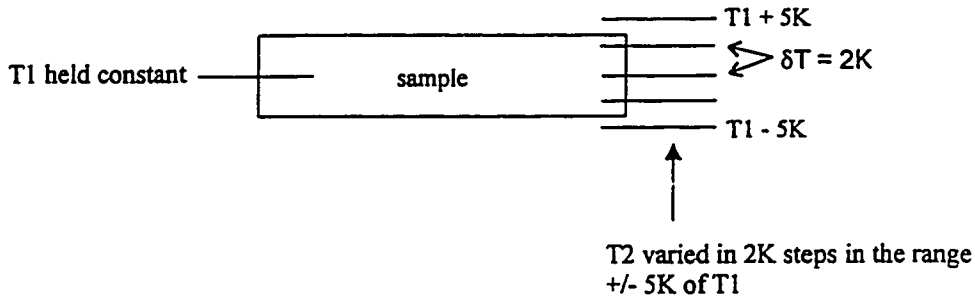

Fig. 2.4. An example of a temperature profile across the sample during the thermopower experiment.

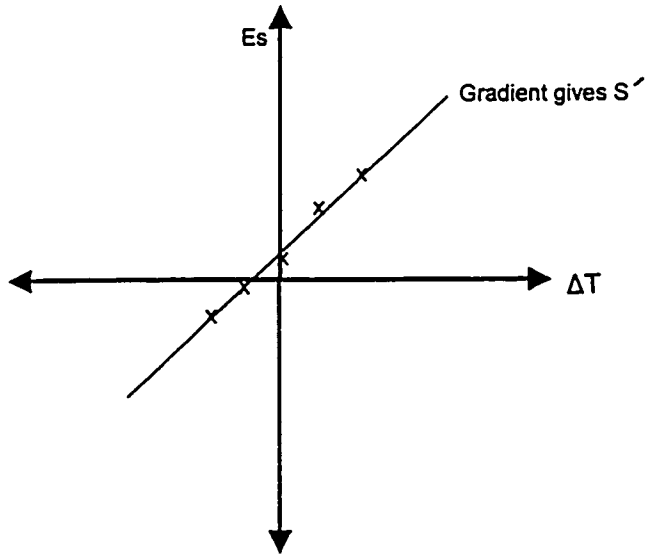

Fig. 2.5. Seebeck voltage, E_s vs. temperature gradient, ΔT. The Seebeck coefficient is obtained from the slope of the graph.

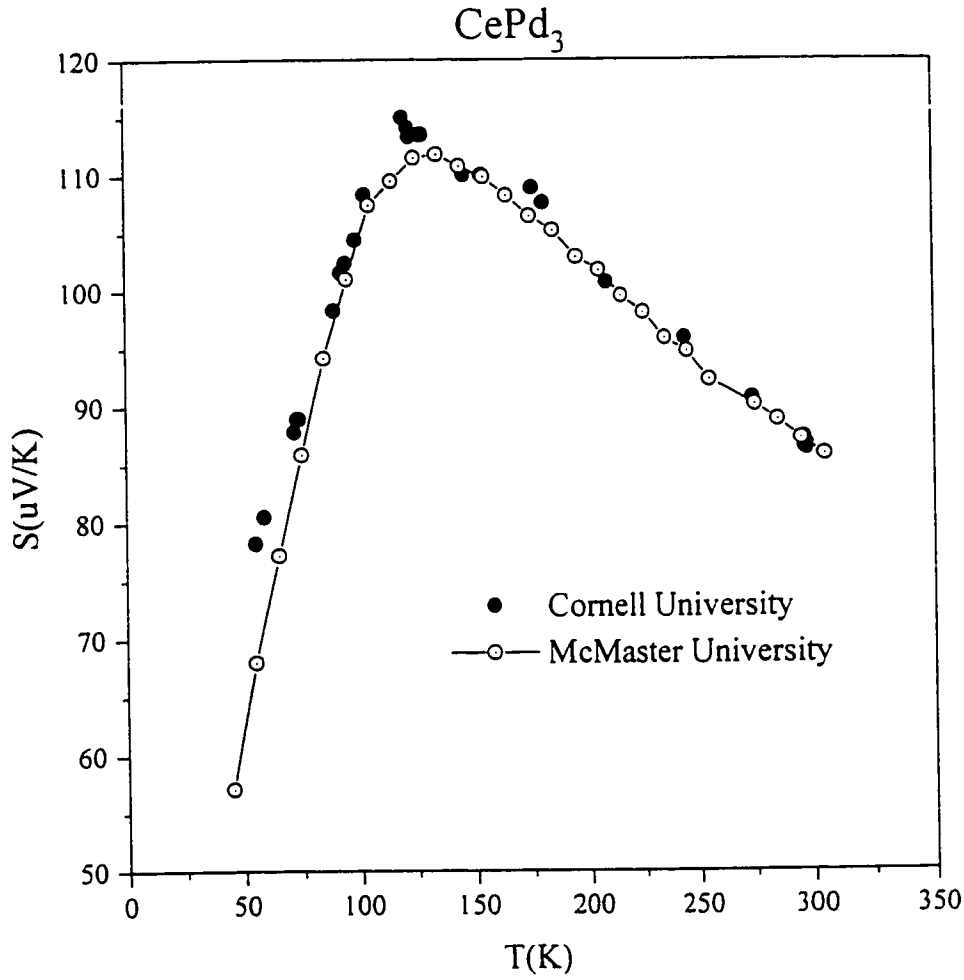

Fig. 2.6. Comparison of thermopower data for the $CePd_3$ standard obtained by Cornell University.

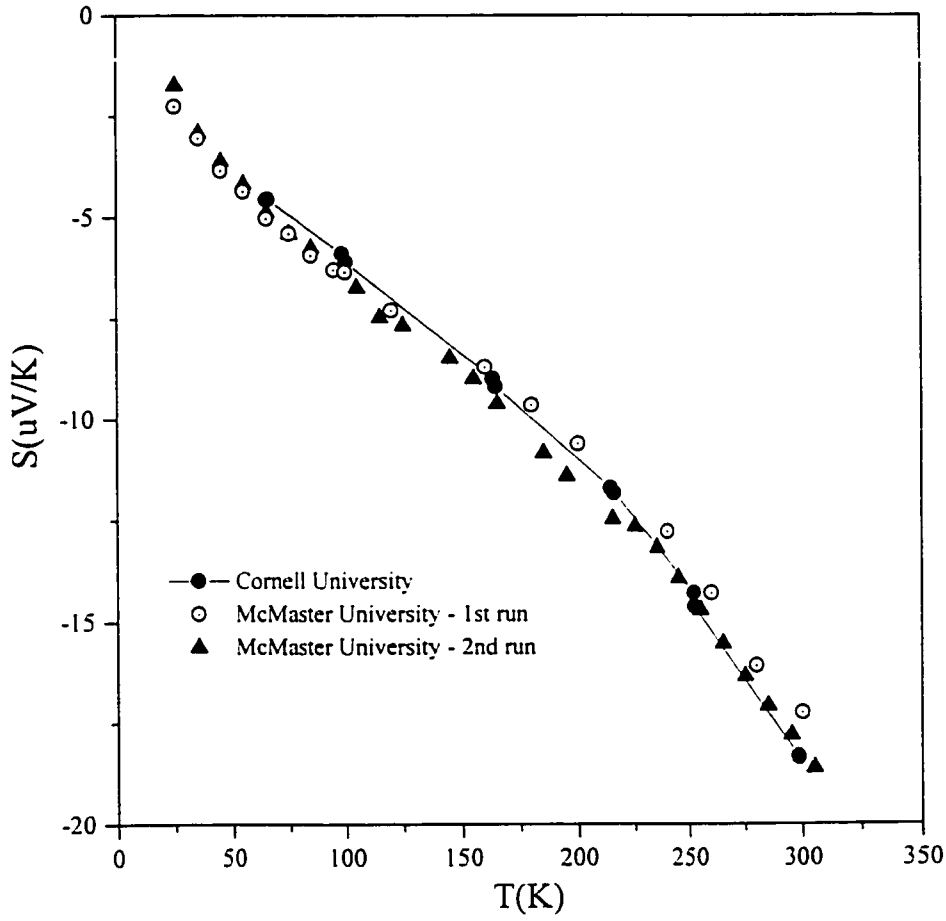

Fig. 2.7. Comparison of thermopower data for the $Nd_{0.85}TiO_3$ standard obtained by Cornell University.

length and were constrained to have parallel faces to ensure good thermal contact with the faces of the copper heads.

CHAPTER 3

STRUCTURAL CHARACTERIZATION

In this chapter the structural aspects of the $Nd_{(1-x)}TiO_3$ and $Sm_{(1-x)}TiO_3$ systems are presented and their implications for correlation effects on the physical properties in these systems are discussed. These results are preceded by a brief outline of diffraction theory and the use of Rietveld analysis in structural refinements from powder diffraction data, the principal technique used in this study for structural analysis. This discussion is followed by a survey of previous work carried out for electronically similar systems.

3.1. Fundamental Diffraction Theory:

Generally, there have been two approaches used in the description of diffraction by crystals. The first approach is based upon a series of mathematical expressions developed by Laue (von Laue, 1912). The alternative approach, developed by Bragg (Bragg, 1913), which is conceptually simpler to understand is presented here.

In Bragg's development, only coherent scattering is considered in which the wavelength is conserved during the diffraction process. The crystal is treated as being composed of layers (or planes) each of which serves as a semi-transparent mirror. In the crystalline state the arrangement of these planes is periodic and related to the dimensions of the unit cell. When x-ray radiation is incident on these planes, some of the x-rays are *reflected* from a plane with the angle of reflection equal to the angle of incidence, while the

rest are transmitted to be subsequently reflected by "deeper lying" planes. This situation is illustrated in Fig. 3.1, which shows the process using only two planes.

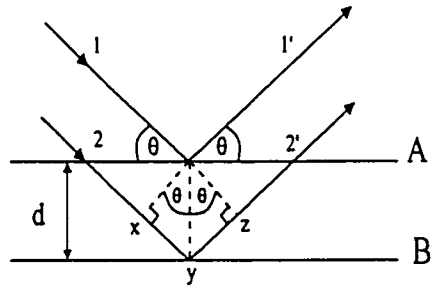

Fig.3.1. Illustration of Bragg's Law.
Adapted from (West, 1984)

In reality, the x-rays are not really reflected by the planes but are scattered in all directions. As x-rays are electromagnetic in nature, their inherent electric fields interact with the electrons on any atom causing the electrons to emit wavelets. When these wavelets interfere constructively, diffraction occurs. This condition is achieved when the extra distance traveled by x-ray 22' (i.e. xy + yz) on the diagram is equivalent to an integral number of wavelengths ($n\lambda$). Therefore, the angle, θ, (called the Bragg angle) associated with a particular interplanar spacing,d, can be determined by geometry, that is,

$$xy = yz = d \sin\theta \qquad (1)$$

$$\therefore xy + yz = 2d \sin\theta = n\lambda \qquad (2)$$

$$n\lambda = 2d \sin\theta \qquad (3)$$

This last expression is known Bragg's law where n is an integral value which describes the

the order of the diffraction. In real crystals, there are thousands of planes so that constructive interference gives rise to a sharp diffraction line and places a stringent condition on the Bragg angles at which reflections may be observed. If this angle is incorrect by more than a few tenths of a degree, destructive interference occurs and no diffraction line is observed.

A consequence of eqn.(3) is that if the Bragg angles, θ, are measured then the interplanar spacing, d, can be determined for a known wavelength. The interplanar distance, d, gives important structural information regarding the lattice parameters and symmetry of the unit cell. Furthermore, the intensities of the diffracted beams contain information related to the arrangement of atoms within the unit cell.

Each atom in the unit cell has an inherent scattering power, f_o, which is dependent on its type and $\sin\theta/\lambda$, where θ is the Bragg angle. When $\sin\theta = 0°$, f_o is equal to the atomic number of the atom, Z. As θ increases, differences in the path length occur which results in the reduced amplitude of the scattered wave. The scattering factor of an atom is also influenced by the thermal motion of the atom about its rest position in the unit cell. The magnitude of this vibration depends to a large extent on temperature, the atomic mass and the bonding nature of the atom. The effect of these factors is to spread the electron cloud over a larger volume causing the scattering power to diminish rapidly. Thus, the scattering power for a real atom is not f_o, but

$$f_n = f_o e^{-2B(\sin^2\theta/\lambda^2)} \quad (4)$$

where B is related to the mean square amplitude of atomic vibration.

The structure factor, F(hkl), represents the summation of N waves scattered in the direction of the hkl reflection by N atoms in the unit cell. The amplitude of each scattered wave is proportional to f_j, the scattering factor of the j-th atom in the unit cell. Mathematically this is expressed as,

$$F(hkl) = \sum f_j \exp[2\pi i(hx_j + ky_j + lz_j)] \quad (5)$$

where hkl represents the Miller indices of the reflecting plane, x_j, y_j, z_j are the atomic positions. The exponential term takes into account the phase differences of the scattered waves with respect to a wave scattered at the origin of the unit cell. Thus, eqn.(5) demonstrates that the structure factor can be derived from a given electron density distribution. The inverse of this is also true as the Fourier transform of the structure factors gives the electron density, ρ(x,y,z), in the unit cell. This is expressed as,

$$\rho(x,y,z) = \frac{1}{V}\sum_h \sum_k \sum_l F(hkl)\exp[-2\pi i(hx + ky + lz)] \quad (6)$$

where V is the volume of the unit cell. Hence in a single crystal determination, through a calculation of the structure factors for each observed reflection, the electron density of the unit cell can be obtained through Fourier synthesis.

In practice, it is the intensities of the diffracted x-rays that are measured and these in turn are related to the structure factors by,

$$I \propto F(hkl)^2 \quad (7)$$

In extracting the structure factors from the intensities several important factors must be considered. The measured intensities must be corrected for systematic errors owing to the physics of diffraction. Consequently, Lorentz, polarization and geometric and absorption corrections are applied. Furthermore, the proper phase of the structure factor must also be determined and phasing techniques such as direct and Patterson methods have been developed for this purpose.

Once the observed structure factors, F_o, have been obtained, they are compared with calculated values, F_c, which are based on trial solutions of a structural model. Refinement of the observed and calculated structure factors is accomplished using a least squares minimization of the function,

$$D = \sum_{hkl} w_{hkl}\left(\left|F_o^{\,2}\right| - k\left|F_c^{\,2}\right|\right)^2 \quad (8)$$

where w_{hkl} is the weight given to the observed reflection and k is a scale factor. The agreement between the observed and calculated structure factors is measured by the residual index, wR, and the goodness of fit, S, shown in TABLE 3.1. Note that eqn. (8) is based on refinement against F^2. The residual index, R1, which is based on traditionally refining against F is also included in TABLE 3.1.

3.2. Profile Analysis: The Rietveld Method.

In cases where single crystals are not available, powder diffraction methods can also be used for structural analysis. The method however presents a severe limitation as being a

TABLE 3.1: Statistical Indicators for A). Single crystal and B). Rietveld method.

A/.

$$wR2 = \left\{ \frac{\sum [w(F_o^2 - F_c^2)^2]}{\sum [w(F_o^2)^2]} \right\}^{1/2}$$

$$R1 = \frac{\sum \left| |F_o| - |F_c| \right|}{\sum |F_o|}$$

$$S = \left\{ \frac{\sum [w(F_o^2 - F_c^2)^2]}{(n-p)} \right\}^{1/2}$$

B/.

$$R_p = \frac{100 \sum |y_i(obs) - y_i(calc)|}{\sum |y_i(obs)|}$$

$$R_{wp} = 100 \sqrt{\frac{\sum w_i [y_i(obs) - y_i(calc)]^2}{\sum w_i y_i^2(obs)}}$$

$$R_{exp} = 100 \sqrt{\frac{N - P + C}{\sum w_i y_i^2(obs)}}$$

$$S = \frac{R_{wp}}{R_{exp}}$$

$$R_{Bragg} = \frac{100 \sum |"I(obs)" - I_c|}{\sum "I(obs)"}$$

structure solution method when compared to the single crystal method. This is primarily due to the problem of severe peak overlap which results in the loss of valuable structural information and is especially problematic for low symmetry structures.

In the late 1960's, Rietveld developed a profile refinement method which surmounts this problem (Rietveld, 1969). The method is based on a curve fitting procedure in which a least squares refinement minimizes the difference between the observed and calculated profiles rather than individual reflections. For this purpose the method uses each point in the intensity profile thus leading to greater efficiency in retrieving information from the superimposed reflections in the diffraction pattern. Mathematically, this minimization is expressed as,

$$M = \sum_i w_i [y_i(obs) - y_i(calc)]^2 \quad (9)$$

where w_i is a weighting factor, $y_i(obs)$ is the observed intensity at the i-th step of the profile which includes a background contribution and $y_i(calc)$ is the calculated intensity at the i-th step.

For a routine structural refinement by the Rietveld method, a starting structural model is highly desirable. In addition instrument related parameters are also required such as the zero point of the instrument and the line profile parameters U, V, W which are used to calculate the full width at half maximum (FWHM), H_k, of a reflection at an angle, θ, where,

$$H_k^2 = U \tan^2\theta + V \tan\theta + W \quad (10)$$

The parameter U is dependent on the wavelength resolution, $\Delta\lambda/\lambda$, while V, which is a

negative quantity, is dependent on the divergence of the primary beam plus the mosaic spread of the sample. The parameter W is defined by the cross section of the incident beam or the diameter of the sample.

Originally, the Rietveld method was developed for the analysis of neutron diffraction data because the peak shape function (PSF) is described by a simple Gaussian function. Thus, the profile of a powder diffraction line can be written as,

$$j_i = tF_k^2 j_k L_k \frac{2\sqrt{\ln 2}}{H_k\sqrt{\pi}} \exp\left\{-\frac{4\ln 2(2\theta_i - 2\theta_k)^2}{H_k^2}\right\} = tF_k^2 j_k L_k \phi_k^* \qquad (11)$$

where t = the aperture of the counter

F_k = the structure factor of the reflection

j_k = the multiplicity of the reflection

L_k = the Lorentz factor

θ_k = the Bragg angle

H_k = the full width at half maximum (FWHM) of the reflection

ϕ^*_k = the shape function of the profile of the reflection (e.g. Gaussian)

The index k is an abbreviation of the Miller indices hkl.

In the case of high resolution data or x-ray diffraction data, the PSF is not adequately described by the Gaussian function and several functions have been suggested to fit the measured profiles accurately in these instances, such as Lorenztian or Cauchy, Pseudo-Voight, Pearson 7 or Split Pearson.

Taking all these considerations into account, refinement of the structural model can then proceed. A measure of good fit from the Rietveld method is gauged by several factors. Most notably is the requirement that no extra peaks are present in the difference intensity plot between the calculated and observed profiles. In addition, statistical indicators are also used, similar to those for single crystal structure analyses. These are summarized in TABLE 3.1. More detailed accounts of single crystal and powder diffraction methods can be obtained in the following references, (Bacon, 1955; Bish and Post, 1989; Stout and Jensen, 1989; Warren, 1969; Young, 1993)

3.3. Previous Results:

Since the alkaline earth doped systems, $R_{(1-x)}A_xTiO_3$, are electronically similar and relevant to this body of work a brief summary of their structural properties is presented here. As mentioned in Chapter 1, the crystal structures of the $RTiO_3$, R= La-Lu, compounds are based on the orthorhombically distorted $GdFeO_3$ structure (Greedan, 1985). With the introduction of alkaline earth metal cations or vacancies on the A-site such as in $La_{(1-x)}Sr_xTiO_3$, $Nd_{(1-x)}A_xTiO_3$, A = Ba, Sr, Ca and $R_{(1-x)}TiO_3$ structural phase changes can be induced. In the $La_{(1-x)}Sr_xTiO_3$ system a phase transition is observed from orthorhombic to cubic with similar observations for the $Nd_{(1-x)}A_xTiO_3$ series. For the mixed rare earth series, $La_{(1-x)}Sm_xTiO_3$ and $R_{(1-x)}Nd_xTiO_3$ (R=Ce, Pr), no structural phase changes have been observed due to the similarity in size of the rare earth ions and that the titanium oxidation state is held constant at +3. The results for such systems are summarized in TABLE 3.2.

TABLE 3.2: Summary of structural phase transitions in related alkaline earth and vacancy doped systems.

System	Structure type	Range	Reference
$La_{(1-x)}Sr_xTiO_3$	Pnma	$x \leq 0.30$	(Sunstrom et. al., 1992)
	Imma	$0.30 < x < 0.80$	
	Pm3m	$x \geq 0.80$	
$R_xBa_{(1-x)}TiO_3$			(Eylem et. al., 1992)
R = La	Pnma	$0.85 \leq x \leq 1.0$	
	Pm3m	$0.15 \leq x < 0.85$	
R = Nd	Pnma	$0.70 \leq x < 0.98$	
	Pm3m	$0.10 \leq x < 0.70$	
	P4mm	$x < 0.05$	
$Nd_{(1-x)}A_xTiO_3$			(Eylem et. al., 1995)
A = Ca	Pnma	$0 \leq x \leq 0.80$	
A = Sr	Pnma	$0 \leq x \leq 0.30$	
	Pm3m	$x \geq 0.70$	
$La_{(1-x)}Sm_xTiO_3$	Pnma	$0 \leq x \leq 1$	(Yoshii and Nakamura, 1997)
$Ln_{(1-x)}Nd_xTiO_3$ (Ln = Ce, Pr)	Pnma	$0 \leq x \leq 1$	(Yoshii, 1998)
$La_{(1-x)}TiO_3$	Pnma	$0 \leq x \leq 0.20$	(MacEachern et. al., 1994)
	Imma	$0.20 < x \leq 0.25$	
	Pban	$0.25 < x \leq 0.33$	

In earlier investigations of the vacancy doped systems, $R_{(1-x)}TiO_3$, only the cell constants have been reported (Bazuev et al., 1978; Bazuev et al., 1979; Kirsanov and Bazuev, 1986). In more recent work the structures of members comprising the $La_{(1-x)}TiO_3$ system have been investigated in detail (MacEachern et al., 1994). In this system three structural phases are encountered from Pnma to Imma and finally to Pban structure types. The latter being an apparently novel perovskite whose structure will be described later.

Very limited structural information has been reported for the $Nd_{(1-x)}TiO_3$ and $Sm_{(1-x)}TiO_3$ systems which are summarized in TABLE 3.3. Of particular interest is the $Nd_{2/3}TiO_3$ phase and the existence of the samarium titanates in the region $0 \leq x \leq 0.18$ (Bazuev et al., 1983). The $Nd_{2/3}TiO_3$ phase was reported to be prepared by two methods, by firing the oxides in vacuum at ~1400°C and by precipitation of the hydroxides (Bazuev et al., 1979; Sych et al., 1976). From these two reports however, some ambiguity is found regarding the cell constants obtained, see TABLE 3.3. As single crystals of this phase have been prepared for the first time in this work some emphasis is placed on a detailed structural study employing a variety of techniques. Overall, however, it is intended to identify any structural phase transitions that may exist in these systems as well as the range of stability for the $Sm_{(1-x)}TiO_3$ solid solution.

3.4. Present Work:

Once each compound of interest has been prepared it is checked for phase purity by Guinier x-ray powder diffraction. If phase purity is achieved, the oxygen content of each composition is determined by thermogravimetric analysis. The results for both the neodymium and samarium

TABLE 3.3: Summary of previous structural work for the $Nd_{(1-x)}TiO_3$ system.

$Nd_{(1-x)}TiO_3$	Symmetry	Cell Constants / Å
†$NdTiO_{3.013}$	Orthorhombic	a = 5.513(3) b = 5.636(3) c = 7.790(3)
†$Nd_{0.90}TiO_{3.019}$	Cubic	a = 3.890(1)
†$Nd_{0.80}TiO_{3.008}$	Cubic	a = 3.872(1)
†$Nd_{0.70}TiO_{3.013}$	Orthorhombic	a = 3.850(1) b = 3.860(1) c = 7.720(2)
†$Nd_{2/3}TiO_{2.875}$	Orthorhombic	a = 3.844(1) b = 3.866(1) c = 7.732(2)
‡$Nd_{2/3}TiO_3$	Orthorhombic	a = 3.97 b = 4.19 c = 8.11

† (Bazuev et. al., 1979) ; ‡(Sych et. al., 1976)

systems are summarized in TABLE 3.4. It is found that the oxygen content is within 3% of the target oxygen content per formula unit based on the nominal rare earth and titanium content. The structural properties of each system are discussed separately below.

3.4.1. $Nd_{(1-x)}TiO_3$: $0 \leq x \leq 0.30$

Guinier x-ray powder diffraction: Guinier analysis identifies three different structural types in this system, with the Pnma structure observed for $0 \leq x \leq 0.17$, an as of yet unidentified structural type for the x = 0.20 phase and the Pban structure for the $0.25 \leq x \leq 0.30$ phases. The indexed powder diffraction lines are shown in TABLES I to VIII of APPENDIX II with the cell constants of all compositions obtained from the least squares refinement program LSUDF shown in TABLE 3.5.

Generally, an almost linear decrease is observed when the cell volume is plotted as a function of the vacancy content, see Fig. 3.2. This is to be expected because of the increased amount of the smaller Ti(IV) being introduced into the lattice with vacancy doping. As expected a systematic decrease is also observed in the dependence of the cell constants on vacancy content as shown in Fig. 3.3. It is to be noted that the a and b cell constants become identical as x increases.

Neutron powder diffraction: Due to the structural ambiguity surrounding the x = 0.20 and 0.33 phases they will be discussed separately in Sections 3.4.2. and 3.4.3.1.a., respectively. Principal structural characterizations for the $0 \leq x \leq 0.30$ phases were carried out at room temperature with neutron powder diffraction collected at the McMaster Nuclear reactor. For the nominal compsoitions, x = 0.00, 0.05, 0.10, 0.15 and 0.17, the refinements converged smoothly when

TABLE 3.4: Oxygen content determination by thermogravimetric analysis for the $Nd_{(1-x)}TiO_3$ and $Sm_{(1-x)}TiO_3$ systems.

Compound	Expected Wt.Gain (%)	Observed Wt. Gain (%)	Formula	Colour
$NdTiO_3$	3.33	3.33	$NdTiO_{3.00}$	Black
$Nd_{0.95}TiO_3$	2.92	2.92	$Nd_{0.95}TiO_{3.00}$	Black
$Nd_{0.90}TiO_3$	2.48	2.38	$Nd_{0.90}TiO_{3.01}$	Black
$Nd_{0.85}TiO_3$	2.01	1.99	$Nd_{0.85}TiO_{3.00}$	Black
$Nd_{0.83}TiO_3$	1.83	1.82	$Nd_{0.83}TiO_{3.00}$	Black
$Nd_{0.80}TiO_3$	1.51	1.42	$Nd_{0.80}TiO_{3.01}$	Black
$Nd_{0.75}TiO_3$	0.97	0.91	$Nd_{0.75}TiO_{3.01}$	Black
$Nd_{0.70}TiO_3$	0.41	0.41	$Nd_{0.70}TiO_{3.00}$	Gray
$SmTiO_3$	3.25	3.08	$SmTiO_{3.03}$	Black
$SmTiO_3$	3.25	3.13	$SmTiO_{3.02}$	Black
$Sm_{0.95}TiO_3$	2.85	2.78	$Sm_{0.95}TiO_{3.02}$	Black
$Sm_{0.90}TiO_3$	2.42	2.25	$Sm_{0.90}TiO_{3.02}$	Black
$Sm_{0.87}TiO_3$	2.15	1.98	$Sm_{0.87}O_{3.02}$	Black
$Sm_{0.85}TiO_3$	1.97	2.00	$Sm_{0.85}TiO_{3.01}$	Black
$Sm_{0.83}TiO_3$	1.78	1.73	$Sm_{0.83}TiO_{3.01}$	Black

TABLE 3.5: Cell Constants Derived From Guinier Hägg X-ray Data.

Compound	a/Å	b/Å	c/Å	V/Å^3
$NdTiO_3$	5.6512(5)	7.7927(8)	5.5228(5)	243.22(3)
$Nd_{0.95}TiO_3$	5.5920(5)	7.7983(8)	5.5059(4)	240.10(3)
$Nd_{0.90}TiO_3$	5.5508(3)	7.7958(5)	5.4880(3)	237.48(2)
$Nd_{0.85}TiO_3$	5.5207(5)	7.7804(7)	5.4800(4)	235.37(2)
$Nd_{0.83}TiO_3$	5.5114(7)	7.7752(10)	5.4780(5)	234.75(3)
$Nd_{0.80}TiO_3$	5.471(1)	7.7448(6)	5.479(1)	232.18(4)
$Nd_{0.75}TiO_3$	5.4530(9)	5.4548(7)	7.7629(11)	230.91(4)
$Nd_{0.70}TiO_3$	5.4410(4)	5.4444(1)	7.7357(8)	229.15(6)
$Nd_{0.67}TiO_3$	5.4373(5)	5.4373(5)	7.6974(7)	227.56(4)
$SmTiO_3$ (crystal)	5.6654(3)	7.7298(4)	5.4623(3)	239.21(2)
$SmTiO_3$	5.6671(5)	7.7314(6)	5.4606(4)	239.25(2)
$Sm_{0.95}TiO_3$	5.6154(6)	7.7416(6)	5.4542(4)	237.11(3)
$Sm_{0.90}TiO_3$	5.5774(7)	7.7450(7)	5.4464(6)	235.27(3)
$Sm_{0.87}TiO_3$	5.5496(7)	7.7442(8)	5.4355(6)	233.43(3)
$Sm_{0.85}TiO_3$	5.5318(5)	7.7454(10)	5.4376(8)	232.98(4)
$Sm_{0.83}TiO_3$	5.5176(2)	7.7345(3)	5.4294(2)	231.70(1)

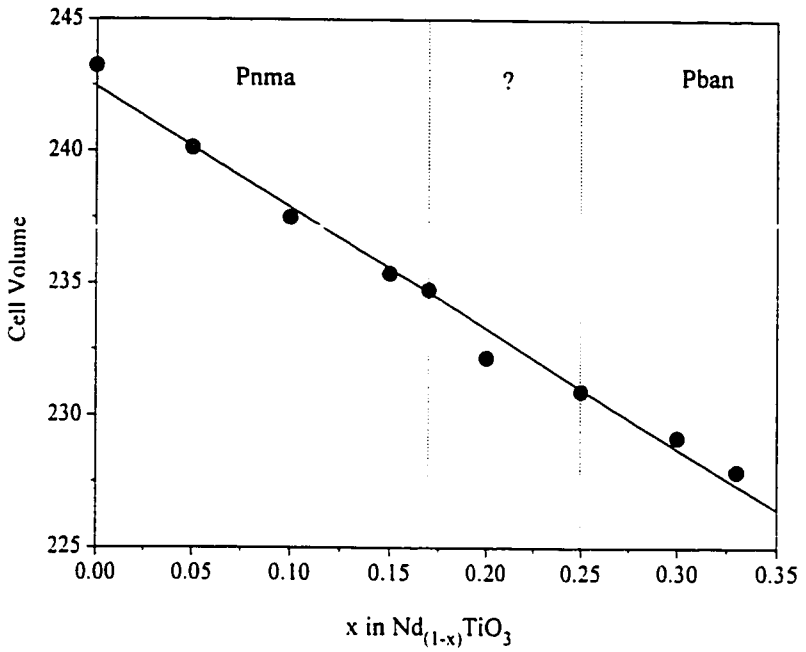

Fig. 3.2. Cell Volume vs. vacancy doping,x, in the $Nd_{(1-x)}TiO_3$ system.

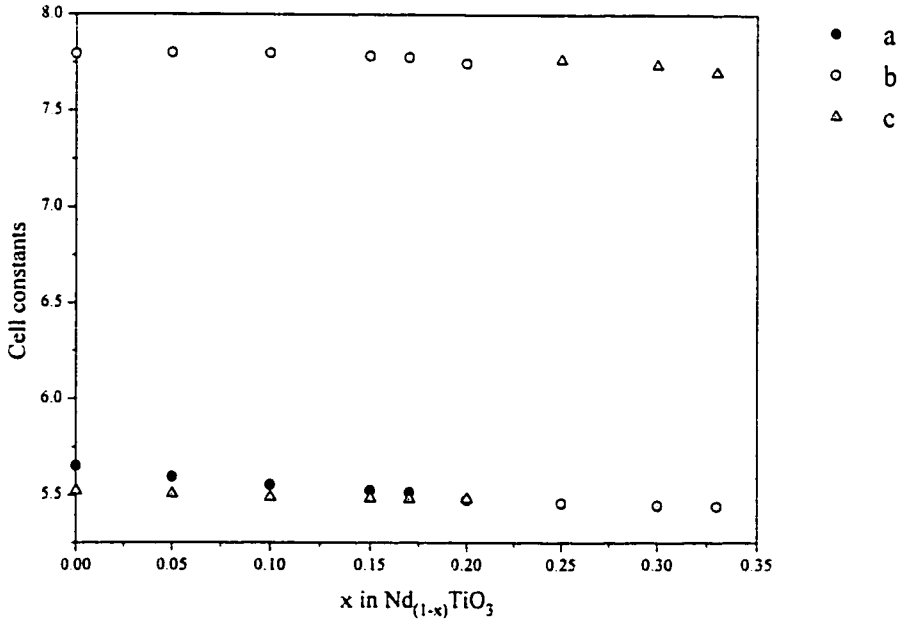

Fig. 3.3. Cell constants vs. vacancy doping,x, in the $Nd_{(1-x)}TiO_3$ system.

the Pnma structural model was used. The refined atomic positions and residuals are summarized in TABLES 3.6 and 3.7, while the refined diffraction profiles can be seen in Figs. 3.4 to 3.6. For the x = 0.17 phase, two extra peaks which did not appear in the calculated profile were observed at $2\theta \sim 45.75°$ (d = 1.7905Å) and ~ 66.50° (d = 1.2694Å) in the neutron diffraction profile. These lines were ascribed to an impurity as they were not detected in the Guinier x-ray diffraction analysis. The lines could not be identified as belonging to any of the precursor materials nor intermediary compounds of the neodymium and titanium oxides. It is supposed that this impurity was introduced during the loading of the sample can for data collection. Consequently, the refinement was performed with the exclusion of these peaks. During the refinement process negative temperature factors for all atoms were obtained with an apparent correlation to the full width at half maximum parameters (FWHMs). Consequently, an overall temperature factor was refined. The refined atomic positions and residuals for this phase can also be found in TABLE 3.7.

For the x = 0.25 and 0.30 phases, the diffraction profiles were clearly different having fewer diffraction peaks and the observation of a low angle peak at ~ 10°. These profiles are similar to the $La_{0.70}TiO_3$ compound and this peak was subsequently assigned as being the '001' reflection in Pban. Consequently, the refinements were carried out using the Pban model, see Fig. 3.7, with a smooth convergence to the residuals shown in TABLE 3.8. As mentioned earlier, this is an apparently novel perovskite and is shown in Fig. 3.8. The structural framework consists of a three dimensional network of TiO_6 corner shared octahedra with the occurrence of a local $Ti\text{-}O_6$ distortion observed for each octahedron. This is attributed to the partial ordering of the

TABLE 3.6: Refined atomic positions and cell constants from neutron data for nominal x = 0.00, 0.05 and 0.10 in the $Nd_{(1-x)}TiO_3$ system.

		$NdTiO_3$	$Nd_{0.95}TiO_3$[a]	$Nd_{0.90}TiO_3$
		Pnma	Pnma	Pnma
Nd	x	0.0598(8)	0.04379(12)	0.0356(12)
	y	0.25	0.25	0.25
	z	0.9927(13)	0.9851(22)	0.9918(20)
	B(Å^2)	0.54(7)	0.62(27)	0.0005(4)
Ti	x	0.5	0.5	0.5
	y	0.0	0.0	0.0
	z	0.0	0.0	0.0
	B(Å^2)	0.77(14)	1.09(43)	0.29(20)
O1	x	0.4770(11)	0.4736(20)	0.4727(15)
	y	0.25	0.25	0.25
	z	0.0900(13)	0.0724(23)	0.0604(20)
	B(Å^2)	1.07(13)	2.07(55)	0.67(18)
O2	x	0.3005(8)	0.3018(12)	0.2944(12)
	y	0.0501(6)	0.0524(9)	0.0447(9)
	z	0.6992(7)	0.7072(14)	0.7093(13)
	B(Å^2)	0.127(77)	0.87(33)	1.03(12)
	a (Å)	5.6471(12)	5.5826(37)	5.5442(17)
	b (Å)	7.7853(17)	7.7990(55)	7.7990(26)
	c (Å)	5.5186(12)	5.4936(38)	5.4868(20)
	V(Å^3)	242.6218(41)	239.184(13)	237.2449(63)
	R_{wp}	6.37	6.16	6.51
	S	1.62	1.66	1.85
	R_p	5.09	4.81	5.19
	R_{Bragg}	9.39	5.50	12.56

[a] Refinement performed in the 2-theta range 17° to 58°.

TABLE 3.7: Refined atomic positions and cell constants from neutron data for nominal x = 0.15 and 0.17 in the $Nd_{(1-x)}TiO_3$ system.

		$Nd_{0.85}TiO_3$	$Nd_{083}TiO_3$[a]
		Pnma	Pnma
Nd	x	0.0411(9)	0.0164(22)
	y	0.25	0.25
	z	0.9938(17)	0.9946(43)
	B(Å^2)	0.28(8)	-
Ti	x	0.5	0.5
	y	0.0	0.0
	z	0.0	0.0
	B(Å^2)	0.145(4)	-
O1	x	0.4864(14)	0.4897(28)
	y	0.25	0.25
	z	0.0799(20)	0.0596(28)
	B(Å^2)	1.62(6)	-
O2	x	0.2863(10)	0.2924(16)
	y	0.0364(7)	0.0378(13)
	z	0.7103(10)	0.7059(18)
	B(Å^2)	0.78(9)	-
	a (Å)	5.5226(17)	5.5140(28)
	b (Å)	7.7837(22)	7.7792(41)
	c (Å)	5.4854(16)	5.4755(35)
	V(Å^3)	235.7968(55)	234.868(1)
	R_{wp}	6.52	9.21
	S	1.88	3.32
	R_p	5.05	6.81
	R_{Bragg}	10.51	14.72

[a] Refined with an overall temperature factor, $B_{overall}$ = 1.91(3)Å^2.

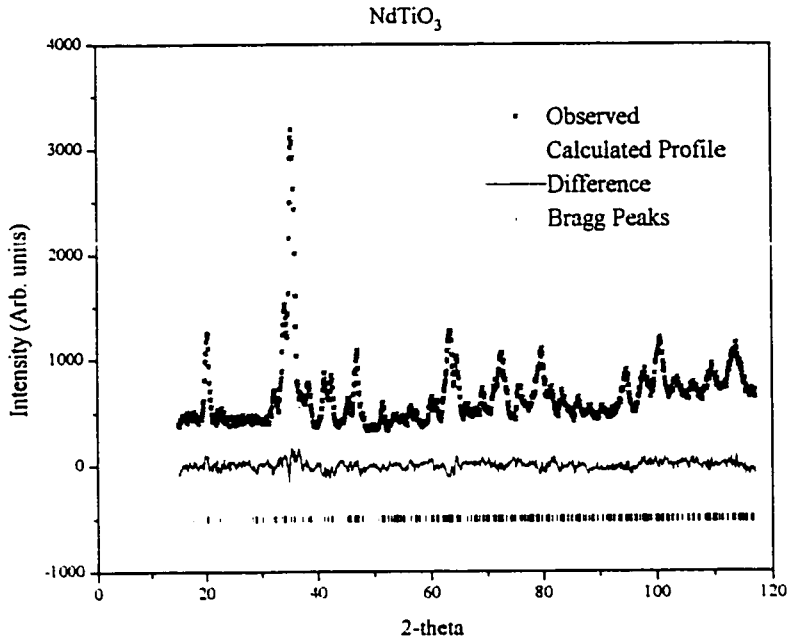

(a).

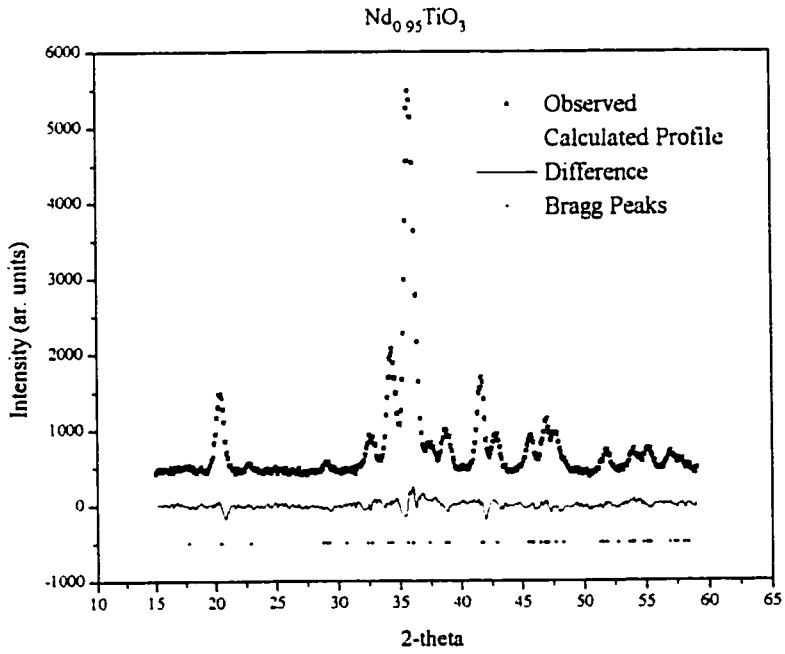

(b).

Fig. 3.4. Refined neutron diffraction profiles for a). x = 0.00 and b). x = 0.05.

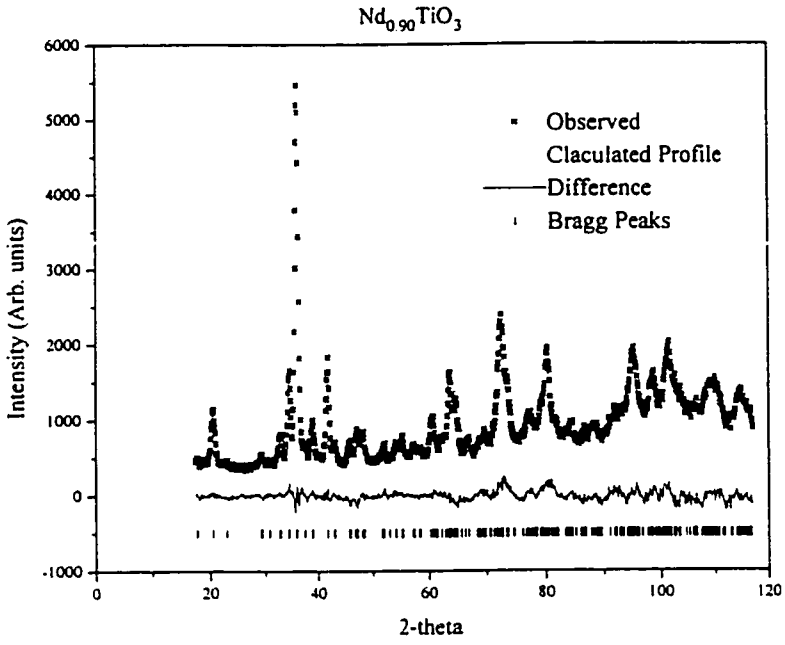

(a).

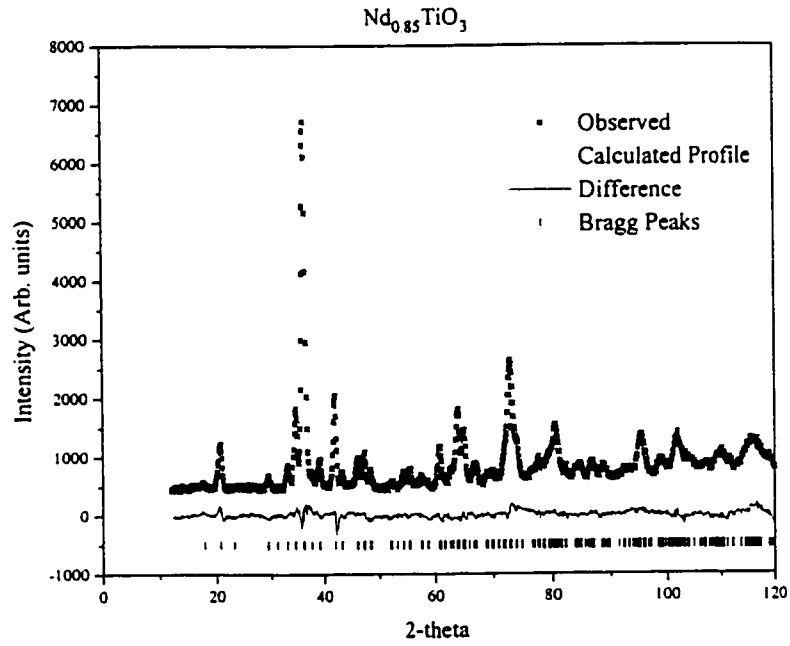

(b).

Fig.3.5. Refined neutron diffraction profiles for a). x = 0.10 and b). x = 0.15

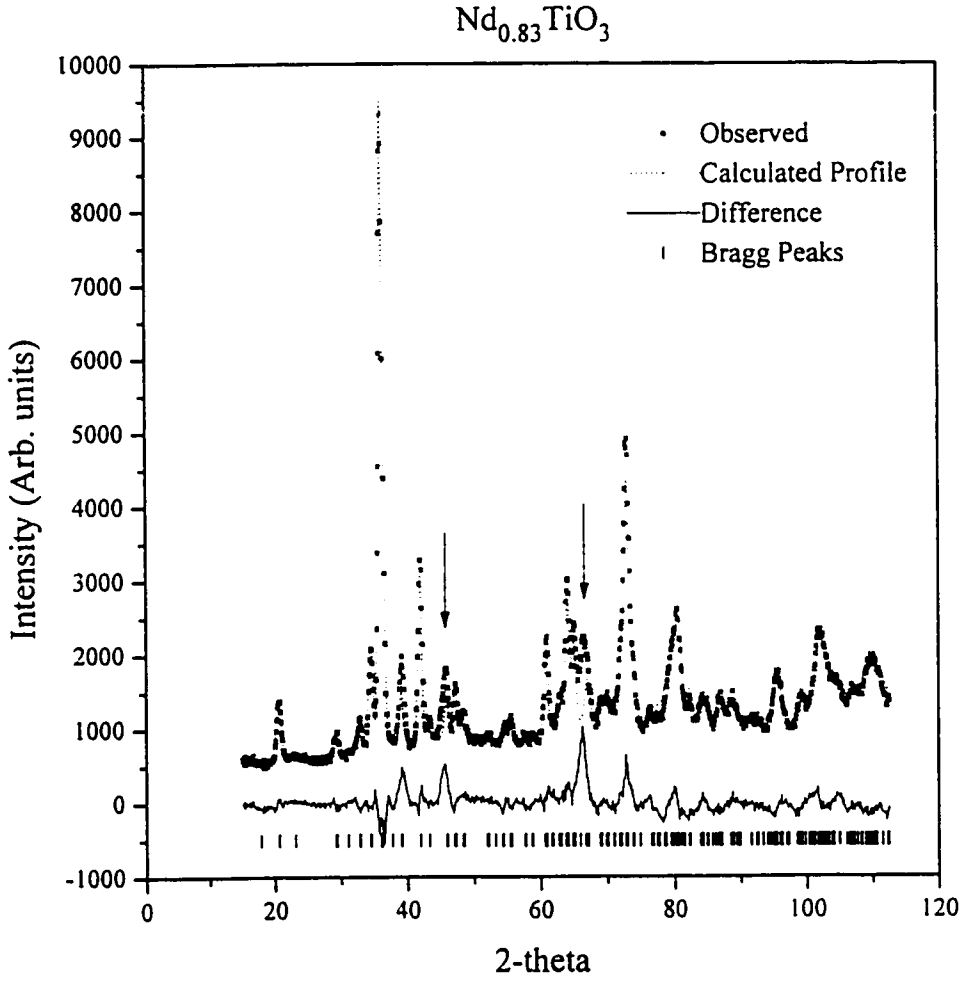

Fig. 3.6. Refined neutron diffraction profile for x = 0.17. The arrows indicate extra peaks.

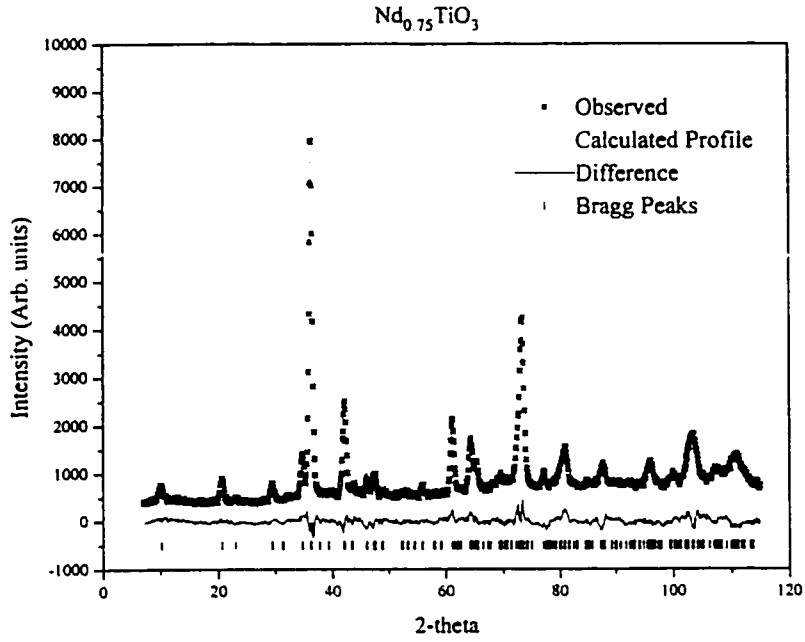

(a).

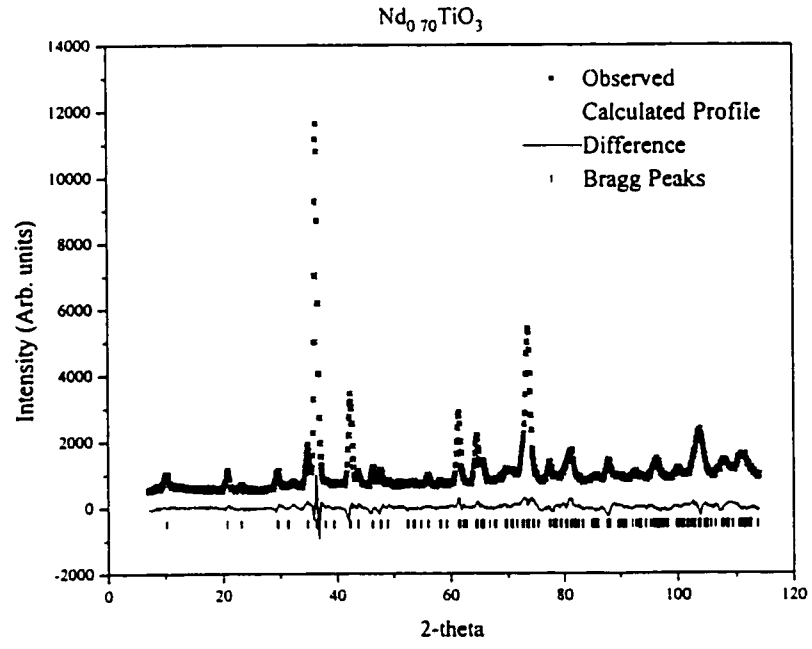

(b).

Fig.3.7. Refined neutron diffraction profile for a). x = 0.25 and b). x = 0.30.

TABLE 3.8: Refined atomic positions and cell constants from neutron data for nominal x = 0.25 and 0.30 in the $Nd_{(1-x)}TiO_3$ system.

		$Nd_{0.75}TiO_3$	$Nd_{0.70}TiO_3$
		Pban	Pban
Nd1	x	0.25	0.25
	y	0.25	0.25
	z	0.0	0.0
	B(Å²)	0.74(14)	0.52(14)
Nd2	x	0.25	0.25
	y	0.25	0.25
	z	0.5	0.5
	B(Å²)	0.084(0)	0.53(37)
Ti	x	0.25	0.25
	y	0.75	0.75
	z	0.2553(24)	0.2573(24)
	B(Å²)	0.33(14)	0.90(14)
O1	x	-0.0379(12)	-0.0358(16)
	y	-0.0392(13)	-0.0392(15)
	z	0.2390(8)	0.2427(9)
	B(Å²)	0.805(3)	0.97(5)
O2	x	0.75	0.75
	y	0.25	0.25
	z	0.5	0.5
	B(Å²)	3.23(42)	4.58(44)
O3	x	0.75	0.75
	y	0.25	0.25
	z	0.0	0.0
	B(Å²)	4.96(56)	2.93(31)
	a (Å)	5.4252(13)	5.4190(15)
	b (Å)	5.4662(14)	5.4470(17)
	c(Å)	7.7476(18)	7.7208(18)
	V(Å³)	229.7568(45)	227.8971(50)
	R_{wp}	7.72	7.67
	S	2.31	2.55
	R_p	6.29	6.06
	R_{Bragg}	16.08	13.23

vacancies in the unit cell as the distortion has a tendency towards the z = 0.5 layer, presumably to compensate for the larger cation deficit in that layer. The result is a tilted framework in the ab plane with the formation of linear chains parallel to the c-axis composed of alternating pairs of long and short Ti-O bonds.

The large R_{Bragg} factor observed for the x = 0.25 and 0.30 compositions indicates that the present structural descriptions are not entirely accurate. This is reflected in the large temperature factors at the O2 and O3 sites which reflect the disorder at the neodymium sites. To improve on these results, an attempt was made to refine the neodymium site occupancies. With the Nd2 site occupancy constrained the refined valued at the Nd1 site exceeded the occupancy at that site. Thus, this was constrained to have 100% site occupancy while the Nd2 site occupancy was refined freely. The overall neodymium content obtained in this manner was close to the nominal content and no significant improvement in the R_{Bragg} was obtained. Finally, an attempt was made to split the O2 and O3 sites by moving from the 2c site to 4j in the case of O2 and from the 2b site to the 4g site for O3, however no significant improvement in the overall refinement was observed. Thus it appears that in order to get a better structural description for these phases, single crystal studies would be essential.

3.4.2. x = 0.20, $Nd_{0.80}TiO_3$

The structural refinement of the data collected for this phase is less straightforward than for those compositions presented in the previous section. Unlike the diffraction patterns obtained for the x = 0.0 to 0.17 phases, fewer lines are observed for this composition. Despite this apparent

(a).

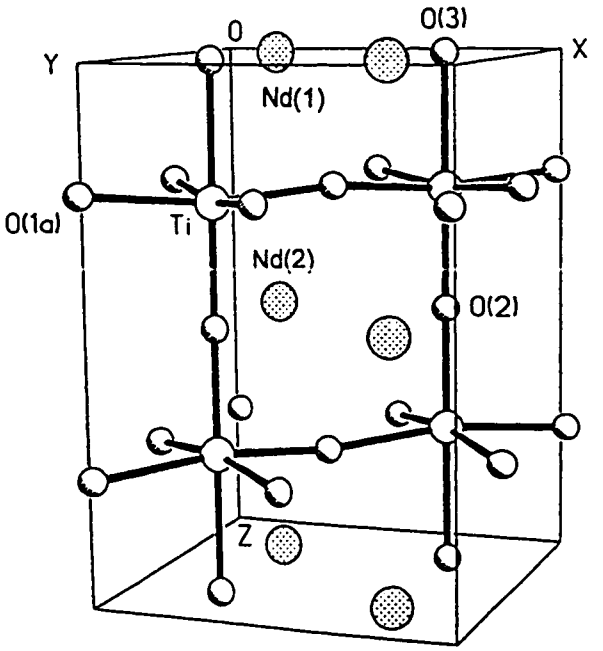

(b).

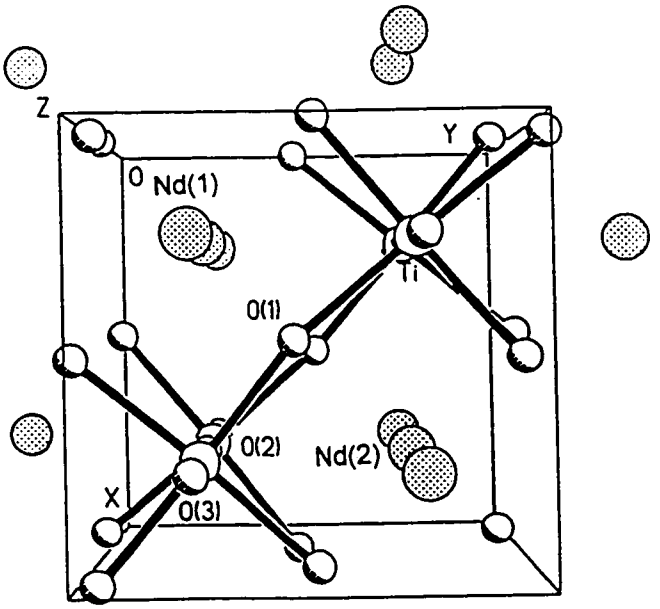

Fig. 3.8. (a). Perspective of the Pban structure and (b). View down c-axis.

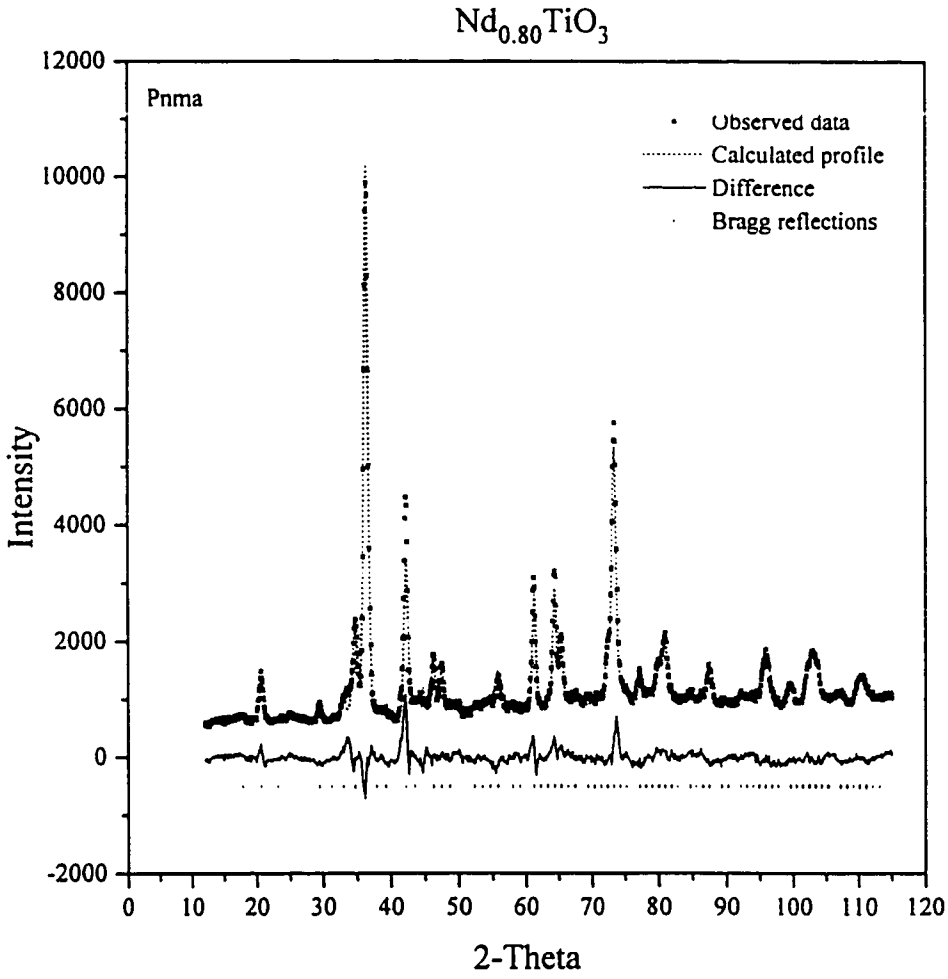

Fig. 3.9. Refined neutron diffraction profile for x = 0.20 in Pnma.

change in symmetry however, the diffraction lines could be indexed successfully in Pnma, see TABLE VI in Appendix II. Initial attempts to refine the neutron data using the Pnma model however, resulted in a poor profile fit, see Fig. 3.9. Similar results were obtained for refinements carried out with the existing Imma and Pban models observed in the $La_{(1-x)}TiO_3$ system thus leading to ambiguity regarding the structure. The difficulty in arriving at a structural solution for this phase is hampered by the apparent presence of a second phase which is evident by the appearance of a broad, diffuse reflection with low intensity observed at 2θ~11°. This corresponds roughly to the '001' reflection which is characteristic of the Pban model. From the Guinier data, it is observed that this reflection becomes significantly sharper and more intense as one goes from the $Nd_{0.75}TiO_3$ to $Nd_{0.70}TiO_3$ compositions, which have already been determined to adopt the Pban structure, see Fig. 3. 10. A similar observation has also been found in the $La_{(1-x)}TiO_3$ system. The diffuse nature of this reflection in $Nd_{0.80}TiO_3$ is thought to be due to the presence of small domains which progressively increase in size as one reaches the x = 0.25 and 0.30 phases.

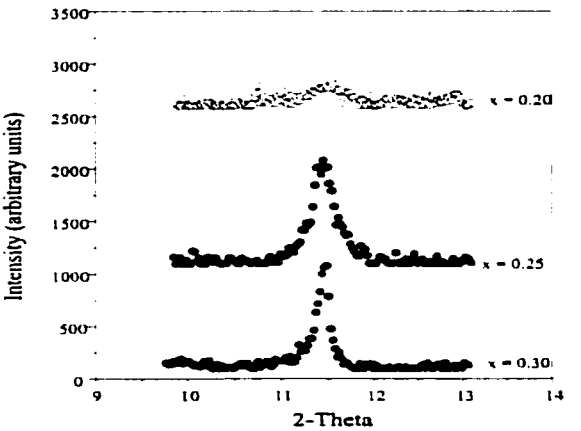

Fig. 3.10. Development of the (001) peak from x = 0.20 to 0.30.

3.4.3. Neodymium metatitanate, $Nd_{2/3}TiO_3$ (x = 0.33).

Several attempts to prepare this phase in the polycrystalline state were unsuccessful when the starting materials (Nd_2O_3, TiO_2) were fired in air or in vacuum using the induction furnace. This observation is in accordance with those previously reported suggesting a more favourable thermodynamic condition for the formation of $Nd_2Ti_2O_7$ under these conditions than the desired phase (Lejus, 1970). Initial attempts to isolate this phase as single crystals involved the use of a $KF/Na_2B_4O_7$ flux. However this resulted in the formation of the layered perovskite $K_2Nd_2Ti_3O_{10}$. The formation of this compound demonstrates the versatility of the basic perovskite framework to accommodate various cations to yield interesting layered structures. As this is the first known case where single crystals of this compound have been synthesized a detailed structural study was performed, the results of which are included in Appendix I. The isolation of the $Nd_{2/3}TiO_3$ phase was subsequently achieved by the flux growth method using a $CsF/Na_2B_4O_7$ flux.

3.4.3.1. Structural Determination of $Nd_{2/3}TiO_3$.

3.4.3.1.a. Guinier analysis: Several crystals obtained from a CsF/NaB_4O_7 flux were ground for Guinier analysis. Data were also collected using a Nicolet powder diffractometer for the purposes of structural refinement as sufficient quantities were not available for analysis by neutron powder diffraction. The diffraction pattern obtained by the Guinier camera indicated that a different structural phase had been obtained as it was similar in appearance to the diffraction pattern of $La_{2/3}TiO_3$ having fewer observed lines including the characteristic '001' reflection

of the Pban structure. Of particular note in the diffraction pattern is the presence of superstructure lines which, interestingly are broad, belonging to the general class *00l (l=2n+1)*. This observation has also been reported for a variety of A-site doped perovskite systems and is usually attributed to the presence of antidomain phase boundaries which arise from the ordering of A-site cations for example, $La_{1/2}Li_{1/2}TiO_3$ (Varez et. al, 1995) and $Na_{(1/2+x)}La_{(1/2-3x)}Th_{2x}TiO_3$ (Mitchell and Chakhmouradian, 1998).

For the $Nd_{2/3}TiO_3$ crystals which were prepared, the relative domain size was observed to increase on annealing. The results obtained from annealing several crystals at 800°C for one week and at 1000°C for several days are shown in Fig.3.11 which illustrates an increasingly sharpened intensity of the *00l* class of reflections. Annealing for longer periods of time resulted in the formation of a thin layer on the surface of the crystals which was later identified as the $Nd_2Ti_2O_7$ phase. Interestingly, the sharpening of these lines on annealing has not been observed in the other A-site doped systems mentioned previously.

The indexing of the diffraction pattern presented a considerable challenge due to the increased pseudocubic nature with higher vacancy doping. Initially it was thought that the structure possessed cubic symmetry owing to the presence of so few diffraction lines and the lack of any discernible peak splitting. Consequently, the diffraction lines in principle could be indexed as either belonging to the ideal cubic perovskite, with cell parameter a_p (~3.8Å), with the broad *00l* class of reflections indexed as superstructural lines having half integral indices or as a doubled cubic perovskite cell ($2a_p \times 2a_p \times 2a_p$). However, a unit cell with cubic symmetry was ruled out due to the physical observation that the crystals rotate plane polarized

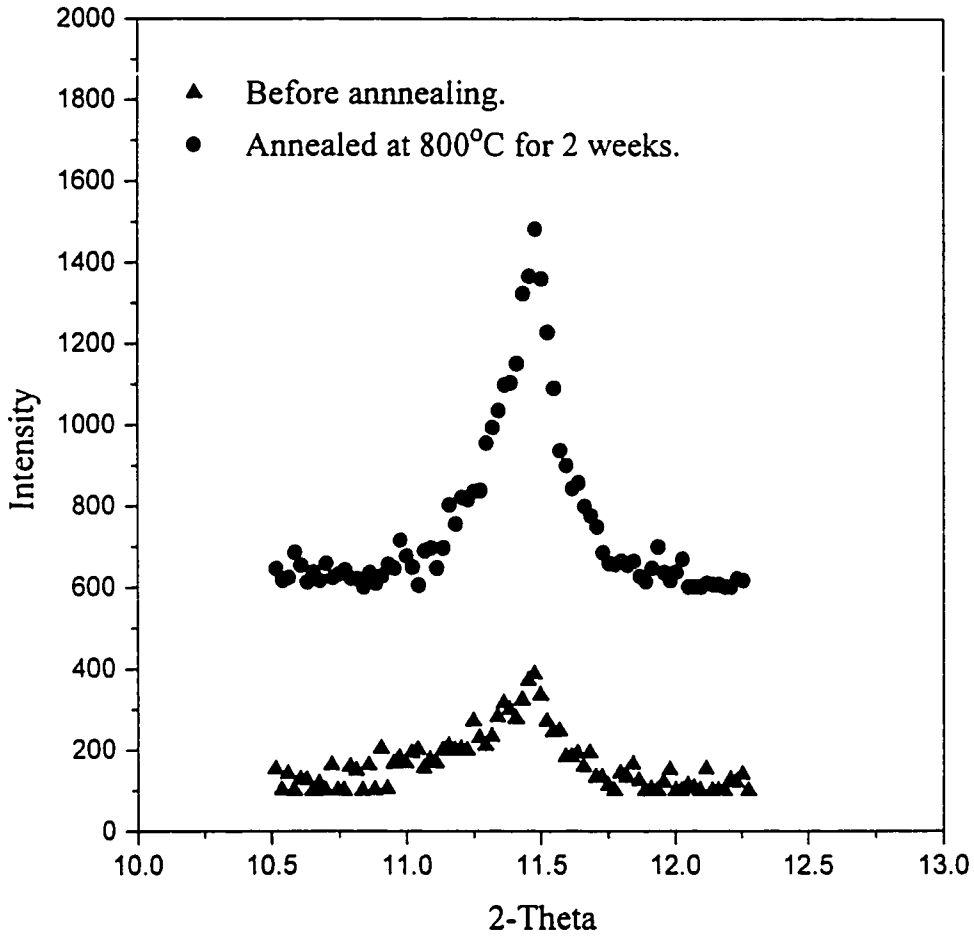

Fig.3.11. Effect of annealing on '001' reflection of $Nd_{2/3}TiO_3$.

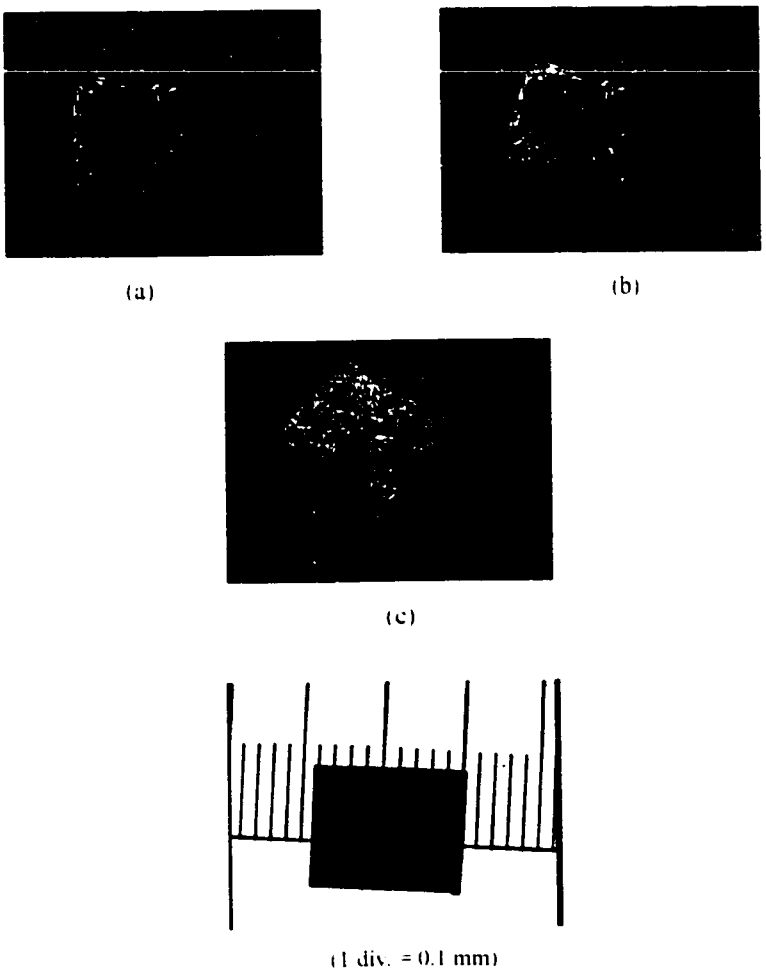

Fig. 3.12. Rotation of plane polarized light by $N_{2/3}TiO_3$ crystal rotated clockwise from a). to c).

light which suggests lower symmetry, see Fig. 3.12. Alternatively, other possibilities for the unit cell included a 'diagonal cell' with cell parameters $\sim 2^{1/2} a_p \times \sim 2^{1/2} a_p \times 2a_p$ as found in $La_{2/3}TiO_3$ (MacEachern et al., 1994) or the smaller $a_p \times a_p \times 2a_p$ cell which was originally proposed to account for the ordering of the vacancies on the A-sites in $La_{2/3}TiO_3$ (Abe and Uchino, 1974). Preliminary investigations by electron diffraction in this study suggested that the smaller cell may have been the correct choice. However attempts to fit the data with these parameters could not fit the diffraction line with d-spacing 2.3180Å. To index this line successfully the larger diagonal cell was used.

Having derived the appropriate unit cell constants for $Nd_{2/3}TiO_3$, the symmetry determination of the unit cell presented a more complex challenge. As one goes from the x = 0.0 to x = 0.30 phase there is an obvious tendency towards tetragonal behaviour due to the increased coincidence of the $a \sim 2^{1/2} a_p$ *and* c *(or* b*)* $\sim 2^{1/2} a_p$ cell constants, while the long b*(or* c*)* $= 2a_p$ axis remains fairly constant. Recall that the long $2a_p$ axis corresponds to the b-axis in Pnma and the c-axis in Pban respectively. The ratio of the $a \sim 2^{1/2} a_p$ *and* c *(or* b*)* $\sim 2^{1/2} a_p$ cell constants have been plotted to illustrate this, see Fig. 3.13. The results obtained from indexing the Guinier x-ray diffraction pattern using orthorhombic and tetragonal symmetry are shown in Tables 3.9 and 3.10 respectively. The small difference in the errors of the cell constants between the two cases does not allow a clear distinction between the two symmetry types. Thus, based on the diffraction pattern alone, the unit cell symmetry is ambiguous again owing to the lack of any discernible peak splitting.

3.4.3.1.b. Single crystal x-ray diffraction: In order to resolve this problem, a single crystal

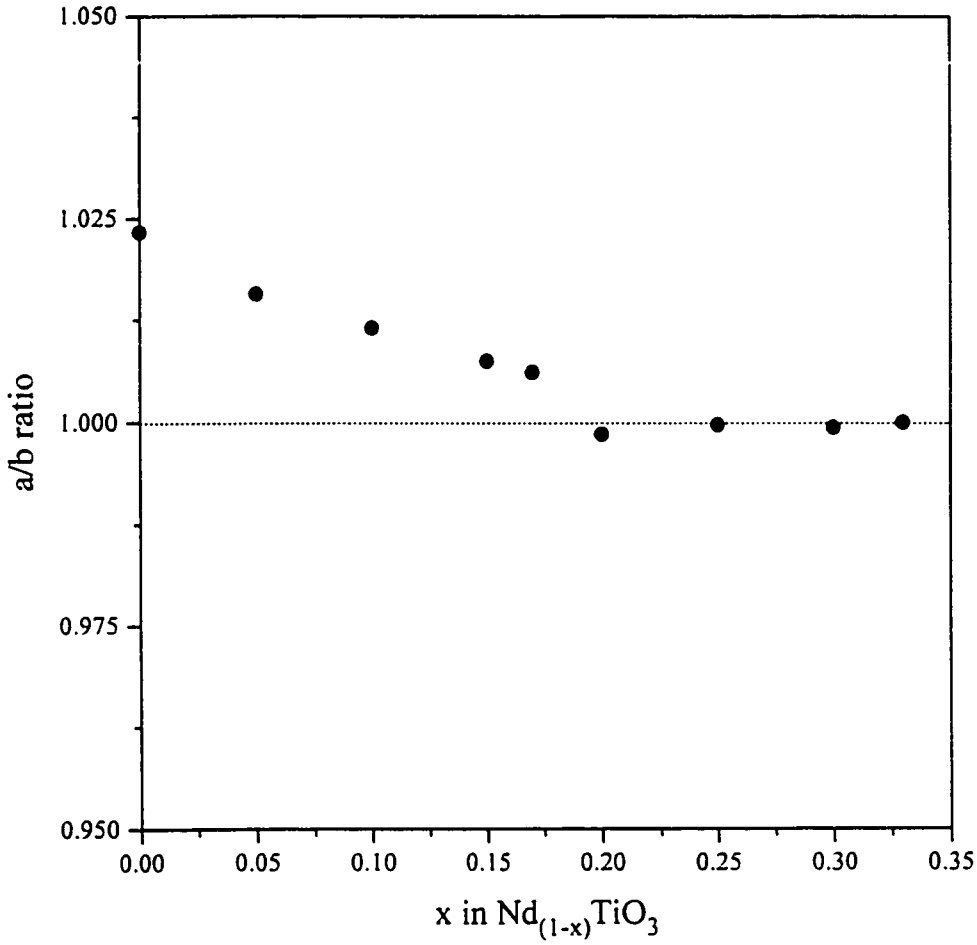

Fig. 3.13. Ratio of a and b cell constants for $Nd_{(1-x)}TiO_3$ system showing the increased tendency towards tetragonal behaviour.

TABLE 3.9: Diffraction lines obtained for $Nd_{2/3}TiO_3$ single crystals from Guinier-Hägg camera indexed using orthorhombic symmetry. [a = 5.4419(5)Å, b = 5.4354(9)Å, c = 7.7043(31)Å, V = 227.88(7)Å^3)

h k l	d_{obs}(Å)	d_{calc}(Å)	I_{obs}
001*	7.7111	7.7043	4.09
110	3.8481	3.8457	4.00
111*	3.4406	3.4408	10.61
200	2.7202	2.7209	100.00
021*	2.5630	2.5626	2.59
121*	2.3180	2.3186	1.60
022	2.2205	2.2207	22.30
221*	1.8650	1.8656	5.04
310	1.7209	1.7207	2.31
131*	1.6778	1.6778	2.45
132	1.5700	1.5698	51.91
400	1.3600	1.3605	27.44
134	1.2824	1.2825	1.60
420	1.2167	1.2165	30.65
422	1.1603	1.1601	5.10

*Indicates a broad diffuse reflection.

TABLE 3.10: Diffraction lines obtained for $Nd_{2/3}TiO_3$ single crystals from Guinier-Hägg camera indexed with tetragonal symmetry. [a = b = 5.4373(5)Å, c = 7.6974(7)Å, V = 227.56(4)Å]

h k l	d_{obs}(Å)	d_{calc}(Å)	I_{obs}
001*	7.7111	7.6974	4.09
002	3.8481	3.8487	4.00
111*	3.4406	3.4395	10.61
112	2.7202	2.7200	100.00
201*	2.5630	2.5634	2.59
211*	2.3180	2.3187	1.60
202	2.2205	2.2205	22.30
221*	1.8650	1.8651	5.04
114	1.7209	1.7208	2.31
311*	1.6778	1.6781	2.45
312	1.5700	1.5699	51.91
224	1.3600	1.3600	27.44
314	1.2824	1.2821	1.60
116	1.2167	1.2169	30.65
206	1.1603	1.1602	5.10

*Indicates a broad diffuse reflection.

of $Nd_{2/3}TiO_3$ grown from the same batch was mounted on a glass pin and single crystal x-ray data were collected. In the preliminary stages of the data collection a doubled ($2a_p$) cubic unit cell was found. Attempts to find the diagonal cell were unsuccessful and the data were consequently collected on a doubled primitive cubic cell. A possible explanation for the presence of the doubled cubic cell can be drawn from structural studies of $LaTiO_3$ and $CaTiO_3$ in which twinning of the orthorhombic lattice gives rise to fictitious cubic symmetry (MacLean et. al., 1979;(Kay and Bailey, 1957). In these cases the twin law has been described as a three fold rotation about the body diagonal of the cubic cell or alternatively as a 90° rotation about an axis perpendicular to the [110] direction with respect to the orthorhombic cell. Due to the severe conditions under which the $Nd_{2/3}TiO_3$ crystals were grown with high evaporation losses, it is likely that the presence of twinning is responsible for the appearance of the cubic cell.

3.4.3.1.c. Electron diffraction: To investigate further the possibility of twinning electron diffraction was employed. The samples were investigated with transmission electron microscopy in the SAED mode for which both electron diffraction patterns and bright field images were obtained, see Figs. 3.14 and 3.15. The electron diffraction pattern shows the presence of superstructure reflections whose d-spacings correspond to the doubled cubic perovskite unit cell. It should be noted that $[100]_c = [110]_o$ where the subscripts 'c' and 'o' refer to the cubic and orthorhombic cell respectively. Furthermore the *00l* reflections are streaked along the c^* direction suggesting the presence of microdomains or disorder and is agreement with the broad diffuse nature of the *00l* ($l = 2n + 1$) lines observed in the Guinier diffraction pattern. Most critical, however,

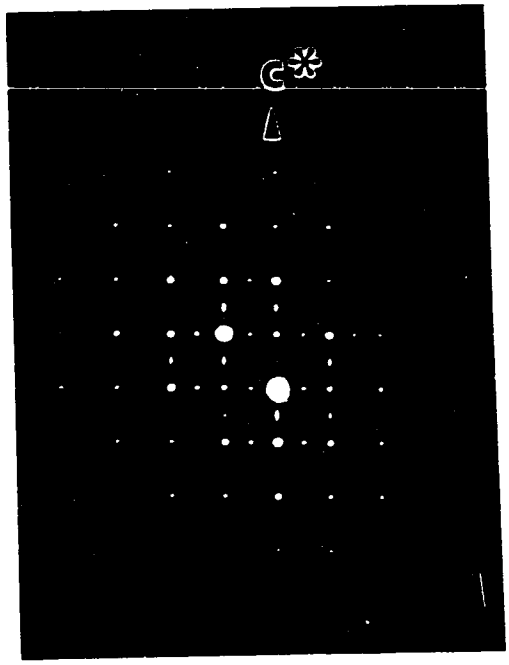

Fig.3.14. Electron diffraction pattern showing the view down the [110] zone axis of the diagonal cell. The fictitious double cubic cell due to twinning can be seen. The streaking in the spots along the c*axis reveals the short range order of the microdomains.

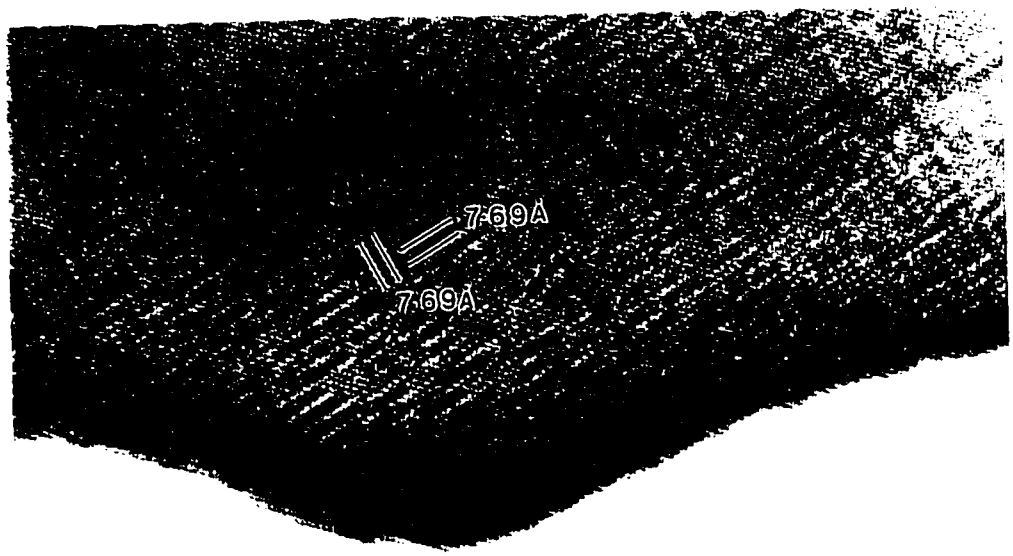

Fig.3.15. Electron micrograph showing the presence of micodomains which are oriented 90° to each other.

in rationalizing the appearance of the doubled unit cell in the electron diffraction pattern and the single crystal data is the physical observation of the domains in the bright field images, see Fig. 3.15. These domains, which have a spacing of ~7.69Å, are of short range order extending over just several unit cells (~15-21 Å). Their relative orientation to each other by 90° gives rise to a patchwork appearance. While this image is only a representation in two dimensions it can be imagined to also extend in three dimensions, resulting in the apparent and misleading doubled cubic unit cell. The literature cites several examples in which similar observations have been made, such as $La_{1/2}Li_{1/2}TiO_3$ (Varez et al., 1995), $CaTiO_3$ (Kay and Bailey, 1957), $La_{(2/3-x)}Li_{3x}\square_{(1/3-2x)}TiO_3$ (Fourquet et al., 1996) and $Na_{(1/2+x)}La_{(1/2-3x)}Th_{2x}TiO_3$ (Mitchell and Chakhmouradian, 1998).

The results from this study thus support the presence of the twin law described previously in which each twin component is oriented 90° to each other such that the $\sim 2a_p$ axis is oriented along each of the x, y and z directions in real space to give rise to the apparent cubic unit cell. With this description, it is easy to see how the electron diffraction pattern is generated, see Fig. 3.16. This illustration shows a non-mehrohedral twin since some of these intensities of all three twin components do not superimpose each other.

3.4.3.1.d. Precession photography: While evidence of twinning has been established from single crystal x-ray and electron diffraction studies, very little information regarding the symmetry of the unit cell was obtained from these methods. Thus, precession photography was employed for this purpose. The information obtained from this technique is essentially the same as that

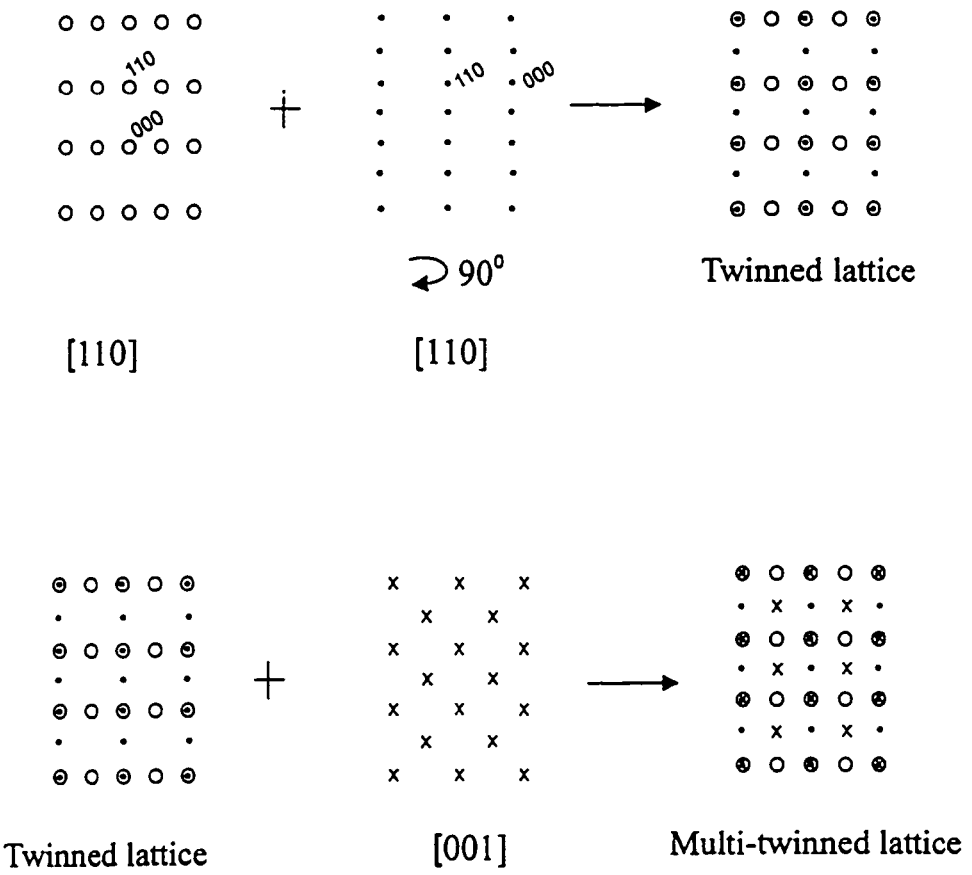

Fig. 3.16. Schematic representation of how the basic electron diffraction pattern is generated with a). two domains and b). three domains. The view is down the [110] axis of the 'diagonal' unit cell. The spots marked 'x' may also be produced by multiple diffraction.

from electron diffraction however it allows us to gain additional insight by being able to choose which part of reciprocal space we wish investigate. Initially, the x-ray beam was placed normal to a major face of the mounted crystal. The resulting precession pattern is shown in Fig. 3.17 which corresponds to the view generally obtained from the electron diffraction study, that is the $[110]_o$ plane of the diagonal cell. Consequently, the crystal was rotated 45° about the c^* axis in order to obtain the a^*c^* ($h0l$) plane of the diagonal cell and from this position the crystal was rotated once more by 90° in order to get the b^*c^* ($0kl$) plane, see Fig. 3.18. Since the patterns of the a^*c^* and b^*c^* reciprocal nets were identical it indicated the presence of a four fold axis along c^* leading to the conclusion that the unit cell has tetragonal symmetry. Thus, the true unit cell constants obtained by Guinier x-ray powder diffraction are, a = 5.4373(5)Å and c = 7.6974(7) Å.

3.4.3.1.e. Single crystal data revisited: The single crystal data were revisited with knowledge of the appropriate unit cell constants and symmetry. Hence, the data collected previously on the doubled cubic unit cell were integrated based on tetragonal symmetry and reindexed on the diagonal cell. In doing so, any reflections which were not superimposed with the prime component, as shown in Fig. 3.16, were removed from the dataset. Using this reindexed dataset a structure solution was obtained in P4/mmm. The refinement of the anisotropic model against F-squared proceeded smoothly, however resulting in high indices, $wR(F^2) = 0.1657$ for all 429 reflections and R(F) = 0.0548 for 362 observed data. These relatively high values indicate that the structure is not being accurately described and this is reflected by the large peaks and

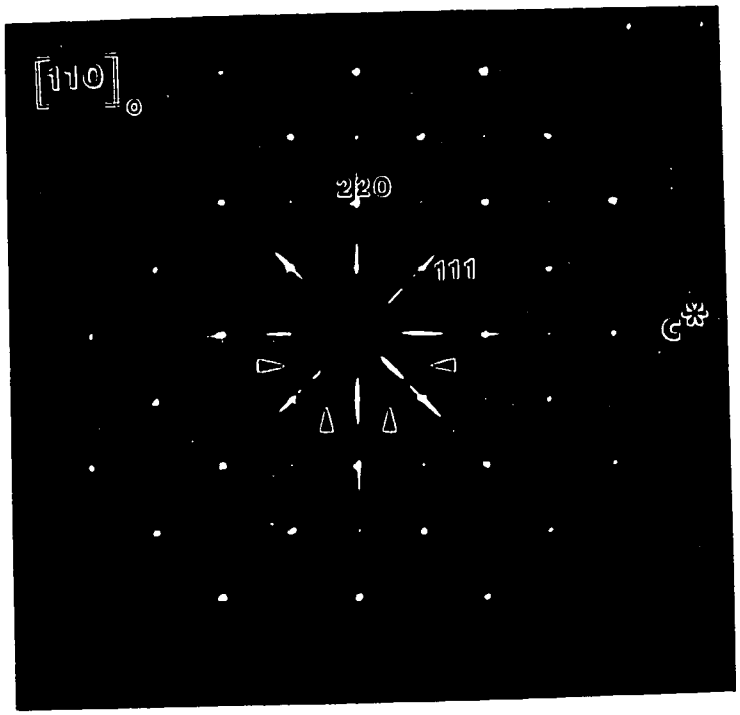

Fig.3.17. Precession photograph of the [110] plane of the diagonal unit cell of $Nd_{2/3}TiO_3$. Note the extra weak spots marked by arrows which is a result of twinning. These are responsible for the fictitious doubled cubic unit cell.

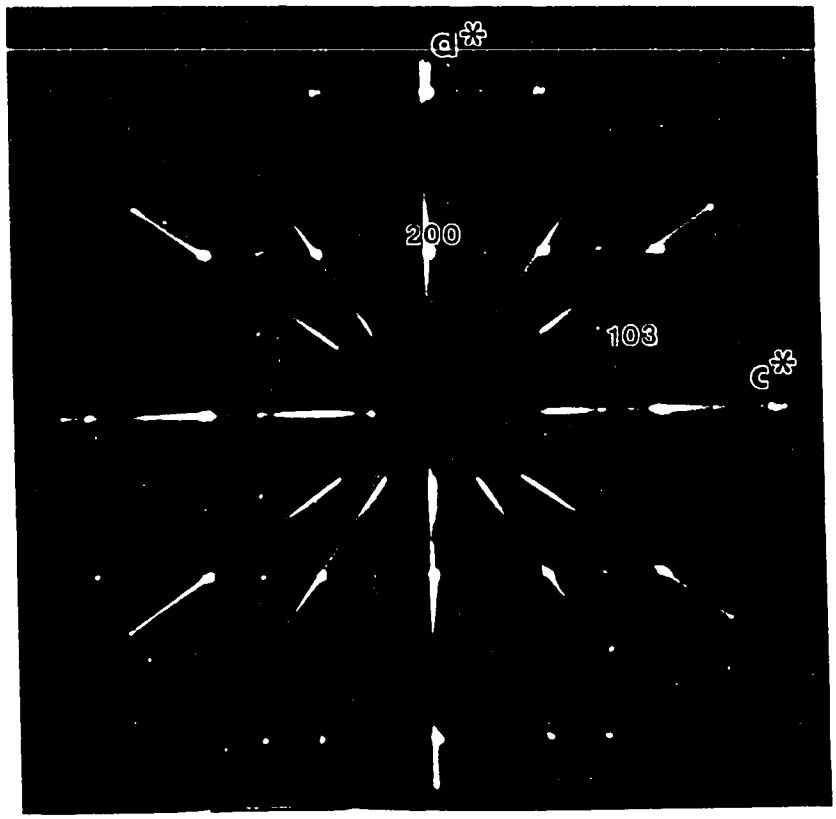

Fig. 3.18. Precession photograph of the a^*c^* plane of the diagonal unit cell of $Nd_{2/3}TiO_3$ showing the $\sim 2^{1/2}a_p$ axis. Rotation by 90° about the c^* axis produces the same diffraction pattern for the b^*c^* plane.

holes in the electron density map. The highest peak, $\Delta\rho_{max} = 3.58eÅ^{-3}$, is located 0.31 Å from O3 and the deepest hole, $\Delta\rho_{min} = -2.59Å$ is at the O2 site. This is attributed to the unresolved twin components within the dataset. With the current software available resolving the contributions from each twin component cannot be easily accomplished, however it is speculated that even so, given the extemely fine scale on which the domains exist a better structural refinement may not at all be possible. Details of the crystal data, data collection and structure refinement can be found in TABLE 3.11. The atomic and displacement parameters are shown in TABLES 3.12 and 3.13 respectively.

The P4/mmm structure of $Nd_{2/3}TiO_3$ is shown in Fig. 3.19 and bears some resemblance to the Pban model observed for $La_{2/3}TiO_3$ in that it consists of a 3D-network of corner shared octahedra with linear chains of alternating pairs of long and short Ti-O bonds along the c-axis. Unlike the Pban model however, the P4/mmm structure exhibits no octahedral tilting in the ab plane. In addition, there are also four distinct neodymium sites which are preferentially ordered with the refined occupancies as follows: 79.6(5)% at the Nd1 site, 88.9(6)% at the Nd2 site, 60.6(5)% at the Nd3 site and 37.8(7)% at the Nd4 site.

This preferential ordering of vacancies is mirrored in the local distortion observed in the Ti-O octahedron. To compensate for the large charge deficit at the Nd4 site, the Ti(IV) ion moves off centre towards the z = 0.5 layer producing a long Ti-O1 bond and a relatively shorter Ti-O2 bond. The strong charge deficit at the Nd4 site is also reflected by the large U_{11} anisotropic temperature factor of the O2. On the other hand, as the O1 atom is furthest away from this site it is only influenced by the charge deficit at the Nd1 and Nd2 sites as shown

TABLE 3.11: Single cyrstal data, data collection and refinement results for $Nd_{2/3}TiO_3$.

Crystal data

$Nd_{2/3}TiO_3$
$M_r = 192.18$
Tetragonal

P4/mmm
$a = 5.4381(18)$ Å
$c = 7.6940(38)$ Å
$V = 227.5(2)$ Å^3
$Z = 4$
$D_x = 5.610$ Mgm^{-3}
D_m not measured

Mo Kα radiation
$\lambda = 0.71073$ Å
Cell parameters from 7868 reflections
$\theta = 5.67° - 38.56°$
$\mu = 18.344$mm^{-1}
$T = 300(2)$K
Thin plate
0.064mm x 0.014mm x 0.006mm
Colourless

Data Collection

Siemens P4 diffractometer with a Siemens SMART 1 K CCD area detector
Area detector scans
Absorption correction:
SADABS (Sheldrick, 1996)
$T_{min} = 0.529$, $T_{max} = 1.000$
7868 measured reflections

429 independent reflections
362 reflections with $I > 2\sigma(I)$
$R_{int} = 0.04$
$\theta_{max} = 38.56°$
$-9 \le h \le 7$
$-9 \le k \le 9$
$-13 \le l \le 12$
Intensity decay: none

Refinement on F^2

Refinement on F^2
$R[F^2 > 2\sigma(F^2)] = 0.0548$
$wR(F^2) = 0.1657$
429 reflections
30 parameters
$S = 1.112$
$w = 1/[\sigma(F^2_o)+(0.0903P)^2+3.2576P]$
where $P = (F_o^2+2F_c^2)/3$

$(\Delta/\sigma)_{max} = 0.0000$
$\Delta\rho_{max} = 3.58$ e Å^{-3}
$\Delta\rho_{min} = -2.59$ e Å^{-3}
$\Delta\rho_{rms} = 0.51$ e Å^{-3}
Extinction correction: 0.0025
Scattering factors from (Hahn, 1983)

TABLE 3.12: Refined atomic positions and overall isotropic temperature factors for $Nd_{2/3}TiO_3$ obtained from single crystal x-ray diffraction.

Atom	Site †	x	y	z	sof	U_{eq} (Å^2)††
Nd1	1a	0	0	0	0.04796(31)	0.00830(38)
Nd2	1c	0.5	0.5	0	0.05358(36)	0.00869(35)
Nd3	1b	0	0	0.5	0.03652(30)	0.01434(57)
Nd4	1d	0.5	0.5	0.5	0.02279(43)	0.01765(99)
Ti1	4i	0.5	0	0.25448(15)	0.2500	0.00684(45)
O1	2f	0.5	0	0	0.1250	0.0676(85)
O2	2e	0.5	0	0.5	0.1250	0.0633(79)
O3	8r	0.24909(86)	0.24909(86)	0.2404(13)	0.5000	0.0559(37)

†*P4/mmm*;††$U_{eq} = 1/3\ \Sigma_i\Sigma_j\ U^{ij}a^i a^j\ \mathbf{a}_i.\mathbf{a}_j$

TABLE 3.13: Anisotropic displacement parameters (Å^2) for $Nd_{2/3}TiO_3$

Atom	U_{11}	U_{22}	U_{33}	U_{23}	U_{13}	U_{12}
Nd1	0.0083(4)	0.0083(4)	0.0084(5)	0.00	0.00	0.00
Nd2	0.0095(4)	0.0095(3)	0.0072(4)	0.00	0.00	0.00
Nd3	0.0154(7)	0.0154(6)	0.01218(8)	0.00	0.00	0.00
Nd4	0.0213(11)	0.0214(11)	0.0102(13)	0.00	0.00	0.00
Ti1	0.0074(6)	0.0069(6)	0.0062(7)	0.00	0.00	0.00
O1	0.1264(207)	0.0732(128)	0.0033(40)	0.00	0.00	0.00
O2	0.0209(52)	0.1667(239)	0.0039(38)	0.00	0.00	0.00
O3	0.0362(36)	0.0362(36)	0.0954(97)	0.0290(35)	0.02902(35)	0.0309(40)

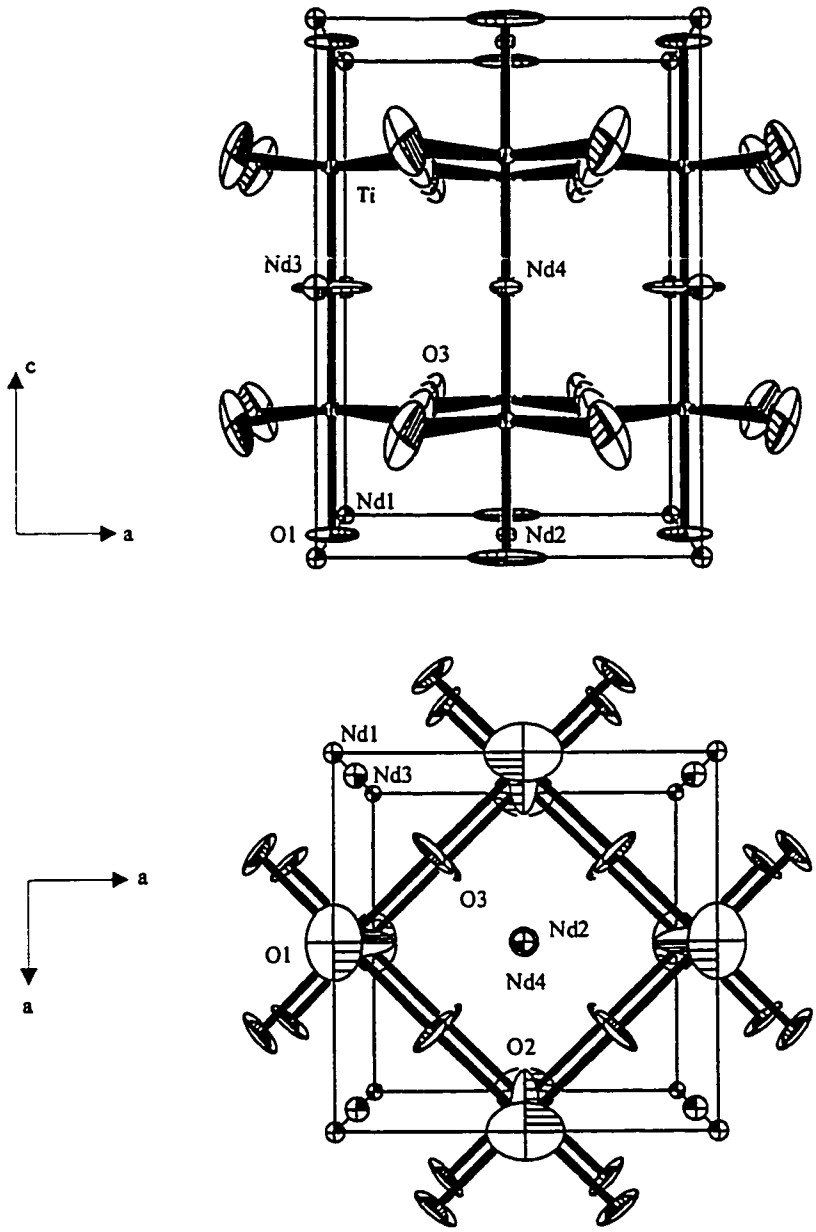

Fig. 3.19. The P4/mmm structure for $Nd_{2/3}TiO_3$. View along a). a-axis and b). c-axis. Thermal ellipsoids are drawn at a 50% probability level.

by its large U_{11} and U_{22} parameters while its z-component, U_{33}, remains relatively small.

The large anisotropic displacement parameters for O1 and O2 suggests that these sites may be split into two half occupied sites each. By moving from the 2f to 4l site for O1 and from the 2e to 4o site for the O2 site the new residuals obtained were $wR(F^2) = 0.1584$ for all 429 data and $R(F) = 0.0532$ for the 362 observed data. In conjunction with the residuals from the previous model the Hamilton significance test was performed (Hamilton, 1964). This test was developed in order to assess whether or not changes in the R-indices obtained when the structural model is altered are meaningful. The result of our test indicated that no significant gain is obtained by splitting these sites, thus indicating that the original model is an adequate structural description of $Nd_{2/3}TiO_3$ based on the current data.

3.4.4. Geometrical trends in the $Nd_{(1-x)}TiO_3$ system : Since it is known that a strong correlation exists between the structural features of the titanates and their physical properties, a study of the bond angle and bond distance trends in the $Nd_{(1-x)}TiO_3$ system is presented here. The disorder arising from the systematic increase of the vacancies in this family of compounds is reflected by the increasingly larger thermal parameters as one moves from $x = 0.00$ to 0.30 at the neodymium and oxygen sites. Selected bond distances and angles can be found in TABLES 3.14 to 3.17. The average Ti-O-Ti bond angles and Ti-O bond distances are plotted in Figs. 3.20 and 3.21 respectively. It was shown previously that the cell volume decreases almost linearly with decreasing neodymium content due to the introduction of the smaller Ti(IV) ions introduced in the lattice. Following this trend is the observed decrease in the average Ti-O

TABLE 3.14: Selected bond distances (Å) and angles (°) for x = 0.00, 0.05 and 0.10 phases in $Nd_{(1-x)}TiO_3$ system obtained from neutron diffraction study.

	M†	$NdTiO_3$	$Nd_{0.95}TiO_3$	$Nd_{0.90}TiO_3$
Nd-O1	x1	2.42(4)	2.447(13)	2.452(11)
Nd-O1	x1	3.33(5)	3.219(13)	3.143(11)
Nd-O1	x1	2.350(130)	2.462(17)	2.482(15)
Nd-O1	x1	3.250(12)	3.088(18)	3.050(16)
Nd-O2	x2	2.625(24)	2.604(11)	2.650(10)
Nd-O2	x2	3.53(3)	3.484(10)	3.364(10)
Nd-O2	x2	2.717(14)	2.792(9)	2.756(9)
Nd-O2	x2	2.38(3)	2.305(10)	2.360(9)
Ti-O1	x2	2.0129(19)	1.995(3)	1.984(20)
Ti-O2	x2	2.044(4)	1.995(7)	1.991(7)
Ti-O2	x2	2.059(4)	2.074(7)	2.026(7)
O1-Ti-O1		180.0	180.0	180.0
O2Ti-O2		180.0	180.0	180.0
O2Ti-O2		90.89(17)	91.9(3)	91.3(3)
		89.11(17)	88.1(3)	88.7(3)
O1-Ti-O2		88.87(23)	85.4(4)	85.3(4)
		91.13(23)	94.6(4)	94.7(4)
		89.90(22)	91.3(4)	90.7(3)
		90.10(22)	88.7(4)	89.3(3)
Ti-O1-Ti		150.4(4)	155.5(7)	158.8(6)
Ti-O2-Ti		148.40(24)	148.5(4)	152.3(4)

†Multiplicity

TABLE 3.15: Selected bond distances (Å) and angles (°) for x = 0.15 and 0.17 phases in the $Nd_{(1-x)}TiO_3$ system obtained from neutron diffraction study.

	M†	$Nd_{0.85}TiO_3$	$Nd_{0.83}TiO_3$
Nd-O1	x1	2.502(13)	2.634(20)
Nd-O1	x1	3.098(13)	2.926(20)
Nd-O1	x1	2.369(17)	2.45(3)
Nd-O1	x1	3.150(17)	3.04(3)
Nd-O2	x2	2.649(11)	2.746(18)
Nd-O2	x2	3.297(10)	3.256(17)
Nd-O2	x2	2.700(9)	2.732(15)
Nd-O2	x2	2.449(10)	2.336(16)
Ti-O1	x2	1.994(3)	1.973(3)
Ti-O2	x2	2.000(7)	1.998(10)
Ti-O2	x2	1.978(7)	1.989(9)
O1-Ti-O1		180.0	180.0
O2Ti-O2		180.0	180.0
O2Ti-O2		90.7(3)	90.8(2)
		89.3(3)	89.2(4)
O1-Ti-O2		90.6(4)	88.4(5)
		89.4(4)	91.6(5)
		89.1(4)	88.4(5)
		90.9(4)	91.6(5)
Ti-O1-Ti		154.9(7)	160.7(9)
Ti-O2-Ti		156.2(4)	154.1(5)

†Multiplicity

TABLE 3.16: Selected bond distances (Å) and angles (°) for x = 0.25 and 0.30 phases in $Nd_{(1-x)}TiO_3$ system obtained from neutron diffraction study.

	M†	$Nd_{0.75}TiO_3$	$Nd_{0.70}TiO_3$
Nd1-O1	x4	2.893(7)	2.897(8)
Nd1-O1	x4	2.466(6)	2.485(8)
Nd1-O3	x2	2.7126(6)	2.7095(8)
Nd1-O3	x2	2.7331(7)	2.7235(8)
Nd2-O1	x4	3.005(7)	2.971(8)
Nd2-O1	x4	2.596(6)	2.571(8)
Nd2-O2	x2	2.7126(6)	2.7095(9)
Nd2-O2	x2	2.7331(7)	2.7235(8)
Ti-O1	x2	1.945(7)	1.931(9)
Ti-O1	x2	1.959(7)	1.960(8)
Ti-O2	x1	1.896(19)	1.873(19)
Ti-O3	x1	1.978(19)	1.987(19)
O1-Ti-O1		90.1(3)	90.0(4)
O1-Ti-O1		89.4(3)	89.6(4)
O1-Ti-O1		172.6(11)	173.3(11)
O1Ti-O2		93.7(6)	93.4(6)
O1Ti-O3		86.3(6)	86.6(6)
O2-Ti-O3		180.0	180.0
Ti-O1-Ti		161.0(5)	161.7(6)
Ti-O2-Ti		180.0	180.0
Ti-O3-Ti		180.0	180.0

† Multiplicity

TABLE 3.17: Selected bond distances (Å) and angles (°) for the $Nd_{2/3}TiO_3$ phase as determined by single crystal x-ray diffraction.

Bond type	M†	Bond Distance (Å)
Nd1-O1	x4	2.7191(9)
Nd1-O3	x8	2.6631(97)
Nd2-O1	x4	2.7191(9)
Nd2-O3	x8	2.6732(74)
Nd3-O2	x4	2.7191(9)
Nd3-O3	x8	2.7673(75)
Nd4-O2	x4	2.7191(9)
Nd4-O3	x8	2.7770(98)
Ti1-O1	x1	1.9580(15)
Ti1-O2	x1	1.8890(15)
Ti1-O3	x4	1.9257(9)
O1-Ti-O2		180.00
O2-Ti-O3		93.20(33)
O1-Ti-O3		86.80(33)
O3-Ti-O3		89.48(43)
O3-Ti-O3		90.16(41)
O3-Ti-O3		173.55(63)

† Multiplicity

bond distance, shown in Fig. 3.21, coupled with an almost linear increase in the average Ti-O-Ti bond angle, shown in Fig. 3.20. The bars in these figures represent the deviation about the average values in the Ti-O bond distances and Ti-O-Ti bond angles plotted. From the relative magnitudes of these bars, it can be inferred that on traversing the series from x = 0.00 to 0.30 the distortions in the local Ti-O octahedron in the Pban structure become very large when compared to those in the Pnma structure and reflect the partial ordering of vacancies in the lattice. Furthermore, the trends observed in Figs. 3.20 and 3.21 suggest a shrinking of the d^1 electron bandwidth as x decreases consequently setting the stage for increased electron correlation effects in these compounds.

3.4.5. $Sm_{(1-x)}TiO_3$ ($0 \leq x \leq 0.17$)

Through x-ray powder Guinier diffraction data, it was determined that this solid solution exists only in the range $0 \leq x \leq 0.17$. Several attempts to prepare more highly doped samples resulted in the formation of multiphase mixtures. This observation is in accordance with that reported earlier (Bazuev et al., 1983). Thermogravimetric analysis results are shown in TABLE 3.4. The oxygen contents are within 3 % of the target oxygen content per formula unit based on the nominal samarium and titanium content. A survey of the diffraction profiles obtained by the Guinier camera show that these compounds are of the same structure type.

Generally, the cell volumes of each composition are smaller than their neodymium counterparts reported earlier and reflect the influence of the smaller sized Sm(III) ion. Similar to the observations made for the neodymium system, a linear decrease is observed when the

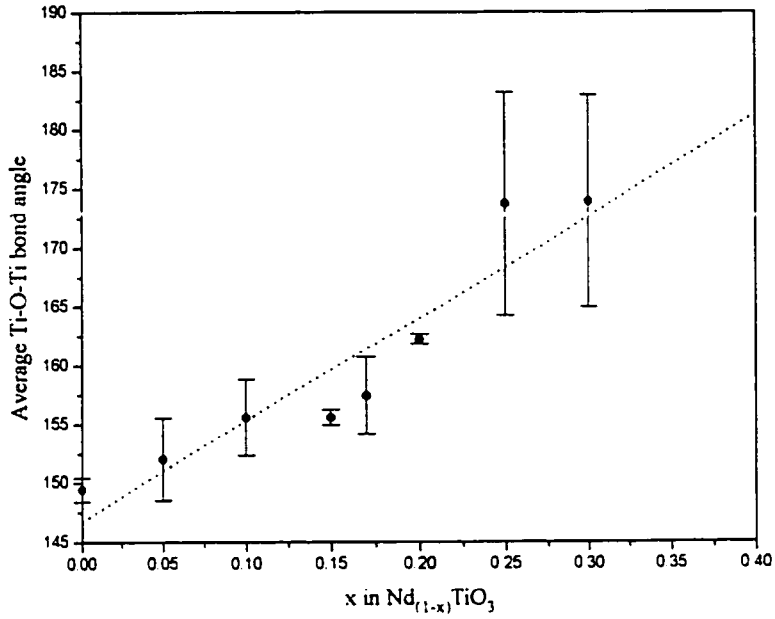

Fig. 3.20. Average Ti-O-Ti bond angle vs. vacancy content for $0.00 \leq x \leq 0.30$

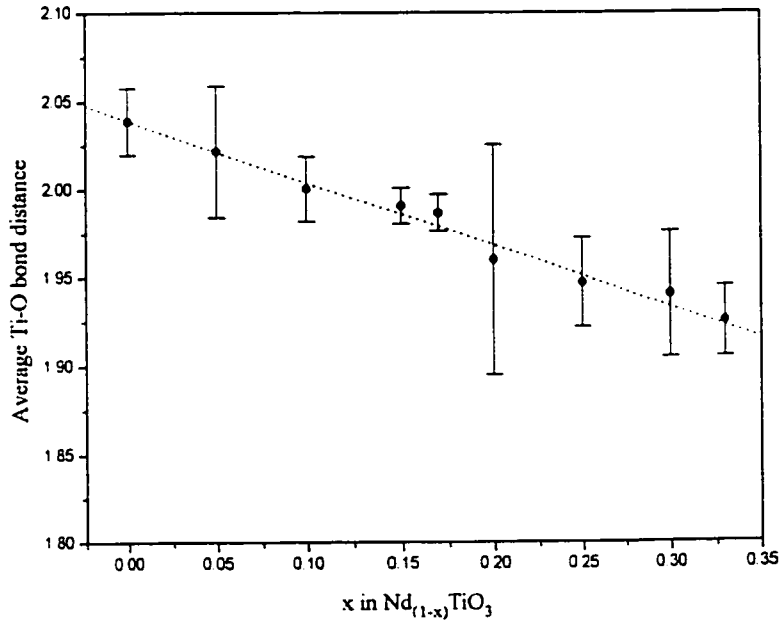

Fig. 3.21. Average Ti-O bond distance vs. vacancy content for $0.00 \leq x \leq 0.30$

cell volume is plotted versus the samarium content, see Figs. 3.22 and 3.23. The shift in the diffraction lines to higher 2θ angles from the nominal x = 0.00 to x = 0.17 compositions reflects the decreasing unit cell size as the Ti^{4+} content is increased with increasing samarium vacancy doping. Indeed the diffraction data for all phases could be indexed successfully using a Pnma model and these are summarized in TABLES IX to XIV (APPENDIX II). For this system, single crystals were prepared only for the nominal $SmTiO_3$ phase. Structural characterization for this phase was subsequently carried out using room temperature single crystal x-ray and short wavelength single crystal neutron diffraction. The details of these refinements are not presented in this section as they are already included in the paper on the determination of the magnetic structure of this phase presented in Chapter 4, Section 4.4.2.

Due to the enormously large absorption cross section for thermal neutrons by samarium these phases were not suitable candidates for structural characterization by conventional wavelength neutron powder diffraction. Consequently, the polycrystalline phases were investigated with x-ray powder diffraction albeit with limited results. As the diffraction lines obtained from the Guinier camera could be indexed reasonably well in Pnma, this model was used for the structural refinements using the x-ray powder obtained from the Nicolet diffractometer. With the exception of the $Sm_{0.85}TiO_3$ sample, there were major complications with the refinements of the remaining samples as reflected by the poor residuals obtained. The refined atomic positions and residuals for $Sm_{0.85}TiO_3$ can be found in TABLE 3.18 with the profile fit shown in Fig. 3.24.a. Selected bond angles and distances are shown in TABLE 3.19. Indeed it was surprising to find such poor residuals for a polycrystalline sample of nominal $SmTiO_3$ which is known

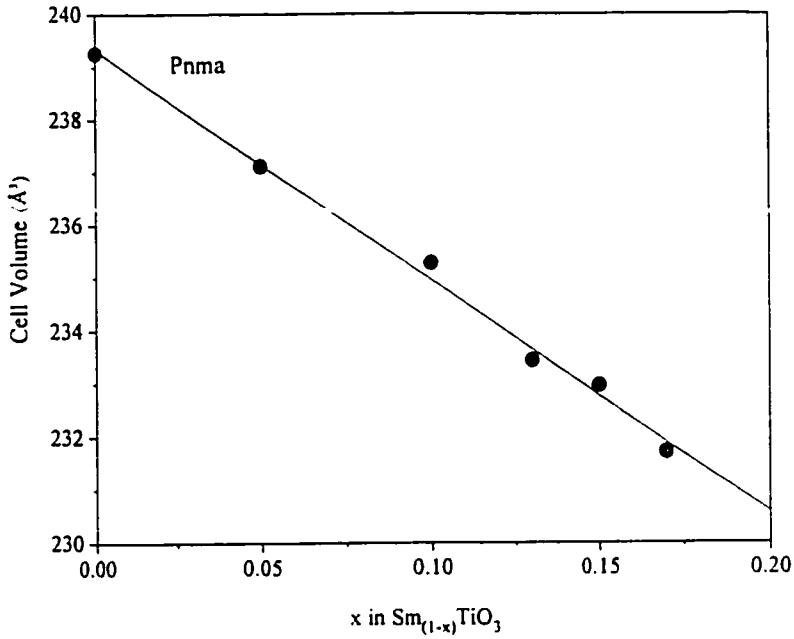

Fig. 3.22. Cell Volume vs. vacancy doping, x, in the $Sm_{(1-x)}TiO_3$ system.

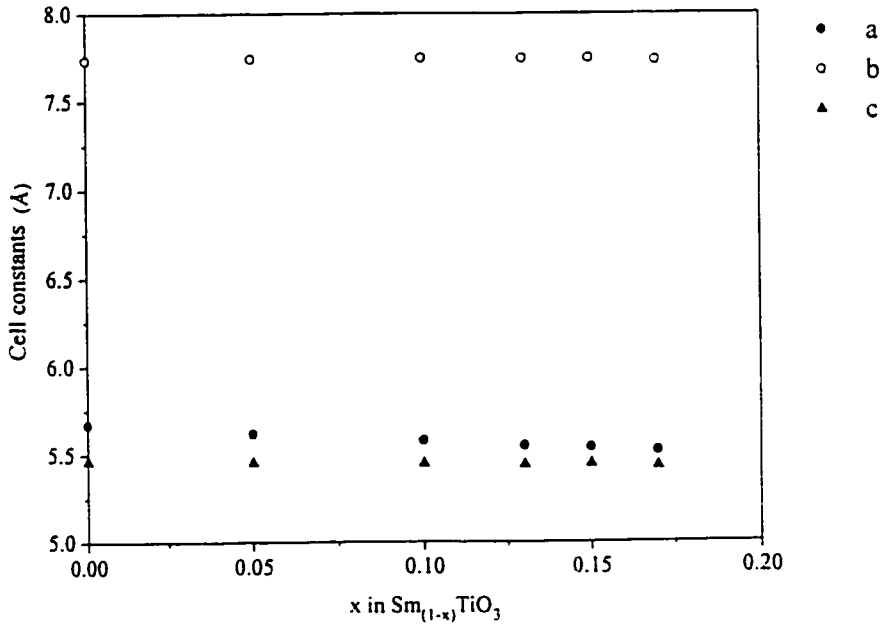

Fig. 3.23. Cell constants vs. vacancy doping, x, in the $Sm_{(1-x)}TiO_3$ system.

TABLE 3.18: Refined atomic positions and cell constants from x-ray data for nominal x = 0.15 in the $Sm_{(1-x)}TiO_3$ system.

		$Sm_{0.85}TiO_3$
		Pnma
Sm	x	0.0471(5)
	y	0.25
	z	0.9931(16)
	B(Å^2)	1.09(9)
Ti	x	0.5
	y	0.0
	z	0.0
	B(Å^2)	1.89(18)
O1	x	0.4830(43)
	y	0.25
	z	0.0763(58)
	B(Å^2)	1.00
O2	x	0.3038(41)
	y	0.0452(36)
	z	0.7080(46)
	B(Å^2)	1.00
	a (Å)	5.5423(5)
	b (Å)	7.7498(9)
	c (Å)	5.4401(5)
	V(Å^3)	233.6616(19)
	R_{wp}	12.10
	S	1.69
	R_p	9.34
	R_{Bragg}	11.19

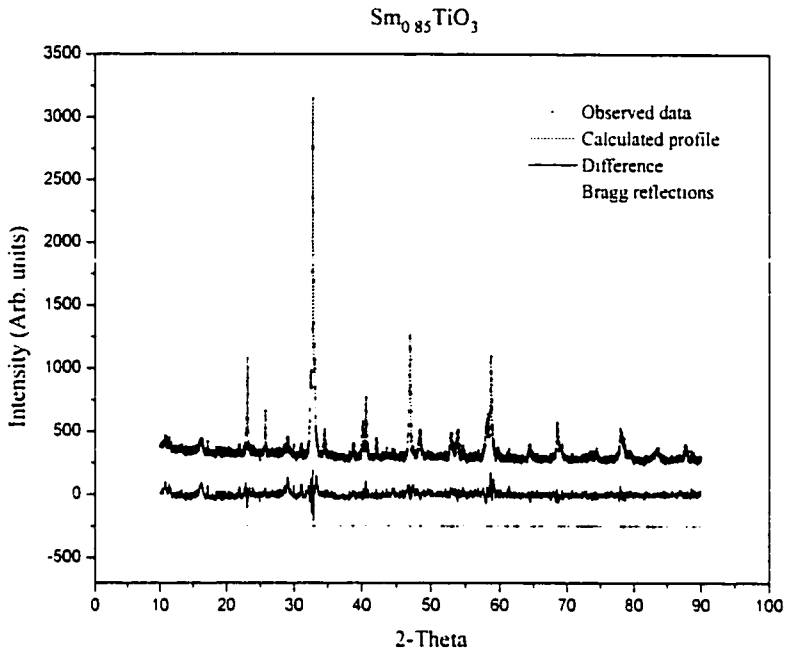

(a).

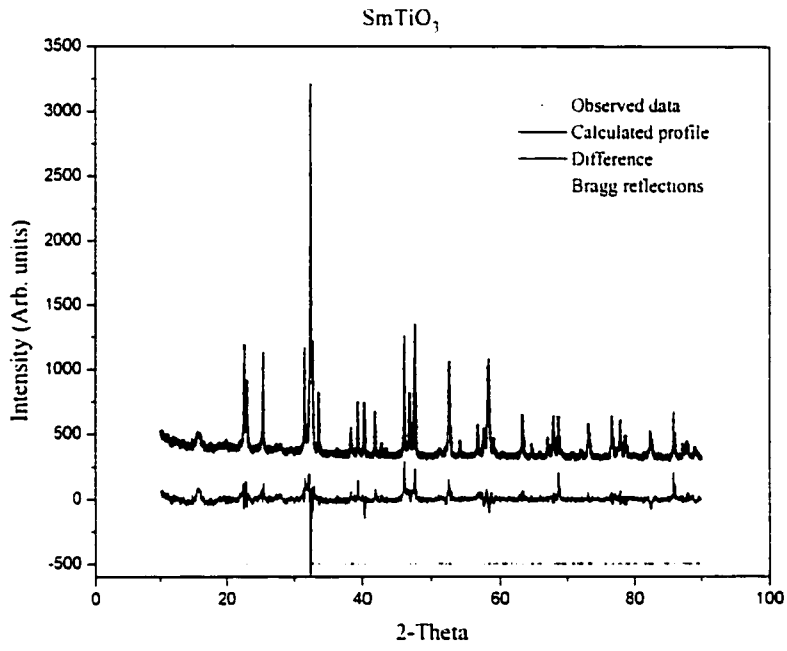

(b).

Fig. 3.24. Refined x-ray powder diffraction profiles for a). x = 0.15 and b). x = 0.00

TABLE 3.19: Selected bond distances (Å) and angles (°) for x = 0.15 in the $Sm_{(1-x)}TiO_3$ system as determined from powder x-ray diffraction.

	M†	$Sm_{0.85}TiO_3$
Sm-O1	x1	2.458(24)
Sm-O1	x1	3.159(24)
Sm-O1	x1	2.37(3)
Sm-O1	x1	3.12(3)
Sm-O2	x2	2.64(3)
Sm-O2	x2	3.41(1)
Sm-O2	x2	2.70(3)
Sm-O2	x2	2.35(3)
Ti-O1	x2	1.984(7)
Ti-O2	x2	1.957(24)
Ti-O2	x2	2.059(24)
O1-Ti-O1		180.0
O2Ti-O2		180.0
O2Ti-O2		91.3(10)
		88.7(10)
O1-Ti-O2		88.2(12)
		91.8(12)
		90.7(11)
		89.3(11)
Ti-O1-Ti		155.2(18)
Ti-O2-Ti		150.5(14)

†Multiplicity

to possess the Pnma structure type (MacLean et. al., 1979) This disagreement can be best rationalized by the data collection process itself. While the x-ray powder diffraction method is susceptible to exhibit preferred orientation effects due to sample preparation, it appears that there are additional instrumental sources of errors which may contribute to the poor refinements. This is seen in the data collected for $SmTiO_3$ where unusually large spikes in the diffraction peaks are observed, possibly due to voltage irregularities on the power lines, see Fig. 3.24.b and 3.25 to 3.26. Unfortunately, it is difficult to extract anything meaningful in terms of an analysis of the bond distance and angles with the current data and this should be investigated at a later date when more reliable means of intensity measurement are available. However, based on the systematic decrease in the cell volume, it is expected that such studies would reveal a similar trend as observed in the $Nd_{(1-x)}TiO_3$ system reflecting a decrease of the d^1 electron bandwidth, W, with smaller vacancy content.

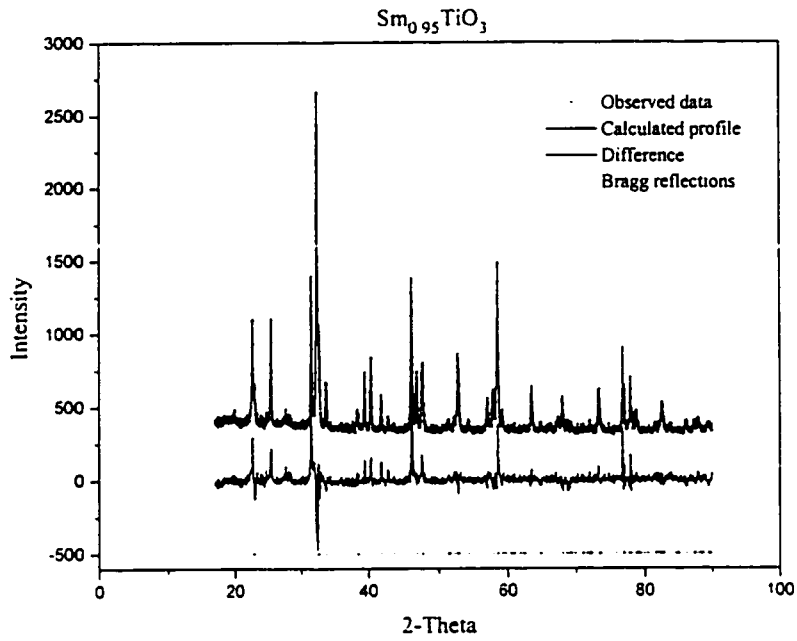

(a).

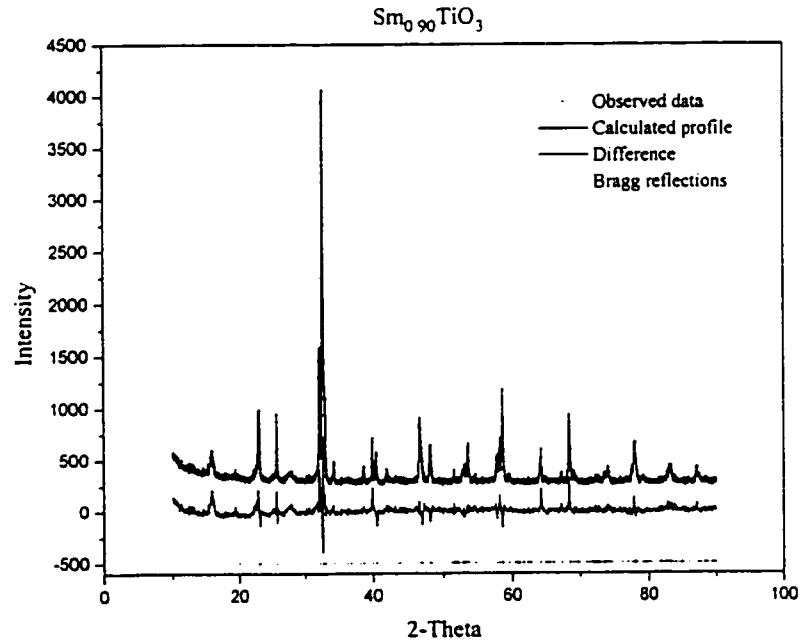

(b).

Fig. 3.25. Refined x-ray powder diffraction profiles for a). x = 0.05 and b). x = 0.10

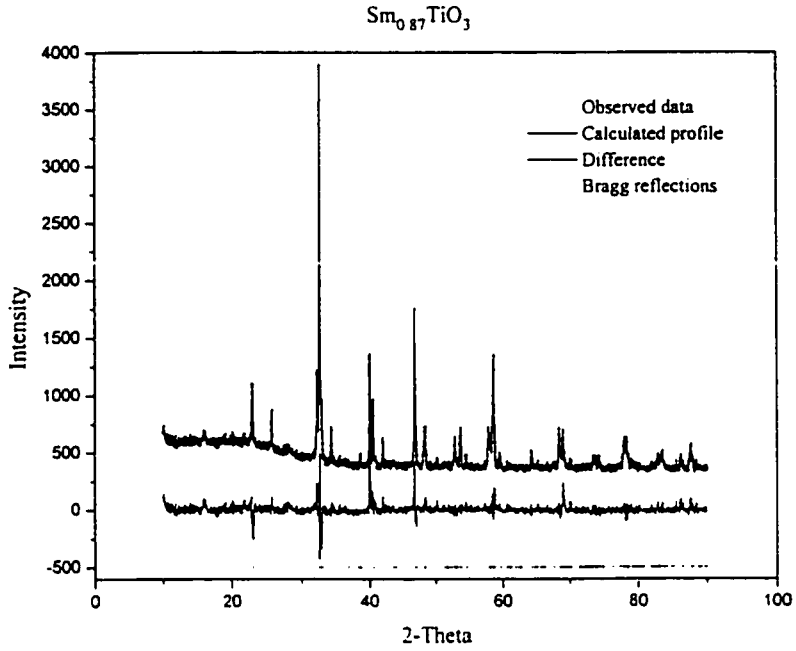

(a).

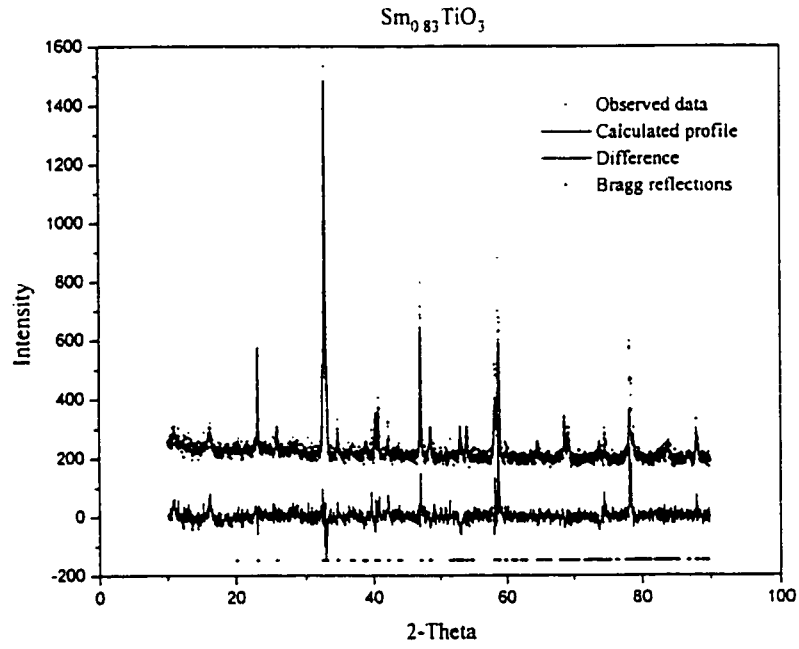

(b).

Fig. 3.26. Refined x-ray powder diffraction profile for a). x = 0.13 and b). x = 0.17.

CHAPTER 4

MAGNETIC PROPERTIES.

In this chapter the results of the magnetic studies carried out for the $R_{(1-x)}TiO_3$, R = Nd, Sm are presented. Discussions on the use of neutron diffraction as a tool for magnetic structure determinations and allowed magnetic structures in the $RTiO_3$ system are given in Sections 4.1. and 4.2., respectively. This is followed by an outline of previous work carried out for the $RTiO_3$ system including the doped systems $Nd_{(1-x)}TiO_3$ and $Nd_{(1-x)}A_xTiO_3$ (A = Ca, Sr, Ba) in Section 4.3. Finally, the results of the current work are presented in Section 4.4.

4.1. Determination of magnetic structures using neutron diffraction.

The discussion here outlines the general concepts associated with the use of neutron diffraction in magnetic studies. The reader is referred to several sources for further details (Bacon, 1955; Izyumov and Ozerov, 1970; Rossat-Mignod,). Once it has been established that a material undergoes a transition to a magnetically ordered state, neutron diffraction techniques can be applied to probe this behaviour further. This technique remains today as the primary tool for routine magnetic structural determinations. Its suitability in this area takes advantage of the inherent magnetic moment of the neutron arising from its spin. It is known that the scattering of neutrons by nuclei can be used to obtain crystallographic information. In a similar fashion the magnetic scattering of neutrons, which originate from

the dipole-dipole interaction between the magnetic moment of the neutron and the localized atomic moment, can be used to obtain information about the arrangement of localized moments in a material. For a magnetically ordered material this interaction will give rise to coherent diffraction peaks and it is the measurement of these reflections together with a knowledge of the crystal structure that leads to a description of the magnetic structure, that is the magnitude and orientation of the moments with respect to the crystallographic unit cell.

For magnetic scattering, two situations are considered, scattering by paramagnetic materials in which the moments are randomly oriented and scattering in the magnetically ordered state, such as in ferro- and antiferromagnetic materials, in which the moments are aligned. For paramagnetic scattering, the differential cross section is described by (Halpern and Johnson, 1939),

$$d\sigma_{para} = 2/3.S(S+1)[e^2\gamma/mc^2]^2.f^2 \qquad (1)$$

where S = spin quantum number, γ is the neutron magnetic moment and f is the form factor which describes the spatial distribution of the unpaired electrons. Generally, the paramagnetic scattering manifests itself as a diffuse contribution to the background scattering of the diffraction pattern.

For the scattering of magnetically ordered materials, the differential cross section is modified to,

$$d\sigma_{mag} = q^2S^2\,(e^2/mc^2).\gamma.f^2 \qquad (2)$$

where S is the spin quantum number of the atom, and q is the magnetic interaction vector defined as,

$$\mathbf{q} = \epsilon(\epsilon.\mathbf{K})-\mathbf{K} \qquad (3)$$

where **K** is a unit vector in the direction of the atomic moment (a.k.a the magnetization vector) and ϵ is a unit vector in the direction perpendicular to the reflection plane, see Fig. 4.1. The numerical value of q based on the above equation is,

$$|q^2| = 1-(\epsilon.\mathbf{K})^2 = \sin^2\alpha \qquad (4)$$

where α is the angle between the scattering vector, ϵ, and the magnetization vector, **K**. Consequently, the orientation of the spins relative to the crystallographic axes can be determined from the dependence of the magnetic scattering vector on q.

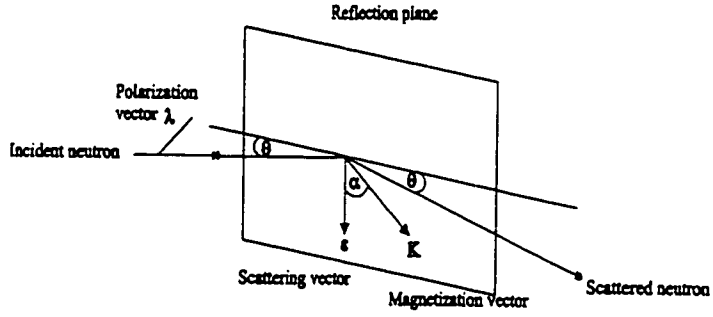

Fig. 4.1. Identification of the unit vectors ϵ, **K** and λ (Adapted from Bacon, 1955).

Halpern and Johnson (1939) have shown that the overall differential scattering cross section allowing for both magnetic and nuclear scattering can be expressed as,

$$d\sigma = b^2 + 2bp.\mathbf{q}\lambda + p^2q^2 \qquad (5)$$

where λ is a unit vector in the direction of polarization of the neutrons and p refers to the magnetic scattering amplitude of the atom. p is the magnetic analog of the nuclear scattering amplitude, b, and is defined as,

$$p = (e^2/mc^2).\gamma.S.f \qquad (6)$$

For an unpolarized beam, eqn. (5) reduces to,

$$d\sigma = b^2 + p^2q^2 \qquad (7)$$

which implies that the intensities from the nuclear and magnetic scattering are additive. Consequently, it can be written that,

$$I = F^2_{total} = F^2_{hkl} + q^2(F_{hkl}^{mag})^2 \qquad (8)$$

where F^2_{hkl} is the structure factor for the chemical cell defined by,

$$F_{hkl} = \sum_j b_j \, exp[2\pi i(hx_j + ky_j + lz_j)]e^{-2W} \qquad (9)$$

where b is the neutron scattering length, which unlike the atomic scattering factor encountered in x-ray scattering has no angular dependence and F_{hkl}^{mag} is the magnetic structure factor. Since the magnetic structure can be considered as being composed of a regular array of spin arrangements, the magnetic structure factor is expressed as,

$$F_{hkl}^{mag} = \Sigma p_j.\exp[2\pi i(hx_j + ky_j + lz_j)]e^{-2W} \qquad (10)$$

Consequently, eqn. (8) is reduced to,

$$I = [\Sigma\, b_j \exp(i\phi)]^2 + [\Sigma q.p_j. \exp(i\phi)]^2 \qquad (11)$$

where ϕ represents $2\pi(hx_j + ky_j + lz_j)e^{-2W}$ from eqn. (10).

Having defined this last expression, it is now possible to determine the magnetic structure from a measure of the intensities by neutron diffraction. It follows that in a typical experiment, the measured intensities can have contributions from both magnetic and nuclear scattering. In order to determine the magnetic structure from the collected data three basic

steps must be taken, a) identification of the propagation vector, k, b) determination of the spin orientation and c) evaluation of the magnitude of the moment. The first generally requires a knowledge of the crystal structure beforehand. The propagation vector, k, defines the periodicity of the magnetic unit cell and is usually found by determining the positions of the magnetic Bragg reflections and deriving a vector which best describes these positions. In simple cases the value of k may be (0,0,0) which indicates that the nuclear and magnetic unit cells are identical. This is typical for ferromagnetic materials. In the case of antiferromagnetic or ferrimagnetic materials, however, this may or may not be the case and a new periodicity may be introduced due to the antiparallel spin arrangement. An example of this is MnO in which the magnetic cell is doubled along the three axes of the chemical cell resulting in a wave vector k= (1/2, 1/2, 1/2) (Schull and Smart, 1949). There are also cases where the determination of the wave vector is not as simple and can sometimes be found to be incommensurate with the chemical nuclear cell, for example, $TbRuSi_2$ where the k is (0.232, 0, 0) (Chevalier et al., 1985).

Once the propagation vector is found it is then necessary to determine the orientation and magnitude of the spins in order to obtain a complete description of the magnetic structure. This is usually obtained by deriving a model for the spin configurations on the magnetic sublattices which is consistent with the observed magnetic intensities. Generally, this may be achieved by trial and error methods or systematically by the use of Shubnikov groups or representation analysis. The latter method is discussed in some detail in Section 4.2. with regard to the titanate systems.

In practice, most routine magnetic structural determinations are carried out with the use of powdered materials due to their ease of preparation. However, due to the random nature of polycrystalline samples it is often difficult to get an exact description of the spin directions. This is because in such samples, each magnetic peak obtained from a powder pattern represents the superposition of intensities scattered by a number of equivalent planes such that an independent measurement of the intensity of each reflection is sometimes difficult or impossible to obtain. This shall be demonstrated most convincingly in the determination of the magnetic structures of $NdTiO_3$, $Nd_{0.95}TiO_3$ and $Sm_{0.97}TiO_3$ presented in Section 4.4.2.

4.2. Introduction to Bertaut's notation: Allowed spin configurations in the $RTiO_3$ system.

As mentioned in the previous section, obtaining a magnetic structure that is consistent with the intensity data collected can be achieved either by trial and error methods or by systematic approaches. One systematic approach is the use of Shubnikov groups, which is based on symmetry invariance, where one determines a set of symmetry operations that leave the magnetic structure invariant (Belov et al., 1975; Donnay et al., 1958). An alternative approach is taken by Bertaut whose method is based on representation analysis. The method investigates the transformation properties of the magnetic structure under the symmetry operations of the known 230 crystallographic space groups and in some cases is shown to be superior to the use of Shubnikov groups. The general features of Bertaut's method are

outlined here with an emphasis on the determination of the allowed magnetic structures in the $RTiO_3$ system. For very detailed accounts of the theory, the reader is referred to Bertaut's original work (Bertaut, 1963; Bertaut, 1968). In these references, the space group Pbnm was used which is the non-standard setting of the space group Pnma. This nomenclature is retained in this discussion so as to avoid confusion with the original treatment. However, in the discussion of magnetic structures in Sections 4.4.2 the standard Pnma setting is utilized. This transformation simply requires a permutation of the axes xyz in Pbnm to yxz in Pnma (Hahn, 1983). The Pbnm unit cell used for the analysis is shown in Fig.4.2 with the atomic positions below,

Ti (4b) ½ 0 0 ; ½ 0 ½ : 0 ½ ½ : 0 ½ 0

R (4c) x,y,1/4 ; x, y, 3/4 ; ½ + x, ½ - y, 3/4 ; ½ - x, ½ +y, 1/4

O (8d) ± [x,y,z; ½ - x, ½ + y, ½ -z ; x, y, ½ + z; ½ + x , ½ - y, z]

The theory assumes a bilinear exchange Hamiltonian of order two, which is commonly used to describe the spin interactions on a given magnetic sublattice,

$$H = -2\sum_{ij} J_{ij} S_i S_j \qquad (12)$$

where J_{ij} is the exchange integral and $S_{i,j}$ is the spin on the i-th and j-th atoms respectively. To arrive at the possible magnetic structures four essential steps are performed which involve the determination of the independent symmetry elements, the basis of the irreducible representation, the transformation properties and the invariants.

The independent symmetry elements are determined from an inspection of the

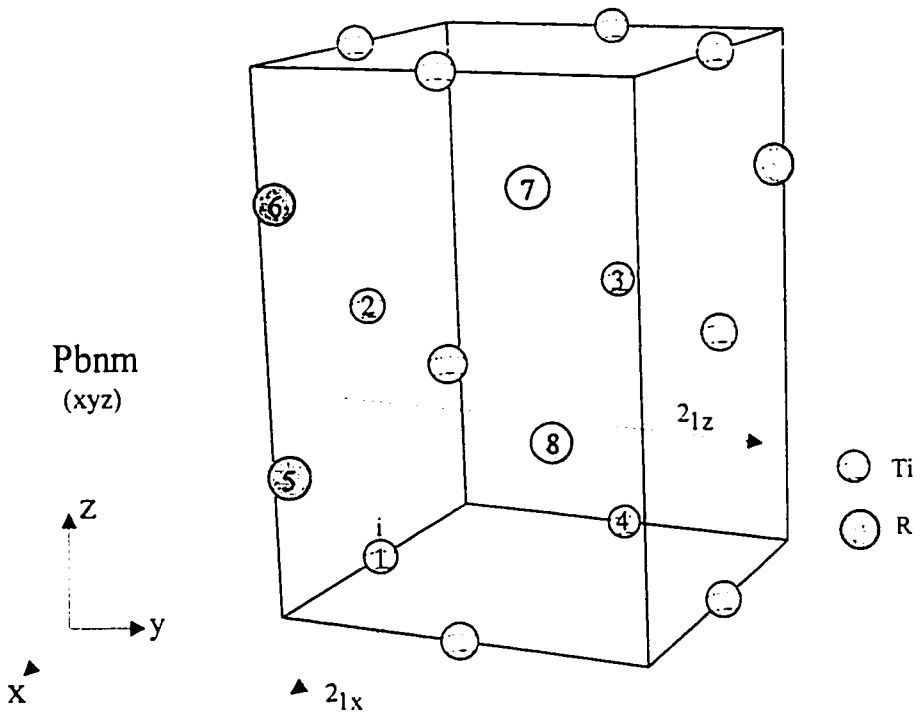

Fig. 4.2. $RTiO_3$ unit cell in the Pbnm setting. The oxygen atoms have been left out for clarity.

crystallographic space group and are essentially those operations which generate all equivalent positions defined by the general positions of the space group. For simplicity, these were chosen to be the 2_1 screw axes along x and y denoted by 2_{1x}, 2_{1y} respectively and an inversion centre at the 4b site, *i*, shown in Fig. 4.2. So, 2_{1x} takes 1 to 4 and 2 to 3 whereas S_{1y} takes 4 to 2 and 3 to 1. Having chosen these elements it is necessary to determine how the spin vectors, S_i, where i = 1, 2, 3....8 transform under these operations. For illustrative purposes the Ti(III) sublattice is used. A simplified approach to this determination is to take the linear combinations of the components which transform into themselves under these operations. In this manner, the following linear combinations are obtained.

$$F = S_1 + S_2 + S_3 + S_4$$

$$G = S_1 - S_2 + S_3 - S_4$$

$$C = S_1 + S_2 - S_3 - S_4$$

$$A = S_1 - S_2 - S_3 + S_4$$

These are the vectors which form the basis of the irreducible representation and they describe the possible spin configurations on the magnetic sublattice. The '+' and '-' signs indicate opposite spin directions, S_i, on the Ti(III) ions i = 1, 2, 3, 4. Consequently, it is possible to have a ferromagnetic sublattice denoted by F, in which all the spins are aligned in one direction or an antiferromagnetic sublattice with opposite spins having different spin arrangements described by G, C and A. This analysis applies to the rare earth sublattice as well where atoms 5,6,7 and 8 are used instead. As an aside, if each of these various spin arrangements were substituted into the magnetic structure factor, eqn. (10), the reflection

conditions for the observance of magnetic intensities can be derived. These correspond to,

F:	h+k = 2n, l=2n	*(k+l = 2n, h = 2n)*
G:	h+k = 2n+1, l=2n+1	*(k+l = 2n+1, h=2n)*
C:	h+k = 2n+1, l=2n	*(k+l = 2n+1, h = 2n)*
A:	h+k = 2n, l=2n+1	*(k+l = 2n, h=2n+1)*

The conditions in the Pnma setting are shown in italic. The transformation properties of the separate x,y,z components of these linear combinations are then determined under the independent symmetry elements. For example,

$$2_{1x}F_x = 2_{1x}(S_{1x} + S_{2x} + S_{3x} + S_{4x}) = S_{4x} + S_{3x} + S_{2x} + S_{1x}$$

TABLE 4.1 summarizes the transformation properties of both sublattices under the 2_{1x}, 2_{1y} and *i* independent symmetry elements. All that remains is to construct the invariants by taking bilinear combinations (since the Hamiltonian is of order 2) of components that belong to the same representation. These invariants represent the allowed magnetic couplings that are likely. For example, the possible spin configurations for the Ti(III) moments using Γ_4 in TABLE 4.1, are G_x^2, A_y^2, F_z^2, G_xA_y, A_yF_z and F_zG_x. The notation F_zG_x indicates that a ferromagnetic component along the z-direction can only be coupled with a G-type mode that is oriented along the x-axis. The invariants derived for the remaining representations are listed in TABLE 4.2.

One of the important implications of Bertaut's theory is that, based on symmetry arguments, not only can one predict which spin configurations may couple to each other on a given sublattice but also how two different sublattices may couple to each other. Generally,

TABLE 4.1: Transformation Properties in space group Pbnm for the $RTiO_3$ system.

Representation	Generators			Transition metal in 4b site			Rare Earth in 4c site		
	2_{1x}	2_{1y}	i						
Γ_1	+	+	+	A_x	G_y	C_z	•	•	C_z
Γ_2	+	-	+	F_x	C_y	G_z	F_x	C_y	•
Γ_3	-	+	+	C_x	F_y	A_z	C_x	F_y	•
Γ_4	-	-	+	G_x	A_y	F_z	•	•	F_z
Γ_5	+	+	-	•	•	•	G_x	A_y	•
Γ_6	+	-	-	•	•	•	•	•	A_z
Γ_7	-	+	-	•	•	•	•	•	G_z
Γ_8	-	-	-	•	•	•	A_x	G_y	•

TABLE 4.2: Invariants constructed from the base vectors of the irreducible representation.

Representation	T(III)	R(III)
Γ_1	A_x^2, G_y^2, C_z^2, A_xG_y, G_yC_z, C_zA_x	C_z^2
Γ_2	F_x^2, C_y^2, G_z^2, F_xC_y, C_yG_z, G_zF_x	F_x^2, C_y^2, F_xC_y
Γ_3	C_x^2, F_y^2, A_z^2, C_xF_y, F_yA_z, A_zC_x	C_x^2, F_y^2, C_xF_y
Γ_4	G_x^2, A_y^2, F_z^2 G_xA_y, A_yF_z, F_zG_x	F_z^2
Γ_5	•	G_x^2, A_y^2, G_xA_y
Γ_6	•	A_z^2
Γ_7	•	G_z^2
Γ_8	•	A_x^2, G_y^2, A_xG_y

the spin modes on the rare earth and titanium sublattices are expected to couple with each other if they belong to the same representations. For example, the spin structures belonging to Γ_4 on the Ti(III) sublattice would be expected to couple to the Γ_4 spin structures on the rare earth sublattice. This theory has been applied successfully to various $RTiO_3$ systems, such as $LaMO_3$ where M = Mn, Cr and Fe and $RFeO_3$ where R = Nd, Ho. In these systems, good agreement is found with experimental results (Koehler and Wollan, 1957; Koehler et al., 1960).

4.3. Previous Work:

As mentioned previously in Chapter 1, the parent titanates, $RTiO_3$, exhibit a rich variety in magnetic properties which range from Ti-Ti antiferromagnetic coupling observed in the lighter rare earth compounds (R = La, Ce, Pr, Nd, Sm) to ferro-magnetic Ti-Ti coupling observed for the heavier rare earth titanates, R = Gd-Lu, Y (Goral and Greedan, 1983; Greedan, 1984; MacLean and Greedan, 1981; Turner and Greedan, 1983). In addition to these observations made about the nature of the magnetism in these compounds, their magnetic structures were also determined where possible using powder neutron diffraction. The magnetic properties of these compounds and their magnetic structures are summarized in TABLE 4.3

Interestingly, the discovery of magnetic ordering behaviour in the neodymium and samarium titanates have only recently been reported. Despite their unique positions in the series, juxtaposed between the antiferromagnetic $PrTiO_3$ and the ferrimagnetic $GdTiO_3$,

TABLE 4.3: Summary of the magnetic properties of the $RTiO_3$ compounds described in Pbnm.

Rare Earth	La	Ce	Pr	Nd	Sm	Gd	Tb	Dy	Ho	Y	Er	Tm	Yb
T_N, T_C (K)	125	116	90	~90	~50	34	49	64	56	29	41	58	41
Paramagnetism													
Ti	TIP	TIP	C-W	C-W	?	F_1	F_1	F_1	F_1	C-W	F_1	F_1	–
R	-	Non C-W	C-W	C-W	?					–			–
Ordered													
Ti	AF(G)	AF(G)	AF	?	?	F_z	F_x	F_y	F_y	F_z	F_z	F_z	F_z
R	-	F, CF	CF	?	?	F_z	C_yF_x	C_xF_y	C_xF_y	-	F_z	F_z	F_z

evidence for magnetic ordering in these compounds went unobserved for at least four decades since initial investigations began in 1956 (Bozorth et al., 1956). Several studies on $NdTiO_3$ have reported only paramagnetic behaviour for measurements performed in the range 4.2K to 450K (Bazuev and Shveikin, 1976; Ganguly et al., 1976; MacLean et al., 1981). In addition, a low temperature neutron powder diffraction study (Greedan, 1984) of this compound appeared to provide the most compelling evidence for the absence of magnetic ordering behaviour as measurements taken down to 7K revealed no evidence of magnetic behaviour. Recently, however, in an investigation of the $Nd_{(1-x)}A_xTiO_3$ (A = Ca, Sr, Ba) system (Eylem et al., 1995) results obtained from low field susceptibility and remanent moment measurements implied magnetic ordering behaviour in $NdTiO_3$ at ~90K. In conjunction with the previous neutron diffraction study (Greedan, 1984), the observations were interpreted by attributing the ordering behaviour to canted antiferromagnetism on the titanium sublattice, with the assumption that the neodymium sublattice remains paramagnetic even down to low temperatures forming a spin glass.

In the case of $SmTiO_3$, the investigation of this property has not been as extensive with only paramagnetic behaviour reported initially in the temperature range of 77K - RT (Ganguly et al., 1976) . The first report of any magnetic ordering behaviour was reported recently during investigation of the $La_{(1-x)}Sm_xTiO_3$ system (Yoshii and Nakamura, 1997). While it was reported in this study that some type of magnetic phenomenon was observed at ~50K, investigations of the magnetic structure were not pursued. Given these recent reports of ordering behaviour for these compounds as well as from our own findings, further

investigations into their magnetic behaviour and the determination of their magnetic structures by neutron diffraction techniques were undertaken.

With regard to previous work carried out on vacancy doped systems, in which the Ti(III) concentration is systematically changed, magnetic susceptibility data were reported for the vacancy doped $Nd_{(1-x)}TiO_3$ system for x = 0.00, 0.10, 0.20, 0.30 and 0.33 which initially appeared to obey Curie-Weiss paramagnetism (Bazuev and Shveikin, 1986). However, a closer inspection of the data revealed a subtle departure from this law and was explained by pronounced crystal field effects. Additionally, it was shown that the overall susceptibility was comprised of contributions from both Nd(III), which has a strong temperature dependence while Ti(III) exhibits a weak temperature dependence.

In contrast to this, the work done on the alkali earth doped system, $Nd_{(1-x)}A_xTiO_3$ (A = Ca, Sr, Ba) revealed antiferromagnetic behaviour which disappears with the onset of the metallic regime, i.e. $x \geq 0.20$ for A = Ca and $x \geq 0.10$ for A = Ba. Interestingly, the data in the paramagnetic regime was fit to a Curie-Weiss plus a temperature independent term which was assumed to consist of only a Ti(III) contribution.

4.4. Present Work

4.4.1. D.c. magnetic susceptibility:

a). $Nd_{(1-x)}TiO_3$ system: The susceptibility data for all the compositions studied in this series can be seen in Figs. 4.3 to 4.7. For the nominal x = 0.0 and 0.05 compositions, paramagnetic behaviour is observed above ~100K and the data could be fit, after making

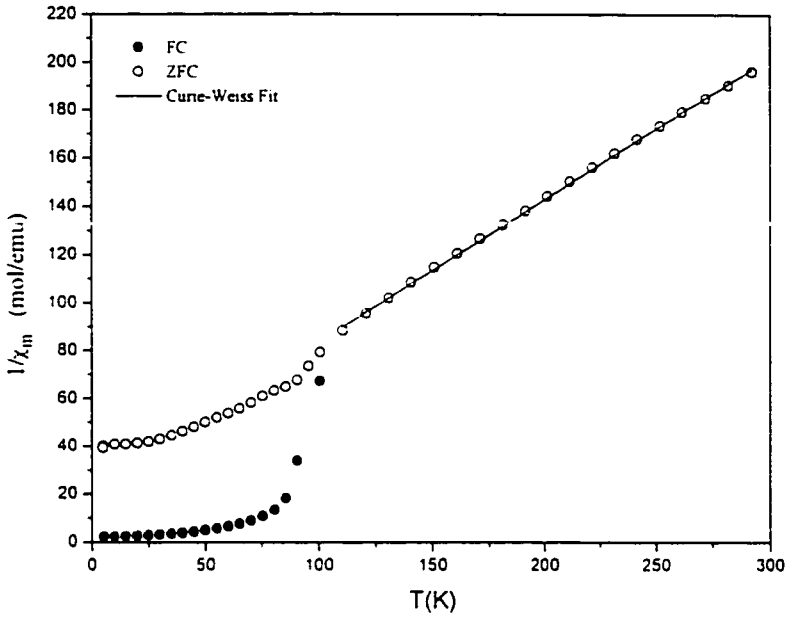

(a).

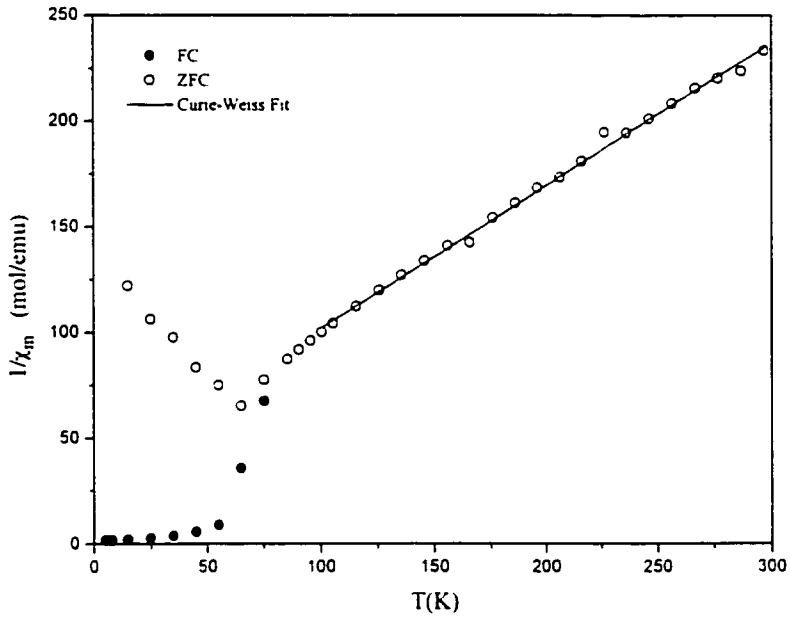

(b).

Fig. 4.3. Inverse susceptibility plots for a). $NdTiO_3$ and b). $Nd_{0.95}TiO_3$.

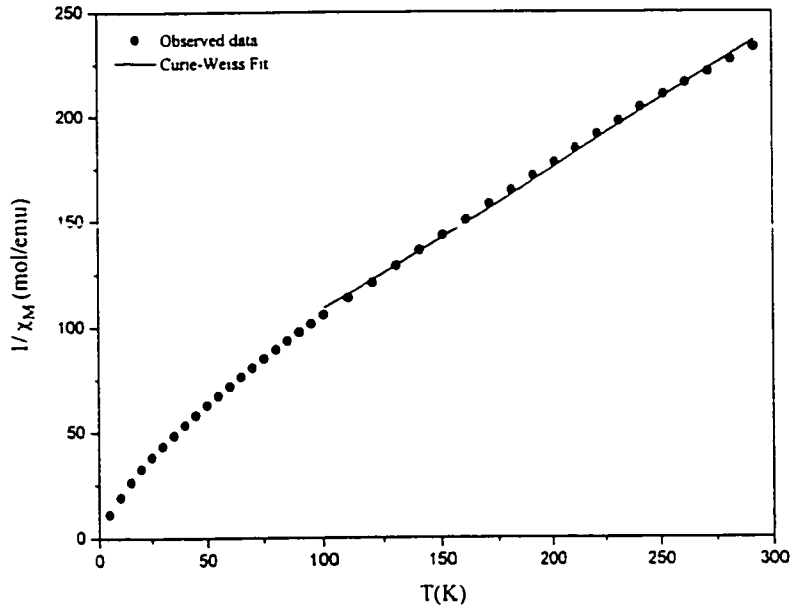

(a).

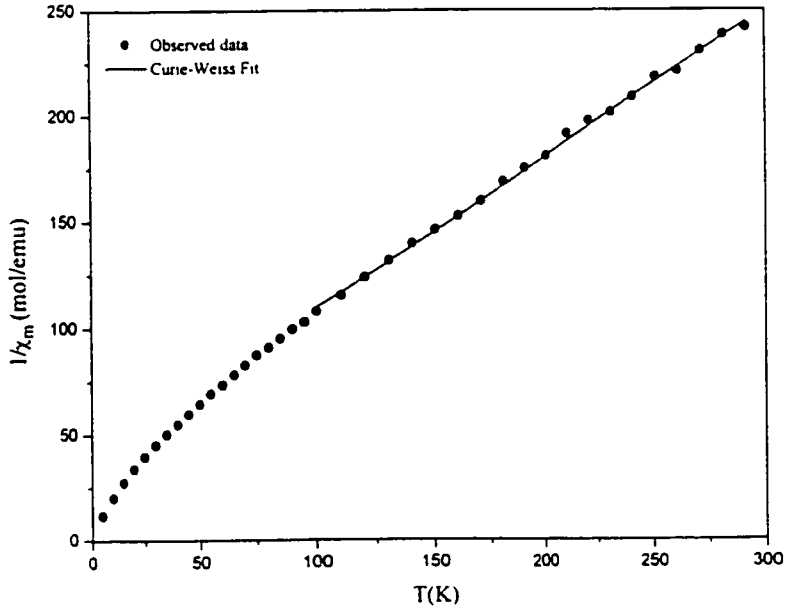

(b).

Fig.4.4. Inverse susceptibility plots for a). $Nd_{0.90}TiO_3$ and b). $Nd_{0.85}TiO_3$.

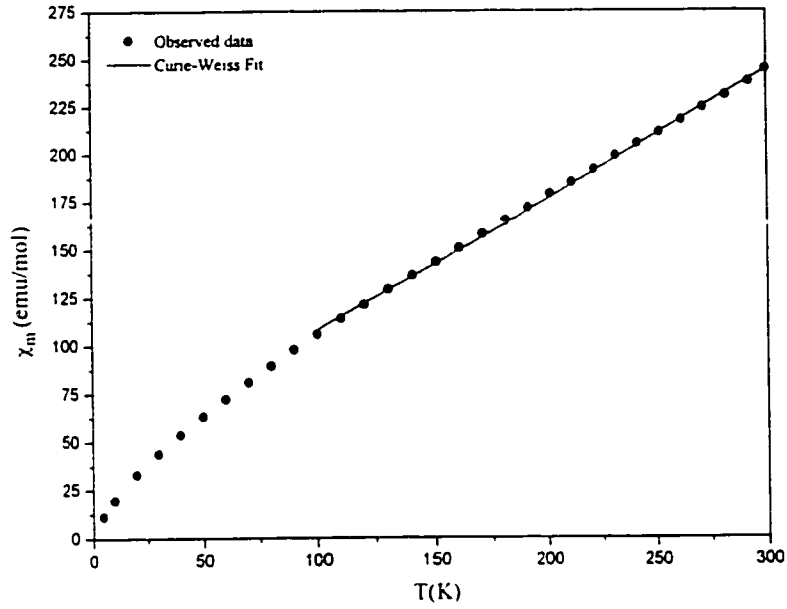

(a).

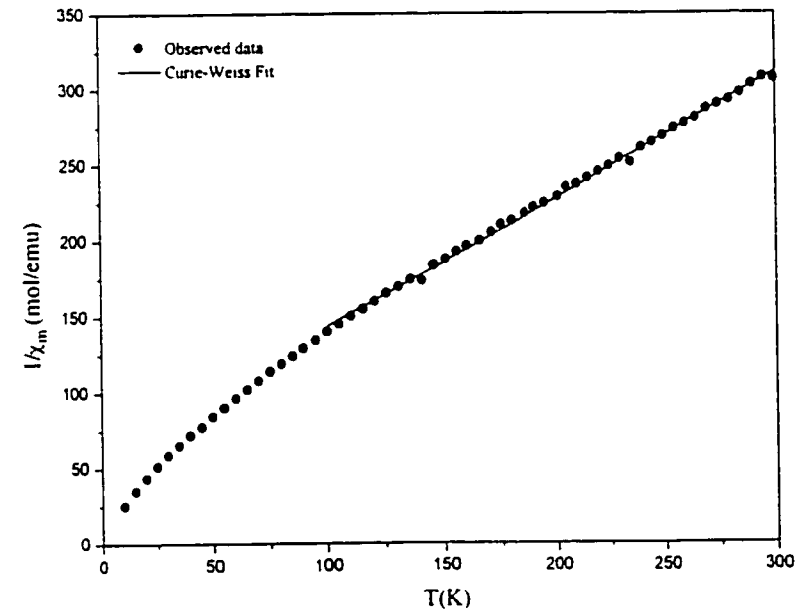

(b).

Fig.4.5. Inverse susceptibility plots for a). $Nd_{0.83}TiO_3$ and b). $Nd_{0.80}TiO_3$.

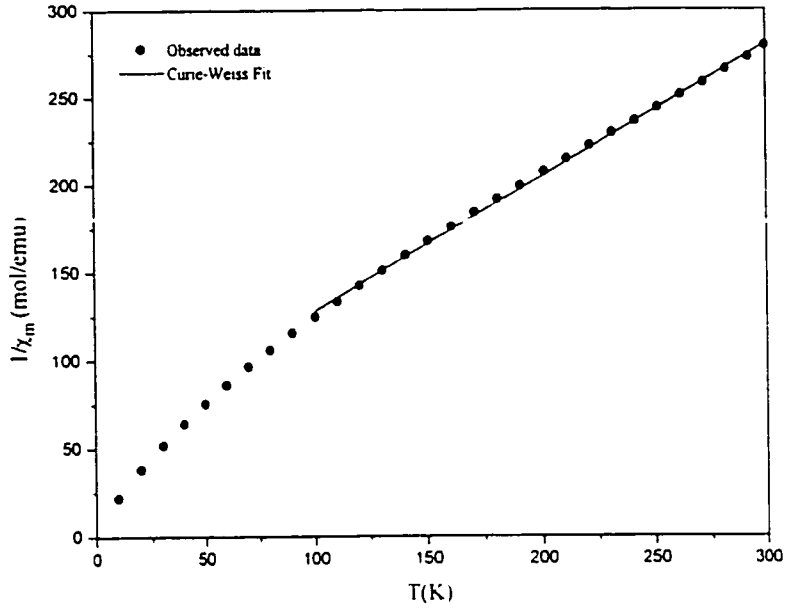

(a).

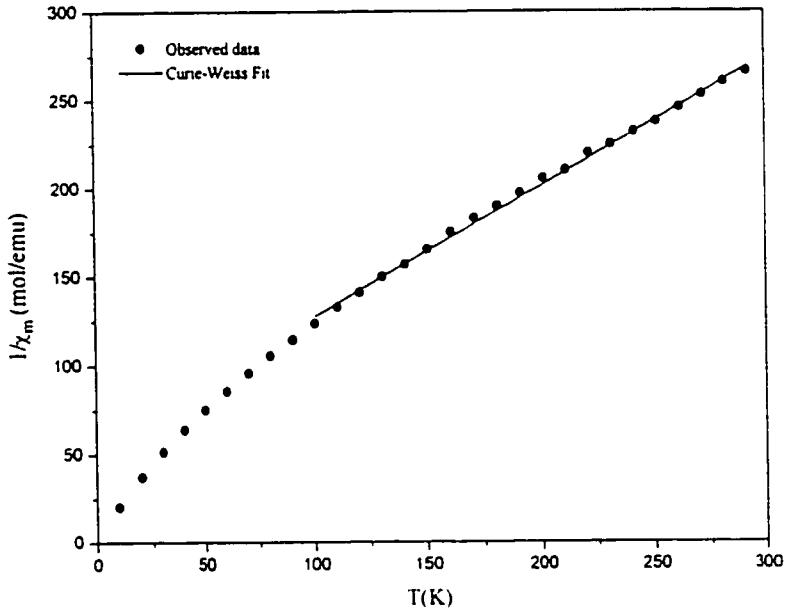

(b).

Fig.4.6. Inverse susceptibility plots for a). $Nd_{0.75}TiO_3$ and b). $Nd_{0.70}TiO_3$.

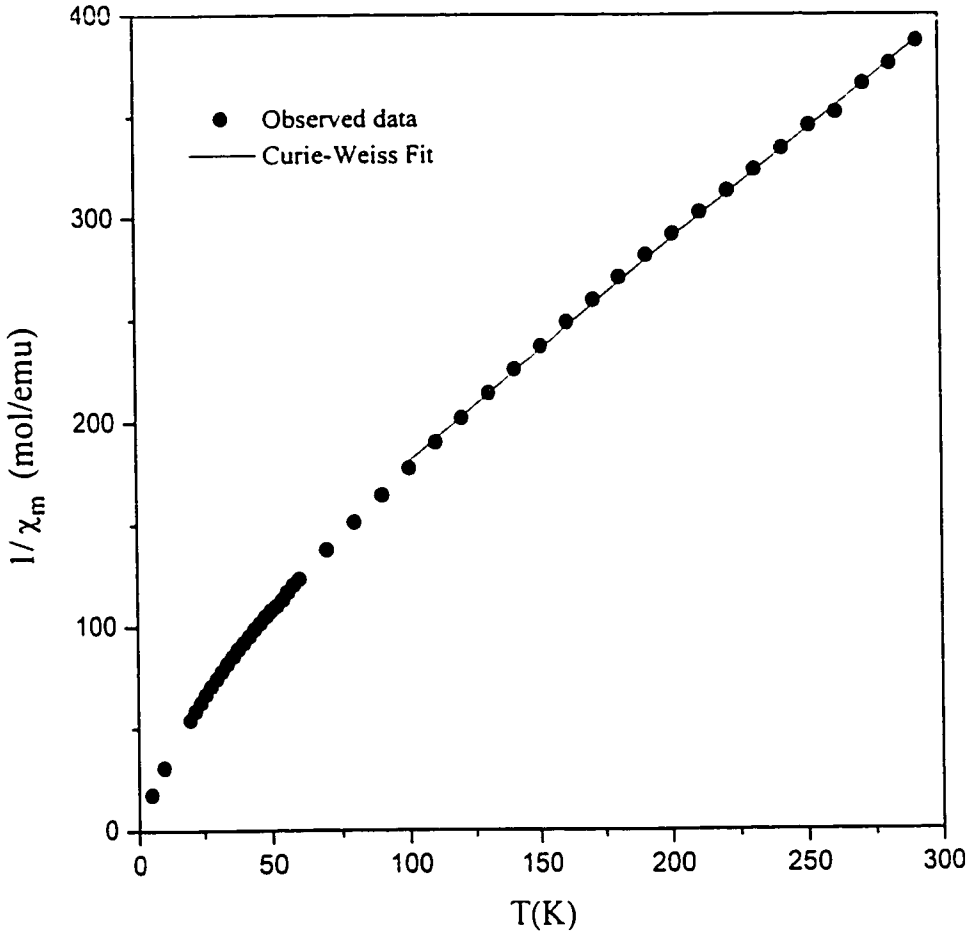

Fig.4.7. Inverse susceptibility plot for $Nd_{2/3}TiO_3$.

diamagnetic corrections, to the Curie-Weiss law,

$$\chi = C / (T-\theta) \qquad (13)$$

where C is the Curie constant and θ is the Weiss constant. The experimentally determined values of C and θ can be found in TABLE 4.4. The observation of Curie constants larger than the expected value, based on the Nd^{3+} free ion value, strongly suggests individual contributions from both Nd(III) and Ti(III) ions and compare favourably with those published previously (MacLean et al., 1981). From this same study it was shown that by comparing the observed Curie constant of $NdTiO_3$ with the isostructural $NdScO_3$, it is possible to estimate the individual contributions from each ion. Since in $NdScO_3$, the diamagnetic Sc(III) ion replaces Ti(III), the observed Curie constant is solely due to a Nd(III) contribution and was found to be 1.51(3) emu.mol/K. This value is significantly smaller than the free ion value of 1.64 emu.mol/K and has been ascribed to crystal field effects. Using this experimental value for Nd(III), the Curie constant obtained for Ti(III) in $NdTiO_3$ was found to be 0.30(6) emu.mol/K. This compares reasonably with the expected free ion value of 0.37 emu.mol/K. This suggests a localized electron model and is in agreement with the semiconducting behaviour of this phase which is reported in Chapter 5.

At temperatures below 100K, a distinct divergence is observed between the zero field cooled (ZFC) and field cooled (FC) data for the x = 0.0 and 0.05 compositions at ~90K and 75K, respectively. The divergence signals some type of magnetic phenomenon at these temperatures resulting in a weak ferromagnetic component. In light of the previous results obtained for $RTiO_3$, R = La, Ce and Pr, this observation is attributed to moment canting on

TABLE 4.4: Summary of Curie and Weiss constants from magnetic susceptibility fits.

Compound	C(emu.mol/K)	θ(K)	Expected C(Nd^{3+}) value[a]
$NdScO_3$	1.51(3)		1.64
$NdTiO_3$	1.71(1)	-45(1)	1.64
$Nd_{0.95}TiO_3$	1.49(2)	-54(3)	1.56
$Nd_{0.90}TiO_3$	1.50(2)	-63(3)	1.46
$Nd_{0.85}TiO_3$	1.42(1)	-56(2)	1.38
$Nd_{0.83}TiO_3$	1.47(1)	-58(2)	1.35
$Nd_{0.80}TiO_3$	1.19(1)	-71(2)	1.30
$Nd_{0.75}TiO_3$	1.31(1)	-67(2)	1.22
$Nd_{0.70}TiO_3$	1.31(2)	-72(3)	1.15
$Nd_{0.67}TiO_3$	0.92(1)	-67(2)	1.10
$SmTiO_3$	1.07(1)	-229(5)	-
$Sm_{0.95}TiO_3$	1.20(1)	-414(10)	-

[a] Based on the Nd(III) free ion value of 1.64 emu.K/mol

the magnetic sublattices.

For the remaining compositions in this series, $0.10 \leq x \leq 0.33$, the magnetic anomaly disappears abruptly at $x = 0.10$ revealing only paramagnetic behaviour over the entire temperature range investigated. As will be seen later in Chapter 5, this disappearance of magnetic behaviour coincides with a point where a metal-insulating transition occurs in the series. At higher temperatures, the data appears to exhibit temperature independent behaviour which is usually associated with Pauli paramagnetism in these types of systems. Consequently, after correcting for core diamagnetism, an attempt was made to fit the data over the entire temperature range to the Curie-Weiss law plus a temperature independent term, χ_{TIP}, according to,

$$\chi = C / (T-\theta) + \chi_{TIP} \qquad (14)$$

where χ_{TIP} comprises of four components a). core diamagnetism, b). Van Vleck paramagnetism, c). a diamagnetic contribution from the conduction electrons and d). a paramagnetic contribution from the conduction electrons (a.k.a. *Pauli* paramagnetism). The inverse susceptibility versus 1/T can be seen in Figs. 4.3 and 4.4. This description assumes that the Ti(III) contributes only to the temperature independent term, so that the Curie constant consists solely of a Nd(III) contribution. Using this model, the experimentally determined value of the Curie constants for these compositions were found to be quite unreasonable tending to be significantly smaller than the expected value. For example, for the $x = 0.10$ phase, the experimentally determined value of the Curie constant was found to be 0.99(1) emu.mol/K which is significantly smaller than the expected value of 1.46

emu.mol/K. Futhermore, it was observed that below ~100K, the data deviated significantly from linear behaviour. This deviation can be ascribed to the crystal field splitting of the 10-fold degenerate ground state of the Nd(III) ion. This produces a series of multiplets whose energies are comparable to kT so that the temperature dependence of χ is different from that of the free ion.

A more reasonable fit could be found by fitting the data above ~100K using the Curie Weiss law described by eqn.(13), with the experimentally determined values also shown in TABLE 4.4. Overall, the Curie constants are larger than that predicted by the free ion value and reflects the likely contribution of Ti(III) to the overall paramagnetism. The Curie constants generally decrease as expected as one goes from a large Ti(III) content as in $NdTiO_3$ to low Ti(III) content as in $Nd_{2/3}TiO_3$. However, no obvious trend is noted from compound to compound. Since for $x \geq 0.10$ only paramagnetic behaviour is observed down to 5K it is apparent that the Weiss constant is dominated by crystal field effects as the values are significantly large. Note that the experimentally determined value of the Curie constant for $Nd_{2/3}TiO_3$, 0.93emu.K/mol, is smaller than the expected value of 1.08 emu.K/mol, see Fig. 4.7. Again, as in $NdScO_3$, this is a result of crystal field effects as there are no Ti(III) ions present. While the Curie-Weiss model appears to be reasonable, it must be noted that it is not an ideal one as closer inspection of the data above 100K reveals a subtle deviation from the 1/T linear dependence and points to the need of finding a more thorough description as afforded by Van Vleck's equation. In general, the paramagnetic susceptibility may be calculated according to eqn. (15), (Carlin and van Duyneveldt, 1977; van Vleck, 1932),

$$\chi = \frac{N\sum_{n}[(E_n^{(1)})^2 / kT - 2E_n^{(2)}]exp(-E_n^0 / kT)}{\sum_{n} exp(-E_n^0 / kT)} \qquad (15)$$

where E_n is the energy of the *n*-th level and $E_n^{(1)}$ and $E_n^{(2)}$ are the energies of the first and second order Zeeman terms. The solution to this equation requires knowledge of the energies and wavefunctions of each level and this information is not currently available.

b). $Sm_{(1-x)}TiO_3$ system: The magnetic susceptibility behaviour over the temperature range of 5K to 298K for x = 0.03 and 0.05 can be seen in Fig. 4.8. Above 100K it was found that Curie-Weiss paramagnetism exists and the data could be fitted to eqn. (13). The data were corrected for core diamagnetism and experimentally determined values are summarized in Table 4.4. Below 100K, similar divergences between the ZFC and FC data are observed as in the neodymium system, however occurring at lower temperatures, specifically ~52K and ~48K for x = 0.03 and 0.05 respectively. When plotted on a larger scale the susceptibility data for the x = 0.03 composition shows a small maxima at ~40K which may be associated with a spin reordering process on the samarium sublattice. These observations are attributed to a canting of the moments on the magnetic sublattices.

For the remaining compositions, $x \geq 0.10$, the magnetic behaviour is again observed to disappear, as in the neodymium system, coinciding with a metal-insulating boundary. Interestingly, in the x = 0.10 phase, there is a very subtle broad maximum over the range ~100K-200K which disappears for the remaining doped compositions and is thought to arise

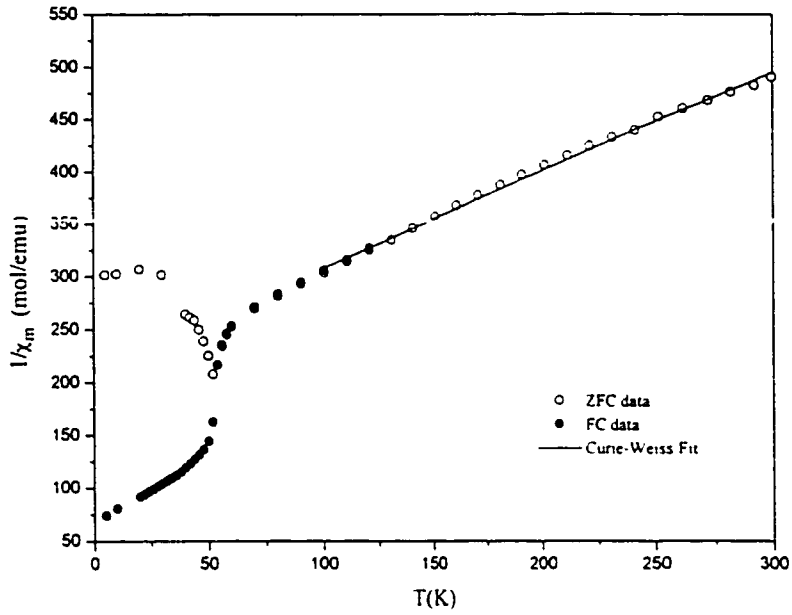

(a).

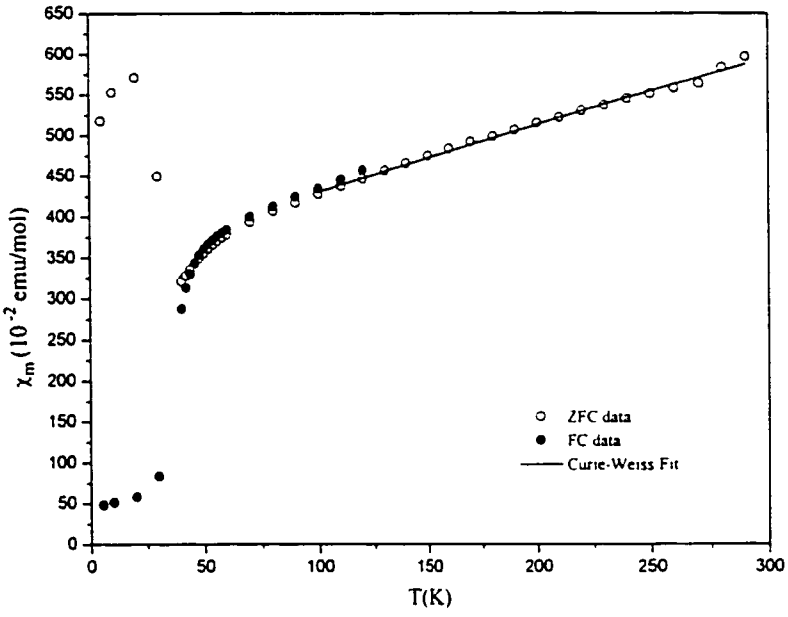

(b).

Fig.4.8. Inverse susceptibility plots for a). $Sm_{0.97}TiO_3$ and b). $Sm_{0.95}TiO_3$.

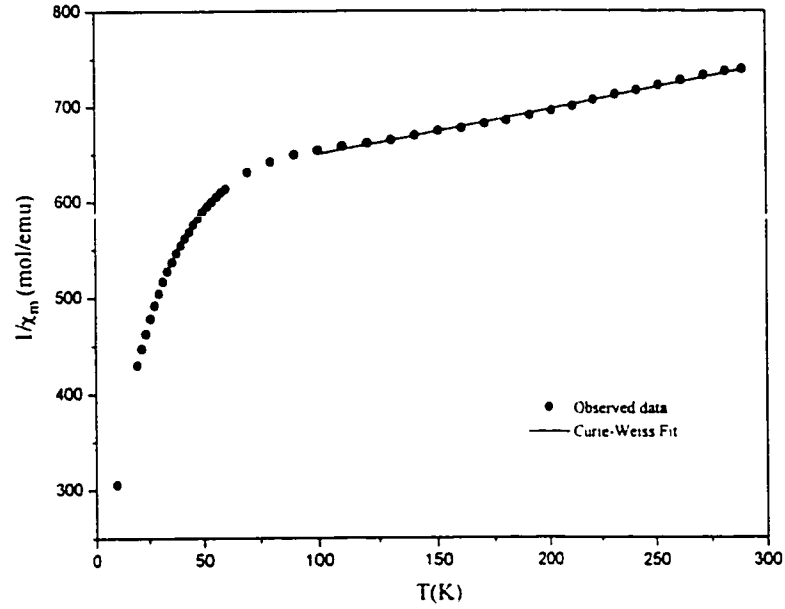

(a).

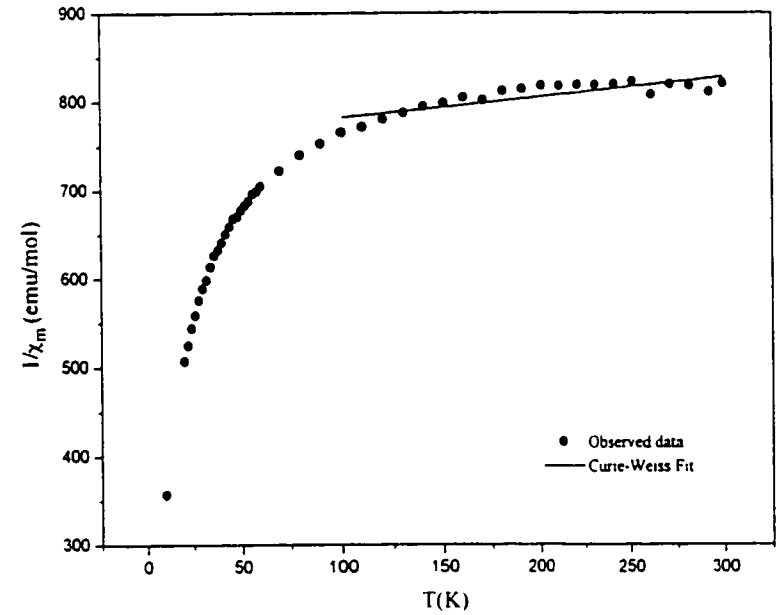

(b).

Fig.4.9. Inverse susceptibility plots for a). $Sm_{0.90}TiO_3$ and b). $Sm_{0.87}TiO_3$.

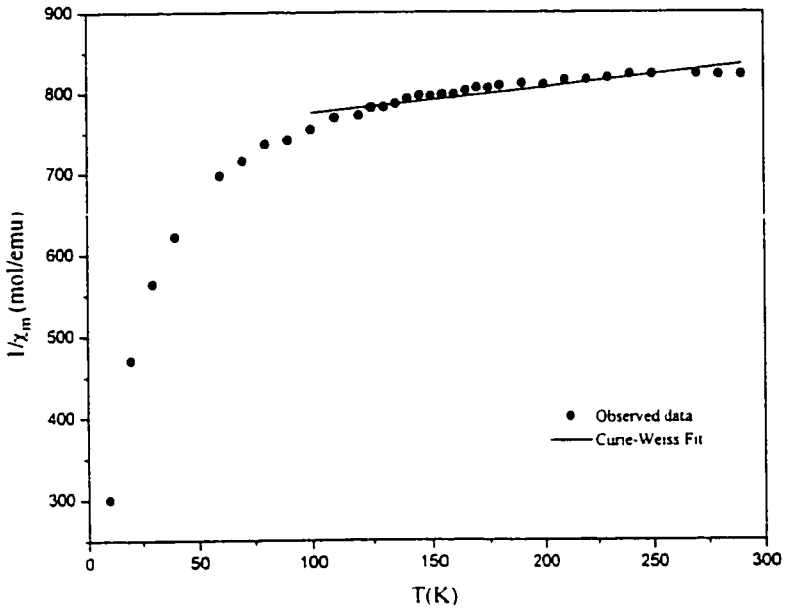

(a).

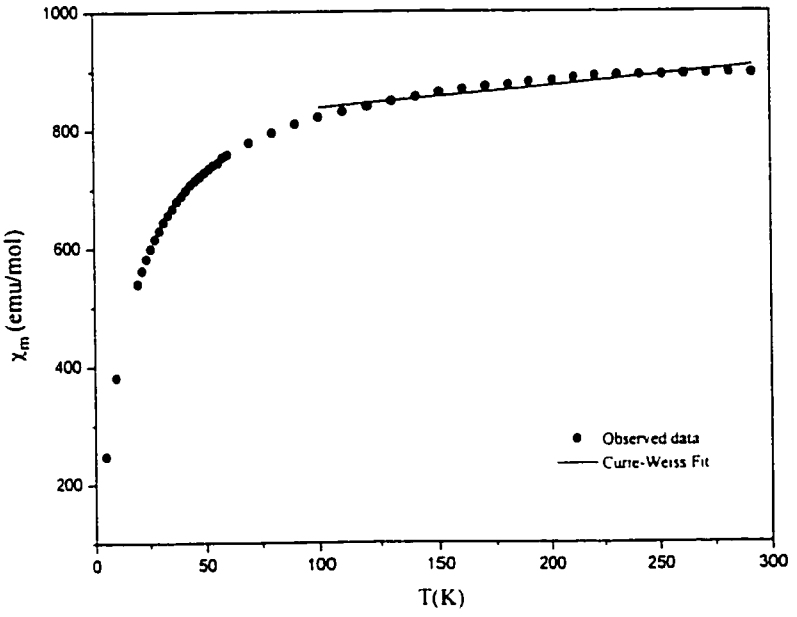

(b).

Fig.4.10. Inverse susceptibility plots for a). $Sm_{0.85}TiO_3$ and b). $Sm_{0.83}TiO_3$.

from some type of short range magnetic behaviour. For these compositions, the paramagnetic behaviour is complex as attempts to fit the data to either to eqns. (13) or (14) were unsuccessful, see Figs.4.9 to 4.10. These observations point to the difficulty in extracting meaningful values of the Curie and Weiss constants from samarium compounds. It is known that unlike the other rare earth ions, with the exception of Eu^{2+}, the separation of the ground state multiplet levels of samarium is comparable to kT and the problem is again reduced to solving eqn. (15).

4.4.2. Magnetic structure determination $NdTiO_3$, $Nd_{0.95}TiO_3$ and $Sm_{0.97}TiO_3$.

The following papers report the magnetic structure determinations of $NdTiO_3$ and $Nd_{0.95}TiO_3$ by powder neutron diffraction at the McMaster Nuclear Reactor. The magnetic structure determination of $Sm_{0.97}TiO_3$ was performed with short wavelength single crystal neutron diffraction at the Institut Laue Langevin, Grenoble, France.

JOURNAL OF SOLID STATE CHEMISTRY 121, 443–450 (1996)
ARTICLE NO. 0061

The Structural and Magnetic Properties of $Nd_{1-x}TiO_3$ for $x = 0$, 0.05, and 0.10

G. Amow and J. E. Greedan

Department of Chemistry and Brockhouse Institute for Materials Research, McMaster University, Hamilton, Ontario, L8S 4M1 Canada

Received August 7, 1995; accepted October 26, 1995

The structural and magnetic properties of members belonging to the perovskite family, $Nd_{1-x}TiO_3$ for $x = 0$, 0.05, and 0.10, have been investigated. It is found that these compounds adopt the $GdFeO_3$-type structure belonging to the space group *Pnma*. Magnetic susceptibility measurements indicate paramagnetic Curie–Weiss behavior at temperatures typically above 100 K. Antiferromagnetic ordering of the titanium sublattice is observed at T_N of 90 and 75 K for $x = 0$ and 0.05, respectively. Investigation by low-temperature neutron diffraction reveals evidence for magnetic ordering on both the titanium and neodymium sublattices. The magnetic structure is found to be consistent with that of $PrTiO_3$ and $CeTiO_3$, having an F_xC_y configuration on the Nd^{3+} sublattice and a G_xF_z configuration for the moments on the Ti^{3+} sublattice. At 10 K, the refined magnetic moments on the Nd^{3+} sublattice are determined to be 1.11(5) and 0.99(5) μ_B and on the Ti^{3+} sublattice, 0.87(8) and 0.74(9) μ_B, for $x = 0$ and 0.05, respectively. The antiferromagnetic behavior vanishes at the $x = 0.10$ composition.

INTRODUCTION

It is well known that the rare earth titanates, $RTiO_3$, form an isostructural series of compounds whose physical properties are influenced by the size and electronegativity of the rare earth ions (1). Members belonging to this family of compounds possess the orthorhombically distorted $GdFeO_3$-type structure belonging to the space group *Pnma*. In general, these compounds are semiconducting and exhibit an impressive variety of magnetic behavior (2, 3). It has been found that $LaTiO_3$ is antiferromagnetic below 125 K, and using Bertaut's notation (4), is described as having a G_xF_z spin configuration on the titanium sublattice. Similar but more complex are $CeTiO_3$ and $PrTiO_3$, which are both antiferromagnetic below 125 K, with a magnetic structure composed of a G_xF_z spin configuration on the titanium sublattice and an F_xC_y spin configuration on the rare earth sublattice (5, 6). The weak ferromagnetic component in these magnetic structures presumably arises from a canting of the antiferromagnetic moments. For the remaining rare earth titanates, R = Gd to Tm, ferri- and ferromagnetic behavior is observed (3).

Interestingly, with such a rich variation in the magnetic properties across the titanate series, evidence for magnetic behavior and the determination of the magnetic structure of neodymium titanate, $NdTiO_3$, remained elusive. The magnetic properties of this compound were first investigated by Bazuev and Shveikin (7), who found it to be paramagnetic in the temperature range 77–450 K. Similar observations were reported by Ganguly *et al.* (8) and Maclean *et al.* (9). In addition, a low-temperature neutron study by Greedan (6) seemed to provide the most conclusive evidence for paramagnetic behavior, since measurements revealed no evidence of any magnetic ordering down to 7 K. Only recently, however, Eylem *et al.* (10) reported low field susceptibility and remanent moment measurements, which indicate that $NdTiO_3$ orders antiferromagnetically at a temperature of 90 K. Their observations were interpreted by attributing the ordering behavior to a canted antiferromagnetism on the titanium sublattice, with the assumption that the neodymium sublattice remains paramagnetic even at low temperatures. They also reported similar behavior for the calcium-doped system, $Nd_{1-x}Ca_xTiO_3$ for $0 \le x \le 0.2$. These observations provide the first evidence for any type of magnetic order for $NdTiO_3$, and based on this some parallels may be inferred for the $Nd_{1-x}TiO_3$ system, using the highly correlated $La_{1-x}TiO_3$ series of compounds. This system was investigated by Crandles *et al.* (11) and MacEachern *et al.* (12), whose investigations encompassed the composition range $0 \le x \le 0.33$. It was found that there exists a strong correlation between the structural and physical properties of the system. With regard to magnetic properties, the antiferromagnetic behavior observed for the $x = 0$ composition vanishes at $x \approx 0.08$, where paramagnetic behavior is reported. Interestingly, at this composition, the system undergoes a metal–insulating transition from the semiconducting $LaTiO_3$ to the metallic $La_{0.92}TiO_3$ and reflects the high degree of correlation in this system.

In light of the aforementioned results, the magnetic behavior of compounds belonging to the $Nd_{1-x}TiO_3$ system

0022-4596/96 $18.00

TABLE 1
Oxygen Content as Determined by Thermogravimetric Analysis

Target composition	Expected gain	Theoretical gain	Actual composition
$NdTiO_3$	3.33	3.33	$NdTiO_{3.00}$
$Nd_{0.95}TiO_3$	2.92	2.92	$Nd_{0.95}TiO_{3.00}$
$Nd_{0.90}TiO_3$	2.48	2.38	$Nd_{0.90}TiO_{3.01}$

is worth reinvestigation with low-temperature neutron diffraction. It is also interesting to determine whether or not there exists a correlation between the magnetic and electrical properties of the compositions studied.

EXPERIMENTAL PROCEDURE

Preparation of Samples

$NdTiO_3$. This composition was prepared by arc-melting stoichiometric amounts of predried Nd_2O_3 (Research Chemicals, 99.99%), TiO2 (Fisher Scientific, 99.97%), and Ti metal, according to the equation

$$Nd_2O_3 + \tfrac{1}{3}TiO_2 + \tfrac{1}{3}Ti \rightarrow 2NdTiO_3.$$

The powders were mixed in acetone, made into 5/8″ pellets and arc-melted together with Ti metal on a water-cooled copper hearth under 1/2 atm prepurified argon gas (99.998%).

$Nd_{0.95}TiO_3$ and $Nd_{0.90}TiO_3$. Stoichiometric amounts of Ti_2O_3 (Cerac, 99.9%) and predried Nd_2O_3 and TiO_2 were ground in acetone and made into 5/8″ pellets. The reaction is

$$\frac{(1-x)}{2}Nd_2O_3 + 3xTiO_2 + \frac{(1-3x)}{2}Ti_2O_3 \rightarrow Nd_{1-x}TiO_3$$

The pellets were sealed in a molybdenum crucible, which was placed in a tungsten induction coil, and the crucible was placed in an rf induction furnace. Preparation conditions for both compositions involved heating to 1400°C in a vacuum of approximately 10^{-4} Torr for an average of 8 to 12 hours. Phase purity determination was carried out by X-ray diffraction and on occasion the samples were reground and refired under the initial conditions to produce single-phase materials. For all three compositions, the products were black in color.

TABLE 2
Unit Cell Parameters from X-Ray Powder Diffraction

Compound	a (Å)	b (Å)	c (Å)	Volume (Å^3)
$NdTiO_3$	5.561(5)	7.793(8)	5.522(5)	243.22(3)
$Nd_{0.95}TiO_3$	5.592(5)	7.798(8)	5.506(4)	240.10(4)
$Nd_{0.90}TiO_3$	5.551(3)	7.796(5)	5.488(3)	237.48(2)

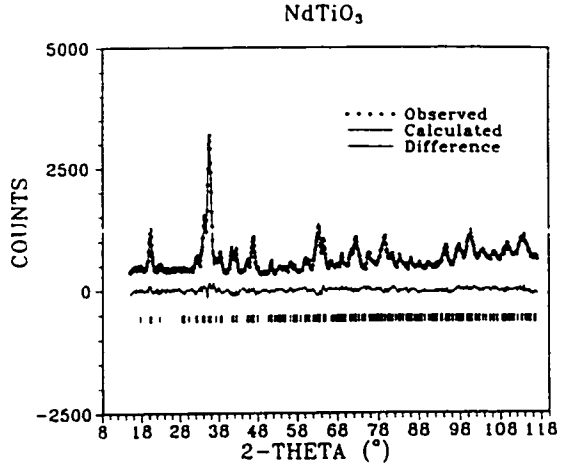

FIG. 1. Refined neutron powder profile of $NdTiO_3$.

X-Ray Powder Diffraction

Phase purity determination and initial structural characterization of the samples were carried out using a Guinier–Haag camera (IRDAB Model XDC700) with Cu$K\alpha_1$ radia-

TABLE 3
Conditions for Neutron Data Collection and Profile Refinement for Structural Determination

	$NdTiO_3$	$Nd_{0.95}TiO_3$	$Nd_{0.90}TiO_3$
2θ Range (°)	15.0–117.0	15.0–118.0	17.5–117.5
Step size (°)	0.10	0.10	0.10
No. of profile points	1021	1021	982
No. of independent reflections	254	253	251
No. of refined parameters	24	24	20[a]
R_{wp}	6.37	5.69	6.53
R_p	5.09	4.38	5.16
R_{exp}	3.94	2.95	3.24
R_{Bragg}	9.39	7.96	16.15
Goodness of fit	1.62	1.93	2.02

[a] Manual background used in refinement. $R_{wp} = 100\{\sum w(y_{obs} - y_{cal}/c)^2/\sum wy_{obs}^2\}^{1/2}$. $R_p = 100\sum|y_{obs} - y_{cal}/c|/\sum|y_{obs}|$. $R_{exp} = 100\{(N-P)/\sum wy_{cal}^2\}^{1/2}$. $R_{Bragg} = 100\sum|I_o - I_c|/\sum I_o$. Goodness of fit $= R_{wp}/R_{exp}$.

TABLE 4
Atomic Positions and Cell Parameters from the Profile Refinement of Neutron Powder Data Collected at Room Temperature

		$NdTiO_3$	$Nd_{0.95}TiO_3$	$Nd_{0.90}TiO_3$	$NdTiO_3$[a]
Nd	x	0.0598(8)	0.0437(12)	0.0374(11)	0.05412(6)
	y	0.25	0.25	0.25	0.25
	z	0.9927(13)	0.9851(22)	0.9936(22)	0.98892(5)
	B (Å^2)	0.54(7)	0.62(27)	0.236(8)	
Ti	x	0.5	0.5	0.5	0.5
	y	0.0	0.0	0.0	0.0
	z	0.0	0.0	0.0	0.0
	B (Å^2)	0.77(14)	1.09(43)	0.11(15)	
O1	x	0.4770(11)	0.4736(20)	0.4781(14)	0.4801(8)
	y	0.25	0.25	0.25	0.25
	z	0.0900(13)	0.0724(23)	0.0654(19)	0.0902(8)
	B (Å^2)	1.07(13)	2.07(55)	0.73(13)	
O2	x	0.3005(8)	0.3018(12)	0.2912(12)	0.2979(5)
	y	0.0501(6)	0.0524(9)	0.043(1)	0.0465(4)
	z	0.6992(7)	0.7072(14)	0.7068(13)	0.7024(5)
	B (Å^2)	0.127(77)	0.87(33)	1.35(11)	
	a (Å)	5.647(1)	5.583(4)	5.546(2)	5.589(3)
	b (Å)	7.785(2)	7.799(6)	7.798(2)	7.779(4)
	c (Å)	5.519(1)	5.489(4)	5.489(2)	5.495(3)

[a] Single crystal data from Ref. (1).

tion and silicon as an internal standard. A KEJ Instruments line scanner (Model LS20) was used to measure the positions and intensities of the diffraction lines. Unit cell constants were refined using the least-squares program LSUDF.

Thermal Gravimetric Analysis

Oxygen contents were determined by the use of a Netzsch STA Thermal Analyzer under an atmosphere of flowing air at 1000°C. A light purple powder was produced as a result of oxidation to $Nd_2Ti_2O_7$ and TiO_2. The oxygen content was calculated on the assumption of the nominal neodymium content in the target composition. The error in the experimental percent weight gain is ±0.05.

Magnetic Susceptibility

Measurements were carried out using a Quantum Design SQUID magnetometer in the temperature range 5–300 K with an applied field of 1000 Oe. The samples used were sintered polycrystalline pellets with typical sizes of 50 mg.

Neutron Powder Diffraction

Neutron diffraction data for powdered samples were collected at the McMaster Nuclear Reactor (MNR). Neutrons of wavelength 1.3920 Å, obtained by reflection from a Cu (200) single crystal monochromator, were used in combination with a position-sensitive detector. For routine chemical structural determination the samples were placed in a thin-walled vanadium can. Measurements were made over a 2θ range of 15° to 120° at room temperature. For low-temperature measurements a thin-walled aluminum can filled with He exchange gas and sealed with an indium gasket was used. Low temperatures to 10 K were obtained using a CTI Inc. Model 21 closed-cycle refrigerator with a Cryogenics Inc. Model DRC 80C controller. Measurements were made over a 2θ range of 10° to 40° for a series of temperatures down to 20 K and an extended data set with a 2θ range of 10° to 78° was collected at 10 K for magnetic structure refinements.

STRUCTURAL CHARACTERIZATION

Thermogravimetric analysis indicated that for each compound the target composition was achieved with the oxygen stoichiometry deviating by less than 1% from the expected value of 3.00 per formula unit, assuming the nominal neodymium composition (see Table 1). Using a $GdFeO_3$-type *Pnma* model, preliminary structural determinations carried out with Guinier–Haag powder X-ray diffraction data yielded the refined unit cell parameters found in Table 2.

Structural characterization was achieved with the use of neutron diffraction data for which a typical diffraction

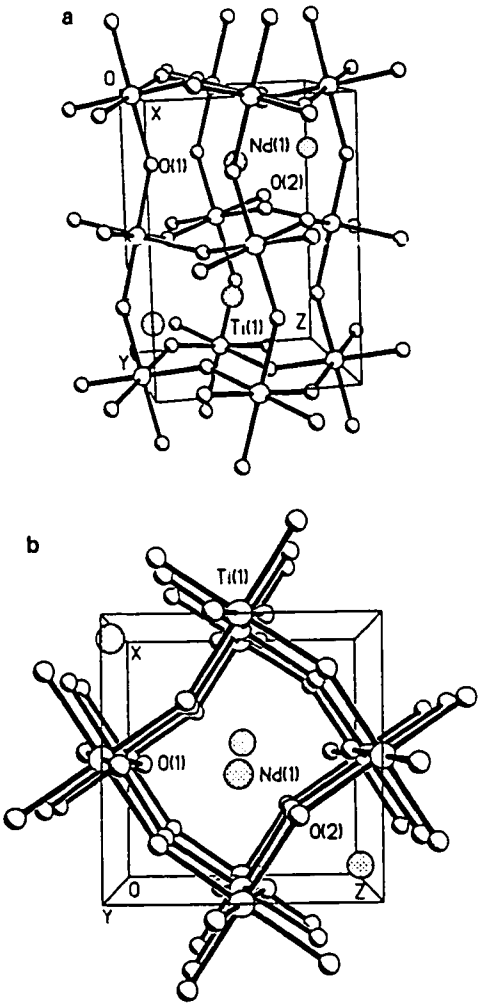

FIG. 2. (a) Perspective of *Pnma* structure and (b) view down the *b* axis.

profile can be seen in Fig. 1. Atomic positions and thermal parameters were determined by Rietveld profile refinement using the program DBWS 9600PC and the data refined smoothly in the space group *Pnma*. The results of the refinements and the refined structural parameters can be found in Tables 3 and 4, respectively. An illustration of the structure can be seen in Fig. 2. In order to accommodate the smaller sized neodymium cation, the corner-shared TiO_6 octahedra tilt along each of the *a*, *b*, and *c* axes. It is found that as the neodymium content is decreased, the tilting becomes less severe, as reflected by the Ti–O–Ti bond angles shown in Table 5.

TABLE 5
Bond Distances (Å) and Selected Bond Angles (°)

		$NdTiO_3$	$Nd_{0.95}TiO_3$	$Nd_{0.90}TiO_3$
Nd–O1	×1	2.42(4)	2.447(13)	2.476(20)
Nd–O1	×1	3.33(5)	3.219(13)	3.127(10)
Nd–O1	×1	2.350(13)	2.462(17)	2.443(16)
Nd–O1	×1	3.250(12)	3.088(18)	3.086(16)
Nd–O2	×2	2.625(24)	2.604(11)	2.656(11)
Nd–O2	×2	3.53(3)	3.484(10)	3.356(10)
Nd–O2	×2	2.717(14)	2.792(9)	2.740(9)
Nd–O2	×2	2.38(3)	2.305(10)	2.381(10)
Ti–O1	×2	2.0129(19)	1.995(3)	1.9860(20)
Ti–O2	×2	2.044(4)	1.995(7)	2.011(7)
Ti–O2	×2	2.059(4)	2.074(7)	2.003(7)
O1–Ti–O1		180.0	180.0	180.0
O2–Ti–O2		180.0	180.0	180.0
O2–Ti–O2		90.89(17)	91.9(3)	91.0(3)
		89.11(17)	88.1(3)	89.0(3)
O1–Ti–O2		87.87(23)	85.4(4)	86.8(4)
		91.13(23)	94.6(4)	93.2(4)
		89.90(22)	91.3(4)	90.8(3)
		90.10(22)	88.7(4)	89.2(3)
Ti–O1–Ti		150.4(4)	155.5(7)	158.0(6)
Ti–O2–Ti		148.40(24)	148.5(4)	152.8(4)

Similar observations were reported previously for $NdTiO_3$, based on single crystal studies (1). However, the cell parameters and bond distances reported were significantly smaller than those in Tables 4 and 5. This suggests that the previous results were for a compound whose composition had less than the desired neodymium stoichiometry of $x = 0$. Using an extrapolation and the cell volume reported, this corresponds to a neodymium content of $x \approx 0.07$, i.e., $Nd_{0.93}TiO_3$.

MAGNETIC PROPERTIES

1. Susceptibility Measurements

The temperature dependence of the magnetic susceptibility for each compound can be seen in Figs. 3a–3c. In all cases the data were corrected for core diamagnetism and above 100 K, a good fit to the Curie Weiss law could be found,

$$\chi = C/(T - \theta),$$

where C is the Curie constant, T is the temperature, and θ is the Weiss constant. The experimentally determined values of the Curie and Weiss constants can be found in Table 6. For each composition, the experimentally determined value of the Curie constant deviates from the ideal free ion value for Nd^{3+} of 1.64 emu · K · mol^{-1}. This suggests that the total susceptibility is composed of contributions from both Nd^{3+} and Ti^{3+}. It has been suggested that by

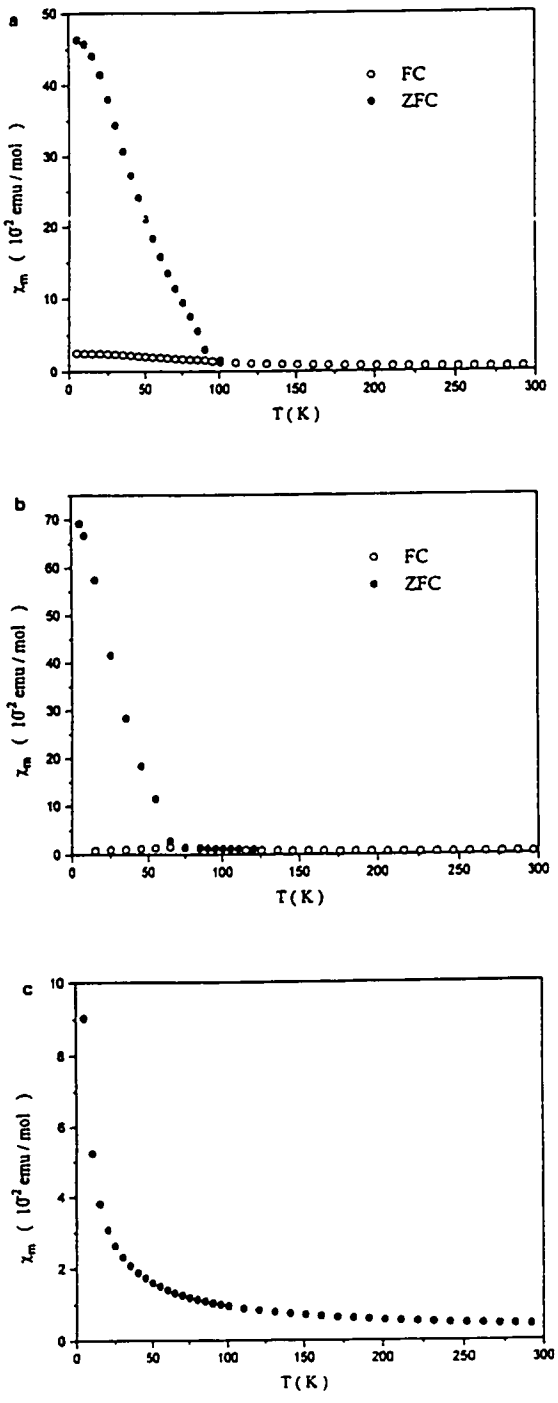

FIG. 3. Magnetic susceptibility vs temperature curves for (a) $NdTiO_3$, (b) $Nd_{0.95}TiO_3$, and (c) $Nd_{0.90}TiO_3$.

TABLE 6
Experimentally Determined Values for C, θ, and T_N

Compound	C (emu · K · mol^{-1})*	θ (K)	T_N (K)
$NdTiO_3$	1.71	−45.0	100
$Nd_{0.95}TiO_3$	1.49	−54.7	75
$Nd_{0.90}TiO_3$	1.58	−75.7	—

* Per mole of compound

comparing $NdTiO_3$ with the isostructural $NdScO_3$ a reasonable approximation can be made (9), in order to determine the contribution from the titanium ions. However, it becomes extremely difficult to separate the individual contributions to the total susceptibility for the vacancy-doped compositions.

Below 100 K, deviation from the Curie–Weiss law is observed for all cases. This deviation can be readily explained by the crystal field splitting of the 10-fold degenerate ground state of the Nd^{3+} ion. More interesting are the divergences that are observed between the zero field and field-cooled measurements for $NdTiO_3$ and $Nd_{0.95}TiO_3$ at 100 and 75 K, respectively, which suggests the onset of some type of magnetic order. This compares favorably with the ordering temperature of 90 K reported by Eylem *et al.* (10) for the $x = 0$ case. No divergences between the zero field and field-cooled measurements were observed for $x = 0$ case. No divergences between the zero field and field-cooled measurements were observed for $x = 0.10$, indicating the absence of magnetic order for this composition.

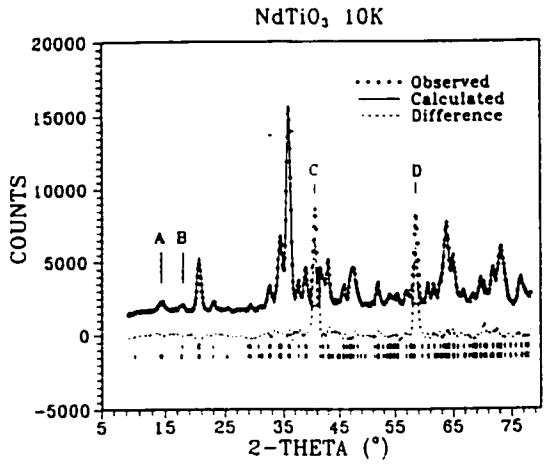

FIG. 4. Refined neutron powder data taken at 10 K for $NdTiO_3$. Magnetic peaks are labeled A (100,001) and B (110,011). The peaks labeled C and D are due to aluminum and were excluded in the refinement.

TABLE 7

Conditions and Refinement Results for the Combined Chemical and Magnetic Structures for $NdTiO_3$ and $Nd_{0.95}TiO_3$ at 10 K

2θ range (°)	9.0–78.0	10.0–75.0
Step size (°)	0.10	0.10
No. of profile points	691	651
No of refined parameters	21	21
	Chemical cell	
R_{wp}	6.19	5.96
R_{exp}	1.82	2.30
R_{Bragg}	8.30	8.36
Goodness of fit	3.40	2.60
	Magnetic cell	
R_{Mag}[a]	29.9	26.9
Moment configuration		
Nd^{3+}	F_xC_y	F_xC_y
Ti^{3+}	G_xF_z	G_xF_z
Magnetic moment		
Nd^{3+}	1.11(5) μ_B	0.87(8) μ_B
Ti^{3+}	0.99(5) μ_B	0.74(9) μ_B

[a] Magnetic R factor.

2. Low-Temperature Neutron Diffraction Measurements

Low-temperature neutron diffraction measurements were carried out using powdered samples of $NdTiO_3$ and $Nd_{0.95}TiO_3$ for a series of temperatures below which ordering is observed in the susceptibility measurements. The data collected at 10 K for both $x = 0$ and 0.05 show the emergence of two well-defined peaks of low intensity occurring at 2θ values of ~14° and ~17°, respectively; see Fig. 4. The profiles bear a striking resemblance to those obtained for both $CeTiO_3$ and $PrTiO_3$ for which the magnetic structures were solved to yield a G_xF_z configuration for the Ti^{3+} moments and an F_xC_y configuration for the Ce^{3+} and Pr^{3+} ions (5, 6). Consequently, the peak at ~14°, A, is assigned the (100,001) reflection and is C type in Bertaut's notation and the peak at ~17°, B, is indexed as (110) which is G type. The latter overlaps the (011) reflection, which is allowed in *Pnma*. The magnetic structures were refined using the program FULLPROF (13). For the refinements at low temperatures, the overall temperature factor was fixed at $B = 0.25$ Å^{-2}, due to the strong correlation with the refined moments, especially at the titanium sites. The results for each composition are discussed separately below.

(*a*) *$NdTiO_3$*. The results of a combined magnetic and chemical structure for both $NdTiO_3$ and $Nd_{0.95}TiO_3$ at 10 K are shown in Tables 7 and 8, with the profile fit for $NdTiO_3$ displayed in Fig. 4. The model for the magnetic structure is a G-type configuration for the Ti^{3+} moments and a C-type configuration for the Nd^{3+} moments. The values for the refined moments are reasonable for both ions at 10 K.

Refinements were also done at several temperatures above 10 K for both samples using less extensive data sets. In these cases the half-width parameters were fixed along with the overall temperature factor. The results for $NdTiO_3$ are plotted in Figs. 5a and 5b. The temperature dependence of the Ti^{3+} moment, Fig. 5b, is consistent with an ordering temperature of 90 K as found from the susceptibility data. Because of the restricted conditions under which the refinements were carried out, the temperature dependence was checked by a second method which involved simply fitting the (110,011) doublet to a Gaussian lineshape for each temperature with no reference to a structural model. The temperature dependence of the square root of these intensities is essentially the same as that in Fig. 5b.

The thermal development of the Nd^{3+} moment which is associated with the (100,001) peak is rather different, as seen in Fig. 5a. There is a sharp decline from a low-temperature value of ~1.10(1) μ_B between 10 and 20 K to a roughly constant value of 0.56(9) μ_B at 50 K and above. This is essentially the same type of temperature dependence seen for $PrTiO_3$ and can be explained as a polarization of the Nd^{3+} moments by the coupling to the Ti^{3+} sublattice (6).

Further insight concerning the nature of the ordering on the Nd^{3+} sublattice is seen in Figs. 6a and 6b, where the full width at half-maximum, FWHM, for both sets of magnetic reflections, A (100,001) and B (110,0011), are shown. For B, Fig. 6b, the peak width is essentially constant

TABLE 8

Atomic Positions and Cell parameters from the Refinement of the Combined Chemical and Magnetic Structure of $NdTiO_3$ and $Nd_{0.95}TiO_3$ at 10 K

		$NdTiO_3$	$Nd_{0.95}TiO_3$
Nd	x	0.065(1)	0.0541(9)
	y	0.25	0.25
	z	0.9814(13)	0.9849(15)
Ti	x	0.5	0.5
	y	0	0
	z	0	0
O1	x	0.4871(13)	0.4853(14)
	y	0.25	0.25
	z	0.0931(16)	0.0875(17)
O2	x	0.299(1)	0.298(1)
	y	0.0480(7)	0.0438(8)
	z	0.695(1)	0.6969(11)
	a (Å)	5.600(2)	5.571(2)
	b (Å)	7.752(2)	7.777(2)
	c (Å)	5.504(2)	5.492(2)

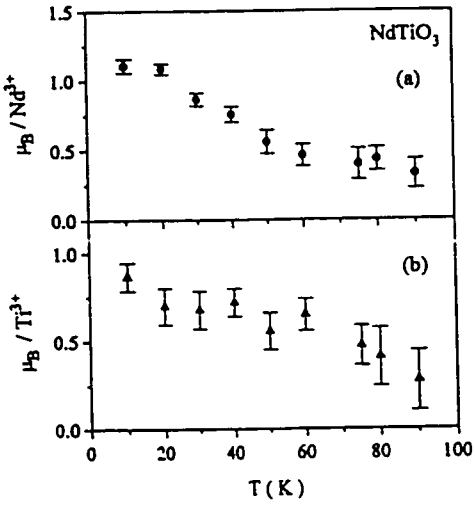

FIG. 5. Magnetic moment vs temperature curves for $NdTiO_3$ (a) Nd^{3+} and (b) Ti^{3+}.

at about 0.88° as a function of temperature. The small increase near 90 K may reflect the presence of subcritical clusters on the Ti^{3+} sublattice. The point at 200 K represents the (011) reflection which is not magnetic in origin, but is at essentially the same position as the (110) magnetic component. Very different behavior is seen for A, Fig. 6a, where the FWHM increases from a constant value of 1.15(5)° at low temperatures to values approaching 2.24(32)° by 50 K. An estimation of the correlation length can be obtained from the expression

$$\xi = 1/[\Gamma^2_{EXP} - \Gamma^2_{RES}]^{1/2},$$

where ξ is the correlation length in Å, and Γ_{EXP} and Γ_{RES} are the experimentally determined and expected resolution-limited Gaussian FWHMs, respectively. Taking into account the changes to the peak width as a function of position on the linear tube detector, the resolution-limited linewidth at 14.20° is 0.91°. The observed linewidths clearly exceed the resolution-limited value at all temperatures. Correlation lengths, determined to be 18(3) Å at 10 K and 6(1) Å at 50 K, indicate that the order on the Nd^{3+} sublattice is of short range in the temperature regime investigated, extending over only a few unit cells.

The inhibition of true long-range order on the Nd^{3+} sublattice can be attributed to the symmetry cancellation or frustration effects which arise from the crystal geometry. The Nd^{3+} moment is roughly in the center of a slightly distorted primitve cube with eight nearest Ti^{3+} neighbors, four with one spin direction and four antiparallel to these. Note that in Figs. 6a, values for the FWHM are reported out to 200 K and that the values for the Nd^{3+} moment remain finite even at temperatures exceeding T_N for the Ti^{3+} sublattice ordering. Both results arise from the observation of a very broad (FWHM ~2.5°) weak feature at the expected position for the (100,001) magnetic peak. While the persistence of this broad peak out to such high temperatures could indicate the presence of short-range magnetic order, this would be very unusual and it is more likely to due to an anomaly in the background. In any case, nothing definitive can be stated with the current data and this matter will be studied further.

(*b*) $Nd_{0.95}TiO_3$. The results for this material parallel those for $NdTiO_3$ but on a slightly lower temperature scale, as seen in Figs. 7 and 8. The thermal development of the Ti^{3+} moment is consistent with $T_N \sim 75$ K from the susceptibility data and the linewidths are in the resolution-limited range. The Ti^{3+} ordered moment is somewhat smaller than that found for $NdTiO_3$ at 10 K.

The behavior of the Nd^{3+} sublattice moment, Fig. 7b, indicates a gradual increase beginning at about 40 K. The two points at 60 and 70 K are at the detection limit, as indicated by the large error bars. The broad, temperature robust feature at the (100,001) position found for $NdTiO_3$ was not observed above 70 K for $Nd_{0.95}TiO_3$, which casts further doubt on its significance in the former material. From the linewidths, Figs. 8a, it is seen that the Nd^{3+} sublattice order is only of short range as in $NdTiO_3$.

SUMMARY AND CONCLUSIONS

Members belonging to the solid solution $Nd_{1-x}TiO_3$, $x = 0$, 0.05, and 0.10, adopt the $GdFeO_3$-type structure.

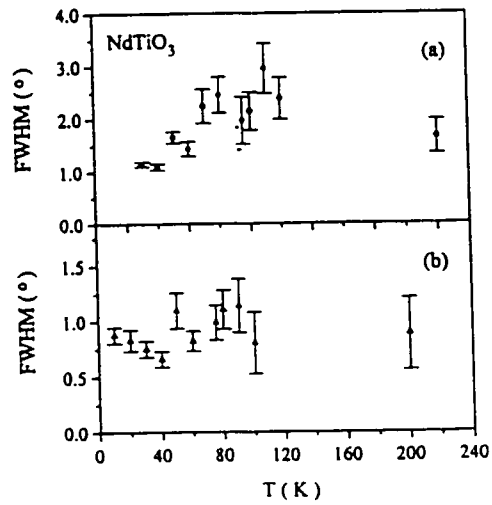

FIG. 6. Full width at half-maximum (FWHM) vs temperature for $NdTiO_3$ (a) A (100,001) and (b) B (110,011) reflections.

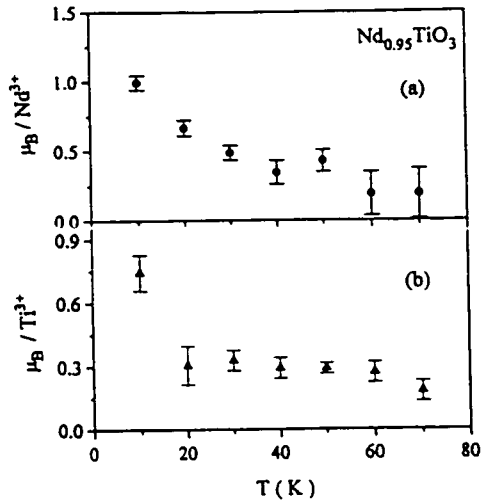

FIG. 7. Magnetic moment vs temperature for $Nd_{0.95}TiO_3$ (a) Nd^{3+} and (b) Ti^{3+}.

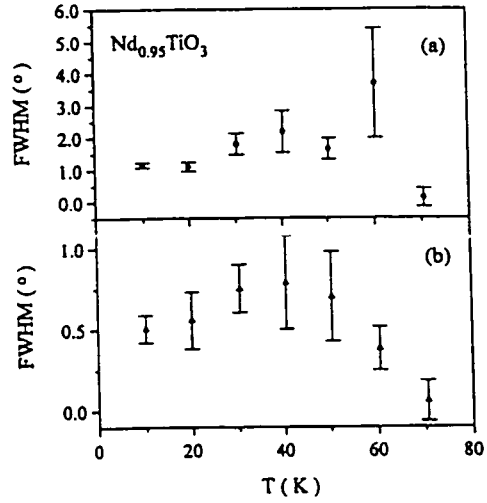

FIG. 8. Full width at half-maximum (FWHM) vs temperature for $Nd_{0.95}TiO_3$ (a) A (100,001) and (b) B (110,011) reflections.

The results reported here suggest that the composition used in the previous low-temperature neutron diffraction study by Greedan (6) contained less than the nominal composition of neodymium, i.e., $x \sim 0.07$. This seems to be the most likely explanation for the nonobservance of any type of magnetic behavior for this composition. It is found that for reasonably stoichiometric compositions, antiferromagnetic behavior on both metal ion sublattices is observed in compositions with $x = 0$ and 0.05. The ordering on the Nd^{3+} sublattice is of short range but is clearly evident and is in sharp contrast to the paramagnetic behavior assumed by Eylem *et al.* (10). The magnetic structure has been determined to be similar to that of $CeTiO_3$ and $PrTiO_3$, where there is a F_xC_y configuration on the Nd^{3+} sublattice and a G_zF_x configuration on the Ti^{3+} sublattice. The antiferromagnetic behavior is observed to vanish on approaching the $Nd_{0.90}TiO_3$ composition. This observation appears to be consistent with those made for the $La_{1-x}TiO_3$ series of compounds, where the antiferromagnetic behavior vanishes as metallic behavior is encountered. It is well known that $NdTiO_3$ is semiconducting, and it is found that this behavior extends to the $x = 0.05$ composition. As part of a larger body of work to be published in the future, evidence will be presented that the $x = 0.10$ composition exhibits an unusual and interesting resistivity behavior. It is clear, however, that the semiconducting behavior vanishes at this composition.

REFERENCES

1. D. A. MacLean, H. N. Ng, and J. E. Greedan, *J. Solid State Chem.* **30**, 35 (1979).
2. G. V. Bazuev and G. P. Shveikin, *Inorg. Mater.* **19**, 92 (1983).
3. J. E. Greedan, *J. Less-Common Met.* **111**, 335 (1985).
4. E. F. Bertaut, *in* "Magnetism" (G. T. Rado and H. Suhl, Eds.), Vol. III, p. 149. Academic Press, New York, 1963.
5. J. P. Goral and J. E. Greedan, *J. Magn. Magn. Mater.* **37**, 315 (1983).
6. J. E. Greedan, *J. Magn. Magn. Mater.* **44**, 299 (1984).
7. G. V. Bazuev and G. P. Shveikin, *Inorg. Mater.* **22**, 1185 (1986).
8. P. Ganguly, O. Parkash, and C. N. R. Rao, *Phys. Status Solid A* **36**, 669 (1976).
9. D. A. Maclean, K. Seto, and J. E. Greedan, *J. Solid State Chem.* **40**, 241 (1981).
10. C. Eylem, H. L. Ju, B. W. Eichorn, and R. L. Green, *J. Solid State Chem.* **114**, 164 (1995).
11. D. A. Crandles, T. Timusk, J. D. Garrett, and J. E. Greedan, *Phys. Rev. B* **49**(23), 16,207 (1994).
12. M. J. MacEachern, H. Dabkowska, J. D. Garrett, G. Amow, W. Gong, G. Liu, and J. E. Greedan, *Chem. Mater.* **6**, 2092 (1994).
13. J. Rodriguez-Carvajal, "FULLPROF: A Program for Reitveld Refinement and Pattern Matching Analysis," Abstracts of the Satellite Meeting on Powder Diffraction on the XV Congress of the International Union of Crystallography, p. 127, Toulouse, France, 1990.

JOURNAL OF SOLID STATE CHEMISTRY 141, 262–269 (1998)
ARTICLE NO. SC987989

An Investigation of the Magnetic Properties of $Sm_{1-x}TiO_3$ for $x = 0.03$, 0.05, and 0.10: Magnetic Structure Determination of $Sm_{0.97}TiO_3$ by Short-Wavelength Neutron Diffraction on Single Crystals

G. Amow,* J. E. Greedan,*,[1] and C. Ritter†

*Department of Chemistry and the Brockhouse Institute for Materials Research, McMaster University, Hamilton, Ontario L8S 4M1, Canada; and †Institut Max von Laue-Paul Langevin, Ave. des Martyrs, B.P. 156, F-38042 Grenoble Cedex 9, France

Received April 16, 1998; in revised form July 27, 1998; accepted August 3, 1998

Single crystals of $Sm_{0.97}TiO_3$ have been prepared and their magnetic properties have been investigated. Dc magnetic susceptibility measurements indicate paramagnetic Curie–Weiss behavior above 100 K whereas two magnetic transitions are observed at $T_N \sim 52$ K and $T_N \sim 40$ K. Similar observations for antiferromagnetic behavior have been made for the $x = 0.05$ compound with $T_N \sim 40$ K whereas for the $x = 0.10$ compound this behavior vanishes. The magnetic structure determination of the $x = 0.03$ compound has been accomplished by using low-temperature single-crystal neutron diffraction. The room temperature crystal structure is a distorted orthorhombic perovskite structure belonging to *Pnma*, which is preserved down to 15 K. The magnetic structure is found to be consistent with a G_xG_z moment configuration on the Ti(III) sublattice and a C_z moment configuration on the Sm(III) sublattice. The magnetic moments are estimated to be 0.72(1) and 0.43(1) μ_B on the Ti(III) and Sm(III) sublattices, respectively. The orientations of the moments were found to be 7(3)° to the x-axis for Ti(III) and 2(2)° to the z-axis for Sm(III).

INTRODUCTION

As part of a greater body of research involving the vacancy-doped rare earth titanate system $R_{1-x}TiO_3$ (R = La, Nd, and Sm), we are interested in the investigation of the magnetic properties of these compounds. In general, the vacancy-doped rare earth titanates as well as the alkaline earth doped systems $R_{1-x}A_xTiO_3$ are of interest as in these cases electron correlation effects strongly influence the physical properties of member compounds. Consequently, they allow systematic studies of the physical properties as a function of band filling (1–4).

The magnetic properties as well as the magnetic structure determination of the samarium titanate $SmTiO_3$ are of special interest in light of the known behavior of the $RTiO_3$ series of compounds (R = La–Gd, Y). A remarkable variation in the magnetic properties as a function of decreasing rare earth radius exists, ranging from antiferromagnetic Ti–Ti coupling for R = La, Ce, Pr, and Nd to ferromagnetic Ti–Ti coupling for R = Gd–Lu, Y (5–8). In spite of the interesting position of Sm in the series, evidence for any type of magnetic ordering for the R = Sm compound had remained elusive (9). Until recently, however, there has been one published report indicating that $SmTiO_3$ undergoes some type of ordering phenomenon at $\sim$ 50 K. Despite this, a detailed investigation into the magnetic properties as well as the magnetic structure determination for this compound has not been performed (10).

Unlike the magnetic structure determinations for the R = La, Ce, Pr, and Nd titanates, for which low-temperature powder neutron diffraction was used, the case of samarium titanate presents an interesting challenge due to the high absorption cross section of Sm at conventional thermal neutron wavelengths >1 Å ($\sim$5760 barns). It is known that this value decreases sharply to $\sim$500 barns at a wavelength of 0.5 Å, thus, in principle, making this problem more tractable if hot source neutrons are available (11). The neutron source at the Institut Laue-Langevin (ILL), Grenoble, France, is ideally suited for this study as it provides accessibility to very short wavelengths coupled with high flux. Furthermore, by utilizing low-temperature single-crystal neutron diffraction, it is possible for the first time to determine the magnetic structure of a rare earth titanate unambiguously. As mentioned previously, the magnetic structure determinations of the rare earth titanates to date have been principally carried out with low-temperature powder neutron diffraction. While this method has had some success, the magnetic structures remain somewhat

[1]To whom correspondence should be addressed. E-mail: greedan@mcmail.cis.mcmaster.ca.

0022-4596/98 $25.00

ambiguous due to the inability of the method to resolve overlapping magnetic reflections. We present in this report an investigation of the magnetic properties of $SmTiO_3$ as well as its magnetic structure determination by low-temperature single-crystal neutron diffraction, the first such study to be carried out for any of the rare earth titanates.

EXPERIMENTAL

Sample Preparation

The nominal $x = 0.00$ composition was prepared by mixing stoichiometric amounts of predried Sm_2O_3 (5.0000 g, Rhone Poulenc, 99.99%), TiO_2 (0.9941 g, Cerac, 99.9%), and $TiO_{1.046}$ (1.0498 g, Cerac, 99.9%) in acetone. In the case of the $x = 0.05$ and $x = 0.10$ compositions, Ti_2O_3 (Cerac, 99.9%) was used. For each sample the reagents were pressed into 1/2-in. pellets and sealed in a molybdenum crucible. The sealed crucible was then placed into an rf furnace and was fired several times at ~1400°C under vacuum (10^{-6} Torr) for ~12 h each time to achieve phase purity. The pellets were reground and pressed between each firing. The polycrystalline products obtained were black.

Single crystals for the nominal $x = 0.00$ phase were obtained by firing the polycrystalline sample to just above its melting point (~1800°C) and then quenching to room temperature. The crystals were obtained as shiny black blocks with defined faces having an average dimension of ~1.5 mm × 1.5 mm × 1 mm.

X-Ray Powder Diffraction

Phase purity determination was carried out with a Guinier–Haag camera (IRDAB Model XDC700) with Cu$K\alpha_1$ radiation and silicon as an internal standard. A KEJ Instruments line scanner (Model LS20) was used to measure the positions and intensities of the diffraction lines. Unit cell constants were refined with the least-squares program LSUDF.

Thermal Gravimetric Analysis

The oxygen content of the sample was determined with a Netzch STA thermal analyzer in flowing air at 1000°C.

Magnetic Susceptibility

Dc magnetic susceptibility measurements were carried out with a Quantum Design SQUID magnetometer in the temperature range of 5–300 K using an applied field of 100 Oe.

Powder Neutron Diffraction

Data were collected at 298 and 1.5 K on the D1B powder diffractometer at the ILL using a wavelength of 2.52 Å over the 2θ range 10–90°. The sample was diluted with aluminum powder to minimize the strong absorption presented by samarium.

Single-Crystal X-Ray Diffraction

Data were collected at room temperature with a Siemens P3 four-circle diffractometer using Ag$K\alpha$ radiation ($\lambda = 0.56086$ Å). The data were corrected for absorption effects by the semiempirical ψ-scan method. For further details of the data collection, see Table 2.

Single-Crystal Neutron Diffraction

Neutron data were collected with the D9 four-circle single-crystal diffractometer at the ILL equipped with a two-dimensional position-sensitive detector. A wavelength of $\lambda = 0.4710$ Å was obtained by reflection from a Cu(220) single-crystal monochromator. To follow the thermal development of the magnetic reflections, measurements were made at room temperature and at 15 K with the use of a Displex cryostat. Several low-angle magnetic reflections were scanned for approximately 6 h each using an ω scan. A full data set for the purpose of structural refinement at 15 K was also collected. The integrated intensities were obtained by RACER (12). No absorption corrections were made to the data. Structural refinement was carried out with SHELXTL-93 (13) and details of the refinement can be found in Table 2.

RESULTS AND DISCUSSION

Structural Characterization

The room temperature crystal structure of $SmTiO_3$ has been reported previously (14). The structure is an orthorhombically distorted perovskite type belonging to the space group *Pnma*, typical for the $RTiO_3$ series, and is found to be preserved for the $x = 0.03$ to $x = 0.10$ compositions (see Fig. 1). The unit cell constants derived from the Guinier–Haag data for all three compositions are summarized in Table 1. The unit cell volume for the sample used in the present study is marginally larger (within 0.5%) than that reported by Maclean *et al.* (13), suggesting that the composition is closer to the nominal composition of $SmTiO_3$. The single-crystal X-Ray data collected at room temperature refined smoothly in *Pnma* to the values shown in Table 2. In addition, the samarium content was refined and in this manner the composition was determined to be $Sm_{0.97}TiO_3$. This result is consistent with the experimental weight gain of 3.08% obtained by TGA, which compares favorably with the expected gain of 3.01% for this stoichiometry. The refined positional and thermal parameters as well as selected geometrical parameters can be found in Tables 3–5.

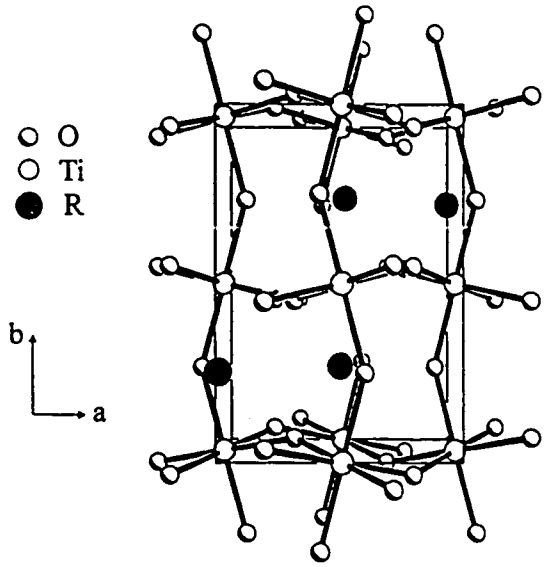

FIG. 1. Crystal structure of $RTiO_3$ (R = rare earth).

With regard to the crystal structure at 15 K, although no absorption corrections were made to the neutron data, the refinement proceeded smoothly in *Pnma*, indicating no change in the crystal structure at this temperature (see Table 2). This observation is further supported qualitatively by the neutron powder profiles obtained, which showed very little change between 298 and 1.5 K. During the refinement process a strong correlation was observed between the site occupancy of Sm and its temperature factor. Consequently the Sm temperature factor was refined to an initial isotropic value and was subsequently constrained throughout the refinement while the temperature factors of the remaining atoms were refined anisotropically. In addition, 22 weak reflections were present in the data set that violated *Pnma* symmetry. However, these are likely to be artifacts of multiple scattering processes and were ignored in the refinement. The positional and thermal parameters as well as selected geometrical parameters can be found in Tables 3–5. Finally, a comparison of the cell volumes as well as the bond distances at 298 and 15 K (Table 5) shows the expected decreases in *values as the temperature is lowered.

TABLE 1

Sample	a (Å)	b (Å)	c (Å)	V (Å^3)
$SmTiO_3$[a]	5.660(2)	7.722(4)	5.454(2)	238.4(2)
$Sm_{0.97}TiO_3$	5.6654(3)	7.7298(4)	5.4623(3)	239.21(2)
$Sm_{0.95}TiO_3$[b]	5.6154(6)	7.74166(6)	5.4542(4)	237.11(3)
$Sm_{0.90}TiO_3$[b]	5.5774(7)	7.7450(7)	5.4464(6)	235.27(3)

[a] From single-crystal work by Maclean *et al.* (5).
[b] Nominal composition.

TABLE 2

Crystal Data and Refinement Parameters for $SmTiO_3$ Obtained from X-Ray and Neutron Data Collected at 298 and 15 K, Respectively

	X-ray data	Neutron data
Color	Black	Black
Crystal size (mm)	0.1 (sphere)	2.5 × 2.5 × 1.5
Crystal system	Orthorhombic	Orthorhombic
Space group	*Pnma*	*Pnma*
Unit cell dimensions (Å)	a = 5.6528(11)	a = 5.5902(11)
	b = 7.7082(15)	b = 7.6467(15)
	c = 5.4478(11)	c = 5.4329(11)
Volume (Å^3)	237.3765(37)	231.8532(37)
Z	4	4
Formula weight	246.26	246.26
Density (calc) (g/cm^3)	6.890	6.890
Wavelength	Ag$K\alpha$ (λ = 0.56086 Å)	λ = 0.4710 Å
T (K)	298	15
2θ range (deg)	3.5–90.25	5–35.93
Scan type	ω–2θ	ω–2θ
Linear absorption coefficient (mm^{-1})	14.63	—
Absorption correction	ψ-scan	None
F(000)	432.0	432.0
Index ranges	$-1 \le h \le 14$,	$0 \le h \le 7$,
	$-1 \le k \le 19$,	$0 \le k \le 10$,
	$-1 \le l \le 13$	$0 \le l \le 7$
Standard reflections	One every 97 reflections	One every 52 reflections
Number of reflections collected	2986	664
Number of independent reflections	2079	289
Restraints/parameters	0/29	1/25
Rms residual electron density, ρ_{rms} (e/Å^3)	1.13	0.22
wR_2[a]	15.20	14.20
R_1[a]	6.21	5.30

[a] $wR_2 = [\sum w(F_o^2 - F_c^2)/\sum w(F_o^2)^2]^{1/2}$; $R_1 = (\sum ||F_o| - |F_c||)/\sum |F_o|$.

Magnetic Properties

The magnetic susceptibility behavior over the temperature range 5–298 K for $Sm_{0.97}TiO_3$ can be seen in Fig. 2. Above 100 K it was found that Curie–Weiss paramagnetism exists and the data could be fitted to

$$\chi = \frac{C}{(T - \Theta)},$$

where C is the Curie constant and Θ is the Weiss constant. The data were corrected for core diamagnetism, and experimentally determined values were found to be C = 1.07(1) cm^3 mol K^{-1} and Θ = − 229(5) K. Clearly apparent

TABLE 3
Refined Positional and Thermal Parameters at 298 and 15 K

	298 K[a]	15 K[b]
Sm		
x	0.06472(4)	0.06632(39)
y	0.25	0.25
z	0.98448(4)	0.98590(38)
U_{eq}(Å^2)	0.01110(6)	0.00251(0)
Ti		
x	0.5	0.5
y	0.5	0.5
z	0	0
U_{eq}(Å^2)	0.00986(13)	0.00921(67)
O1		
x	0.47342(63)	0.47588(34)
y	0.25	0.25
z	0.10239(72)	0.10189(36)
U_{eq}(Å^2)	0.01324(30)	0.01113(45)
O2		
x	0.30387(41)	0.30396(22)
y	0.05175(31)	0.05174(18)
z	0.69654(44)	0.69786(22)
U_{eq}(Å^2)	0.01302(40)	0.01125(45)

[a]X-Ray data.
[b]Neutron data.

TABLE 5
Selected Bond Distances (Å) and Bond Angles (Deg)

		298 K[a]	15 K[b]
Sm–O1	× 1	3.404(4)	3.360(3)
Sm–O1	× 1	3.239(4)	3.228(3)
Sm–O1	× 1	2.398(4)	2.374(3)
Sm–O1	× 1	2.309(4)	2.292(3)
Sm–O2	× 2	3.5737(24)	3.5427(21)
Sm–O2	× 2	2.7012(24)	2.6779(18)
Sm–O2	× 2	2.5736(24)	2.5503(22)
Sm–O2	× 2	2.3414(24)	2.3330(21)
Ti–O1	× 2	2.0630(24)	2.0483(13)
Ti–O2	× 2	2.0301(24)	2.0108(12)
Ti–O2	× 2	2.0118(12)	1.9945(7)
O1–Ti–O1		180	180
O2–Ti–O2		90.34(9)	90.74(5)
		89.66(9)	89.26(5)
O1–Ti–O2		88.80(12)	89.08(7)
		91.20(12)	90.92(7)
		89.82(13)	90.02(7)
		90.18(13)	89.98(7)
Ti–O1–Ti		146.63(21)	146.86(11)
Ti–O2–Ti		147.07(13)	147.26(7)

[a]X-ray data.
[b]Neutron data.

is the sharp transition at ~ 52 K, indicating the onset of antiferromagnetic behavior. At ~ 40 K there is a smaller feature which is likely the result of a spin-reordering process on the magnetic sublattices. Furthermore, the divergence between the zero-field-cooled (ZFC) and field-cooled (FC) data indicates the presence of a weak ferromagnetic moment which can be ascribed to moment canting on the sublattices.

It should be pointed out that the susceptibility behavior in Fig. 2 bears a strong resemblance to that observed for $NdTiO_3$ (8). It has been shown that a likely model for the magnetic structure for this compound (as well as $PrTiO_3$ and $CeTiO_3$) has a *C*-type spin configuration on the Nd(III) sublattice and a *G*-type spin configuration on the Ti(III) sublattice (6, 8).

The magnetic reflections which arise as a consequence of *G*-type and *C*-type ordering belong to $h + 1 =$ odd, $k =$ odd

TABLE 4
Anisotropic Thermal Parameters (Å) for $SmTiO_3$ at 298 and 15 K

298 K[a]	U_{11}	U_{22}	U_{33}	U_{23}	U_{13}	U_{12}
Sm1	0.01071(8)	0.01159(8)	0.01100(8)	0	− 0.00081(4)	0
Ti	0.00961(21)	0.01008(21)	0.00990(21)	0.00020(13)	− 0.00002(13)	− 0.00010(14)
O1	0.01162(60)	0.01566(70)	0.01244(61)	0.00082(51)	− 0.00237(50)	− 0.00181(55)
O2	0.01252(90)	0.01185(83)	0.01470(99)	0	− 0.00082(77)	0
15 K[b]	U_{11}	U_{22}	U_{33}	U_{23}	U_{13}	U_{12}
Sm[c]	—	—	—	—	—	—
Ti	0.00935(130)	0.01113(153)	0.00719(128)	0.00007(107)	0.00028(90)	− 0.00027(115)
O1	0.01039(71)	0.01301(70)	0.01041(79)	0.00040(42)	− 0.00137(48)	− 0.00091(43)
O2	0.01030(86)	0.01123(90)	0.01191(91)	0	− 0.00026(65)	0

[a]X-ray data.
[b]Neutron data.
[c]The Sm temperature factor was refined isotropically.

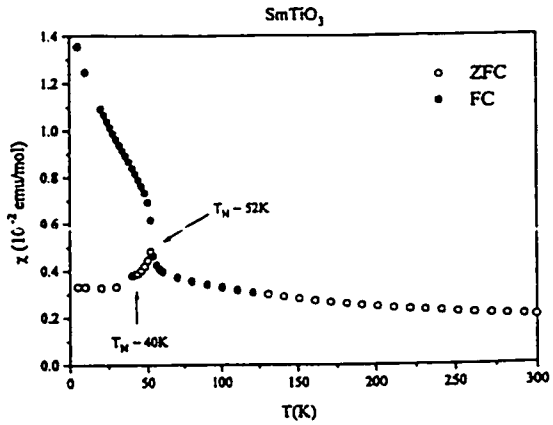

FIG. 2. Magnetic susceptibility (χ) vs T for $SmTiO_3$.

and $h + 1$ = odd, k = even, respectively, in the *Pnma* setting. Thus, in a typical low-temperature powder neutron diffraction experiment involving the rare earth titanates, the proper indexing of the magnetic reflections can give information about the arrangement of spins, i.e., *G*-type or *C*-type. However, since it is not possible to resolve the intensities of overlapping magnetic reflections, for example the *G*-type (110, 011) reflections, it becomes difficult to determine the precise orientation of the spins relative to the principal axes of the unit cell. This point is compellingly exemplified by the magnetic structure determination of $CeTiO_3$, for which three models were found to be possible, each consistent with the intensity data obtained (6). By performing a single-crystal diffraction experiment, it should, in principle, be possible to remove any ambiguity in obtaining the correct description for the orientation of spins as it allows for the resolution and independent measurement of magnetic peak intensities.

Initially, the magnetic structure for $Sm_{0.97}TiO_3$ was assumed to be the same as for the La–Nd titanates. Experience has shown that the strongest reflections are (110) and (011) for *G*-type ordering and (021) and (120) for *C*-type ordering, where the latter three reflections are forbidden in *Pnma*. Consequently, the thermal development of the (110), (011), (120), and (021) reflections was followed by measuring their intensities at 298 and 15 K. Preliminary scans of these reflections at 15 K, lasting 30 min each, revealed negligible intensity in each case. However, with substantially longer counting times (6 h for each reflection), significant intensities were recorded which were observed to have decreased drastically at room temperature (see Figs. 4 and 5). The results

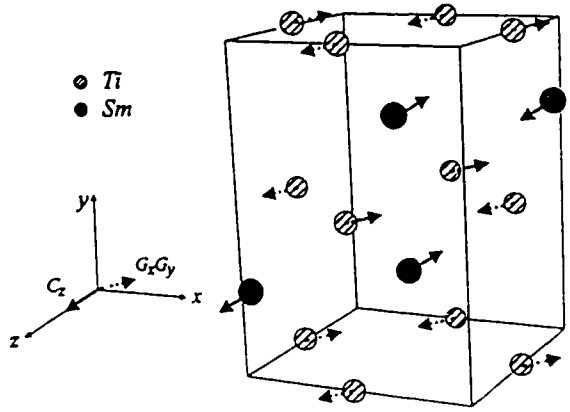

FIG. 3. Diagram showing the arrangement of spins in the *G*-type (solid arrows) and *C*-type (dashed arrows) configuration for the $x = 0$ phase.

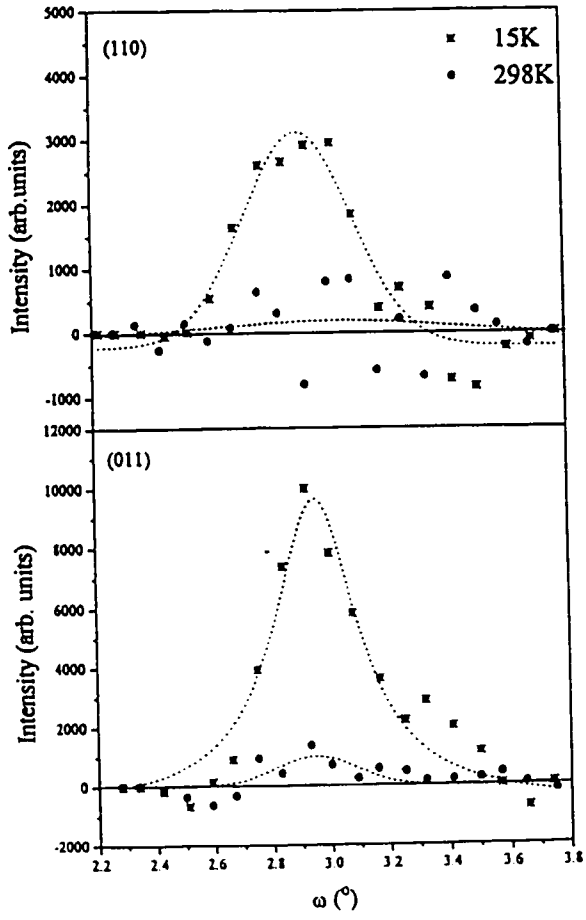

FIG. 4. Peak profiles of the *G*-type reflections (110) and (011) for the $x = 0$ phase. The dashed lines are a guide for the eyes.

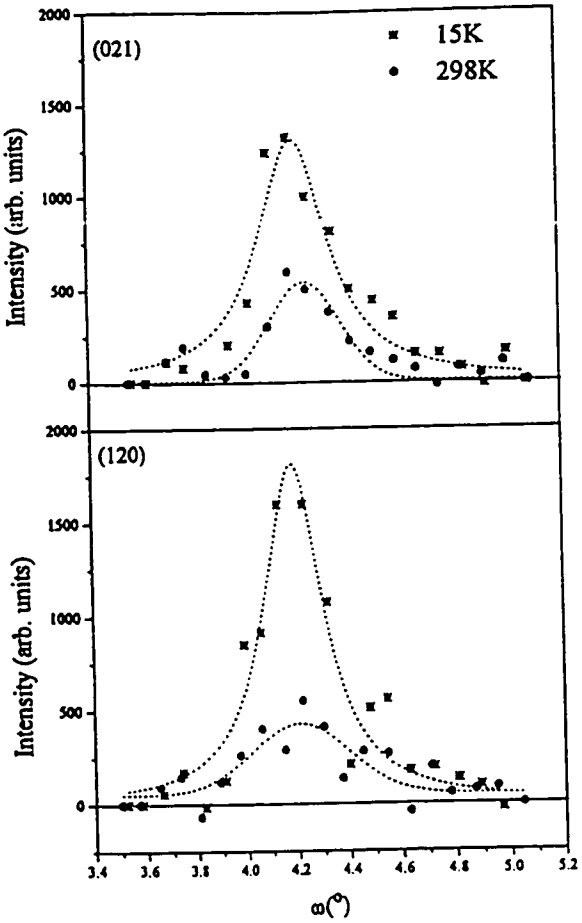

FIG. 5. Peak profiles of the C-type reflections (021) and (120) for the $x = 0$ phase. The dashed lines are a guide for the eyes.

are summarized in Table 6. At 298 K the presence of the (021) and (120) reflections is apparent and is likely due to multiple scattering since these reflections are forbidden in *Pnma*. The long scan times required for the observation of these magnetic peaks reflect the very small magnetic moments associated with the ordering on each sublattice.

The magnitude and orientation of the magnetic moments were determined with the program FULLPROF (16). This was done by achieving a good agreement between the observed intensities of the magnetic reflections with calculated values obtained by varying the magnitude and orientation of the moments. The scattering length of praseodymium was used for the determination due to the noninclusion of the scattering length of samarium in this program. Using the magnetic structure described above for $NdTiO_3$ as an initial model as well as several other models which placed the

TABLE 6
Integrated Intensities of the Magnetic Reflections Measured at 15 and 298 K

h	k	l	15 K	298 K
1	1	0	26(2)	0(2)
0	1	1[a]	86(2)	9(2)
0	2	1	19(1)	7(1)[b]
1	2	0	22(1)	7(1)[b]

[a]Allowed structural reflection.
[b]Due to multiple scattering.

moments along different axes, for example [Ti-(G_y); Sm-(C_z)] and [Ti-(G_z); Sm-(C_z)], we calculated the intensities of the magnetic reflections by varying the magnitude and orientation of the moments on each sublattice. To compare the calculated and observed intensities directly, the relative intensities with respect to a chosen structural peak in each case were determined. Several structural peaks were used for these comparisons and were chosen to have small 2θ values as close to the magnetic reflections as possible, as at higher values the effects of absorption and extinction are expected to become more severe. The magnitude and orientation of the magnetic moment were varied until a good agreement was found between the relative intensities in the calculated and observed cases. The best agreement was found using a model of Ti(III)-G_{xy} and Sm(III)-C_z with moments of 0.72(1) μ_B and 0.43(1) being determined for the Ti(III) and Sm(III) ions with angles of 7(3)° to the x-axis and 2(2)° to the z-axis, respectively (see Tables 7 and 8). The model is illustrated in Fig. 3. While this model appears to be consistent with Bertaut's symmetry rules (15), it must be borne in mind that there also exists a weak ferromagnetic component as evidenced by the susceptibility data. In past studies, this moment has been estimated to be very small ($\sim 10^{-2}$ μ_B) (6); however, nothing definitive can be stated about its magnitude and direction from the current neutron data. The value for Sm(III) compares well with that found for the Sm^{3+} ion in $SmFeO_3$ and $SmCrO_3$ at 0.45 and 0.49 μ_B, respectively (17). Hence, the results presented here show

TABLE 7
Comparison of the Calculated and Observed Relative Intensities When μ[Ti(III)] = 0.72(1) μ_B[a]

h	k	l	$I_{110,calc}/I_{Mf,calc}$	$I_{110,obs}/I_{Mf,obs}$	$I_{011,calc}/I_{Mf,calc}$	$I_{011,obs}/I_{Mf,obs}$
2	0	0	0.159	0.151	0.454	0.455
0	0	2	0.058	0.057	0.166	0.17
2	1	0	6.818	6.684	19.485	20.073

[a]The moment is placed at 7(3)° from the x-axis.
[b]Chosen structural reflection for comparison.

TABLE 8
Comparison of the Calculated and Observed Relative Intensities When μ[Sm(III)] = 0.43(1) μ_B

h	k	l	$I_{120,calc}/I_{hkl,calc}$	$I_{120,obs}/I_{hkl,obs}$	$I_{021,calc}/I_{hkl,calc}$	$I_{021,obs}/I_{hkl,obs}$
2	0	0	0.089	0.089	0.069	0.071
0	0	2	0.032	0.033	0.025	0.027
2	1	0	3.818	3.923	2.939	3.128

[a]The moment is placed at 2(2)° from the z-axis.
[b]Chosen structural reflection for comparison.

that for the first time the magnetic structure of $SmTiO_3$, and thus any other rare earth titanate, can be unequivocally determined using single-crystal neutron diffraction. The errors reported here reflect the uncertainties associated with the measured intensities, which are estimated to be less than 15%.

Finally, it should be mentioned that while magnetic ordering has been observed for $SmTiO_3$, it is found that this behavior extends, at least, to the $x = 0.05$ composition in the $Sm_{1-x}TiO_3$ family where $T_N \sim 40$ K (see Fig. 6). At the $x = 0.10$ composition, no obvious magnetic ordering is observed; however, a very subtle, broad feature is observed over ~100–250 K (see Fig. 7). While this is not fully understood at this time, it is thought to correspond to some degree of short-range magnetic order. Overall these observations parallel those observed for the $La_{1-x}TiO_3$ and the $Nd_{1-x}TiO_3$ systems, where strong electron correlation effects are present and the magnetic ordering disappears with the onset of metallic behavior for higher vacancy-doped members.

SUMMARY AND CONCLUSIONS

The results presented here, show that $SmTiO_3$ belongs to the antiferromagnetic set of rare earth titanates. The single-crystal neutron diffraction method has demonstrated unequivocally that the magnetic structure of $SmTiO_3$ consists of two canted antiferromagnetic sublattices with Ti(III)-G_xG_y and Sm(III)-C_z moment configurations. The magnetic moments were determined to be 0.72(1) and 0.43(1) μ_B for Ti(III) and Sm(III), respectively. The orientation is such that the Ti(III) moments are 7(3)° from the x-axis and the Sm(III) moments are 2(2)° from the z-axis. The magnetic behavior persists for the $Sm_{0.95}TiO_3$ composition and it is reasonable to conclude that it possesses the same magnetic structure as $SmTiO_3$ determined in this study.

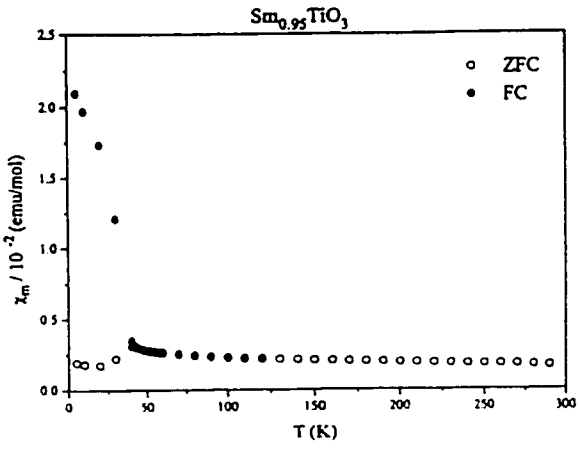

FIG. 6. Magnetic susceptibility (χ) vs T for $Sm_{0.95}TiO_3$.

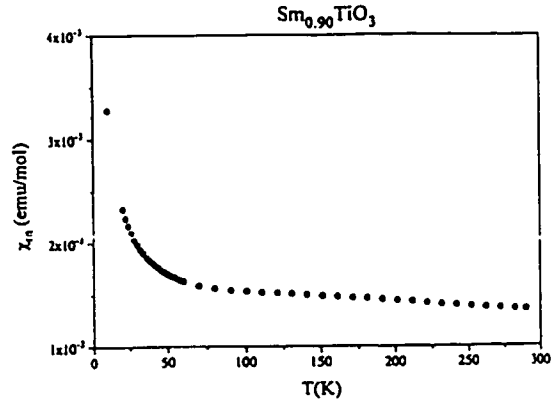

FIG. 7. Magnetic susceptibility (χ) vs T for $Sm_{0.90}TiO_3$.

ACKNOWLEDGMENTS

The authors express their gratitude to Dr. J. Britten for his contribution to this work. Financial support for this project was provided by the Canadian Institute of Neutron Scattering (CINS) and the Natural Science and Engineering Research Council (NSERC).

REFERENCES

1. M. J. MacEachern, H. Dabkowska, J. D. Garrett, G. Amow, W. Gong, G. Liu, and J. E. Greedan, *Chem. Mater.* 6, 2092 (1994).
2. D. Crandles, T. Timusk, J. D. Garrett, and J. E. Greedan, *Phys. Rev. B* 49, 16207 (1994).
3. C. Eylem, H. L. Ju, B. W. Eichorn, and R. L. Greene, *J. Solid State Chem.* 114, 164 (1995).
4. Y. Fujishima, Y. Tokura, and T. Arima, *Phys. Rev. B* 46, 11167 (1992).
5. D. A. Maclean, K. Seto, and J. E. Greedan, *J. Solid State Chemistry* 40, 241 (1981).
6. J. P. Goral and J. E. Greedan, *J. Magn. Magn. Mater.* 37, 315 (1983).
7. C. W. Turner and J. E. Greedan, *J. Magn. Magn. Mater.* 36, 242 (1983).
8. G. Amow and J. E. Greedan, *J. Solid State Chemistry* 121, 443 (1996).
9. P. Ganguly, O. Prakash, and C. N. R. Rao, *Phys. Status Solidi A* 36, 669 (1976).
10. K. Yoshii and A. Nakamura, *J. Solid State Chem.* 133, 584 (1997).

11. J. X. Boucherle, D. Givord, J. Laforest, and P. Morin, *in* "The Rare Earths in Modern Science and Technology" (G. J. McCarthy, J. J. Rhyne, and H. B. Silber, Eds.), Vol. 2. Plenum, New York, 1980.
12. C. Wilkinson, H. Khamis, R. F. D. Stansfield, and G. J. McIntyre, *J. Appl. Crystallogr.* 21, 471 (1988).
13. G. M. Sheldrick, Siemens SHELXTL, Version 5.03, Siemens Crystallographic Research Systems, Madison, WI, 1994.
14. D. A. Maclean, H.-N. Ng, and J. E. Greedan, *J. Solid State Chem.* 30, 35 (1979).
15. E. F. Bertaut, *in* "Magnetism" (G. T. Rado and H. Suhl, Eds.), Vol. III, p. 149. Academic Press, New York, 1963.
16. J. Rodriguez-Carvajal, "FULLPROF: A Program for Rietveld Refinement and Pattern Matching Analysis," Abstracts of the Satellite Meeting on Powder Diffraction of the XVth Congress of the International Union of Crystallography, p. 127, Toulouse, France, 1990.
17. M. Eibschütz, R. L. Cohen, and L. G. Van Uitert, *J. Phys. Colloq.* 32, (Suppl. No. 2-3), C1–C922 (1971).

CHAPTER 5

TRANSPORT PROPERTIES

In this Chapter the results of several studies of the transport properties of the $Nd_{(1-x)}TiO_3$ and $Sm_{(1-x)}TiO_3$ systems are presented. As will be seen, a remarkable variation in the resistivity behaviour in these systems is encountered which includes semiconducting, Fermi liquid and possibly variable range hopping behaviour. A brief discussion of the interpretation of the resistivity data for Fermi liquid behaviour and variable range hopping is given in Section 5.1., followed by a survey of previous results for the electronically analogous $La_{(1-x)}Sr_xTiO_3$ and $Nd_{(1-x)}A_xTiO_3$ (A = Sr, Ca) systems in Section 5.2.

5.1. Background

5.1.a. Resistivity properties:

Fermi Liquid Behaviour: The Fermi liquid description was originally developed by Landau as a means to describe ^{3}He which remains a liquid at very low temperatures (Landau, 1957; Landau, 1957). The theory was later shown to be applicable to the treatment of electrons in metals and nuclear matter. In Fermi liquid theory, it is argued that if electron interactions could be turned on in a smooth adiabatic manner, then the low energy excitations would retain the qualities of the free particles, however with renormalized properties and enhanced masses. These low energy excitations are called quasiparticles and are the quanta of the collective excitations of a Fermi-liquid. Heavy fermions are an example of such renormalized quasiparticles whose

general physical properties are reflected by large electronic specific heat coefficients, γ, which lead to large effective masses ranging from 100-1000 times the free electron mass, m_o and an enhanced Pauli susceptibility.

With regard to resistivity behaviour it has been shown that a material behaves like a Fermi-liquid when a T^2 dependence is observed, generally at low temperatures. More specifically, the resistivity is defined as,

$$\rho = \rho_o + AT^2 \qquad (1)$$

where ρ_o and A are constants. For heavy fermion materials, it has been shown that A scales almost as the square of the electronic specific heat coefficient (Kadowki and Woods, 1986; Miyake et al., 1989),

$$\frac{A}{\gamma^2} = 1.0 \times 10^{-5}[\mu\Omega - cm(mole.K/mJ)^2] \qquad (2)$$

so that the magnitude of A may be taken as a rough measure of the level of electron correlation. Generally, as the metal-insulator transition is approached, the constant becomes larger.

Variable Range Hopping: In the $R_{(1-x)}TiO_3$ (R=Nd,Sm) another important factor which may influence the resistivity behaviour is the presence of disorder. The effect of disorder is expected to increase as the x = 0.33 composition is approached due to the increasing number of vacancies. From the structural data it is evident that this will become more significant as the effects of electron correlation are anticipated to decrease with increasing bandwidth. The presence of disorder in solids is known to give rise to localization effects which influence the transport properties of a material. Localized states in the band structure arise when a high

concentration of defects are introduced in a solid. Due to the disorder present, groups of atoms may have individual energy levels which vary randomly from site to site. When the atomic orbitals overlap to form band states there will be some atoms with energies about an average value and these will have some neighbouring atoms. In addition, there may also be other atoms with energies near the limits of the energy range of the band and these are more likely to be isolated with no similar neighbours. The consequence is that atoms with orbital energies close to the centre of the band may extend throughout the solid whereas states near the band edges may be localized near individual atoms and thus do not extend throughout the lattice. This behaviour is known as Anderson localization and is illustrated in Fig. 5.1.

Mott showed that the localized and delocalized states which arise from Anderson localization cannot coexist at the same energy and are separated by a mobility edge. He also showed that in such localized states, conduction takes place via thermal assisted hopping of the electrons. At low temperatures the electrons jump longer and longer distances in order to find states that have similar energies. This is known as the variable range hopping mechanism and is illustrated in Fig. 5.2. The temperature dependence of the conductivity can be described by the general expression,

$$\sigma = \sigma_o \exp(-T_o/T)^{\beta} \qquad (3)$$

where $\beta = 1/(d+1)$ and d is the dimensionality of the system. Mott has shown that at low temperatures, the temperature dependence of the conductivity for strongly disordered systems should be such that $\beta = 1/4$, assuming that the Fermi level lies within the hopping regime (Mott, 1968; Mott and Davis, 1968). However, Mott's treatment of disordered systems neglects electron

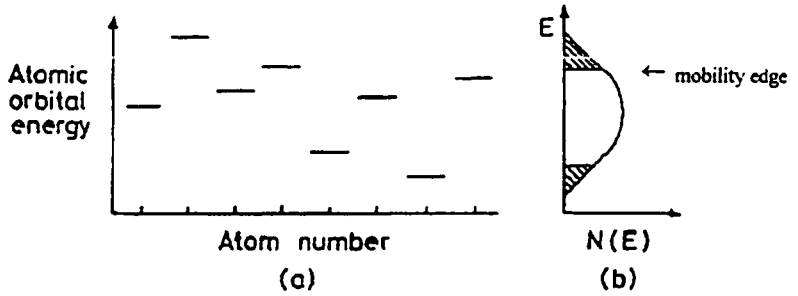

Fig. 5.1. Anderson localization. a) an array of atoms with randomly varying atomic orbital energies due to disorder. b). The density of states resulting from their overlap with two kinds of states separated by mobility edges: extended sates in the band centre and localized states at the band edges. (From Cox, 1992)

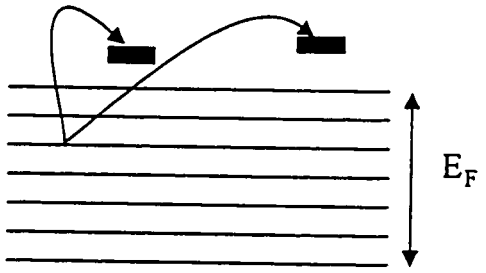

Fig. 5.2. Variable range hopping mechanism.

interactions. The inclusion of electron interactions in disordered systems has been shown to create a gap in the density of states near the Fermi level, called the Coulomb gap, so that the temperature dependence of the conductivity is described by $\beta = 1/2$ (Davis and Mott, 1970; Efros and Shklovskii, 1975; Srinivasan, 1971).

5.1.b. Specific heat theory for metals

By definition, the specific heat of a compound is the amount of heat required to raise the temperature of 1kg of material by 1K. In metals, the specific heat, C, is composed of two components, the electronic specific heat, C_e, which behaves linearly at very low temperatures and the lattice specific heat, C_{latt}. Thus, the specific heat is defined by,

$$C = C_e + C_{latt} = \gamma T + \beta T^3 \qquad (4)$$

where the coefficients, γ and β are defined as,

$$\gamma = 2/3\ \pi^2 k^2 V N(E_F) \qquad (5)$$

and,

$$\beta = 12\pi^4 R/5\theta \qquad (6)$$

where $N(E_F)$ represents the density of states at the Fermi level and θ is the Debye temperature. From eqn.(4), it is apparent that at relatively high temperatures the lattice contribution to the specific heat becomes significantly larger than the electronic contribution. However, at lower temperatures, a point is reached where the electronic contribution dominates the lattice contribution. In this regime, a plot of C/T against T^2 produces a straight line from which the quantities γ and β can be determined separately.

The coefficient, γ, is a particularly useful quantity as it can provide information regarding

the extent of correlation effects in our systems of interest. It can be shown that the specific heat coefficient, γ, scales proportionally to m^* using the relationships below,

$$N(E_F) = \frac{4\pi}{h^3}(2m^*)^{3/2} E_F^{1/2} \qquad (7)$$

$$E_F = \frac{h^2}{2}[3\pi^2 N(E_F)]^{2/3} \qquad (8)$$

From the description of electrons in a crystal, the effective mass is defined as,

$$\frac{1}{m^*} = \frac{1}{\hbar^2}\frac{d^2E}{dk^2} \qquad (9)$$

where k is a wave vector associated with an energy, E. With a decrease of the conduction bandwidth (small d^2E/dk^2), the electron interactions become stronger resulting in an increased effective mass. Thus, the extent to which correlation effects become important in these systems can be determined by comparison of the experimentally determined specific heat coefficient, γ_{expt}, with the free electron value, γ_0 which leads to,

$$\frac{\gamma_{expt}}{\gamma_0} = \frac{m^*}{m_0} \qquad (10)$$

where m_0 is the bare electron mass.

5.1.c. Thermopower

The thermoelectric power (thermopower or Seebeck effect) of a material is a complementary property in the understanding of the transport properties since it is a very sensitive probe of

the charge carriers necessary for electrical transport as well as to changes to the Fermi surface. The basic premise of the technique is to measure the voltage generated in response to a temperature gradient imposed across the sample of interest. Generally, when one measures the Seebeck coefficient it involves an open circuit of the kind illustrated in Fig. 5.3 which is composed of two dissimilar metals, A and B.

With an applied temperature gradient, the voltage $\Delta V = V_b - V_a$ is the *thermoelectric voltage* developed by this pair of metals and the *thermoelectric power* is then defined as,

$$S_{AB} = \lim_{\Delta T \to 0} (\Delta V / \Delta T) \qquad (11)$$

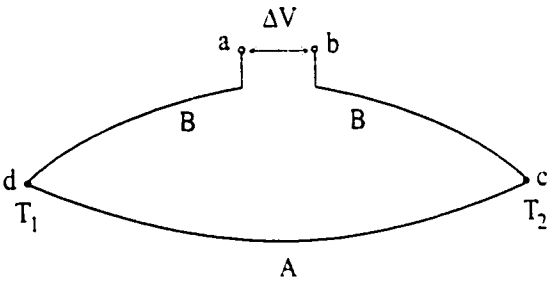

Fig. 5.3. Circuit showing thermoelectric effect (Adapted from Blatt, 1976).

Although the circuit shown in Fig.5.3. is comprised of two dissimilar metals it is possible to determine the *absolute* thermoelectric power (also called the Seebeck coefficient), S, of a material as it can be shown that,

$$\Delta V = \int_{T_1}^{T_2} (S_A - S_B) dT \qquad (12)$$

where, $S_{AB} = S_A - S_B$. Thus, knowing one value of S allows one to determine the other. In addition, as the sign of the thermopower is crucial in determining the carrier type it is very important to use the proper convention which is as follows. If the absolute thermopower of metal A is zero, the terminal of the circuit attached to the high temperature junction will be at a positive potential with respect to the low temperature terminal if S_B is positive (Blatt, 1976).

As pointed out earlier, this technique is very sensitive to the carrier types associated with the transport properties of materials. The more commonly encountered descriptions of the thermopower for metals and semiconductors are described below. The reader is referred to the following sources for further models of various conduction mechanisms (Chaikin, 1990).

Mott has derived the following relationship for metallic conductors.

$$S = \frac{\pi^2 k_B^2 T}{3e} \left| \frac{d \ln \sigma(E)}{dE} \right|_{E=E_F} \qquad (13)$$

where the differential indicates the change in the electrical conductivity, σ, as the energy, E, changes when evaluated at the actual Fermi energy, E_F, of the metal. In the neighbourhood of the Fermi energy, $E = E_F$, the electrical conductivity can be written as $\sigma(E) = a.E^y$ where a is a constant. Thus when evaluated eqn.(13) becomes, (Goodenough, 1971; Mott and Jones, 1958),

$$S \approx \frac{\pi^2 k_B^2 T}{3eE_F} y \qquad (14)$$

Thus, for metals the thermopower varies linearly with T. By substituting E_F which is defined

as,

$$E_F = \frac{h^2}{2m^*}\left(\frac{3n}{8\pi}\right)^{2/3} \qquad (15)$$

an expression is derived in which S is related to the carrier density, n,

$$S = -C_n m^* n^{-2/3} T \qquad (16)$$

where C_n is a constant defined as,

$$C_n = \frac{\pi^{8/3} k^2}{3^{5/3} h^2 e} \qquad (17)$$

For non-degenerate broad band semiconductors, the thermopower follows instead an inverse temperature dependence described by,

$$S = -\frac{k}{e}\left(\ln\frac{N_c(T)}{n} + A_e\right) \qquad (18)$$

where $N_c(T)$ is the effective density of states in the conduction band, n is the carrier density for n-type conduction defined by,

$$n = N_c(T)\exp[-(E_c - E_F)/kT] \qquad (19)$$

where E_c is the energy of the conduction band edge and E_F the energy at the Fermi level. The quantity A_e is called the transport factor which is generally very small and often is neglected (Cox, 1992). The above expression represents the thermopower in the case of n-type conduction, however, an analogous expression is also obtained for p-type conduction,

$$S = +\frac{k}{e}\left(\ln\frac{N_v(T)}{p} + A_e\right) \qquad (20)$$

where $N_v(T)$ now represents the effective density of states in the valence band and p is defined as,

$$p = N_v(T)\exp[-(E_F-E_v)/kT] \qquad (21)$$

where E_v is the energy at the edge of the valence band.

In the presence of electron interactions, conduction in semiconductors may take place via polaron hopping. In this case, the thermopower is described by Heikes' law,

$$S = \left(\frac{k}{e}\right)\left[\ln 2\left(\frac{1-c}{c}\right)\right] \qquad (22)$$

where c and (1-c) are defined as the relative amounts of reduced $[M^{n+}]$ and oxidised $[M^{(n+1)+}]$ ions respectively and is clearly temperature independent.

Recently, the thermopower as applied to systems such as $La_{(1-x)}Sr_xTiO_3$, has been formulated using dynamical mean field theory (Palsson and Kotliar, 1998). From this theoretical treament the thermopower is predicted to behave according to Heike's law eqn.(22) at high temperatures. At lower temperatures, the thermopower is described by,

$$S = -\frac{k}{e}\left(\frac{kT}{Z}\cdot\frac{d\ln\Phi(\tilde{\mu})E_o}{d(\tilde{\mu})}\right)\frac{E_2}{E_0} \qquad (23)$$

where $\Phi(\tilde{\mu})$ is a transport function, $\tilde{\mu}$ is the effective chemical potential, Z is defined as the

where $\Phi(\mu)$ is a transport function, μ is the effective chemical potential, Z is defined as the quasiparticle residue at the Fermi level and the E_n are constants.

Using these results the thermopower of the strontium rich compositions in the $Sr_{(1-x)}La_xTiO_3$ system ($0.02 \leq x \leq 0.70$) were calculated for the range 200K - 1000K At high temperatures Heikes' law is observed while at lower temperatures a sharp decrease in the thermopower values is observed, marking the transition to the Fermi-liquid regime.

It was shown that the thermopower is also dependent on the doping concentrations, as for $x < 0.10$, p-type conduction is generally observed over the temperature range investigated, whilst for $x \geq 0.30$ n-type conduction is predicted. These results are summarized schematically in Fig. 5.4.

Even though the models were investigated at temperatures ≥200K, it may be useful to compare the results of our present study with these expectations as well as experimental results obtained from another study in which the thermopower behaviour of the strontium rich $Sr_{(1-x)}La_xTiO_3$ system was measured (Moos et al., 1995).

5.2. Previous Work:

5.2.a. $R_{(1-x)}A_xTiO_3$ systems

In the $La_{(1-x)}Sr_xTiO_3$ system, a metal-insulator transition is observed with a 5% strontium doping level. The resistivity behaviour of the higher doped compounds show Fermi liquid character having a T^2 temperature dependence whose A coefficients decrease with increased strontium doping indicating decreasing correlation effects as one moves away from the M-I

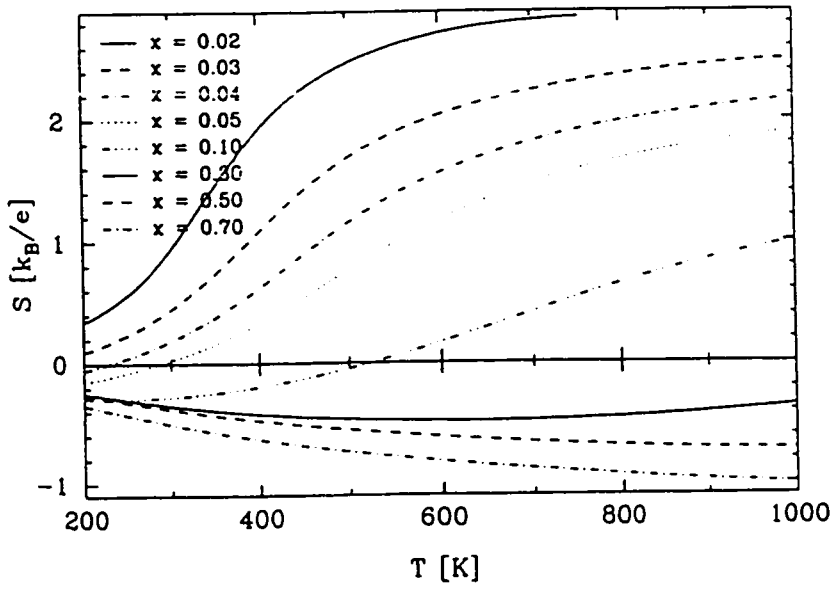

Fig. 5.4. Calculated temperature dependence of the thermopower in the $La_{(1-x)}Sr_xTiO_3$ system for $0.02 \leq x \leq 0.70$. (From Palsson et. al., 1998).

boundary, see TABLE 5.1. The observance of Fermi liquid behaviour in the $La_{(1-x)}Sr_xTiO_3$ system was also shown to be accompanied by a simultaneous enhancement of the Pauli susceptibility and the specific heat coefficient, γ, indicating a divergence in the electron mass as the M-I boundary is approached in accordance with the Brinkman-Rice picture, see Fig.5.5. Furthermore, it was shown that the Kadowki-Wood relationship, eqn. (2), for heavy fermions, applies to this system, despite the fact that the observed specific heat is an order of magnitude smaller than that typically observed for heavy fermion materials.

For the $Nd_{(1-x)}A_xTiO_3$ systems, M-I transitions are also observed, however, these occur at different doping levels depending on the identity of the alkali earth metal, A. The critical values of x are 0.15, 0.20 and 0.72 for A = Ca, Sr, and Ba respectively. In all these studies, only resistivity measurements have been performed with respect to transport properties with evidence of strong electron correlation manifesting itself as Fermi-liquid behaviour. Furthermore, magnetic studies indicate an enhancement of the Pauli susceptibility. To gain further insight into the role of mass enhancement as the M-I transition is approached, an attempt was made to determine the specific heat of the metallic compounds in the $Nd_{(1-x)}Ca_xTiO_3$ system. Due to the expected presence of a lambda transition of the Nd(III) ions at low temperatures, no actual specific heat measurements were made (Ju et al., 1994). Instead, γ was estimated from measured A values using the Kadowki-Wood relationship, eqn.(2). The relationship between the specific heat and the enhanced susceptibility values can be seen Fig. 5.6 which shows a divergence as the M-I boundary is approached, in accordance with the Brinkman-Rice model.

With regard to thermopower measurements, only one systematic investigation has

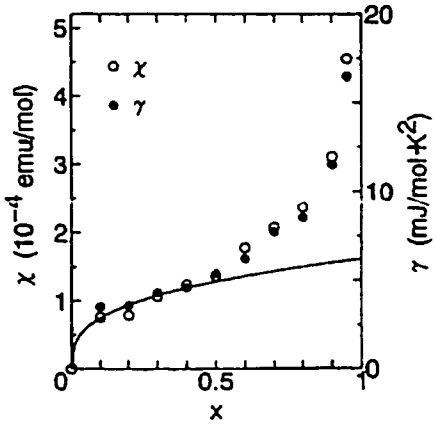

Fig. 5.5. The x-dependence of the linear specific heat coefficient, γ(●), and the nearly temperature independent spin susceptibility, χ(○), at 300K in $La_{(1-x)}Sr_xTiO_3$. (From Tokura et. al., 1993)

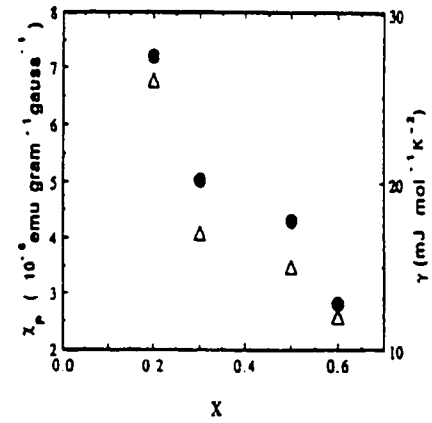

Fig. 5.6. The x dependence of the estimated low temperature specific heat coefficient, γ (Δ), and the Pauli susceptibility (χ) in$Nd_{(1-x)}Ca_xTiO_3$ for $0.2 \leq x \leq 0.6$. (From Ju et. al., 1994)

been carried out for the $Sr_{(1-x)}La_xTiO_3$ system (Moos et al., 1995). The thermopower of the x = 0, 0.01, 0.03, 0.10, 0.20, 0.30, 0.40 and 0.50 compositions were investigated in the range 150K-1200K using polycrystalline samples. From this study it was found that at at high temperature and low carrier concentrations, n, i.e. for $x \leq 0.20$, the thermopower behaves as a classical broad band semiconductor according to eqn. (18)

Table 5.1: Values of A coefficients obtained from $\rho = \rho_o + AT^2$

Compound	$\%Ti^{3+}$	$A(\mu\Omega\text{-cmK}^{-2} \times 10^{-9})$
$La_{0.95}Sr_{0.05}TiO_3$	95	2.5
$La_{0.90}Sr_{0.10}TiO_3$	90	1.5
$La_{0.80}Sr_{0.20}TiO_3$	80	1.21
$La_{0.70}Sr_{0.30}TiO_3$	70	1
$La_{0.92}TiO_3$	76	4.08
$La_{0.88}TiO_3$	64	2.47

On the other hand, at low temperatures and high carrier concentrations, i.e. x = 0.20 to 0.50, the Seebeck coefficient follows a linear temperature dependence indicating metallic-like behaviour consistent with Mott's equation, eqn. (16). The suitability of this model in describing this behaviour was demonstrated by the observation of the -2/3 dependence of the carrier concentration, n, as expected from Mott's law when log|S| vs. log $|n = \%Ti^{3+}|$ at constant T is plotted, see Fig. 5.7.

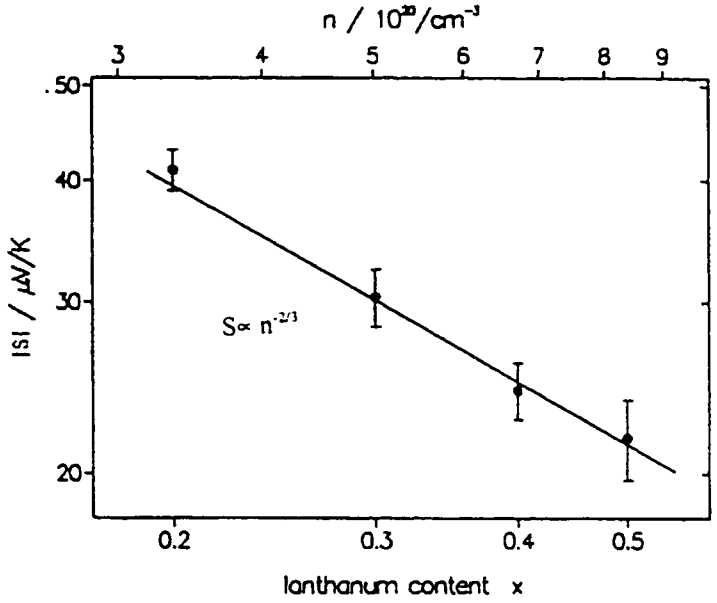

Fig. 5.7. log-log plot of S vs. T in the $Sr_{(1-x)}La_xTiO_3$ system demonstrating the $n^{-2/3}$ dependence. (From Moos et. al.1995)

5.2.b. $R_{(1-x)}TiO_3$ systems:

As pointed out in Chapter 1, the parent titanates, x=0.00, are all semiconducting with activation energies, E_α, which increase with the decreasing radius of the rare earth ion. Recently, an investigation of the transport properties of the $La_{(1-x)}TiO_3$ system was reported (MacEachern et al., 1994) whose results are summarized here. Resistivity measurements reveal the presence of two M-I transitions occurring at x = 0.08 and x = 0.25. It is obvious that a larger concentration of Ti^{4+} is needed to induce the M-I transition in this system as compared to the $La_{(1-x)}Sr_xTiO_3$ system, see Fig. 5.8. Fermi liquid behaviour is observed for the x = 0.08 and 0.12 phases with the larger values of the A-coefficient from the ρ versus T^2 graphs being observed, see TABLE 5.1. This indicates that correlation effects in this system are more significant than for $La_{(1-x)}Sr_xTiO_3$.

With regard to the systems of interest in the present study, a survey of the literature revealed two studies of the transport properties for x = 0.00, 0.10, 0.20, 0.30, 0.33 in the $Nd_{(1-x)}TiO_3$ system and for x = 0.00, 0.10, 0.20 in the $Sm_{(1-x)}TiO_3$ system (Bazuev et al., 1983; Bazuev and Shveikin, 1986). The resistivity measurements were performed in the range 77K-300K and some very limited information from thermopower measurements for $T \geq 290K$ were reported which showed the dominant carrier type to be n-type for $x \geq 0.10$. From these reports it is apparent that metal-insulating transitions occur at x = 0.10 for the $Nd_{(1-x)}TiO_3$ system and at x = 0.20 for $Sm_{(1-x)}TiO_3$ although this composition was reported to contain a pyrochlore impurity.

5.3. Present Work:

5.3.1. Electrical Resistivity:

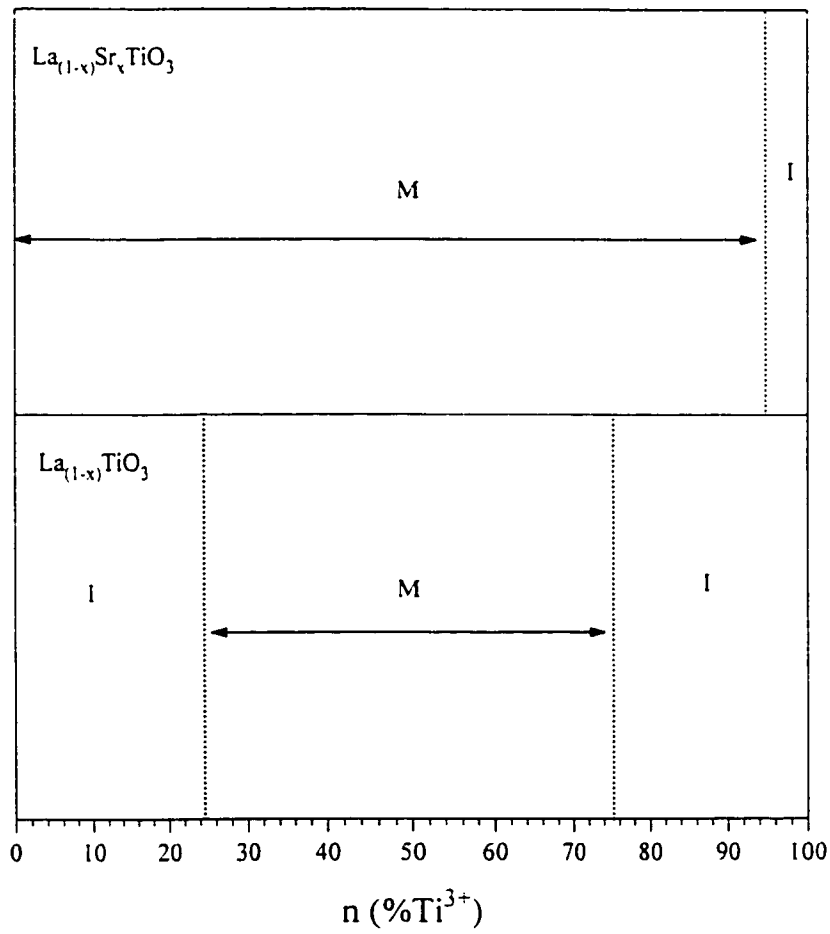

Fig. 5.8. Phase diagram showing the M-I transitions in the $La_{(1-x)}Sr_xTiO_3$ and $La_{(1-x)}TiO_3$ system.

5.3.1.a. $Nd_{(1-x)}TiO_3$ system

The resistivity data for all compounds studied in this system are shown in Fig. 5.9 which clearly shows the presence of two M-I transitions at x = 0.10 and x = 0.20. The resistivity values near room temperature are shown in TABLE 5.2 and individual resistivity plots are shown in Figs. 5.10 to 5.17.

TABLE 5.2: Resistivity values at 290K for compositions studied.

Compound	$\rho_{290K\ (m\Omega\text{-}cm)}$	Compound	$\rho_{290K\ (m\Omega\text{-}cm)}$
$NdTiO_3$	2372	$SmTiO_3$	1763
$Nd_{0.95}TiO_3$	30	$Sm_{0.95}TiO_3$	1600
$Nd_{0.90}TiO_3$	7	$Sm_{0.90}TiO_3$	88
$Nd_{0.85}TiO_3$	1	$Sm_{0.87}TiO_3$	8
$Nd_{0.83}TiO_3$	1	$Sm_{0.85}TiO_3$	5
$Nd_{0.80}TiO_3$	2	$Sm_{0.83}TiO_3$	5
$Nd_{0.75}TiO_3$	11		
$Nd_{0.70}TiO_3$	21		

For the parent titanate, semiconducting behaviour following Arrhenius' law is obeyed,

$$\rho = \rho_o \exp(E_a/kT) \qquad (24)$$

From a plot of lnρ vs 1/T, two linear portions were observed which resulted in activation energies of 0.12 eV in the range 300K to 194K and 0.087eV in the range ~194K to ~90K, see Fig.5.9 These results agree with those obtained previously for $NdTiO_3$ where the activation energy was determined to be 0.03eV, although this sample is now believed to have been non-stoichiometric.

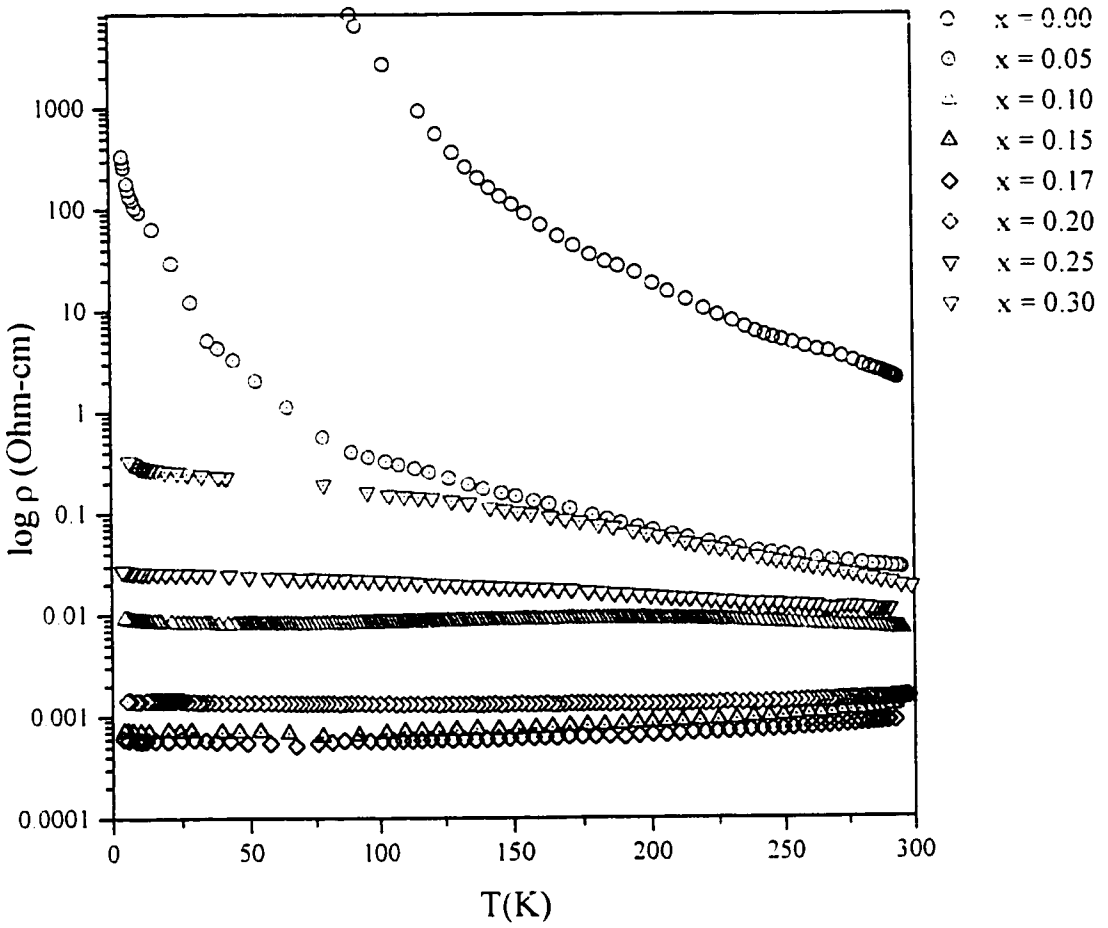

Fig. 5.9. Overall resistivity trends in the $Nd_{(1-x)}TiO_3$ system.

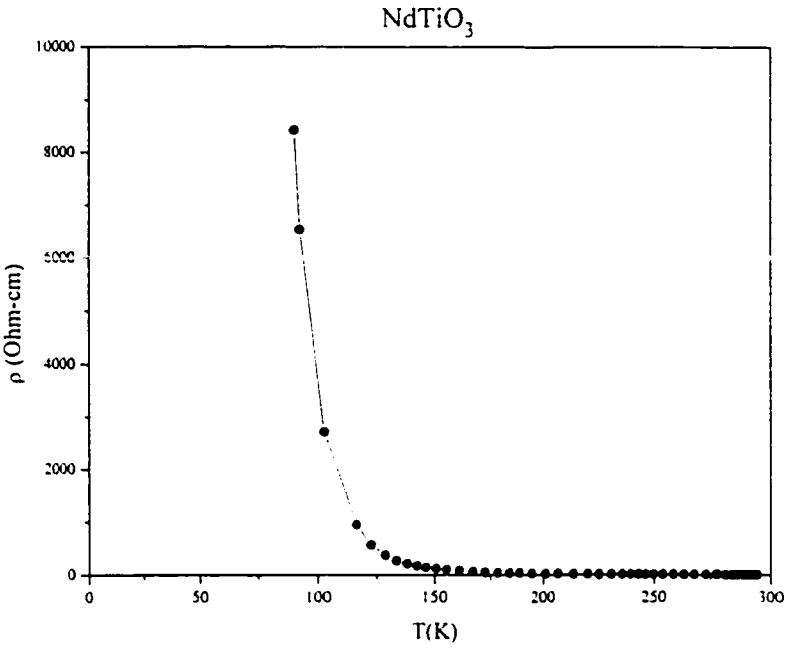

(a).

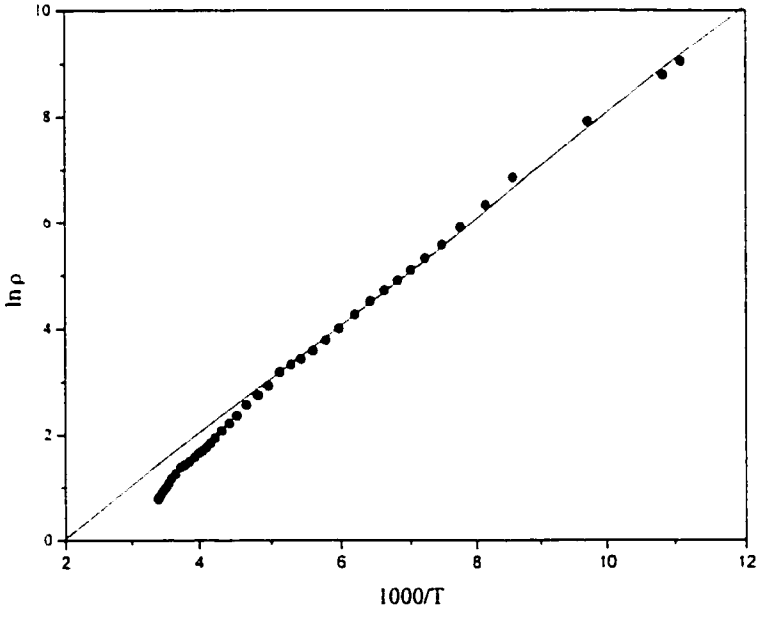

(b).

Fig. 5.10. a). ρ vs. T and b). ln ρ vs. 1000/T for $NdTiO_3$ (x=0.00)

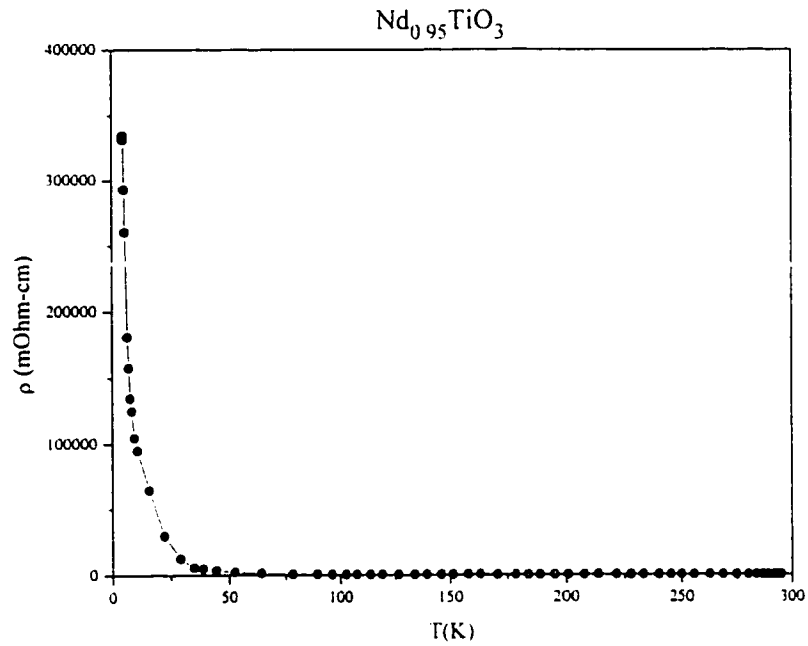

(a).

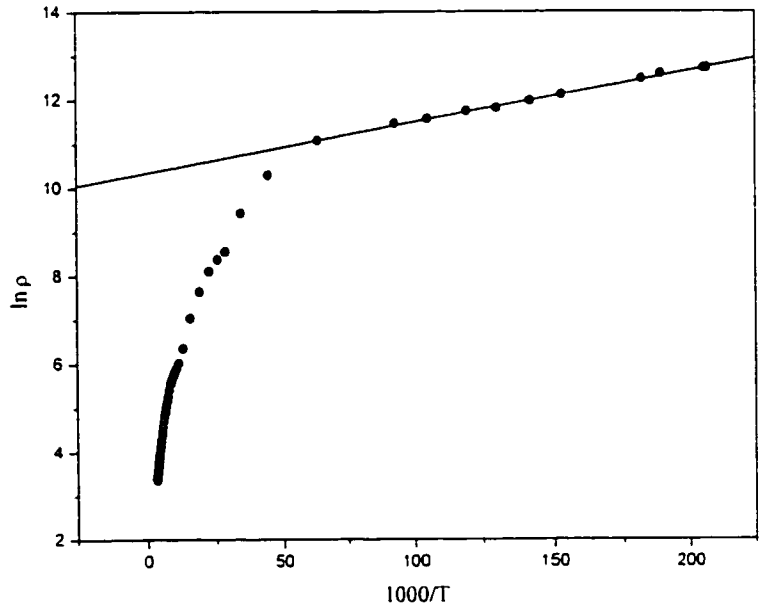

(b).

Fig. 5.11. a). ρ vs. T and b). ln ρ vs. 1000/T for $Nd_{0.95}TiO_3$ (x=0.05)

A better agreement is found by comparison with the study on the $Nd_{(1-x)}Ca_xTiO_3$ system with E_a = 0.16eV for $NdTiO_3$ and E_a = 0.05eV for $Nd_{0.90}Ca_{0.10}TiO_3$ (Ju et al., 1994). A linear fit was also observed for the x = 0.05 compound over the temperature range ~170K-295K with an activation energy determined to be 0.05 eV. Below 170K however, a non linear dependence of ln ρ is observed, see Fig. 5.11.

With increasing vacancy doping level, the semiconducting behaviour gives way in the $Nd_{0.90}TiO_3$ compound to barely metallic behaviour, Fig. 5.12 clearly signalling the first metal-insulating transition in the series. Furthermore, the effects of correlation can be seen here owing to the very unusual sine like dependence of the resistivity on temperature with a broad maximum at ~200K and a broad minimum at ~50K. The broad maximum observed in the range ~125K to ~200K resembles those found in heavy fermion and valence fluctuating materials, for example $Ce_{(1-x)}La_xPb_3$ (Lin et al., 1987) and CeRhSb (Malik and Adroja, 1991), see Fig. 5.13, where the maximum is associated with a Kondo lattice which arises from the interaction of the 4f and the conduction electrons near the Fermi level.

On the low temperature side of the maximum, the resistivity decreases signalling the transition of incoherent (itinerant) to coherent (localized) scattering of the conduction electrons by the rare earth ions (Lee et al., 1986; Stewart, 1984). On further decrease of the temperature, the resistivity goes through a minimum around 50K and rapidly increases below this temperature. This trend suggests the opening of a small band gap as a result of the increased localization of the carriers. This interpretation has also been used to explain similar behaviour observed in other systems such as for the heavy fermion material CeRhSb (Malik and Adroja, 1991)

and the charge transfer system $NiSi_{(2-x)}Se_x$ (Honig and Spalek, 1998). This appears to be a reasonable scenario in light of the optical measurements previously reported for $LaTiO_3$ which shows evidence for the opening of a small gap as the temperature is lowered below the M-I transition at ~138K, consistent with its semiconducting behaviour (Crandles et al., 1994), see Fig. 5.14.

To check the reproducibility of this result a second sample with the same nominal composition was prepared. The resistivity behaviour for this second sample possessed a similar temperature dependence, however occurring on a lower resistivity scale indicating more metallic behaviour. As the features of this sample were more subtle than the first, the normalized resistivity is plotted in Fig. 5.12. The variation in metallic behaviour observed can be explained by comparison of the cell volumes of these two samples. Guinier analysis reveals that the second sample has a smaller cell volume of 237.37(2)Å compared to the first sample with a cell volume of 237.48(2)Å. The smaller value indicates a compound with a marginally higher vacancy doping. A value of $x = 0.89$ was obtained by using the linear relationship between the cell volume and neodymium content shown in Chapter 3, and reveals the sensitivity of the physical properties to doping levels in the system.

For higher doping levels, $x = 0.15$, 0.17 and 0.20, a tendency towards more metallic behaviour is observed, see Figs. 5.15, 5.16a and 5.17a. An attempt was made to fit the resistivity data of these compositions to the Fermi liquid model. However, the T^2 dependence could only be established for the $x = 0.15$ and 0.17 compositions in the ranges ~225K-105K and ~260K to ~109K respectively, see Figs.5.14b and 5.15b. From these fits, the constant A was determined

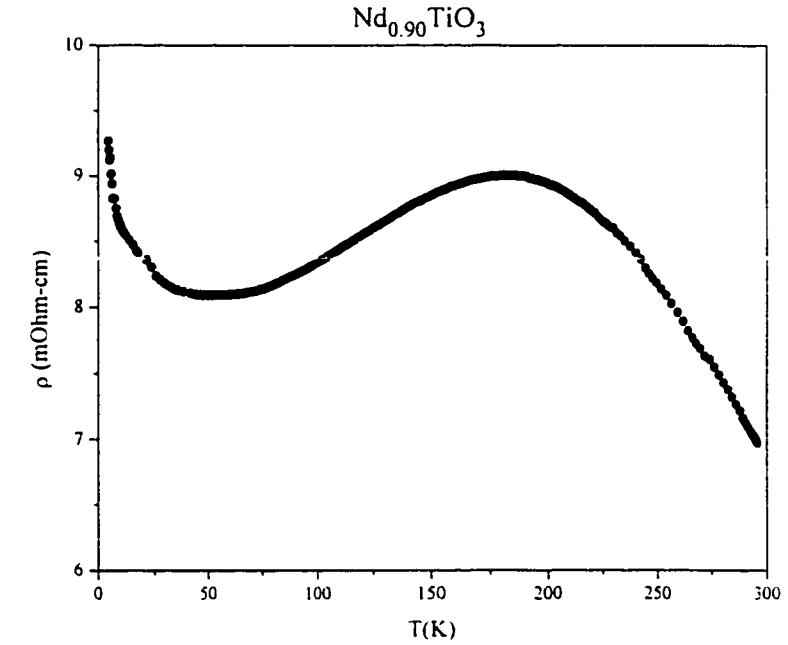

(a).

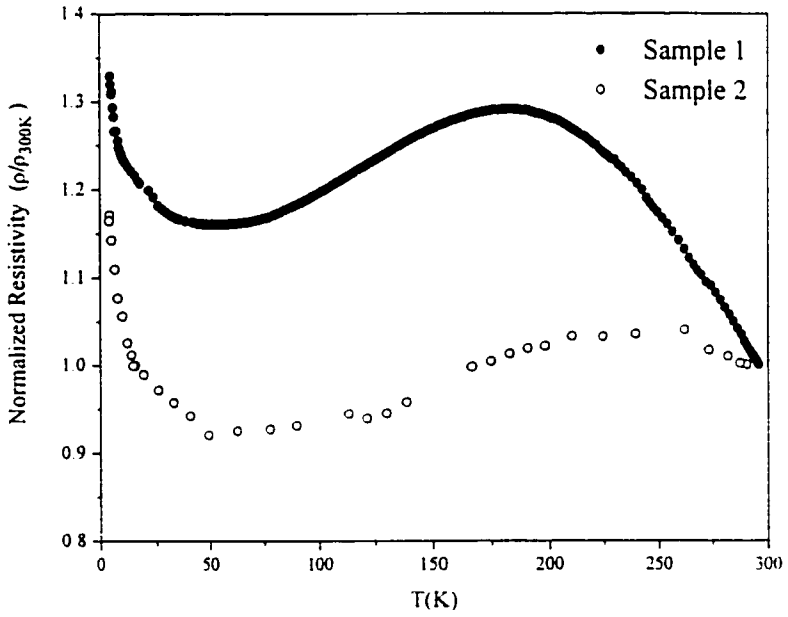

(b).

Fig. 5.12. a). ρ vs. T and b). Normalized resistivity vs. T for Sample 1 and 2.

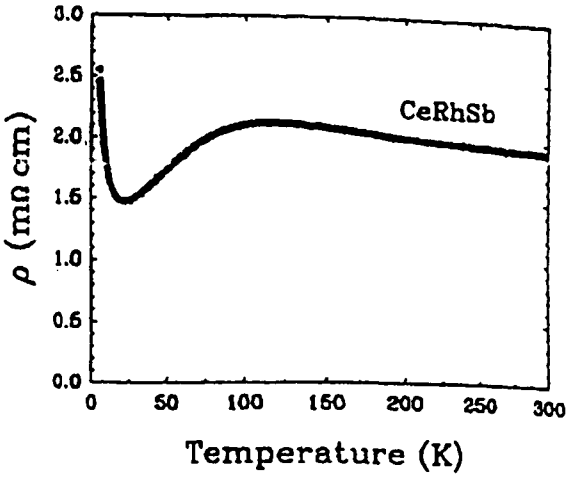

a).

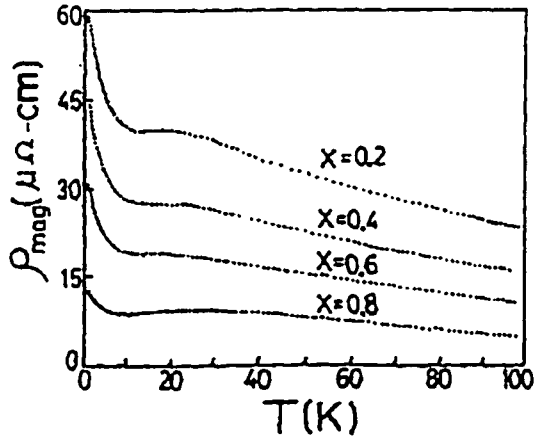

b).

Fig. 5.13. ρ vs. T for a). CeRhSb and b). $Ce_{(1-x)}La_xPb_3$.

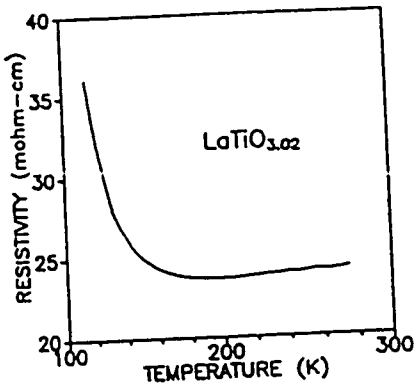

a).

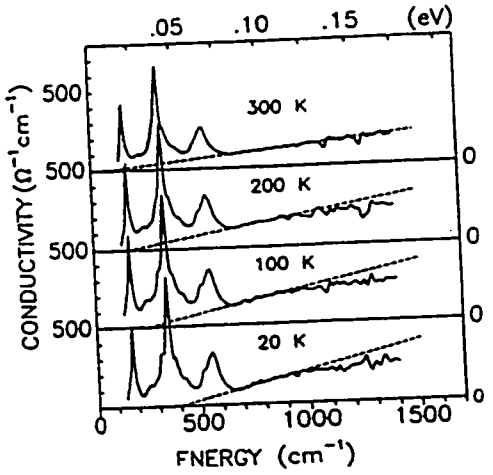

b).

Fig. 5.14. a). ρ vs. T for $LaTiO_{3.02}$. b). Optical conductivity at various temperatures for $LaTiO_{3.02}$ showing the opening of a small gap at low temperatures. (From Crandles, 1992).

to be larger than those previously found in the $La_{(1-x)}TiO_3$ system, for much smaller Ti^{3+} concentrations, reflecting the higher degree of correlation in the $Nd_{(1-x)}TiO_3$ system (MacEachern et al., 1994). These are summarized in TABLE 5.3.

For the remaining phases, x = 0.25 and 0.30 a transition into an insulating regime is observed, thus marking the second metal-insulator transition in this series, Figs. 5.17b and 5.18a. The data for the x = 0.25 composition appears to have an almost linear dependence

TABLE 5.3: Values of A coefficients obtained from $\rho = \rho_o + AT^2$

Compound	$\%Ti^{3+}$	$A(\mu\Omega\text{-cm}K^{-2} \times 10^{-9})$
$La_{0.92}TiO_3$	76	4.1
$La_{0.88}TiO_3$	64	2.5
$Nd_{0.85}TiO_3$	55	6.0
$Nd_{0.83}TiO_3$	49	2.9

of the resistivity with temperature, while the x = 0.30 composition appeared to have a logarithmic dependence. An attempt was made to fit the x = 0.30 data using the Arrhenius expression for semiconductors, however this did not result in a good fit. Instead the data could be better fit using Mott's expression for variable range hopping,

$$\sigma = \sigma_o \exp(-T_o/T)^{1/4} \qquad (25)$$

By plotting log $\sigma T^{1/2}$ against $T^{-1/4}$, it was found that only the x = 0.30 data could be fit to this model over the range ~6.5K-32.5K and 202K-298K, see Fig. 5.18b. Taking into consideration the possible interplay between correlation and disorder, a fit using eqn. (3) with $\beta = 1/2$ was also performed, see Fig. 5.19. In comparing these results, the variable range hopping model

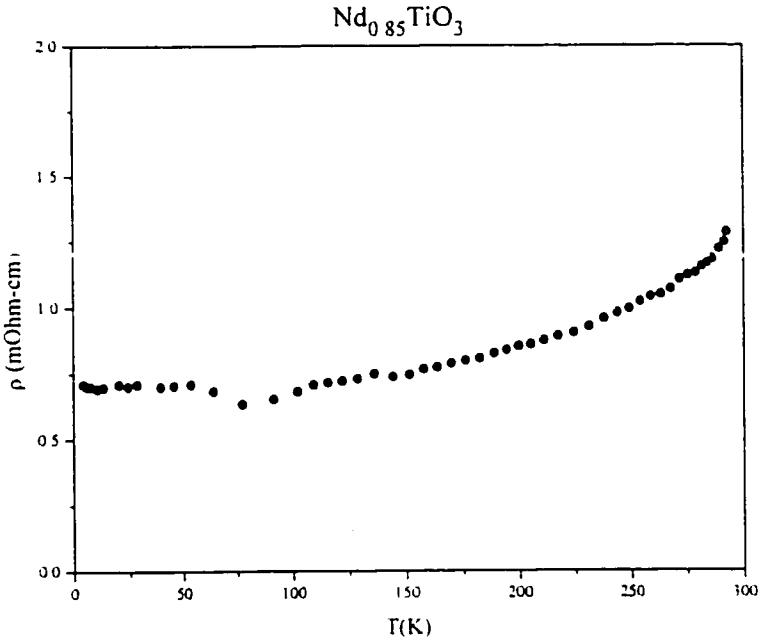

(a).

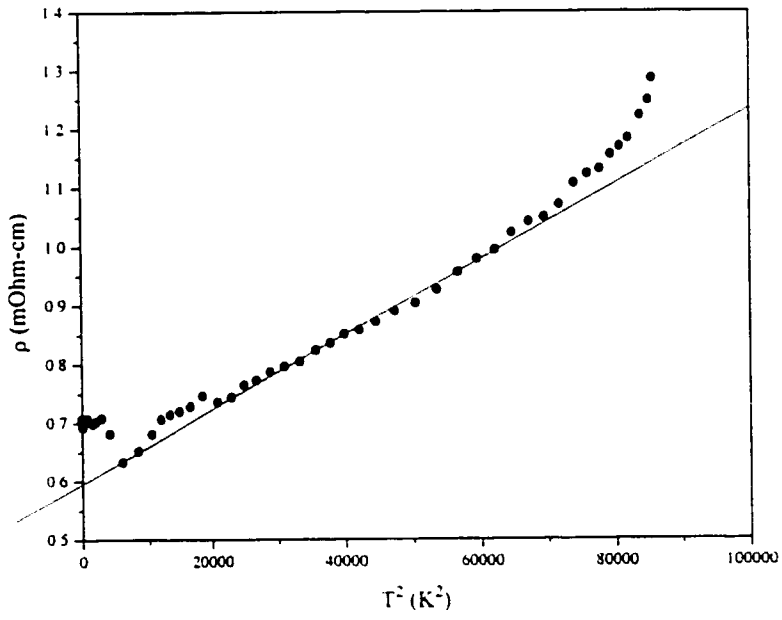

(b).

Fig. 5.15. a). ρ vs. T for and b). ρ vs. T^2 for $Nd_{0.85}TiO_3$ (x = 0.15)

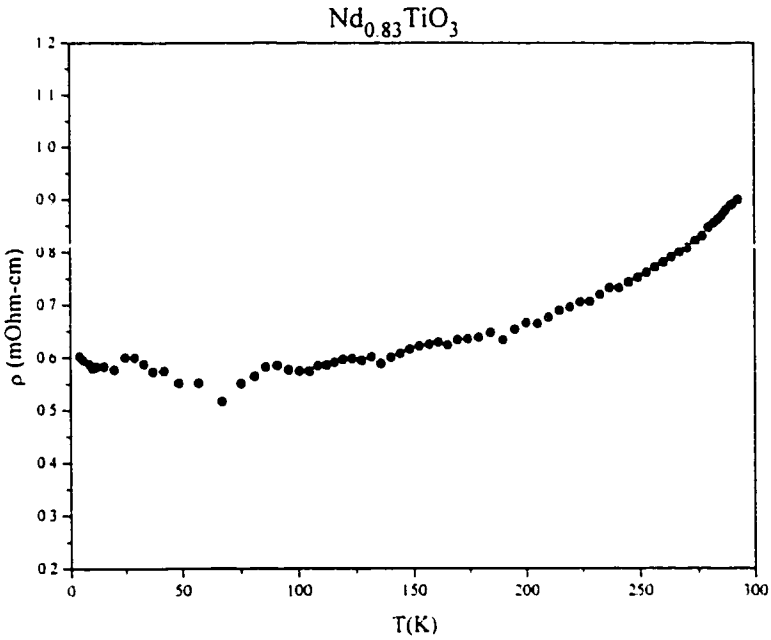

(a).

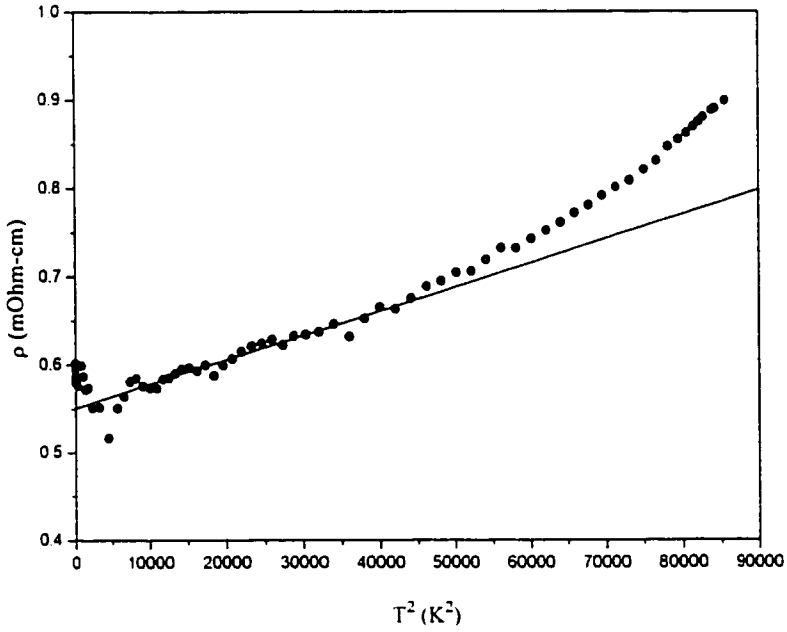

(b).

Fig. 5.16. a). ρ vs. T for and b). ρ vs. T^2 for $Nd_{0.83}TiO_3$ (x = 0.17)

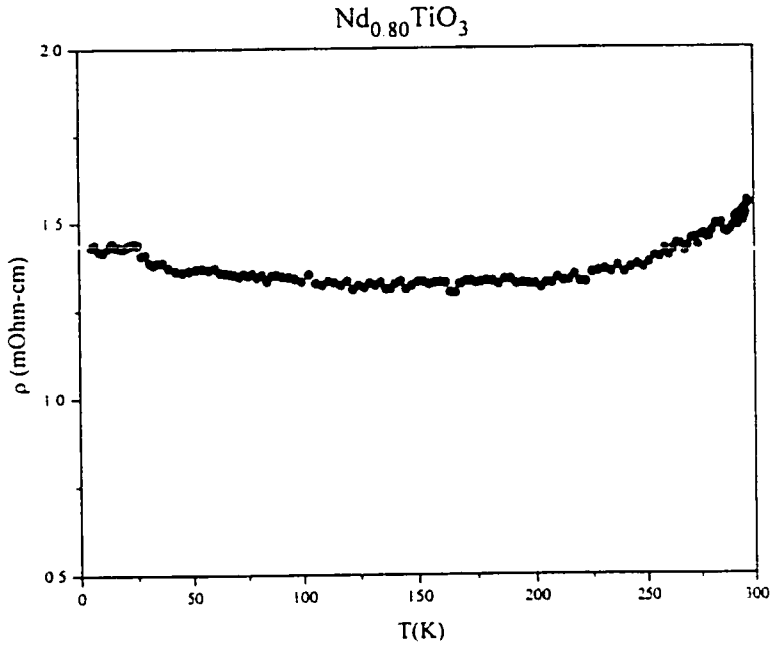

(a).

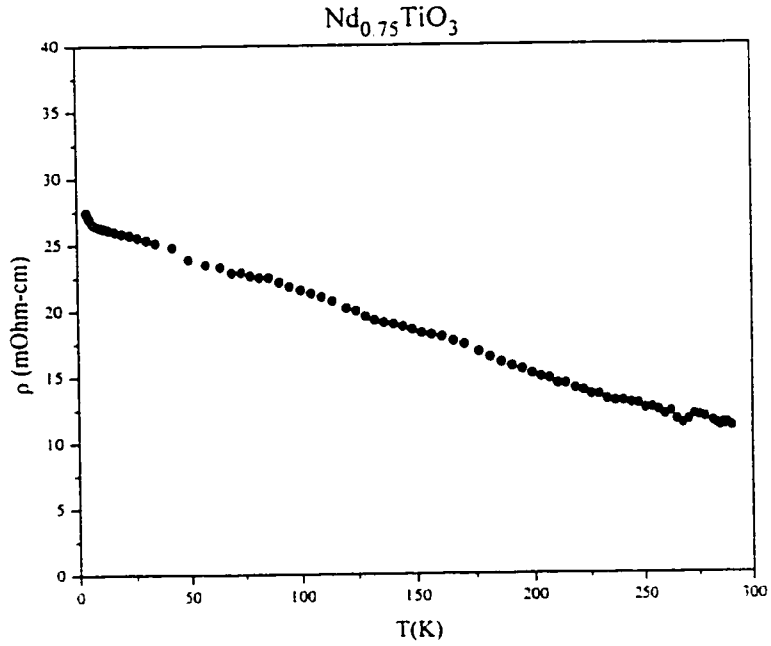

(b).

Fig. 5.17. ρ vs. T for a). $Nd_{0.80}TiO_3$ (x = 0.20) and b). $Nd_{0.75}TiO_3$ (x = 0.25)

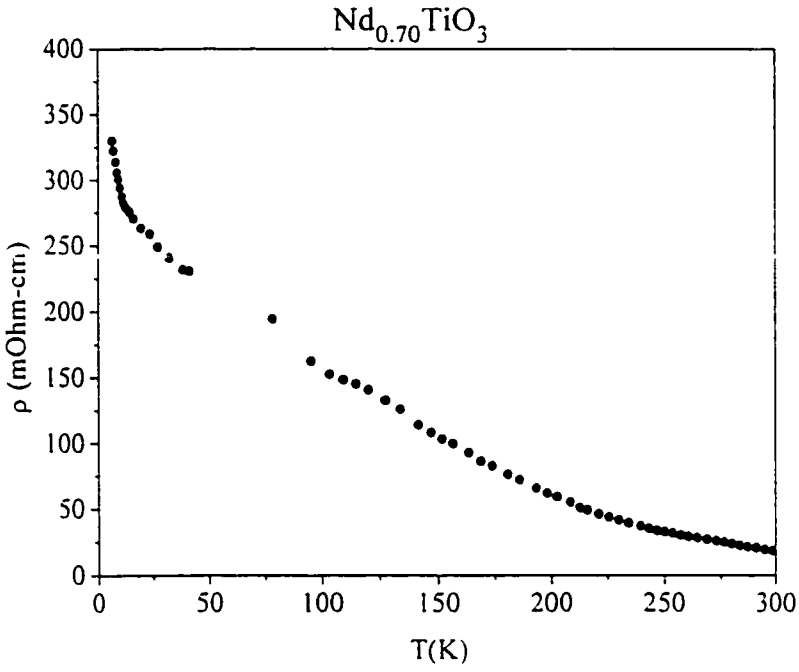

(a).

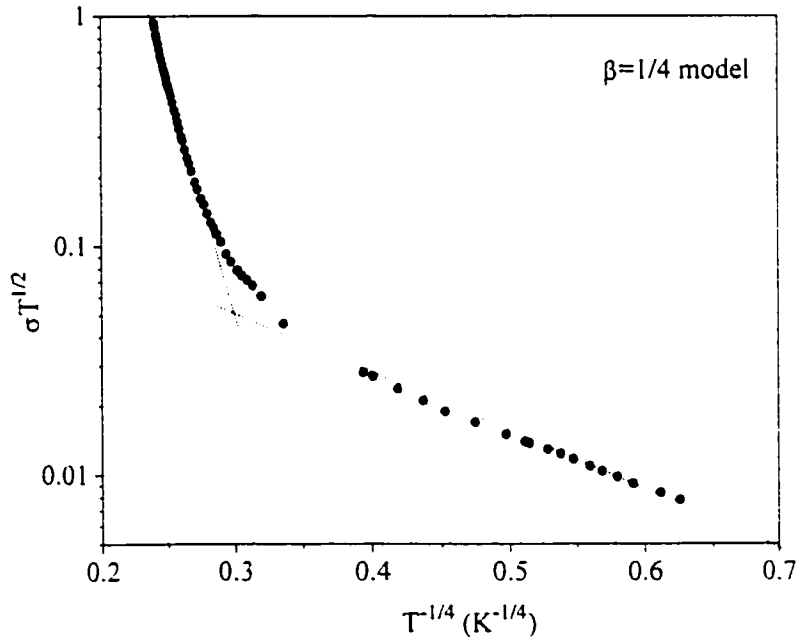

(b).

Fig. 5.18. a). ρ vs. T for and b). log $\sigma T^{1/2}$ vs. $T^{-1/4}$ for $Nd_{0.70}TiO_3$ (x = 0.30)

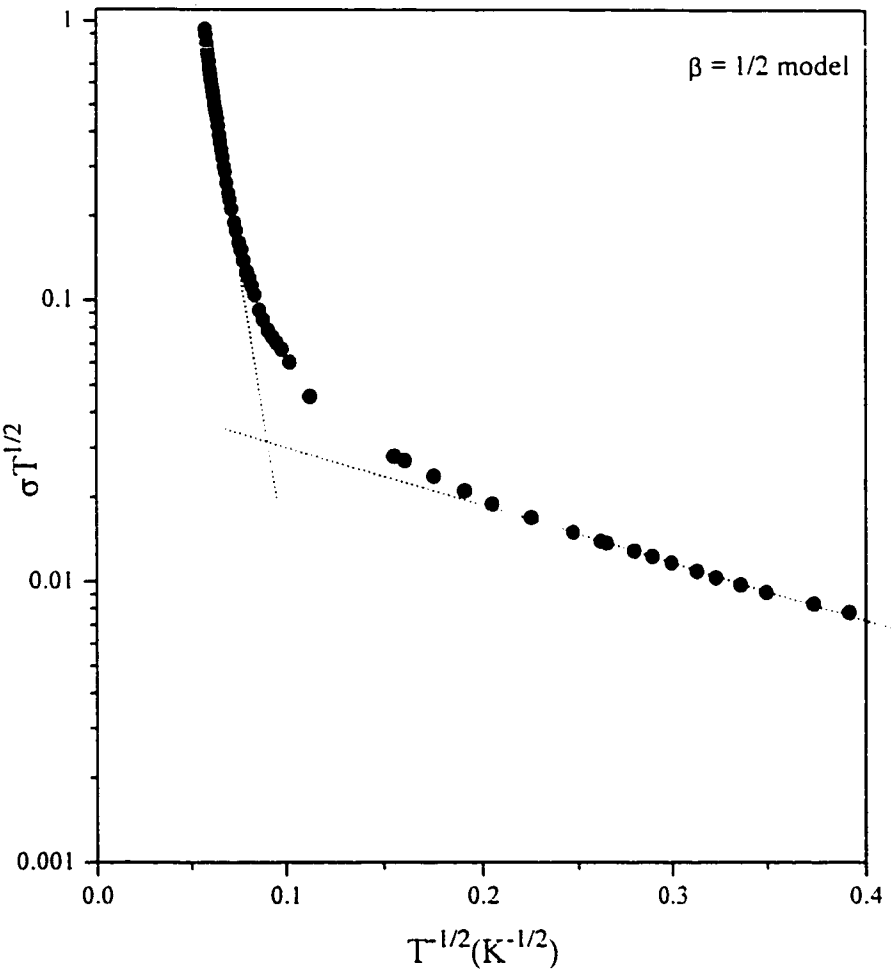

Fig. 5.19. log $\sigma T^{1/2}$ vs. $T^{-1/2}$ for $Nd_{0.70}TiO_3$ (x = 0.30)

($\beta = 1/4$) was marginally better than the $\beta = 1/2$ model, however the distinction between these two cases is ambiguous.

Finally, although the resistivity behaviour of the remaining end member of the $Nd_{(1-x)}TiO_3$ system, $Nd_{2/3}TiO_3$, was not measured due to the small size of the crystals obtained, it is evidently insulating given its transparent nature in visible light.

5.3.1.b. $Sm_{(1-x)}TiO_3$ system

The resistivity behaviour of the samarium samples investigated can be found in Fig. 5.20. As in the $Nd_{(1-x)}TiO_3$ system, semiconducting behaviour obeying Arrhenius' law is obeyed for the x = 0.00 and 0.05 compositions. For the x = 0.00 compound a linear fit could be observed over the temperature range (~75K-RT) resulting in an activation energy of 0.058eV, Fig. 5.21. By contrast, for the x = 0.05 composition, it appears that two activation energies are present in the ranges 298K to 214K and 14K to 5K with E_a = 0.08eV and 0.06eV respectively, see Fig. 5.22.

On further doping to the x = 0.10 composition the resistivity decreases by a factor of 1000 at low temperature, see Fig. 5.23a. Furthermore, it should be noted that when plotted on the same graph, this behaviour resembles that for the x = 0.10 neodymium compound, except on different resistivity and temperature scales, see Fig.5.24. This strongly implies that the conduction mechanism in these compounds is similar. This behaviour is repeated at the higher doping levels x = 0.13 to 0.17, however with the resistivity values decreasing by another factor of 100 and a very complex temperature dependence with minima appearing at ~250K for the

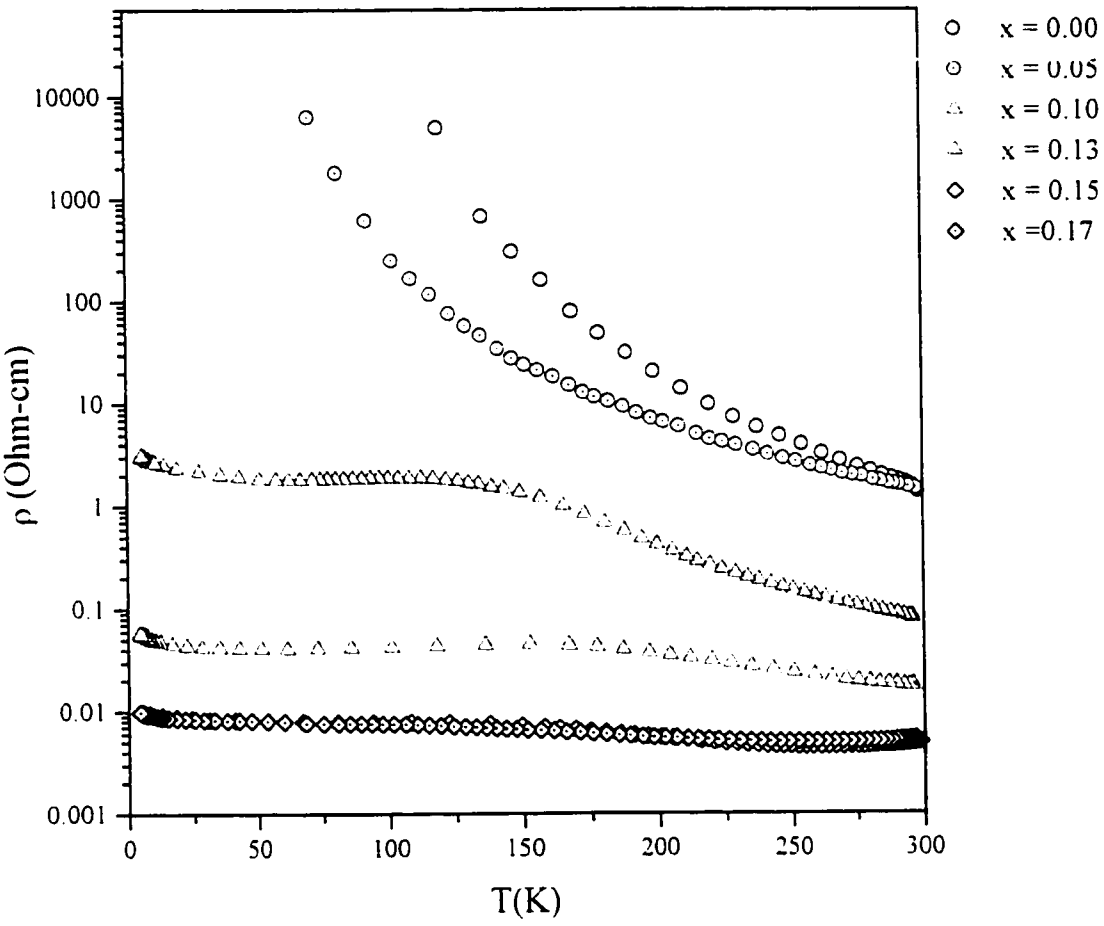

Fig. 5.20. Overall resistivity trends for the $Sm_{(1-x)}TiO_3$ system.

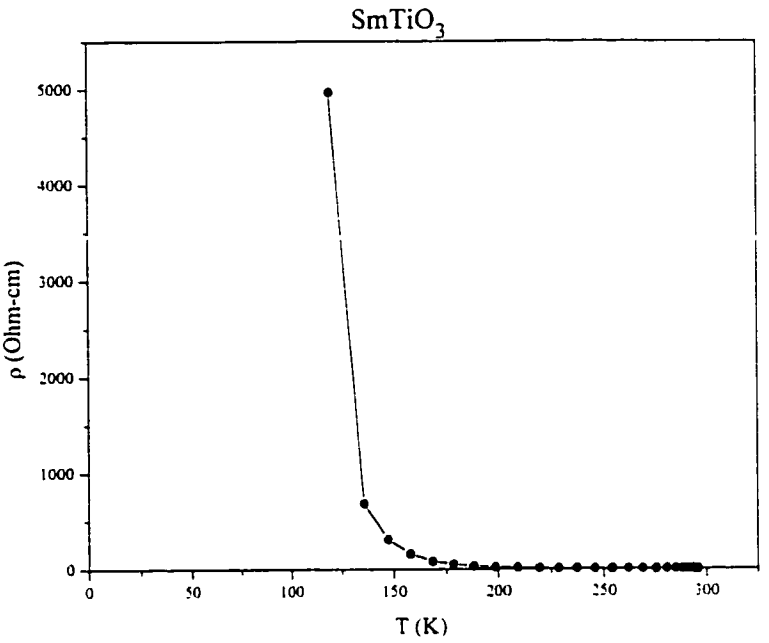

(a).

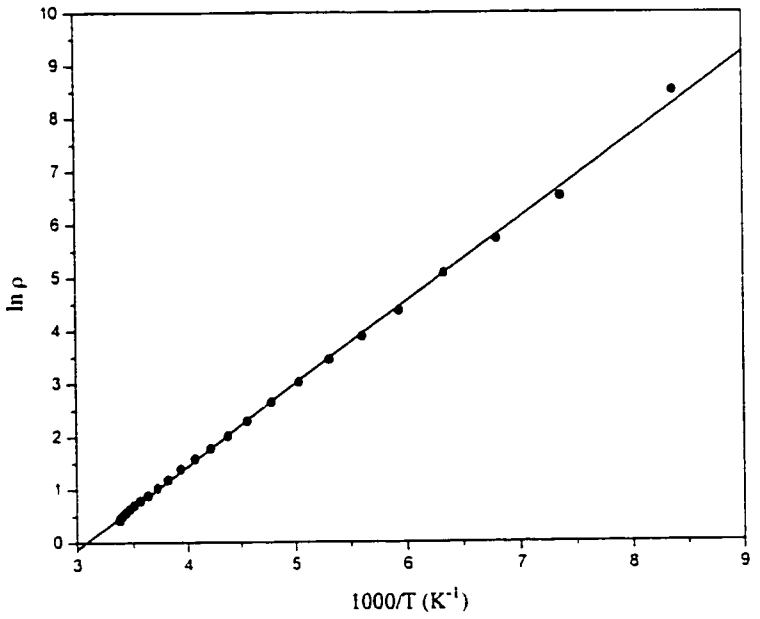

(b).

Fig. 5.21. a). ρ vs. T and b). ln ρ vs. 1000/T for $SmTiO_3$ (x=0.00)

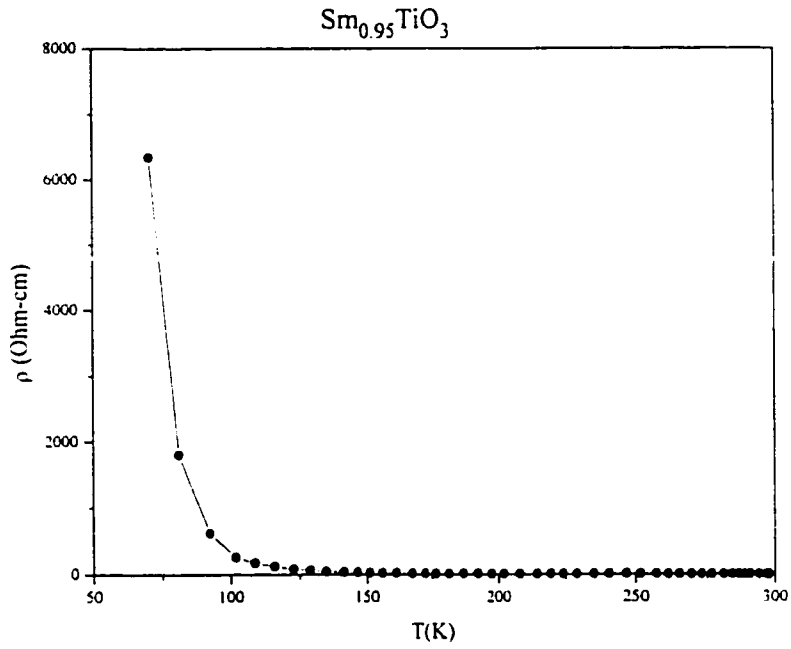

(a).

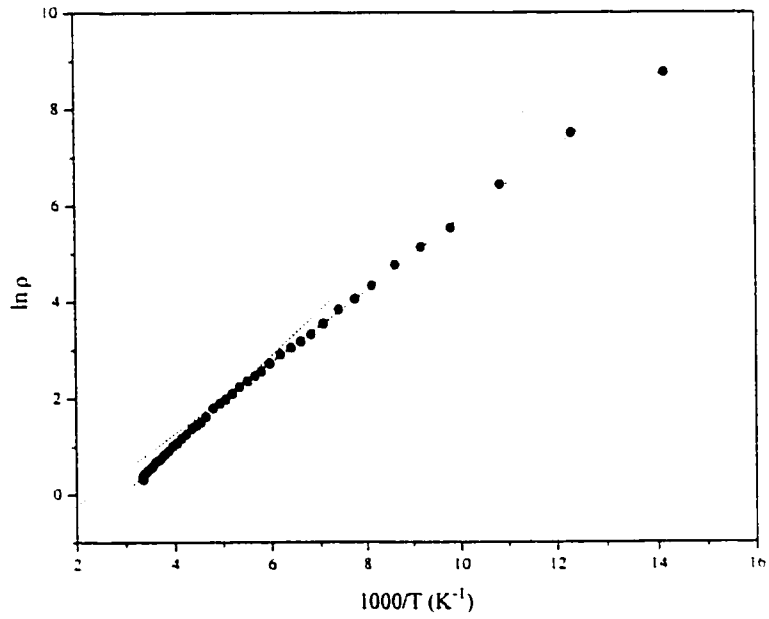

(b).

Fig. 5.22. a). ρ vs. T and b). ln ρ vs. 1000/T for $Sm_{0.95}TiO_3$ (x=0.05)

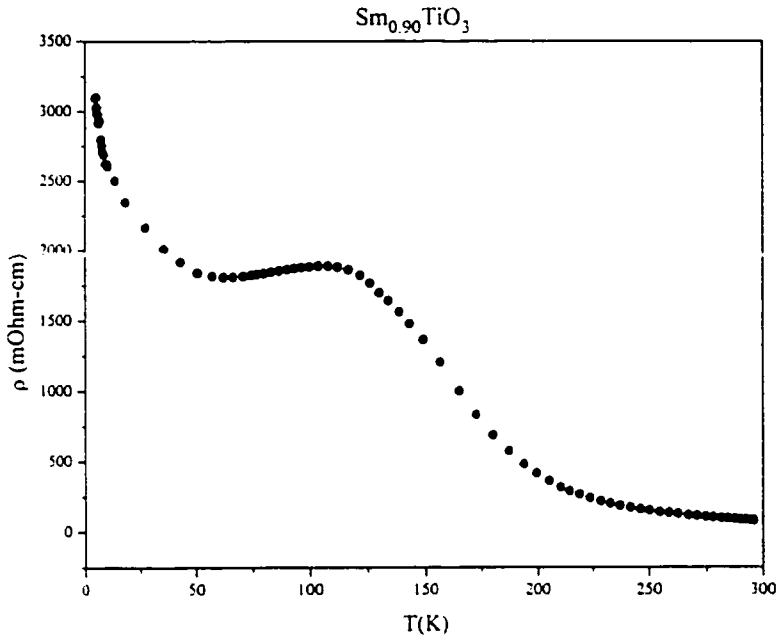

(a).

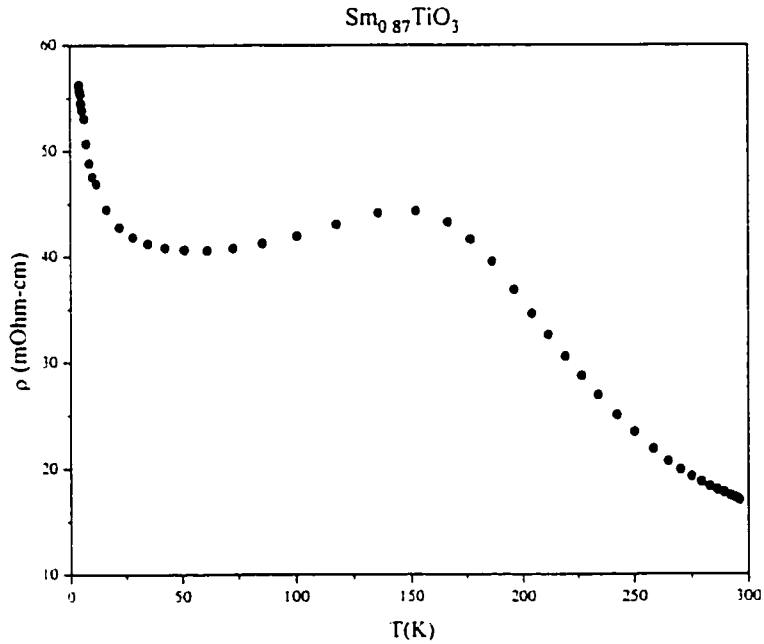

(b).

Fig. 5.23. ρ vs. T for a). $Sm_{0.90}TiO_3$ (x = 0.10) and b). $Sm_{0.87}TiO_3$ (x = 0.13)

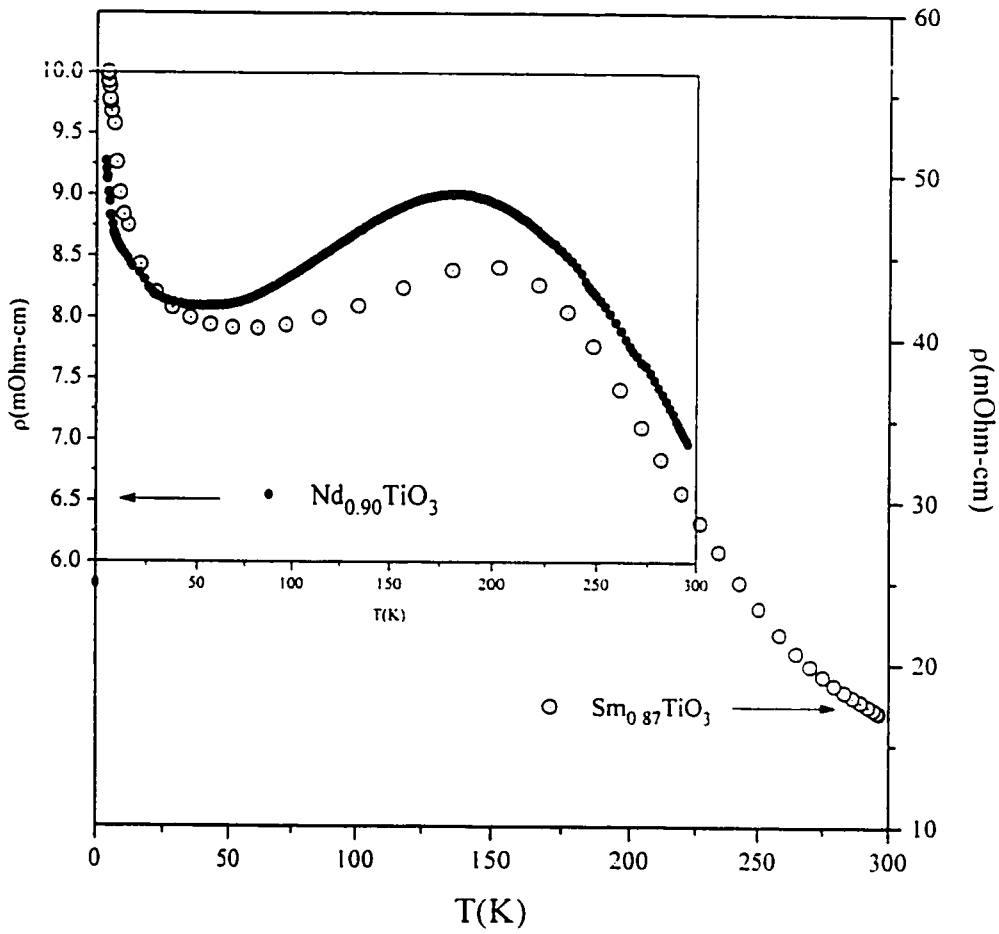

Fig. 5.24. Comparison of the ρ vs. T dependence of the $Nd_{0.90}TiO_3$ and $Sm_{0.87}TiO_3$ compounds.

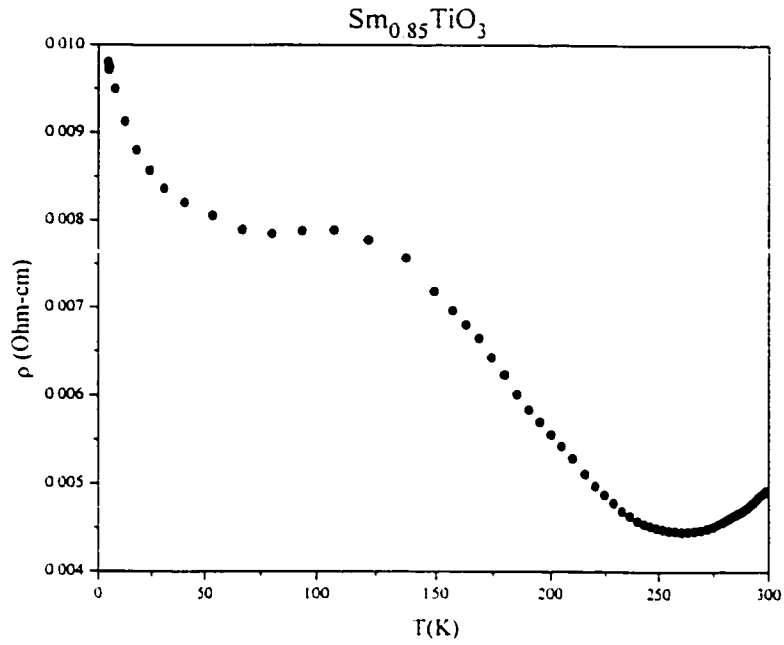

(a).

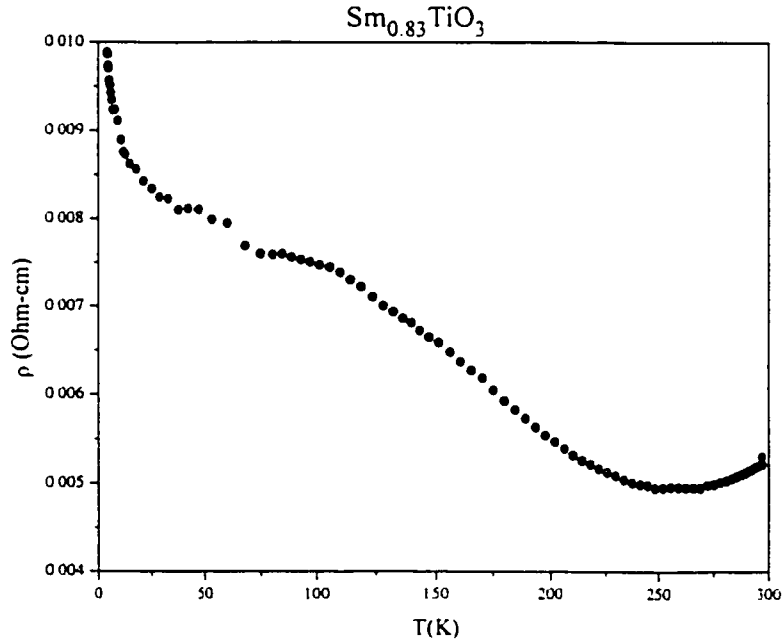

(b).

Fig. 5.25. ρ vs. T for a). $Sm_{0.85}TiO_3$ (x = 0.15) and b). $Sm_{0.83}TiO_3$ (x = 0.17)

x = 0.15 and 0.17, see Figs. 5.25 a & b. It is likely that the nearly consistent resistivity behaviour for the x = 0.10 to 0.17 samarium members is due to correlation effects which persist over a larger stoichiometric range than in the $Nd_{(1-x)}TiO_3$ system. Recall, that for the $Nd_{(1-x)}TiO_3$ system this type of resistivity behaviour is only observed for the x = 0.10 and x = 0.11 members (sample 2) but disappears by the x = 0.15 composition.

For materials such as $Nd_{0.90}TiO_3$, $Sm_{(1-x)}TiO_3$ ($0.13 \leq x \leq 0.17$), the resistivity values at or near room temperature are in the range of poor metals ~ having several mOhm-cm, see TABLE 5.2, but the temperature dependence of the resistivity in the range studied is distinctly non-Fermi liquid like in sharp contrast to the cases of $R_{(1-x)}A_xTiO_3$ and $La_{(1-x)}TiO_3$ We have extended our study of these materials to include specific heat and thermopower in an effort to characterize them in more detail and in particular to determine the degree of carrier mass enhancement present and other manifestations of electron correlation.

5.3.2. Specific Heat:

The specific heat was measured for all the more or less metallic samples and those near the M-I boundary in the temperature range of ~0.6 K to 31 K. Figs.5.26 and 5.27 show the results obtained for both series and corresponding data for the $La_{(1-x)}TiO_3$ compounds, Fig. 5.28. These measurements were carried out using the same samples prepared in the previous study (MacEachern et al., 1994). As the diagrams show, there is a distinct low temperature anomaly obtained for the $Nd_{(1-x)}TiO_3$ and $Sm_{(1-x)}TiO_3$ systems as previously anticipated (Ju et al., 1994). This anomaly is called a lambda transition which arises from the ordering of

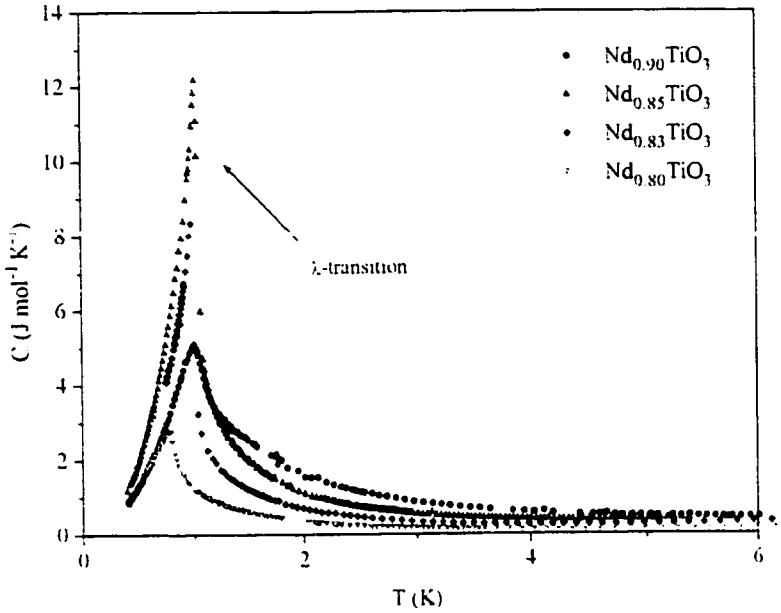

(a).

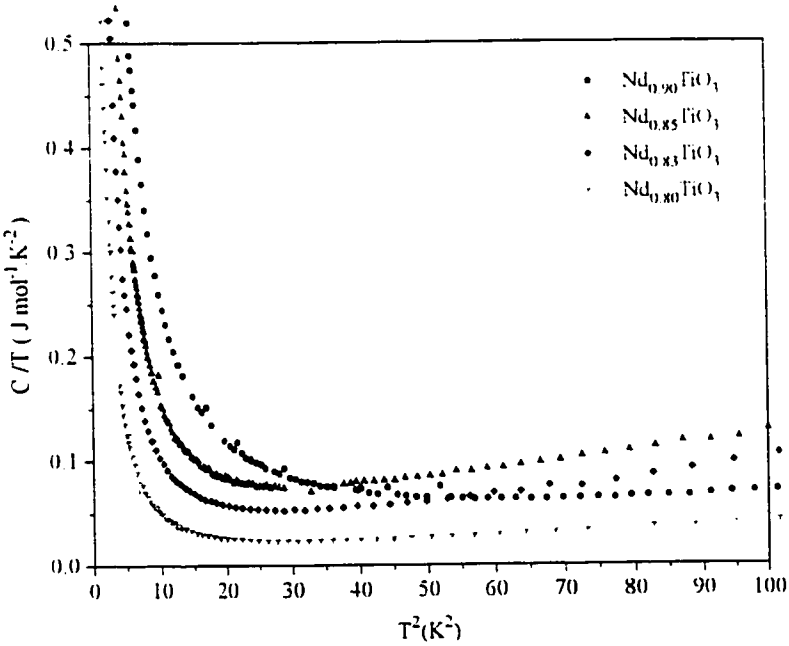

(b).

Fig. 5.26. a). C vs. T and b). C/T vs. T^2 trends in the $Nd_{(1-x)}TiO_3$ system for x = 0.10 to 0.20.

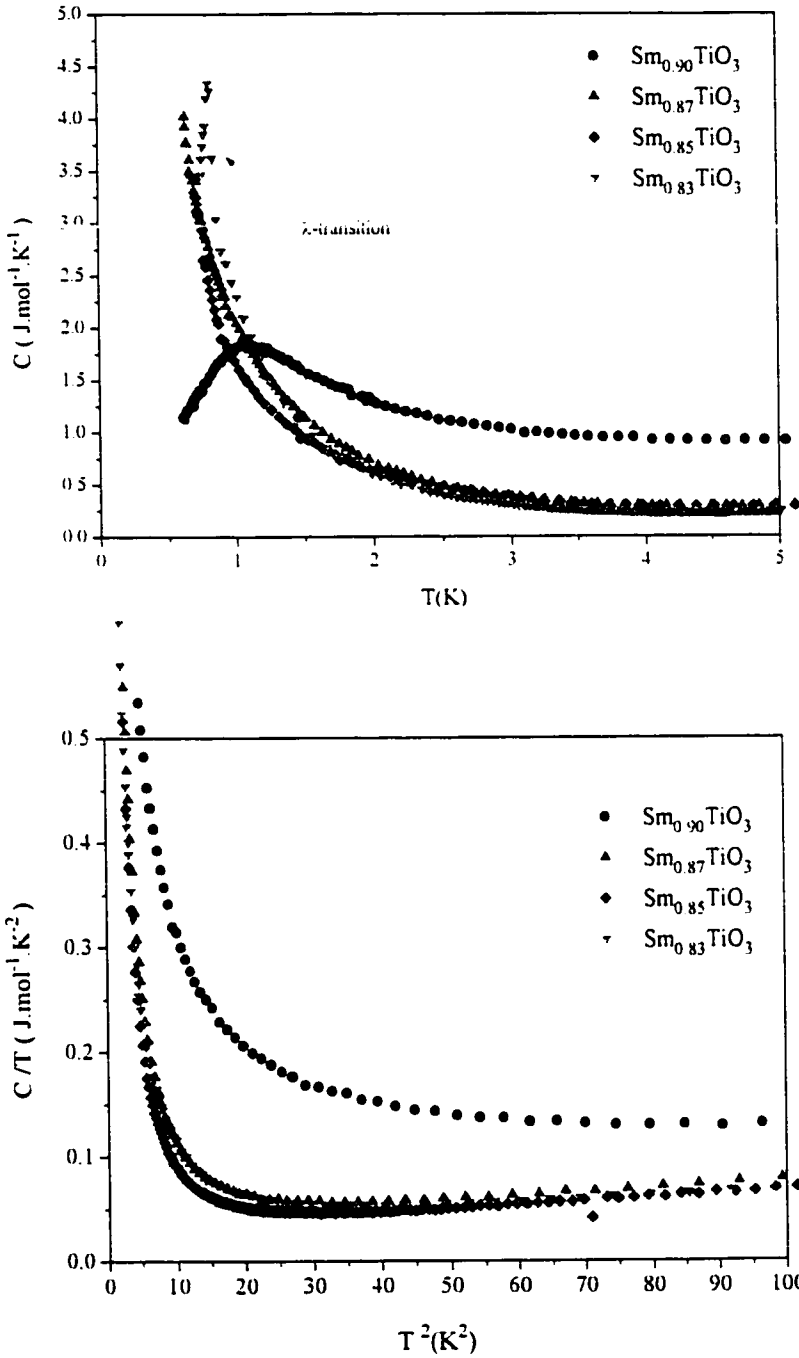

Fig. 5.27. a). C vs. T and b). C/T vs. T trends in the $Sm_{(1-x)}TiO_3$ system for x = 0.10 to 0.17.

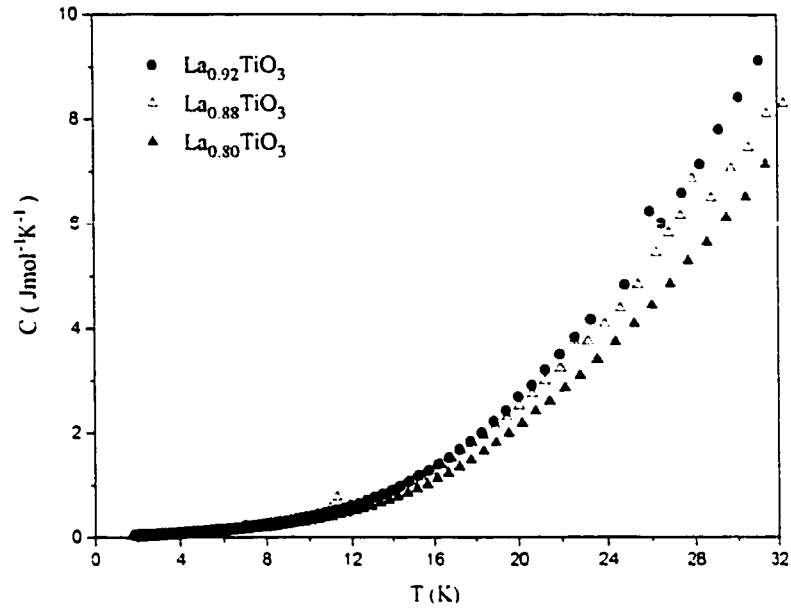

(a).

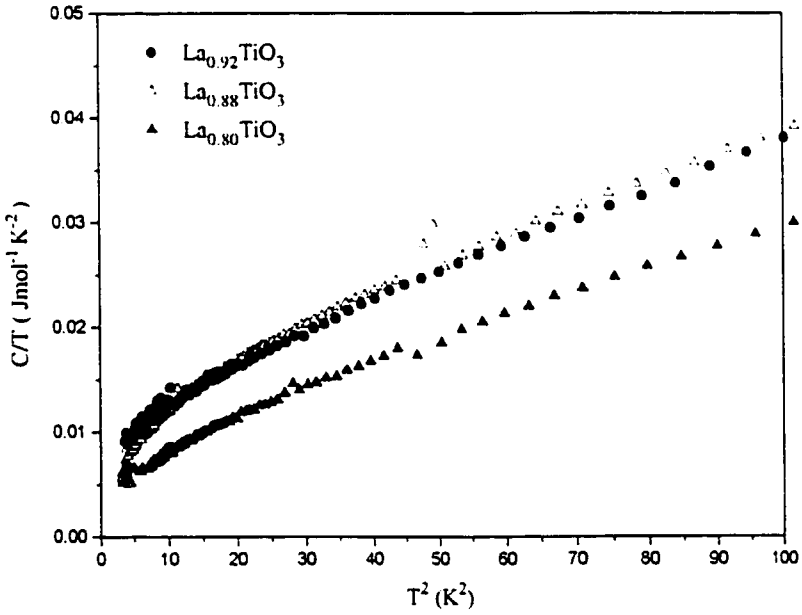

(b).

Fig. 5.28. a). C vs. T and b). C/T vs. T^2 trends in the $La_{(1-x)}TiO_3$ system for x = 0.08, 0.12 and 0.20.

the rare earth moments at these temperatures. The temperature dependence of the specific heat on the high temperature side of this anomaly is expected to follow a $1/T^2$ law. It should be noted that a similar temperature dependence is also expected for the presence of a Schottky anomaly (Gopal, 1966). However, owing to the sharpness of the peak this behaviour is ruled out.

In extracting the electronic specific heat coefficients, γ, the classical heat capacity expression for metals as given by eqn.(4) was used for the $La_{(1-x)}TiO_3$ system. However, due to the presence of the anomalies at low temperatures in the systems of interest, a linear fit of C/T versus T^2 becomes very difficult if one were to use the usual expression for the specific heat of metals. In order to account for the magnetic contributions at low temperatures the following expression was used,

$$C = \gamma T + \beta T^3 + CT^{-N} \qquad (26)$$

As there appeared to be a large variation of the curvature of the lambda anomalies, the fits were performed using the temperature range of 1.5K to 10K. In this manner, the experimentally determined values of γ, β, and the Debye temperature, θ, were obtained and are summarized in TABLE 5.4.

From a survey of the results, some trends may be observed. For the $Nd_{(1-x)}TiO_3$ system, the value of N is almost constant at a value of 2 for all compositions with the exception of $x = 0.10$ for which a value of $N = 1.61(3)$ is obtained, likely as a result of the very broad nature of the peak. A similar observation is made for the $Sm_{(1-x)}TiO_3$ system, where an almost constant value of $N = 2$ is observed for all compositions except for $x = 0.10$ which has a very broad

Table 5.4: Parameters obtained from fitting the specific heat data to $C = \gamma T + \beta T^3 + CT^{-N}$ in the temperature range 1.5K to 10K.

Compound	γ (mJ/mol.K^2)	β (mJ/mol.K^4)	θ(K)	C	N	m*
$La_{0.92}TiO_3$†	9(1)	0.300(3)	186.43	-	-	
$La_{0.88}TiO_3$†	8(1)	0.340(5)	178.82	-	-	
$La_{0.80}TiO_3$†	6(1)	0.250(3)	198.12	-	-	
$Nd_{0.90}TiO_3$	11(3)	0.4764(4)	159.80	4.84(6)	1.61(3)	8
$Nd_{0.85}TiO_3$	18(3)	1.08(4)	121.64	4.54(7)	2.09(3)	15
$Nd_{0.83}TiO_3$	8(1)	0.902(2)	129.17	2.67(3)	1.98(2)	7
$Nd_{0.80}TiO_3$	3(1)	0.360(6)	175.44	1.35(1)	1.99(2)	3
$Sm_{0.90}TiO_3$	74(3)	0.280(3)	190.77	2.13(2)	0.89(2)	56
$Sm_{0.87}TiO_3$	24(1)	0.50(2)	157.24	2.43(4)	1.92(3)	19
$Sm_{0.85}TiO_3$	19(1)	0.468(1)	160.75	1.77(2)	1.61(2)	16
$Sm_{0.83}TiO_3$	21(1)	0.479(9)	159.51	2.41(3)	2.16(2)	18

†The equation $C = \gamma T + \beta T^3$ was used.

peak resulting in N = 0.89(2). The broad nature of the x = 0.10 peaks in both systems is likely to originate from the magnetic frustration of the rare earth moments in the unit cell which resides in a body centered cavity of the TiO_6 framework. It should be recalled that some evidence of frustration had been previously found in the low temperature neutron diffraction study of $NdTiO_3$ (Amow and Greedan, 1996). This interpretation is further supported by the increased broadness of the x = 0.10 peak on going from neodymium to samarium as the rare earth-rare earth bond distance is expected to be smaller for samarium thus leading to increased frustration.

To gauge the degree of correlation in these systems, the electronic specific heat coefficients, γ, were plotted with the results of the $La_{(1-x)}TiO_3$ and $La_{(1-x)}Sr_xTiO_3$ systems with the results for the latter system obtained from a previous study (Kumagai et al., 1993), see Fig.5.29. For the $La_{(1-x)}Sr_xTiO_3$ system it is observed that γ diverges at a Ti^{3+} concentration of 95% corresponding to the M-I boundary at this composition. This divergence is also present at the M-I boundaries in the $R_{(1-x)}TiO_3$ systems. Furthermore, it is observed that the γ values progressively increase as the rare earth ion is decreased in radius from lanthanum to samarium in the $R_{(1-x)}TiO_3$ series. Remarkably, for $Sm_{0.90}TiO_3$ γ has a large value of 74(3) $mJ/mol.K^2$ which is the largest value found in any titanium based perovskite systems and approaches values obtained for so-called heavy fermion materials. To compare with heavy fermion materials, m* was calculated for each composition by comparison with the free electron model using eqn.(10). These values are also included in TABLE 5.4.

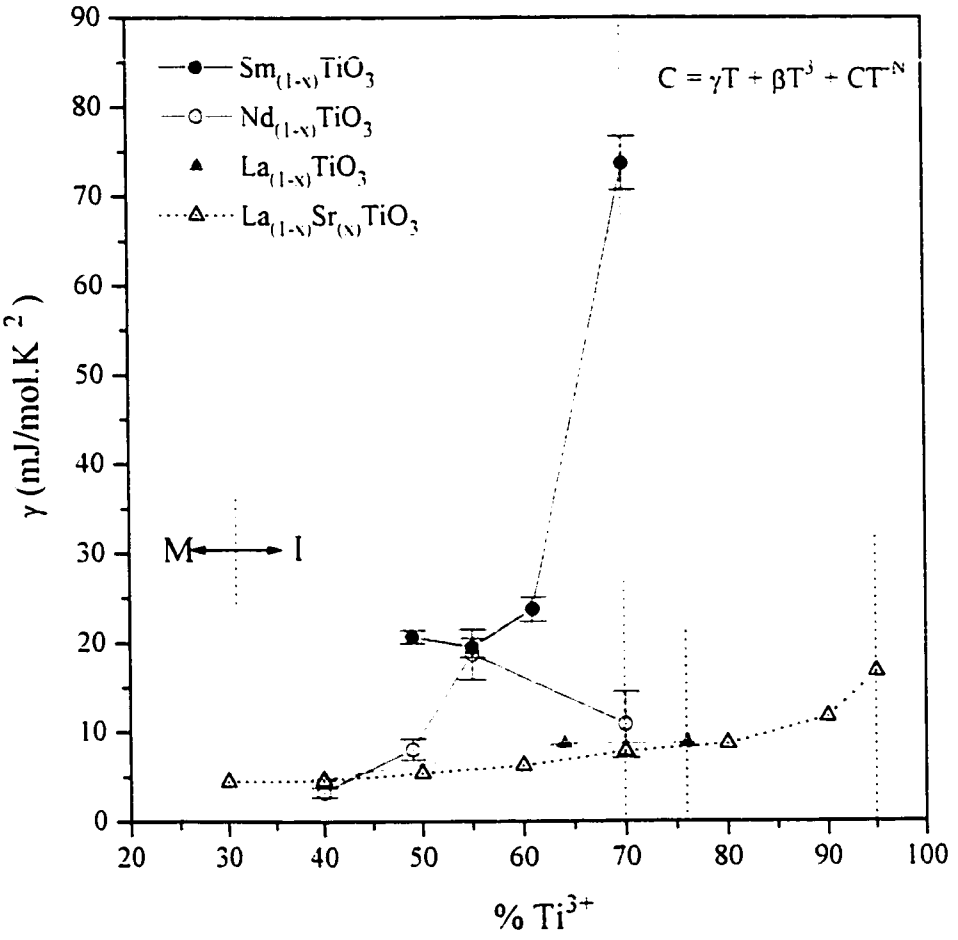

Fig. 5.29. Comparison of the electronic specific heat coefficient, γ, vs. %Ti^{3+} for the $La_{(1-x)}Sr_xTiO_3$ and $R_{(1-x)}TiO_3$ (R = La, Nd and Sm) systems. (Dashed lines represent the M-I boundary in each system shown).

5.3.3. Thermopower Measurements:

The results of the thermopower study on the members that comprise the $Nd_{(1-x)}TiO_3$ and $Sm_{(1-x)}TiO_3$ systems reveal some interesting features. For both systems, two carrier types are observed. In the more lightly doped compounds, x = 0.00 and 0.05, p-type conduction is observed, whereas n-type behaviour is observed for the more heavily doped compositions in both systems, see Figs.5.30 and 5.31. The results from this study show clearly, for the first time, the systematic change in the carrier types as one goes through the metal-insulating transition for temperatures less than 350K. Interestingly, at higher temperatures >350K there is a distinct change in the carrier types of the semiconductors from p- to n-type at least for $Nd_{0.95}TiO_3$ and $Sm_{0.95}TiO_3$ and demonstrates clearly the thermal activation of the n-type carriers as the temperature is increased. The thermopower tends to zero as the temperature is decreased which is the expected behaviour for metals. The results for each system are discussed separately below.

5.3.3.a. $Nd_{(1-x)}TiO_3$ system: For the lightly doped compositions, x = 0 and 0.05, p-type conduction is observed with a broad maximum in the thermopower at higher temperatures. Interestingly, this is unlike the behaviour predicted by Palsson et. al. (Palsson and Kotliar, 1998) where at high temperatures the thermopower obeys Heikes' law. Similar thermopower behaviour has also been observed in the $NiS_{2-x}Se_x$ system ($0.00 \leq x \leq 0.44$), a filling controlled system which has also been used to investigate M-I phenomena (Honig and Spalek, 1998). To explain this very broad maximum, it was suggested that both holes and electrons are present which take part in the transport properties. The thermopower model which accounts for the presence of

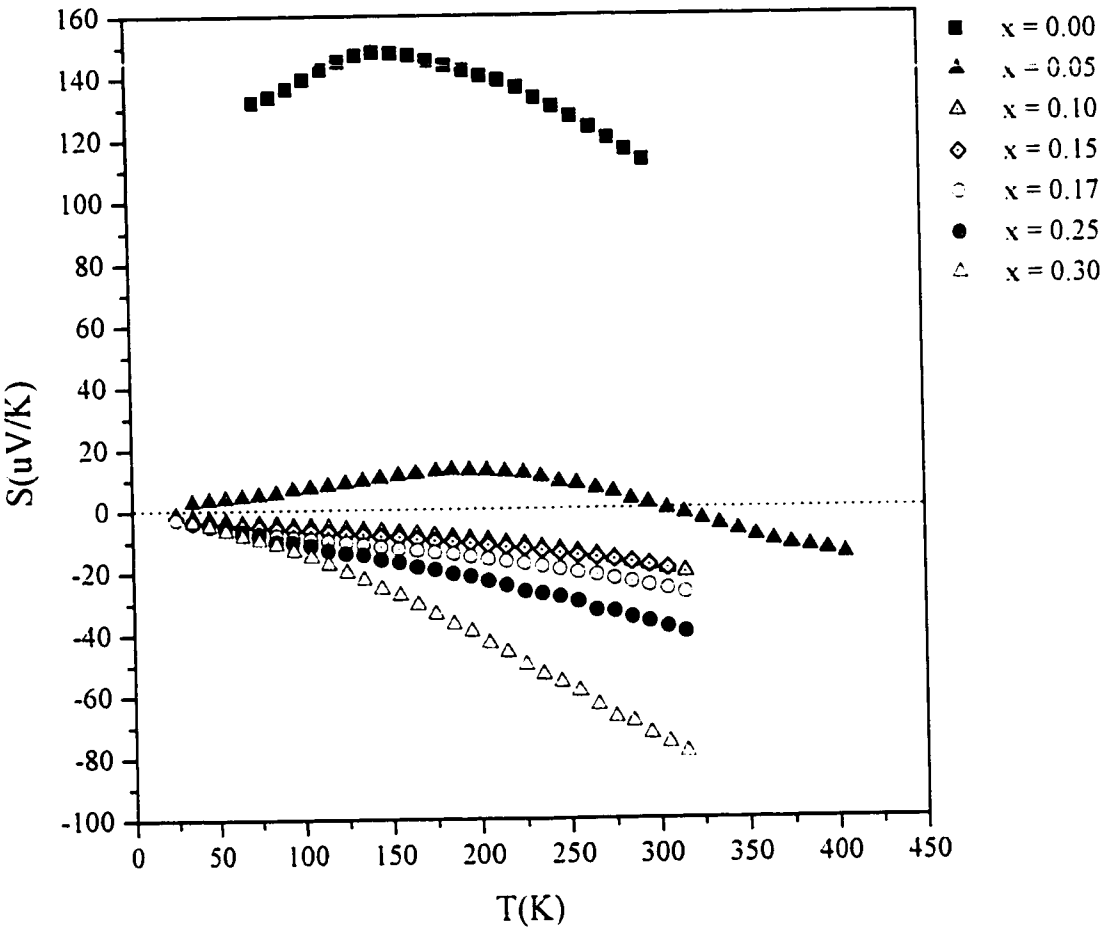

Fig. 5.30. Overall thermopower trends for the $Nd_{(1-x)}TiO_3$ system.

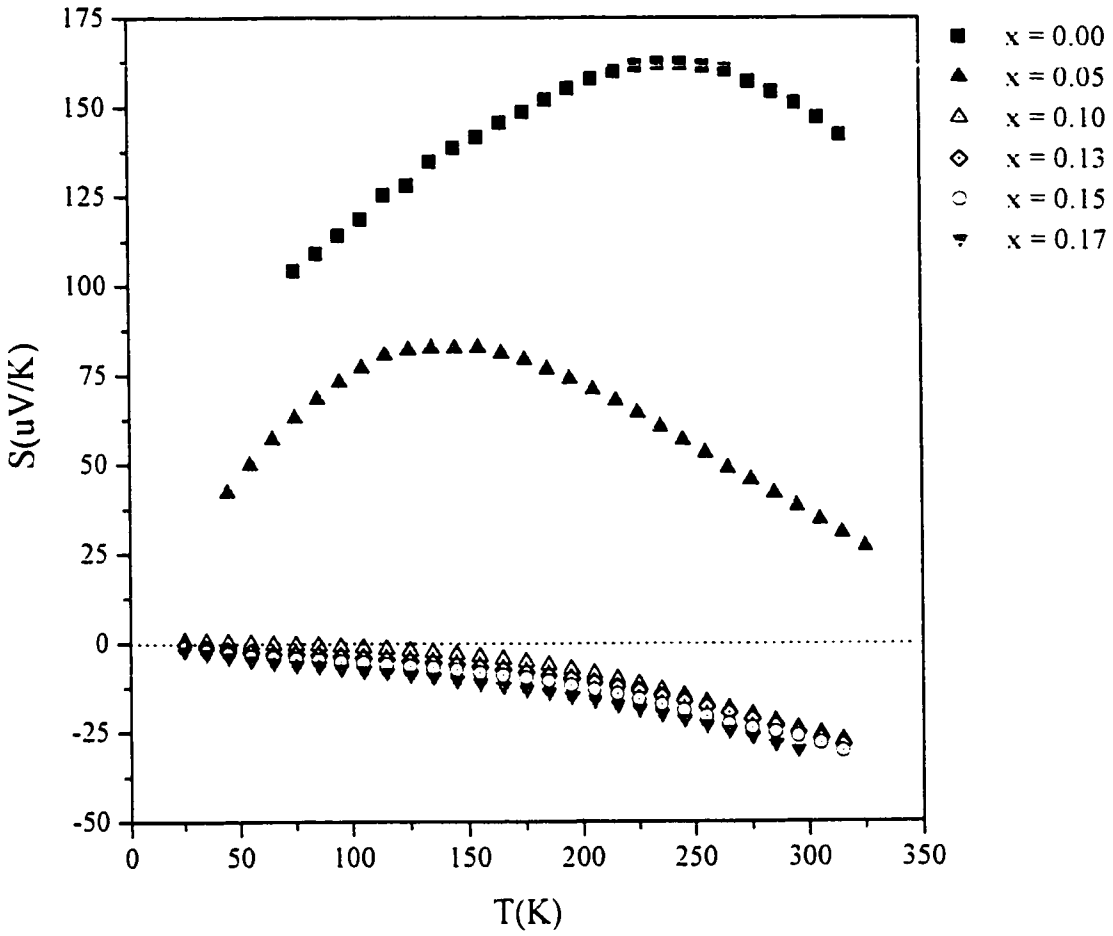

Fig. 5.31. Overall thermopower trends for the $Sm_{(1-x)}TiO_3$ system.

both carrier types has been derived to be the following (Harman and Honig, 1967),

$$S = \frac{-|S_n|\sigma_n + S_p\sigma_p}{\sigma_n + \sigma_p} \qquad (27)$$

where S is the sum of the contribution from the two carriers weighted by the contribution of each to the total conductivity, S_n and S_p are the partial Seebeck coefficients and σ_n and σ_p are the partial conductivities of electrons and holes respectively.

Using this model, it was rationalized that at low temperatures the material is an intrinsic semiconductor so that the hole and electron contributions nearly cancel out which result in small thermopower values. As the temperature is increased, kT becomes comparable to the charge transfer energy, Δ, between the S3pσ* and Ni3de$_g$* levels, so that the thermopower increases with the promotion of carriers to the relatively wider S3pσ band. This trend continues with increasing temperature until the density of the high mobility carriers increases, rendering higher conductivity and a decrease in the thermopower thus resulting in the broad maximum. It is likely that a similar situation exists in the $R_{(1-x)}TiO_3$ system (x = 0.00, and 0.05), except that the thermal excitations involve instead the Ti3d Hubbard sub-bands.

Initial measurements for the x = 0.05 composition revealed a near zero Seebeck coefficient at ~300K, strongly suggesting that a change in the carrier type might be observed at higher temperatures. Consequently, the measurement was repeated out to ~400K and this crossover is indeed observed demonstrating the thermal activation of the carriers in this compound to yield metallic-like thermopower behaviour. Further measurements at higher temperatures would

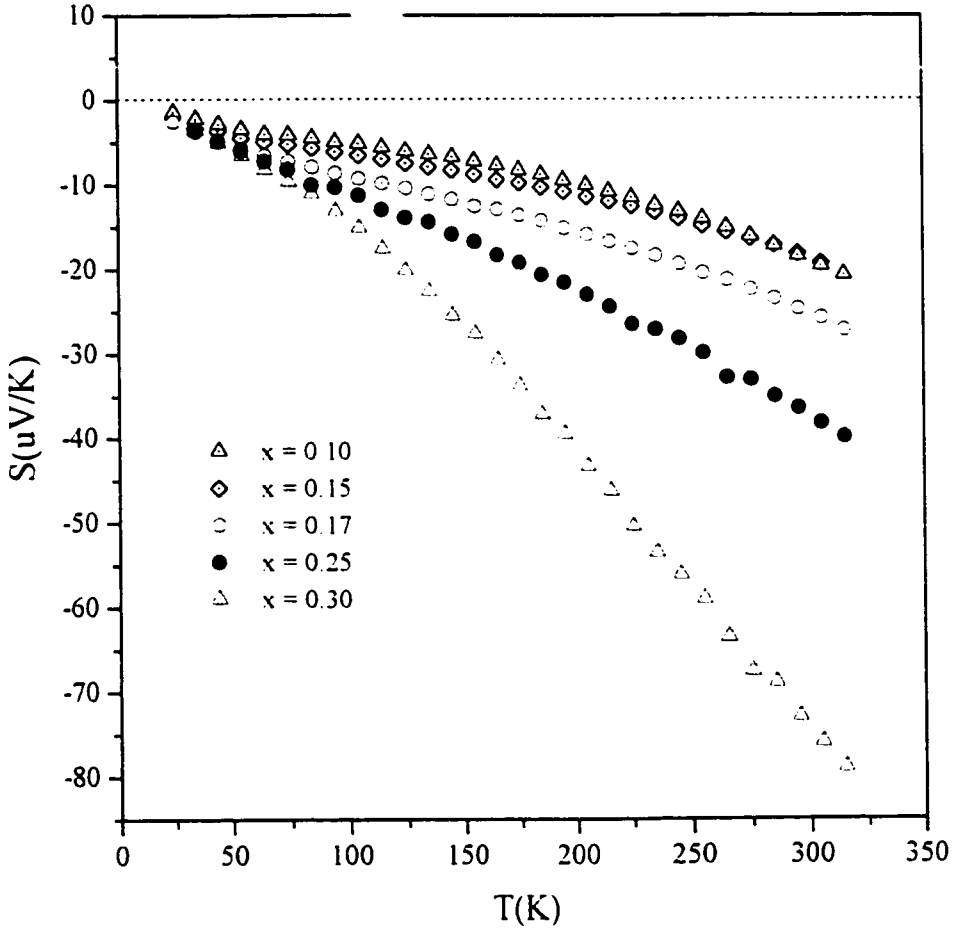

Fig. 5.32. S vs. T in the $Nd_{(1-x)}TiO_3$ system for $0.10 \leq x \leq 0.30$

be necessary to determine if and when the thermopower becomes independent of the temperature in accordance with Heikes' law.

With regard to the "metallic" compositions, $0.10 \leq x \leq 0.30$, a linear temperature dependence is observed for each composition above ~200K, Fig.5.32. Note that the thermopower behaviour of the x = 0.20 composition was not measured due to the unavailability of enough material, however it is expected that the values would lie between the data for the x = 0.17 and 0.25 compositions. This expectation is supported by the measurement of a nominal intermediate x = 0.22 composition. To demonstrate the linear temperature dependence, the linear fit of the x = 0.10 and 0.30 compositions are shown in Fig.5.33.

Invoking Mott's equation for thermopower, it was possible to demonstrate the -2/3 power dependence of *n* by plotting a log-log graph of the thermopower versus *n* at constant T. Using the thermopower values of these compositions at 285K, the value of the exponent was determined to be -0.73(6) within error of the theoretical value of 2/3, see Fig.5.34. This result leads to the conclusion that these materials behave as degenerate semiconductors or low carrier density metals with thermopowers describable by Mott's equation.

5.3.3.b. $Sm_{(1-x)}TiO_3$ system

The thermopower behaviour for all compositions prepared in this system is shown in Fig. 5.31. As pointed out earlier for the lightly doped compositions, x =0 and 0.05, p-type conduction is observed, whereas for the remaining samples, n-type conduction is observed in accordance with the barely metallic nature of these compositions. For clarity, the thermopower

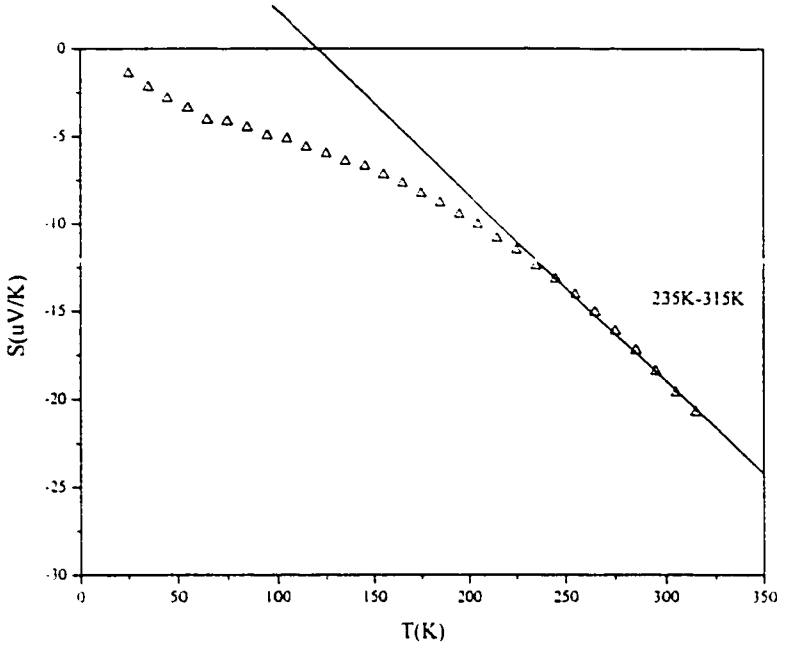

(a).

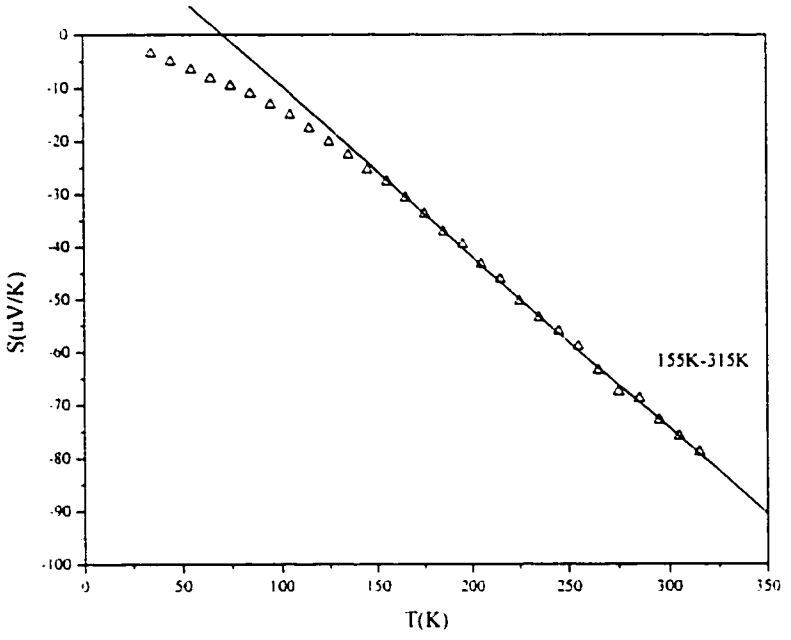

(b).

Fig. 5.33. Linear dependence of S vs. T for a). $Nd_{0.90}TiO_3$ and b). $Nd_{0.70}TiO_3$.

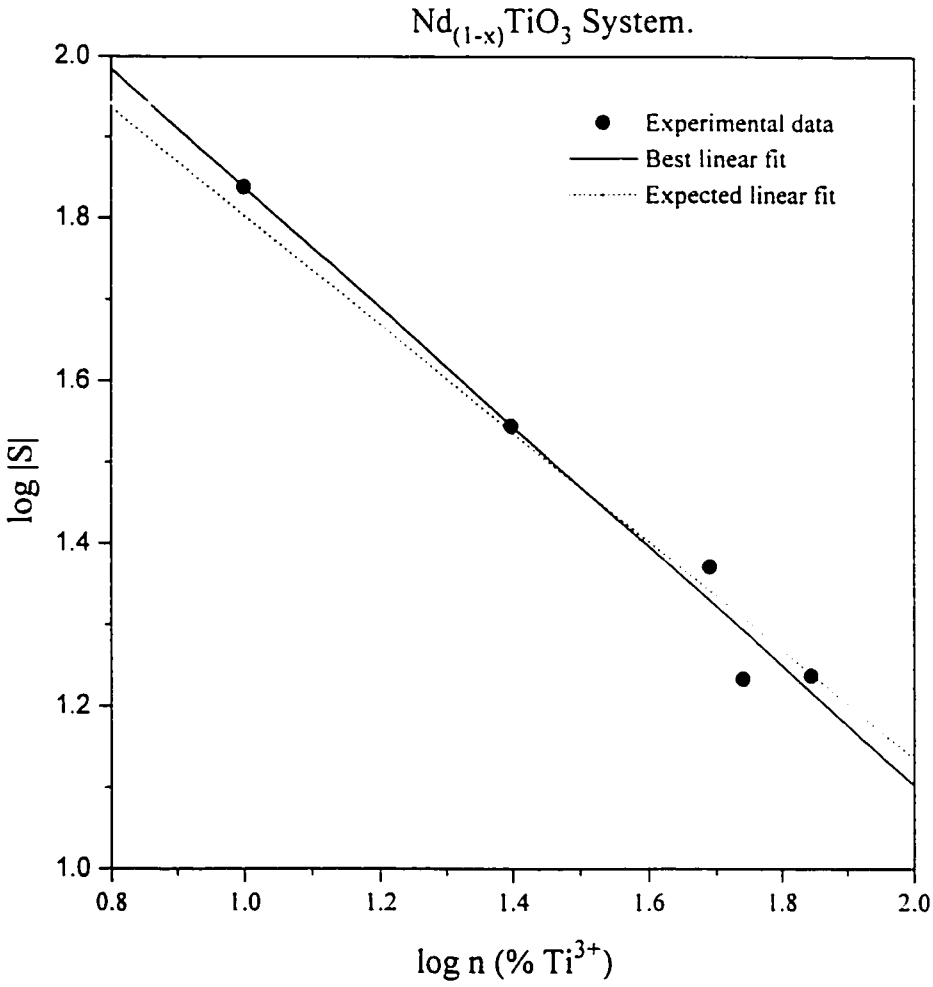

Fig. 5.34. log |S| vs. log n(%Ti^{3+}) for data at 285K. The dashed line represents the ideal -2/3 slope.

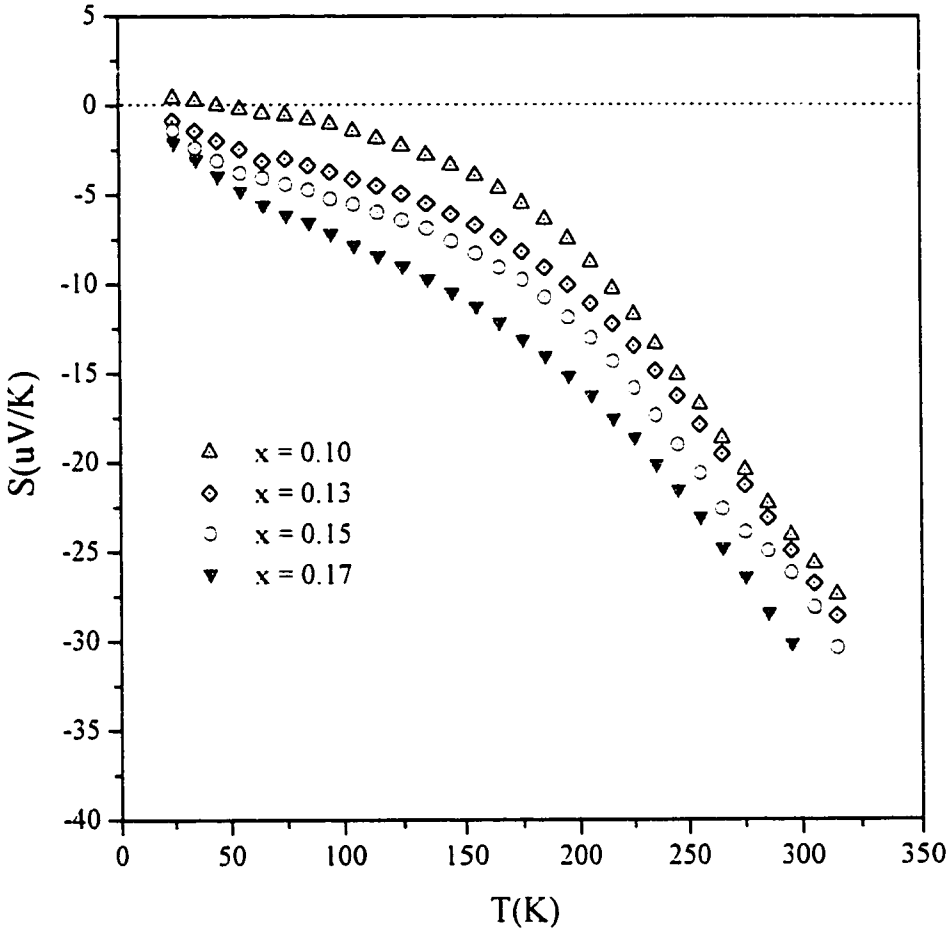

Fig. 5.35. S vs. T in the $Sm_{(1-x)}TiO_3$ system for $0.10 \leq x \leq 0.17$

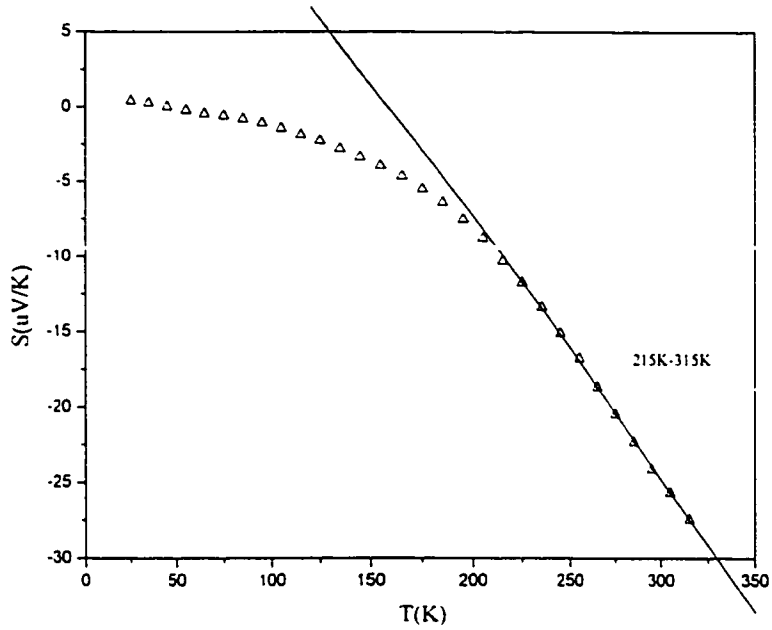

(a).

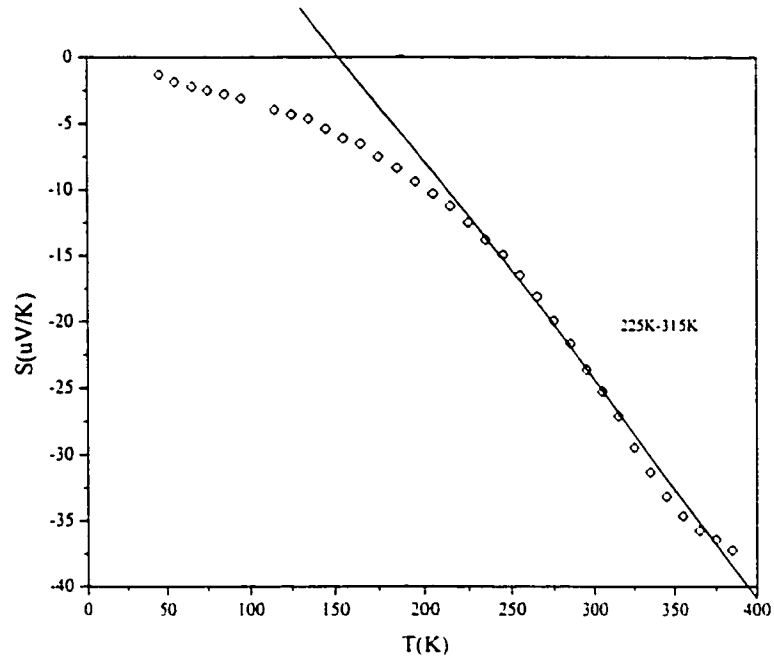

(b).

Fig. 5.36. Linear dependence of S vs. T for
a). $Sm_{0.90}TiO_3$ and b). $Sm_{0.87}TiO_3$.

behaviour of these samples are plotted in Fig. 5.35. As found in the $Nd_{(1-x)}TiO_3$ system a linear dependence of the thermopower is observed however over a narrower range, Fig. 5.36. A similar analysis was performed using Mott's law for thermopower. By plotting the log |S| vs. log|*n*| at 285K, the power dependence of the carrier density was determined to be -0.67(15) in very good agreement with the theoretical value of *-2/3*, see Fig. 5.37, thus leading to the same conclusions made previously for the $Nd_{(1-x)}TiO_3$ system.

Finally, it should be mentioned that the thermopower measurements of the "metallic" compositions also reflect the increasing correlations as one goes from the $La_{(1-x)}Sr_xTiO_3$ to the $Nd_{(1-x)}TiO_3$ and $Sm_{(1-x)}TiO_3$ systems. This can be observed using eqn. (16). by comparing the slopes of the linear portions of the S vs. T graphs. Since the slope scales linearly with m*, it is expected that with increasing correlations the slope should become larger. In order to make a meaningful comparison, compositions having similar carrier densities must be considered. Consequently, since $La_{0.5}Sr_{0.5}TiO_3$ (n = 50% Ti^{3+}) has a comparable carrier density to the x = 0.83 (n = 49% Ti^{3+}) compositions in our study we use these for the comparison. In doing so we find increasing slopes of -0.06, -0.11, and -0.17 $\mu V/K^2$ for $La_{0.5}Sr_{0.5}TiO_3$, $Nd_{0.83}TiO_3$ and $Sm_{0.83}TiO_3$ respectively lending further support to the contention that correlation effects become more pronounced on going from the $La_{(1-x)}Sr_xTiO_3$ system to the $Nd_{(1-x)}TiO_3$ and $Sm_{(1-x)}TiO_3$ systems.

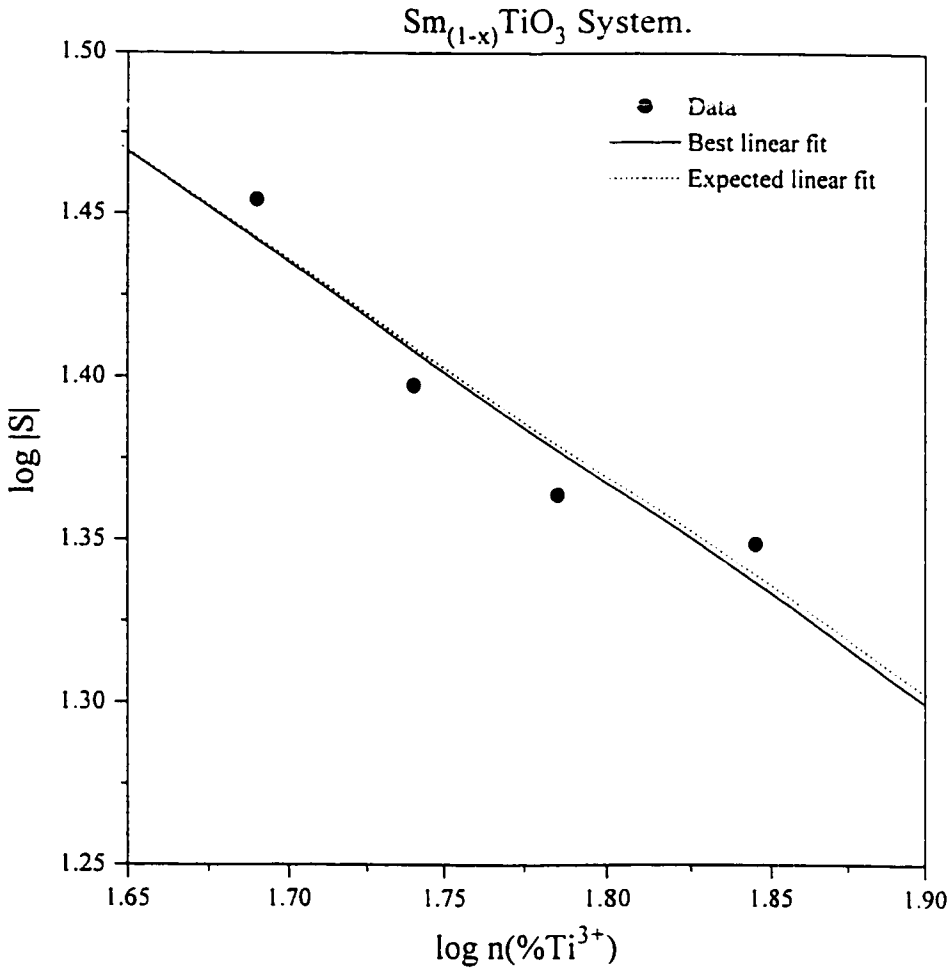

Fig. 5.37. log|S| vs. log n(%Ti^{3+}) for data at 285K. The dashed line represents the ideal -2/3 slope.

CHAPTER 6

CONCLUSIONS AND FUTURE WORK

Various nominal compositions of the vacancy doped $R_{(1-x)}TiO_3$ (R = Nd, Sm) systems have been prepared for the purpose of investigating their structural and physical properties in the context of metal-insulator transitions. It has been determined that the solid solution exists for $0.00 \leq x \leq 0.33$ for the $Nd_{(1-x)}TiO_3$ system while for the $Sm_{(1-x)}TiO_3$ system, a more limited range of $0.00 \leq x \leq 0.17$ has been established. The smaller range observed for the $Sm_{(1-x)}TiO_3$ system likely arises from the inability of the perovskite framework to accommodate the decreasing concentrations of the smaller samarium ion.

These systems have been chosen primarily for the study of M-I transitions as they allow control of the conduction bandwidth, W, as well as the degree of the band filling level by introducing vacancies at the rare earth sites. At least three structural types have been identified in the $Nd_{(1-x)}TiO_3$ system. These are *Pnma* for $0.00 \leq x \leq 0.17$, *Pban* for $0.25 \leq x \leq 0.30$ and an apparently new perovskite structure, described in P4/mmm, for $x = 0.33$. The structural determination of the $x = 0.20$ composition was not conclusive in this study and needs to be re-examined at a later date. With regard to the $Sm_{(1-x)}TiO_3$ system a more limited stoichiometry for the solid solution was determined for $0.00 \leq x \leq 0.17$ with only the *Pnma* structure type identified.

Based on the results from the magnetic susceptibility and transport measurements, the electronic phase diagram for the $R_{(1-x)}TiO_3$ (R=La, Nd, Sm) has been constructed, see Fig.

6.1. The phase diagrams show that two M-I transitions have been identified for the $Nd_{(1-x)}TiO_3$ system, a Mott transition at x = 0.10 and another, possibly due to Anderson localization, at x ~0.25. Only the Mott transition at x = 0.10 for the $Sm_{(1-x)}TiO_3$ system has been determined and preparations of higher doped compositions would be required to determine if another transition exists due to the increased disorder.

With regard to magnetic properties, Mott insulators are found for the x = 0.00 and 0.05 compositions in both systems, which exhibit canted antiferromagnetism generally below 100K. The Neel temperatures appear to be dependent on the nature of the rare earth ion as well as the level of vacancy doping as they tend to decrease on going from R = La to Sm and with higher doping levels. The magnetic structures of the antiferromagnetic $Nd_{(1-x)}TiO_3$ compositions have been investigated with low temperature neutron powder diffraction. In the case of the nominal $SmTiO_3$ composition, short wavelength neutron diffraction using single crystals has been employed and represents the first definitive study of any of the rare earth titanate magnetic structures.

At the x = 0.10 compositions in both systems, the AF order disappears giving way to paramagnetic behaviour. Due to strong crystal field effects, a subtle deviation from the Curie Weiss law is observed, and thus, the enhanced Pauli susceptibility term could not be determined reliably. The situation becomes worse in the $Sm_{(1-x)}TiO_3$ solid solution due to the low lying energy states of Sm(III).

Furthermore, from Fig. 6.1, it is observed that the metallic regime becomes progressively smaller as one goes from R = La to Sm. On the parent titanate side, the doping level required

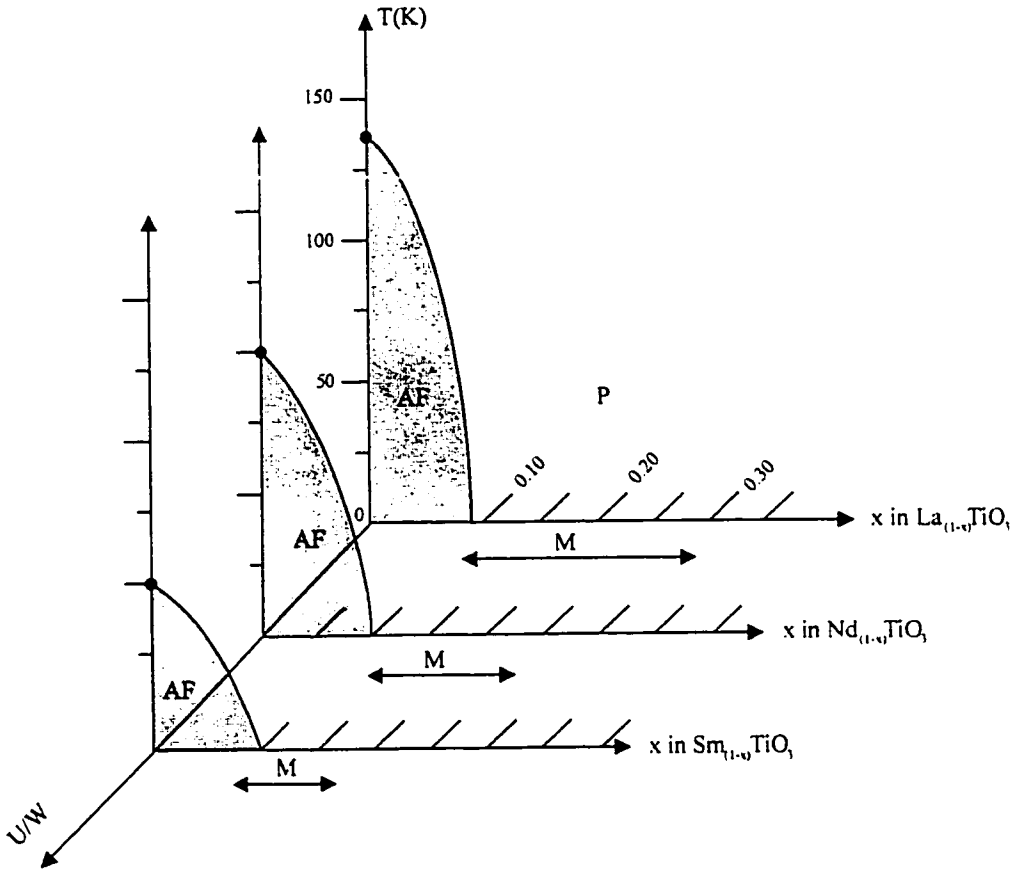

Fig. 6.1. The electronic and magnetic phase diagram for the $R_{(1-x)}TiO_3$ (R = La, Nd, Sm) systems.

for the Mott transition increases as one goes from R = La to Nd. A similar trend has been found in a study on the $R_{(1-x)}Ca_xTiO_3$ system where it was shown that an almost linear dependence of the critical vacancy doping concentration with the rare earth ion exists (Katsufuji et. al., 1997). When compared to the prototypical $La_{(1-x)}Sr_xTiO_3$ and various other $R_{(1-x)}A_xTiO_3$ systems, it becomes obvious that the doping level required for the M-I transition is higher for the vacancy doped systems, see Fig. 6.2. Furthermore, the narrowing of the metallic regime is also influenced by the increasing disorder in the systems.

Through four probe resistivity measurements it was evident that the disappearance of the antiferromagnetic insulating behaviour, coincides with the onset of paramagnetic behaviour at the x = 0.10 compositions in both systems. For the $Sm_{0.90}TiO_3$ phase, it is not obvious that this is a true Mott M-I transition due to the very large resistivity values observed. Thus, the transition may be closer to the $Sm_{0.87}TiO_3$ phase, see Fig. 6.2. It should however be remembered that the $Sm_{0.90}TiO_3$ composition also exhibits a small, electronic like thermopower suggestive of metallic behaviour, and in doing so presents a very interesting paradox.

Despite this, the $R_{(1-x)}TiO_3$ compounds (x = 0.10) near the Mott M-I transition exhibit similar transport properties. The x = 0.10 composition in the $Nd_{(1-x)}TiO_3$ system as well as the $0.10 \leq x \leq 0.17$ samarium compositions appear to exhibit heavy fermion like behaviour which maybe possibly associated with a Kondo lattice. These compounds are poor metals due to their large resistivity values and are highly correlated as evidenced by their unusual resistivity behaviour particularly near the Mott M-I transition.

Furthermore, Fermi liquid behaviour is observed in the $Nd_{(1-x)}TiO_3$ system for the x

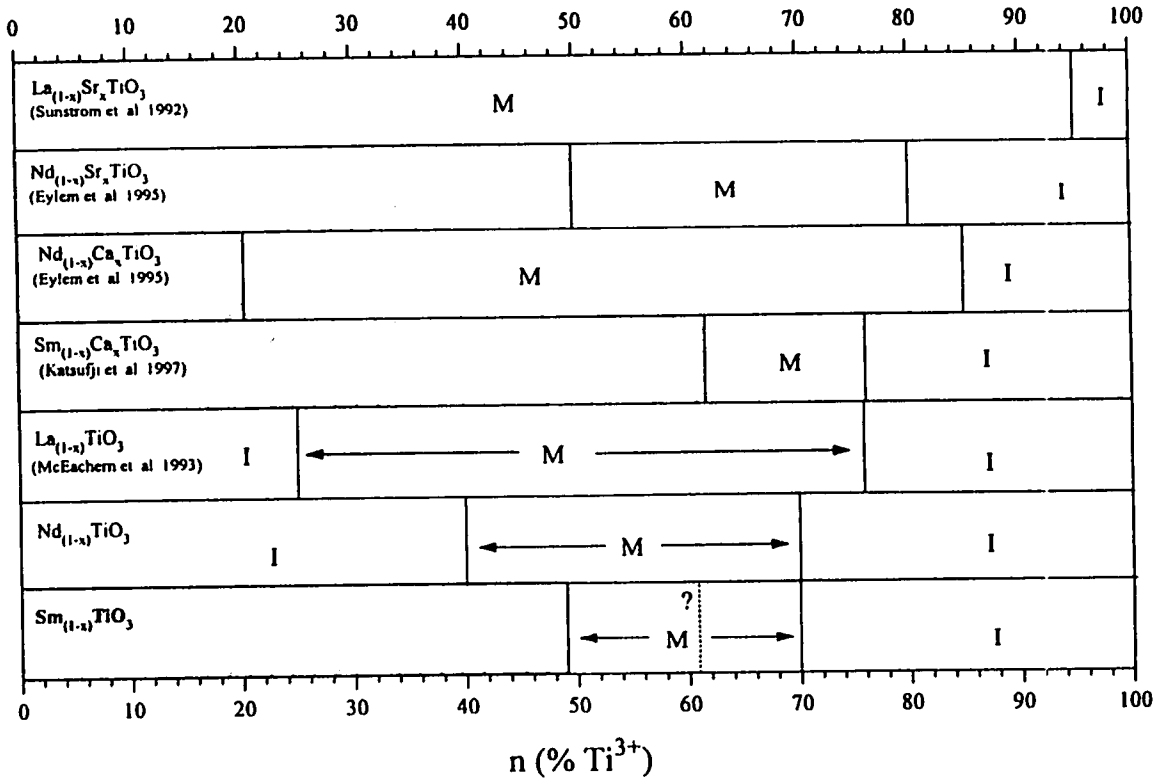

Fig. 6.2. Phase diagram illustrating the M-I boundaries for various $R_{(1-x)}A_xTiO_3$ system and the results from the present study. The shaded regions indicate compositions which have not been investigated. The dashed line for the $Sm_{(1-x)}TiO_3$ system may possibly represent the real Mott M-I transition.

= 0.15 and 0.17 phases. In conjunction with the specific heat measurements and the constant A extracted in Chapter 5, Section 5.3.1.a., the A/γ^2 ratio for these phases were calculated and compared to the Kadowki-Wood relation for heavy fermion materials. Interestingly, although γ is an order of magnitude less than heavy fermion materials, the ratio A/γ^2 is found to be in fair agreement with values of $\sim 1.7\times10^{-5}$ and $\sim4\times10^{-5}$ μ-cm(mol.K/mJ)^2 for x = 0.15 and x = 0.17 respectively. The less favourable agreement determined for x = 0.17 suggest that electron correlations become less important as one moves away from the M-I boundary. In the other extreme, disorder becomes increasingly important for the higher doped compositions, x = 0.25 and 0.30, as some evidence for variable range hopping is observed. However, it was shown that this case could not be distinguished unambiguously from a situation in which both correlation and disorder may coexist.

Further insights into the transport properties of the "metallic"phases were obtained by specific heat and thermopower measurements. As previously shown in Chapter 5, both methods give direct information regarding the extent of correlation in these systems, as γ and S scale proportionally to m*. A divergent enhancement of the carrier mass in both $R_{(1-x)}TiO_3$ (R = Nd, Sm) system is observed as the Mott M-I transition is approached. The results from this study parallel those trends observed in the $La_{(1-x)}Sr_xTiO_3$ and $Nd_{(1-x)}Ca_xTiO_3$ systems, thus indicating the importance of the enhanced carrier mass in driving the M-I transition, in agreement with the Brinkman-Rice model. Based on the values of the specific heat coefficient and the calculated effective masses, it is obvious that the vacancy doped titanates are more strongly correlated than the alkali earth doped systems.

Thermopower measurements reveal a transition from p-type carriers in the lighter doped samples, x = 0.00 and 0.05, to n-type behaviour for the "metallic" $x \geq 0.10$ compositions in both systems. This is the first study that clearly illustrates a transition of the carrier types as a function of doping for the titanates. From a thermopower standpoint, the "metallic" compositions in both systems, i.e. $x \geq 0.10$ have been interpreted to be as degenerate semiconductors or low carrier density metals.

The results presented in this study all indicate that the $Nd_{(1-x)}TiO_3$ and $Sm_{(1-x)}TiO_3$ systems exhibit the effects of correlation effects to a greater extent than any other titanate system investigated to date. Interestingly, the observed M-I transitions do not correspond with a discontinuous change in the cell volume as anticipated by Goodenough (Goodenough and Zhou, 1998) who argued, using the virial theorem, that M-I transitions of the kind investigated here should undergo a discontinuous change in the cell volume which may not necessarily be associated with a change in structural symmetry. It is speculated that the severe disorder in these systems may be the reason for this conundrum.

Future Work: As we have seen throughout this work, the $Nd_{(1-x)}TiO_3$ and $Sm_{(1-x)}TiO_3$ solid solutions are very interesting systems from both structural and physical property points of view. Consequently, they are excellent candidates for further avenues of research. Specifically, the $Sm_{(1-x)}TiO_3$ compounds still remain to be structurally characterized. This may be accomplished through a variety of techniques such as x-ray powder diffraction, short wavelength neutron powder diffraction, single crystal diffraction or the preparation of isotopic samarium phases which may subsequently be characterized by neutron diffraction using conventional wavelengths.

Furthermore, it also remains to be determined whether higher doped compositions, $x > 0.17$, can be prepared via alternative routes.

From the physical properties aspect, optical methods such as photoelectron, reflectance and Raman spectroscopy can be utilized to gain insight into the electronic structures of these compounds. Particularly, these methods would be very useful in revealing the evolution of the electronic structure as it goes through the Mott transition. Based on the results from optical measurements on the $La_{(1-x)}Sr_xTiO_3$ system, a transfer of spectral weight from the coherent (itinerant) to incoherent (localized) states should be observed near the Mott M-I transition, in accordance with the Brinkman-Rice model. Recently, investigations by reflectance spectroscopy have already begun, at least for the nominal $SmTiO_3$ compound prepared in this study (Hildebrand et. al., 1999).

It would also be of interest to perform resistivity and thermopower measurements above room temperature in light of the very unusual resistivity behaviour of the $Sm_{(1-x)}TiO_3$ $0.10 \leq x \leq 0.17$ compositions observed near room temperature. Furthermore, Hall measurements would be particularly useful for the determination of the carrier densities of these compounds. In conjunction with the thermopower measurements, this can be another route in obtaining a quantitative measure of the effective mass in these systems.

APPENDIX I

The following paper highlights the structural determination of the layered perovskite, $K_2Nd_2Ti_3O_{10}$, which was grown by the flux method.

Acta Cryst. (1998). C54, 1053–1055

The Layered Perovskite $K_2Nd_2Ti_3O_{10}$

GISELE AMOW AND J. E. GREEDAN

Department of Chemistry, McMaster University, 1280 Main St West, Hamilton, Ontario, Canada L8S 4K1. E-mail: greedan@mcmail.cis.mcmaster.ca

(Received 31 July 1997; accepted 3 February 1998)

Abstract

Single crystals of dipotassium dineodymium trititanium decaoxide, $K_2Nd_2Ti_3O_{10}$, have been obtained by the flux growth method. The structure is of the Ruddlesden–Popper type and can be described as being composed of blocks of triple perovskite layers separated by rock salt layers.

Comment

In general, there has been interest in members of the $A_2Ln_2Ti_3O_{10}$ series of compounds, where A = Na, K or Rb and Ln = rare earth ion. These compounds are known to exhibit ion exchange and intercalation reactions. In addition, they readily undergo protonation on treatment with dilute acids, making them potentially useful in catalysis and electrochemistry (Richard *et al.*, 1994; Gondrand & Joubert, 1987; Gopalakrishan & Bhat, 1987).

To date, members of this series have only been isolated in the polycrystalline phase, with principal structural determinations carried out by the use of X-ray powder diffraction. Notably, for the case where A = K and Ln = Nd, only the cell constants and space group have been reported (Richard *et al.*, 1994). In this paper, we report the preparation of single crystals of $K_2Nd_2Ti_3O_{10}$, and its structural determination by single-crystal X-ray diffraction.

The structure is described as *I4/mmm*, and the cell parameters obtained are in agreement with those reported for the polycrystalline phase (Richard *et al.*, 1994). It is related to the Ruddlesden–Popper phases $A_4Ti_3O_{10}$ (A = Sr, Ca), in that it is composed of triple blocks of corner-shared perovskite layers intergrown with individual rock salt layers (Ruddlesden & Popper, 1958) (Fig. 1). There are two very interesting structural features present in $K_2Nd_2Ti_3O_{10}$. First, we observe in Fig. 1 a marked anisotropy in the displacement parameters of all the O atoms. For O1 and O3, the ellipsoid principal axes are parallel to the c axis, while for O2, in particular, and O4, it lies in the ab plane. In addition, the O1 site exhibits strong disorder. Initially, O1 was assigned to the 4*c* site, but an extremely high isotropic displacement parameter resulted. Consequently, this site was split by moving to the 8*j* position. These features can be explained by noting that these atoms coordinate the Nd^{3+} ion, which is much smaller than the ions, such as Sr^{2+}, which normally occupy the perovskite A-site in the Ruddlesden–Popper phases. In perovskite materials such as $NdTiO_3$, the Ti–O octahedra exhibit a coherent cooperative tilting to accommodate the smaller Nd^{3+} ion, lowering the symmetry from *Pm3m* to *Pnma* (Maclean *et al.*, 1979). However, in the case of $K_2Nd_2Ti_3O_{10}$, the requirement for intergrowth between the perovskite and rock salt layers with dissimilar cations may inhibit coherent cooperative tilting.

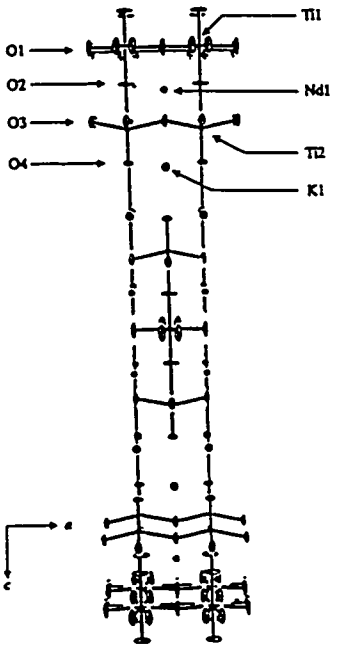

Fig. 1. View of the unit cell of $K_2Nd_2Ti_3O_{10}$ along [010], showing the local Ti2–O octahedron distortion. Displacement ellipsoids are plotted at the 50% probability level.

This case can be contrasted with the classic Ruddlesden–Popper phase $Sr_4Ti_3O_{10}$, as well as with $Ca_4Ti_3O_{10}$. For $Sr_4Ti_3O_{10}$, the structure is tetragonal and described as *I4/mmm*, representing the case where no octahedral tilting is observed. However, substitution of the smaller Ca^{2+} cation in both the perovskite and rock salt layers, as in $Ca_4Ti_3O_{10}$, induces a cooperative

coherent tilting in the octahedral network, such that a lowering of symmetry to orthorhombic *Pcab* is observed. (Elcombe *et al.*, 1991). An attempt was made to refine the data for $K_2Nd_2Ti_3O_{10}$ using this model, but this proved to be unsuccessful. The compound $K_2Nd_2Ti_3O_{10}$ thus appears to represent an intermediate case, where the octahedral tilting appears to be disordered or incoherent in nature, as shown by the strongly anisotropic O-atom displacement parameters, such that the *I4/mmm* symmetry is preserved.

The second remarkable feature is a local distortion in the Ti2–O octahedron, which is closest to the rock salt layer. The distortion arises when the Ti^{4+} cation is displaced from the centre of the coordination sphere towards the rock salt layer. Such distortions are not uncommon for Ti^{4+} compounds, *e.g.* $BaTiO_3$. A rationale for explaining such distortions is based on the nature of the bond network as well as on electronic effects (Kunz & Brown, 1995). For our particular case, a bond valence analysis (Brown, 1992) of the ideal undistorted bond network was carried out, and it was found that the O4 atom is severely underbonded, with only 1.22 valence units. Consequently, it is presumed that the Ti^{4+} cation moves off-centre in the coordination sphere to compensate for the deficiency of electronic charge at this site. The end result is a distorted octahedron with an unusually strong Ti2—O4 bond [1.734 (5) Å] and a very weakened Ti2—O2 bond [2.291 (6) Å].

Experimental

Single crystals of $K_2Nd_2Ti_3O_{10}$ were obtained by the flux method, in which a potassium fluoride/sodium tetraborate flux was used. 0.989 g of prefired Nd_2O_3 (99.99% Rhone Poulenc), 1.124 g of TiO_2 (99.999% CERAC), 8.711 g KF (99.999% CERAC) and 1.662 g $Na_2B_4O_7$ (99.99% Fisher Scientific) were ground together in an inert atmosphere. The reagents were placed and sealed in a 20 ml platinum crucible. The growth conditions involved heating the crucible to 1373 K at 110 K h^{-1}, holding it at this temperature for 2 h, and then cooling to 1273 K at a rate of 1 K h^{-1}. On reaching 1273 K, the crucible was quenched, hot poured and allowed to cool to room temperature. The crystals were obtained as transparent light purple blocks varying from 0.25 to 0.75 mm^2 in area, each consisting of very thin plates several microns thick. The presence of the metal ions was confirmed by EDAX.

Crystal data

$K_2Nd_2Ti_3O_{10}$
M_r = 670.38
Tetragonal
I4/mmm
a = 3.8588 (1) Å
c = 29.6561 (7) Å
V = 441.59 (2) $Å^3$
Z = 2
D_x = 5.042 Mg m^{-3}
D_m not measured

Mo $K\alpha$ radiation
λ = 0.71073 Å
Cell parameters from 4039 reflections
θ = 5.67–38.57°
μ = 15.129 mm^{-1}
T = 300 (2) K
Thin plate
0.356 × 0.194 × 0.006 mm
Colourless

Data collection

Siemens *P*4 diffractometer with a Siemens SMART 1 K CCD area detector
Area detector scans
Absorption correction: analytical (Sheldrick, 1996)
T_{min} = 0.114, T_{max} = 0.912
4977 measured reflections

437 independent reflections
416 reflections with $I > -3\sigma(I)$
R_{int} = 0.072
θ_{max} = 38.57°
$h = 0 \rightarrow 4$
$k = 0 \rightarrow 6$
$l = 0 \rightarrow 51$
Intensity decay: none

Refinement

Refinement on F^2
$R[F^2 > 2\sigma(F^2)]$ = 0.026
$wR(F^2)$ = 0.067
S = 1.129
436 reflections
26 parameters
$w = 1/[\sigma^2(F_o^2) + (0.0315P)^2 + 4.0449P]$ where $P = (F_o^2 + 2F_c^2)/3$

$(\Delta/\sigma)_{max} < 0.001$
$\Delta\rho_{max}$ = 1.883 e $Å^{-3}$
$\Delta\rho_{min}$ = −2.801 e $Å^{-3}$
Extinction correction: none
Scattering factors from *International Tables for Crystallography* (Vol. C)

Table 1. *Fractional atomic coordinates and equivalent isotropic displacement parameters* ($Å^2$)

$U_{eq} = (1/3)\Sigma_i\Sigma_j U^{ij} a^i a^j \mathbf{a}_i . \mathbf{a}_j$.

	x	y	z	U_{eq}
Nd1	1/2	1/2	0.07246 (1)	0.00971 (10)
Ti1	0	0	0	0.0054 (2)
Ti2	0	0	0.14066 (3)	0.0059 (2)
K1	1/2	1/2	0.20832 (6)	0.0169 (3)
O1†	1/2	0.111 (2)	0	0.030 (2)
O2	0	0	0.0634 (2)	0.051 (3)
O3	0	1/2	0.1269 (2)	0.0176 (7)
O4	0	0	0.1991 (2)	0.0202 (11)

† Site occupancy = 0.5.

The results reported are those for which the O1 atom has been split, with 0.5 occupancy on each site. In addition, the residual electron density $\Delta\rho$ of 1.883 e $Å^{-3}$ is closest to Nd1 at a distance of 0.66 Å.

Data collection: *SMART* (Siemens, 1996). Cell refinement: *SAINT* (Siemens, 1996). Data reduction: *SAINT*. Program(s) used to solve structure: *SHELXTL93* (Sheldrick, 1993*a*). Program(s) used to refine structure: *SHELXL93* (Sheldrick, 1993*b*). Molecular graphics: *XP* in *SHELXL93*. Software used to prepare material for publication: *SHELXL93*.

The authors express gratitude to Drs I. D. Brown, H. Dabkowska and J. Britten, and to the National Science and Engineering Research Council (NSERC), Canada.

Supplementary data for this paper are available from the IUCr electronic archives (Reference: TA1188). Services for accessing these data are described at the back of the journal.

References

Brown, I. D. (1992). *Acta Cryst.* B48, 553–572.
Elcombe, L. L., Kisi, E. H., Hawkins, K. D., White, T. J., Goodman, P. & Matheson, S. (1991). *Acta Cryst.* B47, 305–314.
Gondrand, M. & Joubert, J. C. (1987). *Rev. Chim. Miner.* 24, 33–41.
Gopalakrishan, J. & Bhat, V. (1987). *Inorg. Chem.* 26, 4299–4301.

Kunz, M. & Brown, I. D. (1995). *J. Solid State Chem.* 115, 395–406.
Maclean, D. A., Ng, H. N. & Greedan, J. E. (1979). *J. Solid State Chem.* 30, 35–44.
Richard, M., Brohan, L. & Tournoux, M. (1994). *J. Solid State Chem.* 112, 345–354.
Ruddlesden, S. N. & Popper, P. (1958). *Acta Cryst.* 11, 54–55.
Sheldrick, G. M. (1993*a*). *SHELXTL93*. Version 5.03. Siemens Analytical X-ray Instruments Inc., Madison, Wisconsin, USA.
Sheldrick, G. M. (1993*b*). *SHELXL93. Program for the Refinement of Crystal Structures*. University of Göttingen, Germany.
Sheldrick, G. M. (1996). *SADABS. Siemens Area Detector Absorption Correction Software*. University of Göttingen, Germany.
Siemens (1996). *SMART* and *SAINT*. Release 4.05. *Area Detector Control and Integration Software*. Siemens Analytical X-ray Instruments Inc., Madison, Wisconsin, USA.

APPENDIX II

The following tables contain the observed and calculated x-ray diffraction patterns obtained by a Guinier Hägg camera for the $Nd_{(1-x)}TiO_3$ and $Sm_{(1-x)}TiO_3$ system. The observed intensities were measured with a KEJ LS20 line scanner.

TABLE I: Observed and calculated x-ray powder diffraction lines for $NdTiO_3$ indexed in Pnma.

hkl	d_{OBS} (Å)	d_{CALC} (Å)	I_{OBS}
101	3.9476	3.9499	21.57
020	3.8944	3.8963	10.72
111	3.5215	3.5231	19.63
200	2.8241	2.8256	18.09
121	2.7734	2.7739	100.00
002	2.7605	2.7614	24.24
210	2.6561	2.6564	11.33
112	2.3632	2.3641	5.38
031	2.3512	2.3506	2.87
220	2.2872	2.2874	7.85
022	2.2527	2.2530	15.46
131	2.1696	2.1703	6.64
202	1.9745	1.9749	21.49
040	1.9482	1.9482	13.35
230	1.9132	1.9123	18.37
222	1.7605	1.7616	1.98
141	1.7471	1.7472	8.09
311	1.7378	1.7380	15.38
113	1.7080	1.7079	3.52
240	1.6038	1.6039	8.94
123	1.5964	1.5967	27.52
042	1.5918	1.5919	11.13
232	1.5723	1.5721	4.13
331	1.4703	1.4699	9.31
410	1.3903	1.3901	4.41
242	1.3871	1.3869	13.23
004	1.3808	1.3807	2.99
114	1.3223	1.3218	1.70
143	1.3020	1.3021	4.21
313	1.2982	1.2982	4.09
402	1.2577	1.2578	1.17

TABLE II: Observed and calculated x-ray powder diffraction lines for $Nd_{0.95}TiO_3$ indexed in Pnma.

hkl	d_{OBS} (Å)	d_{CALC} (Å)	I_{OBS}
101	3.9213	3.9233	19.60
020	3.8995	3.8991	7.16
111	3.5038	3.5047	10.38
200	2.7956	2.7959	18.50
121	2.7656	2.7656	100.00
002	2.7533	2.7530	17.04
210	2.6314	2.6319	7.13
112	2.3534	2.3546	2.62
220	2.2722	2.2722	7.82
022	2.2490	2.2489	2.25
131	2.1670	2.1670	3.93
202	1.9614	1.9617	21.44
040	1.9498	1.9496	13.44
212	1.9028	1.9024	11.17
141	1.7453	1.7459	4.54
311	1.7218	1.7220	9.45
113	1.7018	1.7018	1.45
321	1.6084	1.6083	8.09
240	1.5990	1.5992	8.90
123	1.5914	1.5918	32.32
232	1.5659	1.5658	1.86
331	1.4607	1.4605	5.18
242	1.3829	1.3828	11.20
004	1.3764	1.3764	6.72
143	1.3000	1.2997	3.03
313	1.2899	1.2898	2.36

TABLE III: Observed and calculated x-ray powder diffraction lines for $Nd_{0.90}TiO_3$ indexed in Pnma.

hkl	d_{OBS} (Å)	d_{CALC} (Å)	I_{OBS}
020	3.8974	3.8979	32.81
111	3.4875	3.4898	10.10
200	2.7745	2.7754	29.62
121	2.7577	2.7579	100.00
002	2.7439	2.7440	29.54
210	2.6143	2.6147	7.53
211	2.3606	2.3604	4.43
112	2.3465	2.3458	4.49
220	2.2611	2.2609	15.02
022	2.2439	2.2438	17.52
131	2.1632	2.1630	4.61
202	1.9509	1.9513	51.44
230	1.8969	1.8969	4.19
212	1.8930	1.8929	7.38
141	1.7441	1.7436	8.99
103	1.7374	1.7373	3.11
311	1.7107	1.7106	11.41
113	1.6960	1.6958	2.27
321	1.5990	1.5990	17.79
240	1.5950	1.5949	11.76
123	1.5870	1.5869	45.10
232	1.5600	1.5604	2.88
331	1.4534	1.4534	5.88
133	1.4444	1.4443	1.54
400	1.3878	1.3877	1.81
242	1.3790	1.3790	18.86
004	1.3719	1.3720	3.80
410	1.3663	1.3662	3.15
114	1.3128	1.3129	1.11
060	1.2991	1.2993	1.31
143	1.2970	1.2969	2.27
313	1.2832	1.2831	4.42

TABLE IV: Observed and calculated x-ray powder diffraction lines for $Nd_{0.85}TiO_3$ indexed in Pnma.

hkl	d_{OBS} (Å)	d_{CALC} (Å)	I_{OBS}
101	3.8879	3.8891	14.39
111	3.4780	3.4787	3.33
121	2.7508	2.7504	100.00
002	2.7400	2.7400	2.74
210	2.6018	2.6015	1.89
112	2.3418	2.3405	1.11
220	2.2518	2.2512	7.28
022	2.2403	2.2400	8.25
131	2.1579	2.1577	1.69
040	1.9451	1.9451	31.40
212	1.8867	1.8865	2.77
141	1.7396	1.7397	3.49
103	1.7339	1.7341	0.88
311	1.7024	1.7022	3.84
113	1.6926	1.6926	0.81
321	1.5916	1.5918	15.11
123	1.5840	1.5839	23.36
232	1.5561	1.5558	1.20
331	1.4477	1.4475	2.01
400	1.3799	1.3802	1.43
242	1.3755	1.3752	9.57
004	1.3700	1.3700	2.47
060	1.2966	1.2967	0.88
143	1.2940	1.2944	2.01
313	1.2787	1.2788	1.73

TABLE V: Observed and calculated x-ray powder diffraction lines for $Nd_{0.83}TiO_3$ indexed in Pnma.

hkl	d_{OBS} (Å)	d_{CALC} (Å)	I_{OBS}
101	3.8844	3.8853	15.26
111	3.4756	3.4755	3.03
121	2.7485	2.7481	100.00
002	2.7401	2.7390	11.63
210	2.5974	2.5974	2.37
031	2.3413	2.3428	1.93
220	2.2485	2.2482	9.20
022	2.2394	2.2391	8.82
040	1.9434	1.9438	33.22
212	1.8845	1.8847	1.82
231	1.7846	1.7849	2.09
141	1.7387	1.7384	5.23
103	1.7328	1.7333	1.60
311	1.6999	1.6997	4.30
321	1.5893	1.5896	21.60
123	1.5835	1.5831	24.41
331	1.4458	1.4457	1.87
242	1.3743	1.3741	13.50
004	1.3695	1.3695	2.70
303	1.2949	1.2951	1.76

TABLE VI: Observed and calculated x-ray powder diffraction lines for $Nd_{0.80}TiO_3$ indexed in Pnma.

hkl	d_{OBS} (Å)	d_{CALC} (Å)	I_{OBS}
020	3.8751	3.8724	17.73
002	2.7402	2.7394	100.00
031	2.3353	2.3353	2.45
022	2.2362	2.2364	27.34
040	1.9364	1.9362	47.75
141	1.7315	1.7317	8.22
240	1.5807	1.5804	54.72
242	1.3689	1.3690	23.95
303	1.2905	1.2905	4.50
161	1.2245	1.2245	26.11

TABLE VII: Observed and calculated x-ray powder diffraction lines for $Nd_{0.75}TiO_3$ indexed in Pban.

hkl	d_{OBS} (Å)	d_{CALC} (Å)	I_{OBS}
001	7.7512	7.7629	7.50
002	3.8763	3.8815	2.49
110	3.8573	3.8565	4.93
111	3.4517	3.4538	2.66
112	2.7350	2.7357	100.00
022	2.2318	2.2316	20.27
004	1.9408	1.9407	11.06
220	1.9282	1.9287	25.03
114	1.7342	1.7336	2.01
222	1.7264	1.7269	4.37
024	1.5813	1.5813	13.97
132	1.5763	1.5763	31.38
224	1.3680	1.3679	11.57
040	1.3637	1.3637	6.82
134	1.2892	1.2893	3.00
402	1.2862	1.2862	1.24

TABLE VIII: Observed and calculated x-ray powder diffraction lines for $Nd_{0.70}TiO_3$ indexed in Pban.

hkl	d_{OBS} (Å)	d_{CALC} (Å)	I_{OBS}
001	7.7402	7.7357	12.35
002	3.8678	3.8679	4.25
110	3.8486	3.8486	5.56
111	3.4449	3.4457	8.42
112	2.7273	2.7281	100.00
202	2.2250	2.2252	24.69
004	1.9343	1.9340	16.35
023	1.8722	1.8721	4.25
311	1.6799	1.6796	2.70
204	1.5760	1.5762	18.32
400	1.3602	1.3602	13.41

TABLE IX: Observed and calculated x-ray powder diffraction lines for $SmTiO_3$ indexed in Pnma.

hkl	d_{OBS}(Å)	d_{CALC} (Å)	I_{OBS}
101	3.9304	3.9323	22.97
020	3.8631	3.8649	14.84
111	3.5038	3.5048	21.86
200	2.8324	2.8327	20.44
121	2.7563	2.7564	100.00
002	2.7313	2.7311	30.07
210	2.6598	2.6597	15.00
112	2.3443	2.3443	5.21
220	2.2847	2.2847	9.08
022	2.2307	2.2305	17.21
131	2.1554	2.1552	9.55
202	1.9663	1.9661	20.52
040	1.9327	1.9325	16.34
230	1.9058	1.9061	27.31
311	1.7389	1.7390	19.97
141	1.7340	1.7343	9.39
113	1.6914	1.6914	3.63
321	1.6201	1.6204	7.58
240	1.5962	1.5964	8.76
123	1.5816	1.5816	25.34
042	1.5776	1.5575	13.65
232	1.5627	1.5630	5.60
331	1.4671	1.4672	12.08
151	1.4390	1.4388	3.08
410	1.3933	1.3932	5.52
242	1.3784	1.3782	11.60
004	1.3657	1.3656	4.50
152	1.3088	1.3090	2.13
421	1.2921	1.2921	7.34
024	1.2877	1.2876	3.71
430	1.2412	1.2412	9.87
204	1.2300	1.2301	.39
161	1.2243	1.2243	11.68
252	1.2151	1.2153	7.26
351	1.1689	1.6855	12.39

TABLE X: Observed and calculated x-ray powder diffraction lines for $Sm_{0.95}TiO_3$ indexed in Pnma.

hkl	d_{Obs} (Å)	d_{CALC} (Å)	I_{OBS}
101	3.9103	3.9125	24.46
020	3.8690	3.8703	13.50
111	3.4907	3.4919	19.24
200	2.8075	2.8077	14.65
121	2.7515	2.7517	100.00
002	2.7272	2.7271	22.93
210	2.6395	2.6395	9.17
112	2.3376	2.3385	4.20
220	2.2729	2.2728	9.17
022	2.2295	2.2294	14.52
131	2.1550	2.1542	8.03
202	1.9565	1.9562	22.55
040	1.9357	1.9354	14.90
141	1.7344	1.7348	5.22
311	1.7264	1.7259	20.51
321	1.6101	1.6100	5.99
240	1.5934	1.5935	8.79
123	1.5789	1.5792	34.78
232	1.5583	1.5589	5.10
331	1.4600	1.4599	8.03
242	1.3756	1.3758	12.74
004	1.3635	1.3636	4.33
060	1.2901	1.2903	5.61
024	1.2861	1.2861	6.11
430	1.2331	1.2332	5.99
161	1.2257	1.2254	17.58
252	1.2141	1.2141	6.24
214	1.2118	1.2115	3.82

TABLE XI: Observed and calculated x-ray powder diffraction lines for $Sm_{0.90}TiO_3$ indexed in Pnma.

hkl	d_{OBS} (Å)	d_{CALC} (Å)	I_{OBS}
101	3.8948	3.8967	19.32
020	3.8727	3.8725	8.03
111	3.4796	3.4809	16.05
200	2.7881	2.7887	22.73
121	2.7469	2.7468	100.00
002	2.7234	2.7232	26.14
210	2.6242	2.6237	10.23
031	2.3330	2.3329	4.76
220	2.2633	2.2630	11.15
022	2.2275	2.2276	15.55
131	2.1528	2.1522	7.32
202	1.9483	1.9483	28.76
040	1.9367	1.9362	19.32
212	1.8894	1.8895	10.01
141	1.7336	1.7340	5.04
103	1.7268	1.7263	2.34
311	1.7160	1.7157	16.69
113	1.6847	1.6850	2.63
321	1.6009	1.6019	6.46
240	1.5905	1.5905	10.51
042	1.5772	1.5780	40.41
232	1.5551	1.5552	5.26
331	1.4540	1.4539	11.01
151	1.4399	1.4394	2.13
242	1.3734	1.3734	17.68
004	1.3614	1.3616	4.12
313	1.2810	1.2810	2.06
323	1.2313	1.2315	3.55
161	1.2253	1.2253	22.51
252	1.2122	1.2125	3.76
214	1.2087	1.2086	2.20
062	1.1665	1.1664	2.63
351	1.1633	1.1626	4.55
333	1.1607	1.1603	2.98

TABLE XII: Observed and calculated x-ray powder diffraction lines for $Sm_{0.87}TiO_3$ indexed in Pnma.

hkl	$_{Dobs}$ (Å)	d_{CALC} (Å)	I_{OBS}
101	3.8789	3.8818	28.21
111	3.4693	3.4703	13.06
200	2.7719	2.7728	21.79
121	2.7411	2.7414	100.00
002	2.7188	2.7178	30.07
210	2.6098	2.6105	9.32
220	2.2542	2.2544	14.34
022	2.2252	2.2245	17.25
131	2.1496	2.1495	5.94
202	1.9413	1.9409	28.44
040	1.9360	1.9360	19.23
230	1.8891	1.8894	5.59
212	1.8829	1.8827	10.60
141	1.7319	1.7325	5.59
311	1.7072	1.7070	11.66
321	1.5947	1.5948	13.06
240	1.5874	1.5874	9.44
123	1.5739	1.5736	26.11
232	1.5512	1.5513	3.38
331	1.4485	1.4486	5.47
242	1.3708	1.3707	13.75
323	1.2271	1.2272	5.13
161	1.2246	1.2248	10.13
204	1.2200	1.2202	11.66
351	1.1603	1.1603	3.15

TABLE XIII: Observed and calculated x-ray powder diffraction lines for $Sm_{0.85}TiO_3$ indexed in Pnma.

hkl	d_{OBS} (Å)	d_{CALC} (Å)	I_{OBS}
020	3.8752	3.8727	22.10
111	3.4689	3.4675	10.59
200	2.7677	2.7659	21.97
121	2.7411	2.7402	100.00
002	2.7185	2.7188	31.44
210	2.6062	2.6048	7.04
112	2.3281	2.3273	4.24
220	2.2521	2.2508	5.89
022	2.2248	2.2252	12.64
131	2.1489	2.1491	5.23
202	1.9383	1.9389	43.81
230	1.8866	1.8873	5.63
222	1.7333	1.7338	5.69
311	1.7034	1.7035	6.35
321	1.5919	1.5919	7.94
123	1.5737	1.5738	17.07
331	1.4462	1.4465	5.56
242	1.3699	1.3701	14.89
143	1.2873	1.2870	1.92
161	1.2248	1.2248	12.64
430	1.2191	1.2191	2.51
412	1.2173	1.2173	2.05
333	1.1559	1.1558	3.11

TABLE XIV: Observed and calculated x-ray powder diffraction lines for $Sm_{0.83}TiO_3$ indexed in Pnma.

hkl	d_{obs} (Å)	d_{CALC} (Å)	I_{OBS}
020	3.8666	3.8672	23.20
111	3.4596	3.4609	12.04
200	2.7583	2.7588	21.31
121	2.7354	2.7355	100.00
002	2.7150	2.7147	33.29
210	2.5977	2.5985	8.64
112	2.3239	2.3233	3.53
220	2.2459	2.2459	14.38
022	2.2219	2.2219	16.77
131	2.1456	2.1456	3.72
202	1.9347	1.9350	51.01
230	1.8833	1.8837	6.12
212	1.8772	1.8771	8.64
141	1.7298	1.7297	8.07
103	1.7198	1.7197	3.09
311	1.6995	1.6994	11.54
321	1.5883	1.5883	15.45
240	1.5833	1.5834	13.43
042	1.5747	1.5749	16.71
123	1.5714	1.5713	27.99
232	1.5473	1.5476	2.71
331	1.4432	1.4434	10.34
400	1.3795	1.3794	2.40
242	1.3677	1.3678	16.33
060	1.2892	1.2891	2.40
143	1.2851	1.2850	2.14
024	1.2806	1.2808	1.95
313	1.2725	1.2724	4.10
161	1.2231	1.2230	15.89
204	1.2179	1.2179	4.22
430	1.2169	1.2163	2.46
412	1.2146	1.2145	4.79
252	1.2082	1.2083	1.89

APPENDIX III

STRUCTURE FACTORS

The observed (F_o^2) and calculated (F_c^2) structure factors obtained from single crystal studies for the following compounds can be found on the floppy disk included in this thesis. The files are in ASCII format.

Compound	**Filename**
$K_2Nd_2Ti_3O_{10}$	k2nd2.str
$Nd_{2/3}TiO_3$	nd23.str
$Sm_{0.97}TiO_3$ (x-ray)	sm97_x.str

The following pages are printed from the included floppy diskette.
The file names are:
K2nd2.str
Nd23.str
Sm97_x.str

```
#
# n,k,l, Fc-squared, Fo-squared, sigma(Fo-squared) and status flag
#
data_xtf9bma
_shelx_title ' K2Nd2Ti3O10 in I4/mmm'
_shelx_refln_list_code   4
_shelx_F_calc_maximum      374.47
_exptl_crystal_F_000       608.00
_shelx_F_squared_multiplier     1.000
loop_
 _refln_index_h
 _refln_index_k
 _refln_index_l
 _refln_F_squared_calc
 _refln_F_squared_meas
 _refln_F_squared_sigma
 _refln_observed_status
   1   1   0   106295.30   107242.69   7546.88 o
   0   2   0   140225.17   146745.88   8135.25 o
   2   2   0    78858.97    73001.41   1480.45 o
   1   3   0    43260.46    42142.67    919.64 o
   3   3   0    25522.22    22492.22    686.34 o
   0   4   0    38937.45    39988.17   1053.14 o
   2   4   0    28967.23    27702.15    721.32 o
   4   4   0    14651.11    12901.45    256.20 o
   1   5   0    15495.91    16375.69    260.82 o
   3   5   0    11113.47     9844.13    346.01 o
   0   6   0    13440.47    14258.06    295.80 o
   2   6   0    10884.61    11595.90    287.39 o
   1   2   1     5639.35     6009.51     96.43 o
   0   3   1     6353.87     5914.23    131.41 o
   2   3   1     4357.82     3783.37     56.72 o
   1   4   1     2430.86     2195.15     61.45 o
   3   4   1     1756.13     1510.70     39.71 o
   0   5   1     2396.95     2637.58     91.70 o
   2   5   1     1663.67     1589.17     33.09 o
   4   5   1      661.16      636.23     29.31 o
   1   6   1      672.45      713.75     27.42 o
   3   6   1      508.18      502.94     33.09 o
   1   1   2     4973.58     5052.05    356.40 o
   0   2   2     7715.17     8016.73    163.55 o
   2   2   2     4595.38     4361.93    128.57 o
   1   3   2     3667.84     3778.64    191.91 o
   3   3   2     2719.36     2188.53    244.85 o
   0   4   2     2667.79     3112.16    289.28 o
   2   4   2     1888.19     1773.51     74.68 o
   4   4   2      926.19      797.89    132.35 o
   1   5   2     1593.58     1738.53     91.70 o
   3   5   2     1351.60      988.86    123.84 o
   0   6   2     1127.88      794.11     98.32 o
   2   6   2      858.07      859.34     61.45 o
   0   1   3     1729.73     1772.57     73.74 o
   1   2   3      731.05      716.59     30.25 o
   0   3   3     1202.49     1106.08     32.14 o
   2   3   3      671.12      553.04     13.24 o
   1   4   3      227.14      252.41     34.03 o
   3   4   3      256.29      193.80     16.07 o
```

0	5	3	467.80	522.79	66.18	o
2	5	3	315.04	265.65	25.52	o
4	5	3	158.09	134.24	27.42	o
1	6	3	132.46	61.45	38.76	o
3	6	3	161.26	165.44	24.58	o
1	1	4	223.54	157.88	8.51	o
0	2	4	3960.82	3869.40	61.45	o
2	2	4	3033.53	2719.83	66.18	o
1	3	4	175.78	251.47	37.81	o
3	3	4	80.12	22.69	34.98	o
0	4	4	1639.78	1806.60	94.54	o
2	4	4	1503.15	1323.52	54.83	o
4	4	4	1030.99	726.99	100.21	o
1	5	4	122.96	242.01	45.38	o
3	5	4	50.05	17.02	31.20	o
0	6	4	598.66	495.37	135.19	o
2	6	4	610.22	516.17	69.01	o
0	1	5	10257.21	10915.23	409.34	o
1	2	5	7761.69	8170.83	268.48	o
0	3	5	4024.48	4350.59	182.46	o
2	3	5	3491.55	3467.61	111.55	o
1	4	5	3564.44	3896.81	138.02	o
3	4	5	1976.26	1784.86	90.76	o
0	5	5	1818.07	1823.62	140.86	o
2	5	5	1399.11	1483.28	40.65	o
4	5	5	948.44	886.76	52.00	o
1	6	5	1240.87	1125.93	39.71	o
3	6	5	771.94	854.61	143.70	o
1	1	6	16430.41	15709.20	939.70	o
0	2	6	7103.58	6535.34	135.19	o
2	2	6	5623.43	5268.54	119.12	o
1	3	6	5669.64	5510.56	107.77	o
3	3	6	2704.85	2373.82	143.70	o
0	4	6	3179.38	3231.27	138.97	o
2	4	6	2681.73	2573.29	49.16	o
4	4	6	1388.87	1297.05	81.30	o
1	5	6	1768.03	1794.31	60.50	o
3	5	6	871.97	736.44	38.76	o
0	6	6	773.79	723.21	35.92	o
2	6	6	690.03	663.65	49.16	o
0	1	7	95950.62	87718.91	6533.45	o
1	2	7	62816.97	60438.40	1043.69	o
0	3	7	39619.84	40073.26	918.90	o
2	3	7	31276.68	29700.67	487.81	o
1	4	7	27168.71	27716.33	415.02	o
3	4	7	16836.80	15403.85	206.09	o
0	5	7	15176.40	16301.95	424.47	o
2	5	7	13033.54	13284.33	187.18	o
4	5	7	8147.70	7667.89	193.80	o
1	6	7	10232.49	10748.85	117.23	o
3	6	7	6984.46	7063.80	155.99	o
1	1	8	37658.54	36372.13	607.87	o
0	2	8	6557.27	6049.42	69.96	o
2	2	8	4929.84	4720.23	80.36	o
1	3	8	10886.95	10622.17	199.47	o
3	3	8	4898.11	4482.00	93.59	o
0	4	8	2612.63	2713.21	63.34	o

2	4	8	2141.44	2019.31	38.76	o
4	4	8	991.14	942.53	144.64	o
1	5	8	2978.62	3025.18	75.63	o
3	5	8	1516.77	1368.89	50.10	o
0	6	8	495.98	461.34	42.54	o
2	6	8	426.18	460.39	29.31	o
0	1	9	6746.58	6851.09	69.01	o
1	2	9	6205.12	6355.72	155.99	o
0	3	9	3504.86	3726.65	79.41	o
2	3	9	3207.84	3220.87	109.66	o
1	4	9	3429.54	3687.89	102.10	o
3	4	9	2001.48	1971.09	54.83	o
0	5	9	1496.07	1725.30	100.21	o
2	5	9	1401.94	1466.27	44.43	o
4	5	9	995.84	895.26	52.00	o
1	6	9	1357.90	1264.30	52.00	o
1	1	10	60.34	95.48	6.62	o
0	2	10	11.66	5.67	6.62	o
2	2	10	17.52	20.80	5.67	o
1	3	10	9.79	34.03	7.56	o
3	3	10	2.00	17.96	19.85	o
0	4	10	28.19	34.98	12.29	o
2	4	10	59.68	57.67	11.34	o
4	4	10	94.67	132.35	19.85	o
1	5	10	14.93	67.12	21.74	o
3	5	10	4.08	18.91	15.13	o
0	6	10	24.68	-65.23	19.85	<
2	6	10	44.82	60.50	36.87	o
0	1	11	4649.79	4796.80	96.43	o
1	2	11	2480.10	2442.83	41.60	o
0	3	11	2567.96	2635.69	61.45	o
2	3	11	1691.75	1713.95	43.49	o
1	4	11	928.77	945.37	22.69	o
3	4	11	776.26	740.22	32.14	o
0	5	11	1044.29	1197.78	46.32	o
2	5	11	778.62	753.46	28.36	o
4	5	11	427.42	357.35	25.52	o
1	6	11	432.73	453.78	40.65	o
0	0	12	2166.88	2864.47	64.29	o
1	1	12	7298.08	7818.20	160.71	o
0	2	12	1912.42	2142.21	97.37	o
2	2	12	1531.93	1577.82	64.29	o
1	3	12	4633.81	4962.24	112.50	o
3	3	12	3255.02	3155.64	154.10	o
0	4	12	1145.48	1278.14	113.44	o
2	4	12	839.64	849.89	32.14	o
4	4	12	428.50	383.82	58.61	o
1	5	12	2007.60	2170.57	61.45	o
3	5	12	1622.90	1589.17	82.25	o
0	6	12	546.96	541.70	42.54	o
2	6	12	412.78	429.20	43.49	o
0	1	13	10430.61	10671.33	151.26	o
1	2	13	6541.97	6347.21	90.76	o
0	3	13	5973.06	6004.04	143.70	o
2	3	13	4166.16	4322.23	84.14	o
1	4	13	2579.78	2649.87	48.21	o
3	4	13	1713.60	1660.07	49.16	o

0	5	13	2078.54	2336.01	75.63	o
2	5	13	1493.29	1583.49	22.69	o
4	5	13	656.04	590.86	40.65	o
1	6	13	748.90	846.11	36.87	o
0	0	14	119527.09	123935.06	1558.91	o
1	1	14	71910.27	71126.74	1059.76	o
0	2	14	67543.12	68630.02	1125.93	o
2	2	14	44574.59	44722.58	1017.22	o
1	3	14	35203.94	35280.23	402.73	o
3	3	14	21893.49	20816.08	500.10	o
0	4	14	25240.19	27403.42	676.88	o
2	4	14	19510.42	18944.25	292.12	o
4	4	14	10452.09	9749.59	354.61	o
1	5	14	13948.67	14696.71	226.89	o
3	5	14	10098.89	9599.28	147.48	o
0	6	14	9527.10	9845.08	189.07	o
2	6	14	7824.02	7843.73	97.37	o
0	1	15	5084.79	4963.19	45.38	o
1	2	15	3892.30	3700.18	45.38	o
0	3	15	4147.03	4085.89	75.63	o
2	3	15	3033.36	2855.02	59.56	o
1	4	15	1849.94	1840.63	34.03	o
3	4	15	1264.72	1219.53	59.56	o
0	5	15	1631.95	1803.76	63.34	o
2	5	15	1150.81	1216.69	22.69	o
4	5	15	486.12	452.83	101.15	o
1	6	15	483.70	660.81	34.98	o
0	0	16	26030.61	28172.95	362.08	o
1	1	16	5335.90	6643.85	73.74	o
0	2	16	13749.87	14667.40	245.80	o
2	2	16	8559.01	9007.48	166.38	o
1	3	16	3107.12	3284.21	65.23	o
3	3	16	2124.74	1984.33	127.62	o
0	4	16	4669.13	5079.47	181.51	o
2	4	16	3483.45	3435.47	74.68	o
4	4	16	1815.61	1556.08	54.83	o
1	5	16	1286.97	1242.22	38.76	o
3	5	16	1029.28	876.36	34.03	o
0	6	16	1832.54	1782.02	83.19	o
2	6	16	1473.93	1420.89	41.60	o
0	1	17	36.35	34.98	7.56	o
1	2	17	17.23	45.38	6.62	o
0	3	17	22.23	53.89	17.02	o
2	3	17	9.06	10.40	10.40	o
1	4	17	3.86	30.25	9.45	o
3	4	17	4.18	25.52	16.07	o
0	5	17	37.34	111.55	43.49	o
2	5	17	22.23	45.38	13.24	o
1	6	17	2.15	34.03	24.58	o
0	0	18	5741.08	5673.16	243.91	o
1	1	18	5534.74	5419.80	87.92	o
0	2	18	4442.20	4614.35	52.94	o
2	2	18	3572.77	3619.82	83.19	o
1	3	18	2713.80	2579.91	38.76	o
3	3	18	1530.47	1548.51	72.79	o
0	4	18	2213.07	2419.20	74.68	o
2	4	18	1923.13	2034.43	42.54	o

4	4	18	1203.98	1281.92	60.50	o
1	5	18	1131.17	1275.30	34.98	o
3	5	18	698.70	862.18	47.27	o
0	6	18	829.14	940.64	78.47	o
2	6	18	764.42	821.53	87.92	o
0	1	19	5932.89	6347.21	88.86	o
1	2	19	4614.88	4883.78	75.63	o
0	3	19	2966.59	3172.66	83.19	o
2	3	19	2479.68	2545.88	59.56	o
1	4	19	2312.10	2382.33	58.61	o
3	4	19	1410.17	1333.92	43.49	o
0	5	19	1212.79	1338.64	106.83	o
2	5	19	1080.88	1133.50	50.10	o
1	6	19	880.14	906.61	41.60	o
0	0	20	6601.70	6827.46	112.50	o
1	1	20	2724.41	2744.41	49.16	o
0	2	20	5350.17	5534.19	87.92	o
2	2	20	4379.82	4596.38	102.10	o
1	3	20	1718.31	1640.22	33.09	o
3	3	20	966.23	862.18	58.61	o
0	4	20	2696.35	2758.59	85.08	o
2	4	20	2252.87	2286.85	42.54	o
4	4	20	1263.00	1397.26	65.23	o
1	5	20	658.04	605.04	28.36	o
3	5	20	355.35	365.86	19.85	o
0	6	20	869.34	916.06	34.03	o
0	1	21	47953.07	48874.64	818.69	o
1	2	21	35619.96	35816.26	375.31	o
0	3	21	25942.63	26359.73	711.86	o
2	3	21	20918.70	20574.07	352.62	o
1	4	21	17746.43	17946.89	189.07	o
3	4	21	11731.72	11948.52	220.27	o
0	5	21	11184.76	11869.11	149.37	o
2	5	21	9554.07	9902.74	140.86	o
1	6	21	7159.04	7411.69	117.23	o
0	0	22	8697.99	8324.92	211.76	o
1	1	22	10136.43	9731.63	140.86	o
0	2	22	5975.77	5972.84	72.79	o
2	2	22	4382.85	4487.67	82.25	o
1	3	22	4546.13	4373.28	71.85	o
3	3	22	2257.45	2165.84	79.41	o
0	4	22	2307.80	2395.57	61.45	o
2	4	22	1782.63	1848.20	33.09	o
4	4	22	784.74	829.09	53.89	o
1	5	22	1314.85	1283.81	44.43	o
3	5	22	670.40	630.56	24.58	o
0	6	22	480.10	539.81	52.94	o
0	1	23	3727.68	3984.73	84.14	o
1	2	23	3501.87	3741.77	41.60	o
0	3	23	2595.32	2785.06	136.13	o
2	3	23	2348.13	2302.92	46.32	o
1	4	23	2316.05	2383.28	50.10	o
3	4	23	1578.86	1713.95	36.87	o
0	5	23	1353.56	1472.89	62.39	o
2	5	23	1235.30	1280.98	29.31	o
0	0	24	502.99	481.19	24.58	o
1	1	24	140.88	160.71	17.02	o

0	2	24	341.16	292.12	10.40 o
2	2	24	234.00	228.78	17.96 o
1	3	24	17.49	43.49	8.51 o
3	3	24	2.87	-1.89	17.96 o
0	4	24	145.63	172.06	20.80 o
2	4	24	94.37	133.30	20.80 o
4	4	24	29.93	40.65	29.31 o
1	5	24	8.90	35.92	20.80 o
3	5	24	4.89	39.71	36.87 o
0	1	25	4865.32	4725.90	60.50 o
1	2	25	3361.91	3455.32	38.76 o
0	3	25	2888.11	2850.29	104.94 o
2	3	25	2187.05	2107.23	32.14 o
1	4	25	1555.54	1600.51	45.38 o
3	4	25	1181.22	1135.39	42.54 o
0	5	25	1313.46	1368.89	44.43 o
2	5	25	1058.45	1061.65	41.60 o
0	0	26	4068.16	3979.06	99.26 o
1	1	26	3837.19	3907.21	78.47 o
0	2	26	3182.37	3113.10	37.81 o
2	2	26	2485.44	2438.11	48.21 o
1	3	26	2664.98	2729.28	43.49 o
3	3	26	1892.67	1985.28	59.56 o
0	4	26	1654.29	1782.97	36.87 o
2	4	26	1309.71	1337.70	34.03 o
4	4	26	732.51	760.08	39.71 o
1	5	26	1261.24	1266.79	40.65 o
3	5	26	964.93	1033.29	73.74 o
0	1	27	5340.41	5497.32	82.25 o
1	2	27	3842.34	3838.20	52.00 o
0	3	27	3135.06	3285.16	68.07 o
2	3	27	2334.43	2364.37	39.71 o
1	4	27	1670.20	1799.04	60.50 o
3	4	27	1093.49	1081.50	41.60 o
0	5	27	1180.32	1260.18	58.61 o
2	5	27	915.29	1029.51	34.03 o
0	0	28	25701.80	25361.42	600.31 o
1	1	28	27013.67	27463.92	699.57 o
0	2	28	19755.77	20061.68	183.40 o
2	2	28	15604.25	15122.13	154.10 o
1	3	28	17340.37	17700.15	187.18 o
3	3	28	12017.00	11725.41	201.36 o
0	4	28	10498.51	10663.76	130.46 o
2	4	28	8651.89	8657.69	88.86 o
1	5	28	8425.08	8629.33	90.76 o
0	1	29	3395.08	3377.80	38.76 o
1	2	29	2576.98	2561.01	29.31 o
0	3	29	2143.84	2112.90	39.71 o
2	3	29	1583.53	1618.47	33.09 o
1	4	29	1094.73	1143.90	28.36 o
3	4	29	652.52	741.17	65.23 o
0	5	29	716.69	756.30	32.14 o
2	5	29	519.93	608.82	52.94 o
0	0	30	8572.98	8563.15	178.67 o
1	1	30	5716.70	6058.87	66.18 o
0	2	30	6096.63	6245.11	62.39 o
2	2	30	4553.29	4569.91	64.29 o

1	3	30	3410.79	3495.03	45.38	o
3	3	30	2290.05	2246.20	105.88	o
0	4	30	2885.56	2925.92	62.39	o
2	4	30	2318.34	2304.81	41.60	o
1	5	30	1541.67	1559.86	30.25	o
0	1	31	599.13	518.06	16.07	o
1	2	31	384.22	398.95	18.91	o
0	3	31	195.41	260.92	44.43	o
2	3	31	139.99	151.26	19.85	o
1	4	31	127.60	155.99	34.98	o
3	4	31	52.34	94.54	57.67	o
0	5	31	32.75	82.25	21.74	o
2	5	31	26.02	96.45	44.43	o
0	0	32	3082.66	3079.07	98.32	o
1	1	32	4829.93	4576.53	47.27	o
0	2	32	2675.38	2682.01	68.07	o
2	2	32	2293.11	2410.69	40.65	o
1	3	32	3211.93	3245.45	60.50	o
3	3	32	2171.47	2261.32	122.90	o
0	4	32	1603.67	1771.62	44.43	o
2	4	32	1373.50	1447.36	46.32	o
1	5	32	1571.69	1762.17	45.38	o
0	1	33	3089.57	2930.64	41.60	o
1	2	33	2422.66	2372.88	50.10	o
0	3	33	1805.69	1913.43	41.60	o
2	3	33	1459.23	1465.32	38.76	o
1	4	33	1304.84	1220.47	28.36	o
3	4	33	884.21	889.59	37.81	o
0	5	33	823.21	846.11	34.98	o
0	0	34	2602.55	2505.23	140.86	o
1	1	34	2104.62	1983.38	43.49	o
0	2	34	2196.21	2166.79	50.10	o
2	2	34	1836.01	1804.71	60.50	o
1	3	34	1381.30	1339.59	29.31	o
3	3	34	899.17	943.48	45.38	o
0	4	34	1240.24	1221.42	35.92	o
2	4	34	1046.52	1199.67	50.10	o
0	1	35	18277.78	17906.24	156.93	o
1	2	35	14704.06	15119.29	102.10	o
0	3	35	11815.33	12556.39	163.55	o
2	3	35	9819.73	10033.20	115.34	o
1	4	35	8321.37	8381.64	132.35	o
3	4	35	5908.77	5664.65	128.57	o
0	0	36	2548.50	2510.90	75.63	o
1	1	36	1505.20	1396.31	24.58	o
0	2	36	1920.67	2046.72	32.14	o
2	2	36	1455.71	1470.99	45.38	o
1	3	36	779.50	768.59	36.87	o
3	3	36	396.04	622.05	45.38	o
0	4	36	821.82	929.30	47.27	o
2	4	36	633.54	655.14	39.71	o
0	1	37	2655.74	2654.60	35.92	o
1	2	37	2334.65	2314.26	32.14	o
0	3	37	1963.12	1829.29	97.37	o
2	3	37	1720.57	1739.48	45.38	o
1	4	37	1538.33	1455.87	46.32	o
0	0	38	41.66	32.14	64.29	o

1	1	38	3.42	-32.14	13.24	o
0	2	38	51.08	51.05	17.96	o
2	2	38	51.42	89.81	26.47	o
1	3	38	13.21	72.79	37.81	o
3	3	38	15.00	42.54	62.39	o
0	4	38	45.20	100.21	53.89	o
2	4	38	37.16	104.94	34.98	o
0	1	39	3925.45	3627.38	50.10	o
1	2	39	3001.92	2943.88	34.98	o
0	3	39	2441.01	2278.34	71.85	o
2	3	39	1951.18	1929.50	95.48	o
1	4	39	1546.07	1609.02	57.67	o
0	0	40	2834.06	2624.54	85.19	o
1	1	40	1884.26	1950.30	47.27	o
0	2	40	2398.20	2318.05	35.92	o
2	2	40	2014.44	1886.01	39.71	o
1	3	40	1379.13	1412.38	49.16	o
3	3	40	997.72	899.99	61.45	o
0	4	40	1437.38	1489.90	97.37	o
0	1	41	2047.62	1829.29	55.78	o
1	2	41	1563.74	1487.07	28.36	o
0	3	41	1265.57	1292.32	72.79	o
2	3	41	1010.90	1015.33	40.65	o
0	0	42	8229.74	8283.33	187.18	o
1	1	42	8080.34	7829.55	122.90	o
0	2	42	7049.85	6949.41	103.99	o
2	2	42	6051.72	5854.67	68.07	o
1	3	42	6021.40	6038.07	98.32	o
0	1	43	1313.70	1288.54	43.49	o
1	2	43	946.16	901.88	23.63	o
0	3	43	699.91	658.92	45.38	o
2	3	43	508.12	547.37	33.09	o
0	0	44	2476.55	2545.88	87.92	o
1	1	44	2680.64	2679.18	69.01	o
0	2	44	2033.08	1944.62	35.92	o
2	2	44	1689.80	1672.36	62.39	o
1	3	44	1988.45	1810.38	44.43	o
0	1	45	431.41	455.67	50.10	o
1	2	45	311.52	313.86	22.69	o
0	3	45	222.65	352.62	43.49	o
0	0	46	1653.28	1660.07	95.48	o
1	1	46	1801.43	1639.27	35.92	o
0	2	46	1481.00	1649.67	40.65	o
2	2	46	1307.22	1382.13	39.71	o
1	3	46	1381.32	1369.84	57.67	o
0	1	47	1849.24	1721.52	39.71	o
1	2	47	1458.35	1418.05	31.20	o
0	0	48	1149.85	1232.76	158.82	o
1	1	48	1335.85	1195.89	70.90	o
0	2	48	1022.31	945.37	34.98	o
0	1	49	5826.39	5623.06	80.36	o
1	2	49	4861.84	4769.39	87.92	o
0	0	50	188.75	260.92	81.30	o
1	1	50	130.13	136.13	29.31	o
0	1	51	1801.49	1829.29	82.25	o

```
#
# h,k,l, Fc-squared, Fo-squared, sigma(Fo-squared) and status flag
#
data_p4mmm
_shelx_title ' p4mmm in P4/mmm'
_shelx_refln_list_code   4
_shelx_F_calc_maximum      207.58
_exptl_crystal_F_000       344.20
_shelx_F_squared_multiplier     1.000
loop_
 _refln_index_h
 _refln_index_k
 _refln_index_l
 _refln_F_squared_calc
 _refln_F_squared_meas
 _refln_F_squared_sigma
 _refln_observed_status
   1   1   0     1561.81     1308.82     32.89 o
   0   2   0    27457.69    24089.40   3492.91 o
   1   2   0       45.60       52.18      1.69 o
   2   2   0    43090.63    44350.93   1151.62 o
   0   3   0       14.39       19.42      1.01 o
   1   3   0     1372.49     1230.16     24.06 o
   2   3   0       28.33       24.69      0.80 o
   3   3   0     1955.97     1827.00     80.95 o
   0   4   0    24509.30    28524.70    252.80 o
   1   4   0       37.01       53.89      2.53 o
   2   4   0    11891.98    13495.83    226.98 o
   3   4   0       21.42       16.27      1.68 o
   4   4   0    11909.49    13112.38    390.20 o
   0   5   0       13.94        6.05      1.36 o
   1   5   0     1299.77     1374.02     36.34 o
   2   5   0       12.71       13.03      1.19 o
   3   5   0      649.85      605.39     19.70 o
   4   5   0       15.04       15.73      2.12 o
   5   5   0      847.49      981.50     30.03 o
   0   6   0     7341.58     8286.48    105.40 o
   1   6   0       21.56       29.36      2.56 o
   2   6   0     8969.02     9617.14    174.11 o
   3   6   0       14.47       39.37      1.93 o
   4   6   0     4500.66     4498.73     90.48 o
   5   6   0        9.94       10.28      2.41 o
   6   6   0     4115.90     4146.64     79.01 o
   0   7   0        8.20        8.68      2.89 o
   1   7   0      461.81      534.73     31.99 o
   2   7   0       11.03        8.17      2.45 o
   3   7   0      562.73      684.30     24.06 o
   4   7   0        9.18       11.70      2.88 o
   5   7   0      121.24      140.46      5.49 o
   6   7   0        7.09       15.39      3.84 o
   0   8   0     4584.94     4701.35    121.92 o
   1   8   0       10.87       33.20      3.04 o
   2   8   0     3368.38     3439.30     75.72 o
   3   8   0        8.24       -3.11      3.26 o
   4   8   0     3351.99     3057.45     96.69 o
   0   9   0        6.86        6.11      5.04 o
   1   9   0      190.90      309.91     10.66 o
```

2	9	0	6.34	-2.64	5.82 o
3	9	0	94.70	131.73	20.41 o
0	1	1	191.02	37.69	8.69 o
1	1	1	1356.76	1108.50	61.21 o
0	2	1	793.16	708.13	25.11 o
1	2	1	259.44	311.18	16.58 o
2	2	1	890.00	885.47	20.31 o
0	3	1	129.93	160.27	6.56 o
1	3	1	925.53	957.98	11.33 o
2	3	1	76.33	84.25	2.92 o
3	3	1	741.82	765.80	17.15 o
0	4	1	634.92	703.29	16.27 o
1	4	1	153.77	175.50	4.46 o
2	4	1	512.58	538.59	8.33 o
3	4	1	96.20	119.31	5.33 o
4	4	1	477.39	516.63	15.87 o
0	5	1	29.50	18.45	0.92 o
1	5	1	644.53	671.88	13.46 o
2	5	1	68.62	80.13	1.76 o
3	5	1	512.13	574.39	11.83 o
4	5	1	40.36	26.91	1.02 o
5	5	1	412.02	391.60	12.88 o
0	6	1	374.91	418.30	14.00 o
1	6	1	75.64	92.62	3.49 o
2	6	1	395.24	423.56	9.45 o
3	6	1	52.54	49.65	1.93 o
4	6	1	315.43	318.04	6.07 o
5	6	1	29.34	29.98	2.05 o
6	6	1	260.07	251.19	8.43 o
0	7	1	36.51	18.62	7.61 o
1	7	1	421.87	438.99	12.44 o
2	7	1	20.67	14.73	2.01 o
3	7	1	369.74	350.14	17.87 o
4	7	1	29.26	12.13	1.98 o
5	7	1	273.69	266.27	8.35 o
6	7	1	14.40	11.60	2.79 o
0	8	1	263.84	238.63	19.12 o
1	8	1	34.73	37.18	4.80 o
2	8	1	245.95	221.59	10.65 o
3	8	1	21.28	27.14	2.58 o
4	8	1	228.68	209.95	6.04 o
0	9	1	10.17	19.32	3.69 o
1	9	1	268.54	225.08	5.56 o
2	9	1	16.58	15.04	4.30 o
3	9	1	229.99	222.05	24.43 o
0	1	2	35.22	41.67	1.82 o
1	1	2	28331.41	28350.03	1129.44 o
0	2	2	10930.26	12789.06	426.39 o
1	2	2	40.75	42.76	1.19 o
2	2	2	1227.98	1097.39	21.58 o
0	3	2	13.44	14.49	0.60 o
1	3	2	19719.55	20913.46	368.92 o
2	3	2	19.69	13.97	0.75 o
3	3	2	12700.34	14071.04	174.17 o
0	4	2	1046.77	920.61	15.01 o
1	4	2	35.94	31.83	1.52 o
2	4	2	3126.99	3388.80	41.24 o

3	4	2	20.95	31.16	0.99	o
4	4	2	580.10	488.99	12.98	o
0	5	2	8.72	5.60	1.19	o
1	5	2	9917.51	11407.47	113.24	o
2	5	2	10.56	11.06	1.26	o
3	5	2	8929.93	10167.00	175.83	o
4	5	2	12.48	9.00	1.14	o
5	5	2	4687.73	4621.02	177.39	o
0	6	2	1459.65	1354.43	20.29	o
1	6	2	24.10	32.36	1.67	o
2	6	2	504.87	409.35	6.57	o
3	6	2	15.96	7.52	1.17	o
4	6	2	810.17	657.07	11.74	o
5	6	2	9.95	26.57	2.15	o
6	6	2	119.23	98.80	4.77	o
0	7	2	5.29	-1.63	2.70	o
1	7	2	5411.56	6164.21	124.46	o
2	7	2	6.65	5.94	1.36	o
3	7	2	4001.23	4099.59	71.64	o
4	7	2	7.09	7.98	2.22	o
5	7	2	3580.39	4110.19	48.18	o
6	7	2	5.95	6.50	2.81	o
0	8	2	251.91	229.69	7.31	o
1	8	2	14.70	17.92	2.20	o
2	8	2	415.93	317.90	9.29	o
3	8	2	10.58	35.07	4.15	o
4	8	2	107.32	106.36	4.76	o
0	9	2	3.05	-4.99	4.02	o
1	9	2	2549.14	2622.54	81.56	o
2	9	2	3.39	7.37	3.81	o
0	0	3	988.55	955.48	69.58	o
0	1	3	234.78	327.00	27.14	o
1	1	3	641.72	616.47	18.51	o
0	2	3	1447.94	1434.47	51.40	o
1	2	3	143.10	156.67	8.65	o
2	2	3	779.20	766.11	23.33	o
0	3	3	22.15	15.44	1.35	o
1	3	3	542.19	507.88	7.59	o
2	3	3	145.42	204.96	10.23	o
3	3	3	410.23	540.22	13.11	o
0	4	3	631.46	659.10	13.79	o
1	4	3	140.54	180.81	8.48	o
2	4	3	796.53	889.65	20.40	o
3	4	3	62.97	53.66	2.59	o
4	4	3	501.25	489.63	9.46	o
0	5	3	89.16	63.32	3.29	o
1	5	3	397.78	428.45	15.54	o
2	5	3	19.15	19.68	1.49	o
3	5	3	367.76	322.41	7.08	o
4	5	3	56.97	63.65	2.81	o
5	5	3	245.94	277.03	12.15	o
0	6	3	533.68	630.70	22.94	o
1	6	3	71.05	66.58	3.19	o
2	6	3	432.85	403.75	6.88	o
3	6	3	42.88	70.11	2.34	o
4	6	3	441.29	454.35	8.95	o
5	6	3	26.23	14.92	3.22	o

6	6	3	283.14	252.56	7.02	o
0	7	3	8.99	19.07	3.56	o
1	7	3	294.69	295.79	11.05	o
2	7	3	44.30	23.65	2.42	o
3	7	3	232.75	263.25	9.66	o
4	7	3	12.78	10.23	2.02	o
5	7	3	211.23	180.16	6.61	o
6	7	3	17.59	26.80	15.37	o
0	8	3	307.04	250.83	19.69	o
1	8	3	28.04	39.20	4.86	o
2	8	3	328.75	350.41	13.27	o
3	8	3	27.77	25.14	2.15	o
4	8	3	257.51	212.29	7.48	o
0	9	3	20.07	17.61	4.03	o
1	9	3	184.07	161.92	5.07	o
2	9	3	5.81	28.91	3.80	o
0	0	4	41712.75	29457.70	611.12	o
0	1	4	17.98	30.13	2.44	o
1	1	4	1368.93	1059.36	42.66	o
0	2	4	20182.08	20328.05	1122.18	o
1	2	4	28.22	19.21	1.03	o
2	2	4	23538.08	24112.88	868.07	o
0	3	4	16.29	8.73	1.72	o
1	3	4	1252.88	1047.48	22.25	o
2	3	4	10.90	16.96	0.84	o
3	3	4	1335.15	1303.19	45.08	o
0	4	4	15723.21	17360.35	453.56	o
1	4	4	22.99	21.54	1.29	o
2	4	4	9823.47	10321.61	193.42	o
3	4	4	16.40	9.15	1.74	o
4	4	4	8657.19	8972.84	307.55	o
0	5	4	5.20	15.85	2.23	o
1	5	4	967.38	1002.90	30.39	o
2	5	4	12.85	3.58	1.62	o
3	5	4	615.36	538.21	11.46	o
4	5	4	8.94	11.97	1.47	o
5	5	4	552.82	682.00	25.92	o
0	6	4	6166.00	6446.08	158.62	o
1	6	4	15.24	9.88	1.74	o
2	6	4	6852.90	6817.07	120.61	o
3	6	4	10.94	18.50	1.19	o
4	6	4	3979.95	3877.75	54.79	o
5	6	4	7.42	3.18	1.73	o
6	6	4	3250.11	2789.62	108.30	o
0	7	4	8.51	-0.99	3.45	o
1	7	4	377.63	398.23	13.20	o
2	7	4	5.65	9.92	2.43	o
3	7	4	389.31	484.76	16.53	o
4	7	4	8.53	5.37	2.38	o
5	7	4	131.16	126.90	3.39	o
0	8	4	3773.48	3347.19	178.07	o
1	8	4	8.67	10.17	4.22	o
2	8	4	2919.84	2839.24	68.72	o
3	8	4	5.47	12.44	2.98	o
4	8	4	2727.59	2370.16	62.96	o
0	0	5	531.18	453.15	10.36	o
0	1	5	81.20	96.12	6.51	o

1	1	5	1039.47	1023.35	30.65 o
0	2	5	237.88	225.09	11.49 o
1	2	5	143.04	193.57	10.21 o
2	2	5	422.92	442.99	11.84 o
0	3	5	109.73	174.12	10.54 o
1	3	5	828.12	896.88	27.38 o
2	3	5	35.15	34.89	1.66 o
3	3	5	720.37	681.44	28.10 o
0	4	5	341.02	412.35	19.59 o
1	4	5	91.37	79.54	4.69 o
2	4	5	220.94	198.21	9.23 o
3	4	5	73.11	130.10	9.25 o
4	4	5	279.62	338.05	16.70 o
0	5	5	9.92	21.75	3.13 o
1	5	5	636.88	617.09	14.13 o
2	5	5	66.26	67.05	2.97 o
3	5	5	508.63	549.08	11.13 o
4	5	5	22.41	16.15	2.87 o
5	5	5	436.01	365.91	10.32 o
0	6	5	179.58	160.74	10.48 o
1	6	5	83.01	62.12	2.01 o
2	6	5	233.73	295.52	9.65 o
3	6	5	38.18	23.79	2.30 o
4	6	5	161.75	132.66	2.91 o
5	6	5	22.78	37.80	2.02 o
6	6	5	163.24	176.29	7.46 o
0	7	5	39.66	14.88	2.77 o
1	7	5	429.42	420.45	8.15 o
2	7	5	8.45	17.46	1.76 o
3	7	5	392.04	331.72	13.66 o
4	7	5	28.77	25.38	2.96 o
5	7	5	280.50	287.31	9.28 o
0	8	5	159.25	192.29	11.92 o
1	8	5	27.32	18.99	2.80 o
2	8	5	131.62	104.76	6.31 o
3	8	5	13.97	16.49	3.50 o
0	0	6	2398.95	1901.64	33.01 o
0	1	6	13.34	9.76	1.56 o
1	1	6	12495.92	12632.13	314.58 o
0	2	6	3039.70	3283.86	101.14 o
1	2	6	12.60	11.29	0.95 o
2	2	6	1514.95	1387.75	52.53 o
0	3	6	2.92	13.37	2.99 o
1	3	6	9914.11	10117.11	366.11 o
2	3	6	11.47	3.46	1.59 o
3	3	6	7808.85	7731.04	419.15 o
0	4	6	1075.88	1036.76	34.07 o
1	4	6	16.88	5.27	1.33 o
2	4	6	1371.84	1316.31	46.95 o
3	4	6	8.88	13.09	2.46 o
4	4	6	533.14	533.40	24.54 o
0	5	6	6.67	7.92	3.00 o
1	5	6	6282.99	6423.85	234.28 o
2	5	6	2.83	5.63	1.35 o
3	5	6	5384.02	6155.86	134.30 o
4	5	6	7.83	3.69	1.76 o
5	5	6	3545.57	3548.41	122.35 o

0	6	6	740.34	580.77	31.29 o
1	6	6	13.29	11.68	2.50 o
2	6	6	409.32	406.61	13.51 o
3	6	6	8.63	1.73	1.59 o
4	6	6	393.21	301.79	7.21 o
5	6	6	5.44	8.38	3.01 o
0	7	6	1.16	-3.59	2.58 o
1	7	6	3637.77	3707.87	103.99 o
2	7	6	4.95	2.09	2.69 o
3	7	6	2990.64	2860.08	72.08 o
4	7	6	2.84	7.65	3.12 o
0	8	6	183.08	199.15	23.79 o
1	8	6	8.64	8.17	2.37 o
2	8	6	233.83	138.52	4.88 o
3	8	6	7.03	14.86	16.44 o
0	0	7	732.40	845.31	18.06 o
0	1	7	79.67	107.65	4.99 o
1	1	7	211.00	194.81	3.21 o
0	2	7	830.55	899.26	25.08 o
1	2	7	68.14	55.22	2.40 o
2	2	7	631.52	654.71	15.70 o
0	3	7	23.79	20.65	2.83 o
1	3	7	203.51	183.41	6.98 o
2	3	7	60.68	105.17	7.59 o
3	3	7	178.35	218.06	13.90 o
0	4	7	537.33	519.30	15.90 o
1	4	7	70.58	89.67	7.27 o
2	4	7	607.87	665.70	26.93 o
3	4	7	36.39	23.24	3.03 o
4	4	7	443.00	433.75	26.72 o
0	5	7	39.12	56.38	6.30 o
1	5	7	176.95	197.64	7.30 o
2	5	7	14.66	18.77	1.71 o
3	5	7	159.99	142.43	9.86 o
4	5	7	31.58	54.95	7.14 o
5	5	7	120.39	187.56	18.46 o
0	6	7	454.27	544.00	35.15 o
1	6	7	41.10	21.32	5.47 o
2	6	7	385.01	349.28	10.75 o
3	6	7	27.92	44.11	3.51 o
4	6	7	383.36	409.49	11.16 o
5	6	7	15.85	9.90	2.11 o
0	7	7	6.60	20.66	3.85 o
1	7	7	140.41	133.67	12.30 o
2	7	7	23.72	25.88	2.78 o
3	7	7	115.04	152.78	8.95 o
4	7	7	9.08	7.80	7.01 o
0	8	7	279.18	203.37	18.87 o
1	8	7	19.26	39.96	7.61 o
0	0	8	11567.65	11667.65	210.35 o
0	1	8	4.27	8.54	1.68 o
1	1	8	775.59	648.48	12.47 o
0	2	8	9202.18	9091.28	284.08 o
1	2	8	7.45	3.83	1.40 o
2	2	8	8528.40	8985.75	208.07 o
0	3	8	4.57	2.92	1.50 o
1	3	8	682.42	576.18	15.03 o

2	3	8	2.95	8.75	1.50	o
3	3	8	574.47	575.61	28.59	o
0	4	8	6670.88	6383.43	268.29	o
1	4	8	7.60	4.87	1.34	o
2	4	8	5502.12	5907.27	222.40	o
3	4	8	6.04	4.67	3.09	o
4	4	8	4294.88	4175.80	142.73	o
0	5	8	1.16	8.30	4.66	o
1	5	8	434.61	465.45	15.04	o
2	5	8	4.69	8.30	1.69	o
3	5	8	344.11	342.86	15.93	o
4	5	8	3.05	0.75	3.56	o
5	5	8	222.59	323.27	9.01	o
0	6	8	3726.30	3962.43	111.52	o
1	6	8	6.27	6.64	2.77	o
2	6	8	3614.33	3402.68	99.28	o
3	6	8	4.23	13.16	2.97	o
4	6	8	2586.84	2623.23	102.00	o
0	7	8	3.53	13.16	6.08	o
1	7	8	196.30	258.77	7.79	o
2	7	8	1.77	5.91	4.09	o
3	7	8	168.85	227.52	51.42	o
0	0	9	124.79	78.53	6.32	o
0	1	9	39.59	22.70	2.68	o
1	1	9	617.85	615.69	22.81	o
0	2	9	99.99	88.74	3.51	o
1	2	9	49.15	49.61	2.44	o
2	2	9	118.99	119.31	6.24	o
0	3	9	30.22	48.54	2.40	o
1	3	9	552.32	558.32	13.75	o
2	3	9	24.49	20.29	3.01	o
3	3	9	487.83	476.98	25.03	o
0	4	9	105.48	118.94	9.89	o
1	4	9	42.46	25.93	1.67	o
2	4	9	89.12	85.70	4.36	o
3	4	9	30.82	54.11	4.20	o
4	4	9	97.18	115.77	8.98	o
0	5	9	11.04	25.80	3.34	o
1	5	9	454.46	413.52	12.91	o
2	5	9	21.57	36.69	2.78	o
3	5	9	395.96	419.64	18.19	o
4	5	9	14.57	5.09	3.21	o
0	6	9	71.34	62.24	8.68	o
1	6	9	27.88	33.59	5.49	o
2	6	9	84.80	121.80	8.31	o
3	6	9	18.78	8.18	2.86	o
0	7	9	13.58	-5.89	6.21	o
1	7	9	338.38	300.64	17.83	o
0	0	10	1074.24	1180.16	36.21	o
0	1	10	1.96	1.02	3.21	o
1	1	10	4689.95	4559.35	125.53	o
0	2	10	916.87	802.33	19.27	o
1	2	10	2.67	5.13	1.48	o
2	2	10	705.87	922.92	33.94	o
0	3	10	0.53	9.31	2.81	o
1	3	10	4051.55	3876.55	81.53	o
2	3	10	1.88	4.44	2.29	o

3	3	10	3505.24	3602.84	53.86 o
0	4	10	501.73	641.67	17.84 o
1	4	10	4.54	9.88	2.30 o
2	4	10	446.91	352.20	7.91 o
3	4	10	2.37	-0.62	3.89 o
4	4	10	255.52	362.51	10.63 o
0	5	10	0.78	-7.28	3.31 o
1	5	10	2956.16	3007.20	56.68 o
2	5	10	0.60	4.64	2.58 o
3	5	10	2567.48	2619.57	42.76 o
0	6	10	260.12	161.25	18.13 o
1	6	10	4.43	4.06	5.26 o
2	6	10	200.86	265.43	14.55 o
0	0	11	458.68	533.19	20.57 o
0	1	11	25.24	25.14	4.95 o
1	1	11	63.73	53.56	4.68 o
0	2	11	447.42	422.61	19.87 o
1	2	11	27.85	10.72	3.50 o
2	2	11	416.82	434.70	21.98 o
0	3	11	13.65	10.59	2.74 o
1	3	11	61.99	54.37	5.35 o
2	3	11	18.31	35.50	5.18 o
3	3	11	57.61	92.54	15.25 o
0	4	11	368.97	396.20	16.08 o
1	4	11	28.42	31.64	3.50 o
2	4	11	369.10	319.52	12.15 o
3	4	11	17.62	6.40	3.87 o
0	5	11	9.95	4.34	6.55 o
1	5	11	59.47	62.64	9.40 o
2	5	11	9.43	0.81	3.41 o
0	0	12	4007.07	3829.73	104.35 o
0	1	12	0.41	-6.06	4.00 o
1	1	12	219.69	221.74	9.00 o
0	2	12	3546.34	4188.65	101.31 o
1	2	12	0.93	2.49	3.32 o
2	2	12	3189.45	2888.74	122.56 o
0	3	12	0.20	-4.13	2.91 o
1	3	12	199.40	227.70	5.51 o
2	3	12	0.38	4.18	4.39 o
3	3	12	175.10	191.98	13.61 o
0	4	12	2641.96	2483.24	61.67 o
1	4	12	1.58	6.20	2.74 o
0	0	13	27.31	9.21	6.54 o
0	1	13	14.24	10.75	3.37 o
1	1	13	355.40	356.44	10.48 o
0	2	13	26.75	43.57	5.78 o
1	2	13	16.87	18.36	6.63 o

```
#
# h,k,l, Fc-squared, Fo-squared, sigma(Fo-squared) and status flag
#
data_sm
_shelx_title ' sm in Pnma'
_shelx_refln_list_code   4
_shelx_F_calc_maximum      256.45
_exptl_crystal_F_000       432.00
_shelx_F_squared_multiplier     1.000
loop_
 _refln_index_h
 _refln_index_k
 _refln_index_l
 _refln_F_squared_calc
 _refln_F_squared_meas
 _refln_F_squared_sigma
 _refln_observed_status
   2   0   0    36480.42    34924.36    289.97 o
   4   0   0     2596.99     3469.75     69.71 o
   6   0   0     1538.90     1565.46     43.52 o
   8   0   0     3041.51     2718.13     65.01 o
  10   0   0       53.41       40.83     15.29 o
  12   0   0      136.86      120.33     16.36 o
  14   0   0      435.38      516.55     24.90 o
   2   1   0    16391.46    19749.06    150.11 o
   4   1   0    20810.70    21343.22    257.55 o
   6   1   0     3123.86     3175.95    102.84 o
   8   1   0      108.94      164.38     55.47 o
  10   1   0     1475.02     1306.81     27.74 o
  12   1   0      973.50      920.37     23.48 o
  14   1   0      103.48       98.46     23.37 o
   0   2   0    16442.23    17928.67    167.24 o
   2   2   0    12792.81    16616.00    206.23 o
   4   2   0     1963.45     2506.65     54.30 o
   6   2   0    11001.24     9992.89    179.02 o
   8   2   0     6378.12     5524.43    108.41 o
  10   2   0     2100.29     1810.32     48.11 o
  12   2   0       16.80       58.74     13.98 o
  14   2   0       63.80       67.48     14.41 o
   2   3   0    19097.37    20456.03    249.60 o
   4   3   0    11871.91    13126.47    187.37 o
   6   3   0     4252.24     4063.84     82.66 o
   8   3   0      200.41      217.95     19.22 o
  10   3   0     1440.82     1337.41     39.78 o
  12   3   0      710.71      710.40     29.49 o
  14   3   0      156.55      145.44     15.94 o
   0   4   0    65765.84    50086.49    395.67 o
   2   4   0    27027.42    27345.40    308.29 o
   4   4   0     1349.24     1625.06     43.96 o
   6   4   0     1436.94     1378.14     40.89 o
   8   4   0     1917.33     1734.53     46.80 o
  10   4   0      104.93      103.29     16.16 o
  12   4   0      160.24      133.65     17.25 o
   2   5   0     7101.71     7926.07    145.35 o
   4   5   0    15057.65    14034.67    207.36 o
   6   5   0     1613.45     1592.36     43.30 o
   8   5   0       47.19       47.82     13.76 o
```

10	5	0	1048.46	938.05	33.43	o
12	5	0	860.75	829.53	31.46	o
0	6	0	12805.39	12944.44	184.82	o
2	6	0	2768.66	3256.63	69.46	o
4	6	0	787.97	879.17	30.59	o
6	6	0	5979.51	5323.87	103.37	o
8	6	0	5191.60	4410.38	87.23	o
10	6	0	1079.90	1058.89	34.52	o
12	6	0	37.46	37.12	14.19	o
2	7	0	7158.27	6834.91	128.74	o
4	7	0	6265.93	5730.10	106.75	o
6	7	0	2191.22	1944.18	52.06	o
8	7	0	106.72	121.63	16.60	o
10	7	0	932.68	890.76	31.68	o
12	7	0	472.43	529.88	25.34	o
0	8	0	16448.66	13686.38	254.94	o
2	8	0	11774.66	10780.03	184.22	o
4	8	0	451.13	529.29	24.68	o
6	8	0	853.00	773.49	30.37	o
8	8	0	646.79	677.15	27.53	o
10	8	0	137.45	161.38	16.81	o
12	8	0	141.73	164.00	16.16	o
2	9	0	3349.20	3075.00	72.49	o
4	9	0	4972.57	4436.02	86.38	o
6	9	0	1030.80	891.35	33.00	o
8	9	0	50.29	58.52	15.07	o
10	9	0	574.19	588.90	27.09	o
12	9	0	428.84	518.95	23.81	o
0	10	0	4624.36	4175.72	83.74	o
2	10	0	698.91	712.70	28.40	o
4	10	0	322.30	313.86	21.19	o
6	10	0	2421.12	2135.87	54.46	o
8	10	0	2726.46	2453.59	56.43	o
10	10	0	473.43	515.69	24.68	o
12	10	0	26.43	40.18	12.66	o
2	11	0	1802.24	1710.15	47.01	o
4	11	0	2952.12	2507.30	58.21	o
6	11	0	544.88	522.94	25.78	o
8	11	0	21.70	37.12	13.98	o
10	11	0	411.07	404.28	23.15	o
0	12	0	5338.99	4458.66	87.69	o
2	12	0	3655.34	3056.78	69.40	o
4	12	0	211.61	200.48	18.13	o
6	12	0	269.92	257.93	20.75	o
8	12	0	246.59	233.24	19.66	o
10	12	0	47.44	61.14	12.68	o
2	13	0	1219.00	1152.80	34.53	o
4	13	0	1197.22	1114.07	35.18	o
6	13	0	501.17	484.47	24.25	o
8	13	0	32.11	35.59	13.76	o
10	13	0	254.79	270.15	19.44	o
0	14	0	920.34	874.18	31.68	o
2	14	0	245.69	249.84	20.09	o
4	14	0	145.35	155.05	17.47	o
6	14	0	892.03	892.91	31.46	o
8	14	0	884.21	928.50	31.90	o
2	15	0	435.52	402.98	23.81	o

4	15	0	953.34	1004.60	33.21	o
6	15	0	140.47	146.09	16.81	o
8	15	0	6.88	14.19	12.01	o
0	16	0	1797.32	1720.15	44.81	o
2	16	0	873.74	880.01	31.68	o
4	16	0	88.17	105.91	15.50	o
6	16	0	54.38	73.37	13.76	o
8	16	0	112.31	120.54	15.07	o
2	17	0	304.76	312.53	21.40	o
4	17	0	343.08	383.08	22.50	o
6	17	0	128.80	166.71	16.16	o
0	18	0	156.38	154.83	16.82	o
2	18	0	80.91	89.31	15.80	o
4	18	0	46.80	60.05	12.45	o
2	19	0	125.73	144.56	16.38	o
1	0	1	12210.05	17617.78	107.40	o
2	0	1	53.41	159.72	14.76	o
3	0	1	244.24	617.29	76.79	o
4	0	1	1604.85	2163.96	37.58	o
5	0	1	7877.43	8348.13	146.17	o
6	0	1	5.12	7.59	8.76	o
7	0	1	11490.14	9961.04	229.16	o
8	0	1	21.94	14.99	10.26	o
9	0	1	4282.07	3702.83	84.62	o
10	0	1	0.81	1.34	9.38	o
11	0	1	369.50	387.79	32.98	o
12	0	1	21.50	14.05	9.76	o
13	0	1	16.42	23.60	9.19	o
14	0	1	4.15	9.56	8.11	o
0	1	1	475.51	1096.22	15.80	o
1	1	1	6751.14	11170.01	159.07	o
2	1	1	86.81	255.00	16.17	o
3	1	1	26532.62	27565.82	360.20	o
4	1	1	25.42	46.00	8.36	o
5	1	1	12398.89	12728.32	170.86	o
6	1	1	67.50	75.58	7.92	o
7	1	1	725.46	785.72	20.25	o
8	1	1	87.07	85.09	8.02	o
9	1	1	561.07	550.30	17.12	o
10	1	1	0.14	-3.50	5.98	o
11	1	1	1112.49	1056.62	18.42	o
12	1	1	0.27	3.84	6.28	o
13	1	1	329.05	366.32	16.14	o
14	1	1	4.50	4.26	5.82	o
1	2	1	51387.01	45788.03	422.01	o
2	2	1	1209.41	2116.44	31.47	o
3	2	1	10011.00	12810.97	274.89	o
4	2	1	2.28	10.25	8.95	o
5	2	1	704.48	798.30	24.15	o
6	2	1	303.47	285.20	15.18	o
7	2	1	2838.40	2667.75	66.76	o
8	2	1	2.23	6.08	8.56	o
9	2	1	902.64	830.96	22.32	o
10	2	1	9.84	12.02	8.72	o
11	2	1	10.58	17.06	8.84	o
12	2	1	0.49	1.22	8.85	o
13	2	1	459.96	496.27	24.57	o

14	2	1	4.42	-2.40	7.87 o
0	3	1	669.39	1444.33	77.75 o
1	3	1	7169.53	10008.01	113.84 o
2	3	1	469.90	749.48	17.50 o
3	3	1	19848.97	20857.08	257.34 o
4	3	1	89.37	106.87	11.36 o
5	3	1	10471.64	10608.76	128.72 o
6	3	1	173.54	168.08	12.43 o
7	3	1	790.76	739.05	21.39 o
8	3	1	1.28	7.98	8.64 o
9	3	1	622.18	570.91	19.05 o
10	3	1	38.80	34.90	13.10 o
11	3	1	927.09	858.51	25.46 o
12	3	1	9.74	-0.92	9.83 o
13	3	1	312.12	351.37	15.44 o
14	3	1	3.71	-1.93	8.11 o
1	4	1	7765.59	9668.74	129.78 o
2	4	1	87.43	111.71	19.76 o
3	4	1	15.64	125.88	58.63 o
4	4	1	372.22	449.00	16.60 o
5	4	1	6123.58	6144.84	76.63 o
6	4	1	31.54	43.08	8.98 o
7	4	1	8807.23	7494.97	113.49 o
8	4	1	2.47	0.36	8.11 o
9	4	1	3541.53	3038.00	46.67 o
10	4	1	1.74	3.39	8.45 o
11	4	1	334.87	284.70	15.13 o
12	4	1	6.96	-1.08	9.23 o
13	4	1	19.93	26.47	15.18 o
0	5	1	948.02	1367.64	38.27 o
1	5	1	2681.80	3531.87	33.92 o
2	5	1	176.44	259.10	12.79 o
3	5	1	18197.90	14767.65	184.41 o
4	5	1	2.30	-1.97	8.27 o
5	5	1	8097.71	7662.59	130.07 o
6	5	1	14.63	12.51	8.57 o
7	5	1	442.13	418.09	16.68 o
8	5	1	146.03	123.08	14.19 o
9	5	1	360.04	340.40	15.59 o
10	5	1	8.31	5.58	8.54 o
11	5	1	895.17	868.19	22.24 o
12	5	1	0.67	-4.92	8.26 o
13	5	1	256.31	288.78	19.87 o
1	6	1	22312.10	20096.69	146.94 o
2	6	1	49.17	68.48	9.05 o
3	6	1	4076.39	4500.58	80.83 o
4	6	1	276.41	296.29	14.13 o
5	6	1	236.94	228.34	13.36 o
6	6	1	13.38	10.75	8.72 o
7	6	1	1889.43	1708.92	32.00 o
8	6	1	5.56	-1.63	8.27 o
9	6	1	568.16	511.21	29.16 o
10	6	1	2.83	6.38	8.54 o
11	6	1	14.63	43.25	26.09 o
12	6	1	4.49	0.66	8.80 o
13	6	1	302.55	325.77	22.93 o
0	7	1	27.49	44.80	8.72 o

1	7	1	2453.34	2727.49	40.30	o
2	7	1	113.31	132.86	10.88	o
3	7	1	8940.78	8396.68	100.80	o
4	7	1	26.13	19.19	8.57	o
5	7	1	5378.14	4836.65	112.21	o
6	7	1	93.72	82.05	10.35	o
7	7	1	449.59	446.19	34.51	o
8	7	1	1.24	-3.18	8.17	o
9	7	1	371.36	328.88	15.89	o
10	7	1	20.46	7.98	9.88	o
11	7	1	604.82	602.76	27.85	o
12	7	1	4.48	8.89	8.33	o
13	7	1	206.00	248.12	17.80	o
1	8	1	3120.91	3053.83	34.10	o
2	8	1	195.26	215.96	13.76	o
3	8	1	11.92	353.30	203.95	o
4	8	1	4.86	10.37	8.49	o
5	8	1	3297.77	2892.45	46.52	o
6	8	1	123.55	117.89	22.71	o
7	8	1	4481.48	3760.57	55.30	o
8	8	1	1.80	5.52	8.30	o
9	8	1	2047.13	1877.05	33.39	o
10	8	1	3.64	2.40	8.64	o
11	8	1	229.68	233.76	13.51	o
12	8	1	0.20	7.90	8.41	o
0	9	1	51.79	64.25	9.29	o
1	9	1	1160.04	1207.72	24.14	o
2	9	1	1.24	1.43	8.36	o
3	9	1	5543.56	5055.07	133.83	o
4	9	1	7.90	7.19	8.41	o
5	9	1	3439.15	3040.72	47.45	o
6	9	1	19.24	22.86	8.88	o
7	9	1	240.90	239.52	15.72	o
8	9	1	28.08	24.67	10.48	o
9	9	1	216.41	216.44	13.42	o
10	9	1	0.50	-6.80	8.80	o
11	9	1	465.65	481.22	34.73	o
12	9	1	0.76	-7.53	8.18	o
1	10	1	7670.19	6619.08	60.88	o
2	10	1	1.69	6.01	8.39	o
3	10	1	1453.52	1383.61	61.32	o
4	10	1	195.76	161.15	12.68	o
5	10	1	49.95	64.85	10.27	o
6	10	1	0.24	4.25	7.94	o
7	10	1	796.39	734.37	20.62	o
8	10	1	5.97	12.09	8.48	o
9	10	1	256.94	249.55	13.96	o
10	10	1	0.23	4.91	8.49	o
11	10	1	11.43	20.04	7.71	o
12	10	1	7.06	12.70	8.10	o
0	11	1	44.79	35.77	9.32	o
1	11	1	620.80	598.40	13.32	o
2	11	1	0.50	0.99	8.56	o
3	11	1	3178.46	2817.92	46.27	o
4	11	1	1.66	9.03	8.30	o
5	11	1	2020.08	1761.98	32.93	o
6	11	1	14.40	11.43	8.83	o

7	11	1	154.01	162.05	18.45 o
8	11	1	21.09	16.72	9.02 o
9	11	1	131.98	152.55	20.75 o
10	11	1	0.04	-0.66	7.87 o
11	11	1	316.00	410.99	17.04 o
1	12	1	868.84	802.24	17.91 o
2	12	1	50.94	39.41	9.65 o
3	12	1	1.03	5.72	9.18 o
4	12	1	4.53	11.93	8.26 o
5	12	1	1235.14	1109.30	26.24 o
6	12	1	35.58	28.80	9.65 o
7	12	1	1818.89	1659.88	31.46 o
8	12	1	0.01	3.89	8.64 o
9	12	1	873.83	927.66	22.32 o
10	12	1	2.49	4.82	9.06 o
11	12	1	106.77	143.96	18.23 o
0	13	1	2.94	7.44	8.11 o
1	13	1	405.96	357.98	11.60 o
2	13	1	20.94	21.10	8.87 o
3	13	1	1621.60	1443.38	30.29 o
4	13	1	6.70	10.70	8.80 o
5	13	1	1120.64	1039.24	51.24 o
6	13	1	19.26	18.77	12.99 o
7	13	1	106.60	108.79	11.19 o
8	13	1	0.30	5.47	8.30 o
9	13	1	102.81	121.08	10.38 o
10	13	1	6.63	12.82	7.86 o
1	14	1	2252.82	2047.67	31.58 o
2	14	1	7.74	13.68	8.87 o
3	14	1	523.82	454.45	19.11 o
4	14	1	22.70	32.80	9.26 o
5	14	1	15.73	33.31	11.68 o
6	14	1	5.60	2.78	8.10 o
7	14	1	235.22	241.33	13.51 o
8	14	1	0.07	-0.62	8.48 o
9	14	1	92.93	103.05	10.65 o
0	15	1	26.94	20.83	9.05 o
1	15	1	153.55	154.66	9.38 o
2	15	1	3.08	2.73	8.49 o
3	15	1	917.90	837.24	27.31 o
4	15	1	0.43	7.57	8.54 o
5	15	1	624.07	611.74	19.38 o
6	15	1	1.74	-0.02	8.30 o
7	15	1	45.79	44.16	9.01 o
8	15	1	13.98	17.08	8.41 o
9	15	1	41.54	65.91	10.70 o
1	16	1	206.13	201.42	9.22 o
2	16	1	2.73	2.84	8.80 o
3	16	1	4.66	4.27	8.21 o
4	16	1	17.00	25.98	9.03 o
5	16	1	347.83	380.84	16.14 o
6	16	1	0.86	1.42	8.34 o
7	16	1	610.32	683.77	19.46 o
8	16	1	0.88	4.97	7.49 o
0	17	1	0.15	4.35	7.63 o
1	17	1	101.06	97.25	7.84 o
2	17	1	2.94	1.81	8.39 o

3	17	1	437.77	482.07	16.60	o
4	17	1	1.04	10.36	8.39	o
5	17	1	311.89	342.93	14.96	o
6	17	1	5.80	-11.16	7.83	o
1	18	1	576.45	637.13	13.65	o
2	18	1	7.07	2.86	8.23	o
3	18	1	158.70	194.13	12.09	o
4	18	1	0.56	1.59	7.95	o
5	18	1	5.46	5.81	7.95	o
0	19	1	1.03	5.31	7.64	o
1	19	1	43.50	59.24	7.08	o
2	19	1	0.11	4.63	7.41	o
0	0	2	53950.06	49524.50	438.91	o
1	0	2	177.20	508.21	19.37	o
2	0	2	40702.02	40771.44	448.65	o
3	0	2	960.53	1519.74	44.40	o
4	0	2	956.08	1320.12	46.13	o
5	0	2	229.30	278.04	23.59	o
6	0	2	2238.43	2403.43	57.77	o
7	0	2	32.63	33.63	15.94	o
8	0	2	1451.75	1406.06	43.06	o
9	0	2	23.40	22.71	16.60	o
10	0	2	255.87	310.78	22.06	o
11	0	2	122.81	107.22	17.91	o
12	0	2	252.05	224.94	21.18	o
13	0	2	15.88	33.63	12.45	o
14	0	2	412.21	464.56	25.12	o
1	1	2	3119.71	5703.76	60.48	o
2	1	2	16320.17	20572.52	214.85	o
3	1	2	255.86	452.36	32.11	o
4	1	2	15078.13	16148.18	398.87	o
5	1	2	7.73	18.50	11.16	o
6	1	2	3815.51	3863.35	58.56	o
7	1	2	211.92	195.26	14.82	o
8	1	2	79.93	79.31	12.03	o
9	1	2	67.00	67.06	11.66	o
10	1	2	1193.25	1070.00	27.03	o
11	1	2	0.79	6.34	9.02	o
12	1	2	715.39	705.30	21.70	o
13	1	2	2.28	2.57	8.85	o
14	1	2	110.67	140.37	15.83	o
0	2	2	23521.50	26756.06	328.62	o
1	2	2	819.01	1480.00	58.84	o
2	2	2	2434.62	3870.95	74.35	o
3	2	2	229.57	320.44	22.06	o
4	2	2	1557.60	1997.55	49.88	o
5	2	2	142.80	165.98	19.22	o
6	2	2	8379.52	7961.42	134.69	o
7	2	2	7.82	12.88	13.97	o
8	2	2	7327.75	5947.57	119.67	o
9	2	2	149.42	124.70	17.47	o
10	2	2	1269.45	1161.32	38.03	o
11	2	2	46.39	28.61	15.07	o
12	2	2	46.37	43.89	14.41	o
13	2	2	20.95	17.47	13.10	o
14	2	2	61.32	70.31	14.85	o
1	3	2	1555.11	2496.33	39.48	o

2	3	2	9693.08	12046.29	187.20	o
3	3	2	772.93	1010.56	34.54	o
4	3	2	16625.88	16126.36	233.15	o
5	3	2	160.81	166.63	18.78	o
6	3	2	2341.80	2443.45	58.43	o
7	3	2	83.91	95.65	15.94	o
8	3	2	26.36	41.05	14.19	o
9	3	2	64.68	70.53	14.63	o
10	3	2	1038.57	978.91	33.87	o
11	3	2	7.19	11.57	13.10	o
12	3	2	786.83	814.42	31.46	o
13	3	2	11.81	14.19	11.79	o
0	4	2	39708.65	34452.02	385.79	o
1	4	2	31.74	43.18	10.11	o
2	4	2	21259.03	21600.88	309.38	o
3	4	2	427.70	589.89	25.78	o
4	4	2	793.62	1045.78	34.31	o
5	4	2	159.82	158.33	17.91	o
6	4	2	1516.80	1480.50	44.61	o
7	4	2	4.64	-3.06	11.79	o
8	4	2	1399.61	1261.67	41.75	o
9	4	2	52.09	51.53	14.63	o
10	4	2	129.07	136.05	17.47	o
11	4	2	72.43	69.00	14.19	o
12	4	2	174.03	178.20	19.00	o
13	4	2	16.71	10.04	11.67	o
1	5	2	1528.91	1911.93	59.62	o
2	5	2	10073.90	10429.32	180.04	o
3	5	2	28.50	58.96	13.76	o
4	5	2	8302.91	8199.25	142.51	o
5	5	2	4.96	8.73	11.79	o
6	5	2	3107.37	3000.55	67.87	o
7	5	2	209.25	190.00	18.78	o
8	5	2	83.98	89.97	15.94	o
9	5	2	49.54	48.04	15.29	o
10	5	2	932.60	858.66	32.12	o
11	5	2	0.09	3.71	13.32	o
12	5	2	494.29	444.49	25.56	o
13	5	2	0.15	-0.44	10.92	o
0	6	2	6827.95	7013.73	131.90	o
1	6	2	19.56	25.67	12.88	o
2	6	2	2554.21	2877.43	62.85	o
3	6	2	325.47	332.89	20.97	o
4	6	2	1039.72	1139.02	37.81	o
5	6	2	109.99	107.88	15.29	o
6	6	2	5709.73	5040.20	93.67	o
7	6	2	3.51	9.17	12.45	o
8	6	2	4186.91	3680.76	75.77	o
9	6	2	37.59	33.19	13.76	o
10	6	2	1165.81	1093.25	35.84	o
11	6	2	64.51	65.29	14.41	o
12	6	2	14.90	24.89	12.45	o
13	6	2	11.44	2.40	11.14	o
1	7	2	571.20	663.20	32.56	o
2	7	2	4567.90	4458.92	94.12	o
3	7	2	260.29	275.86	20.75	o
4	7	2	7990.82	7165.66	138.12	o

5	7	2	71.64	59.83	14.19	o
6	7	2	1346.22	1208.57	39.35	o
7	7	2	53.46	53.50	13.76	o
8	7	2	20.48	31.44	13.98	o
9	7	2	36.04	47.82	15.29	o
10	7	2	647.30	594.61	28.62	o
11	7	2	4.98	13.32	12.66	o
12	7	2	523.56	545.19	25.77	o
13	7	2	7.53	9.17	11.14	o
0	8	2	17381.01	14816.09	222.97	o
1	8	2	150.37	143.09	11.97	o
2	8	2	6875.28	6266.18	127.03	o
3	8	2	103.70	89.52	15.07	o
4	8	2	460.00	487.78	24.03	o
5	8	2	62.90	63.98	14.41	o
6	8	2	561.80	505.93	26.65	o
7	8	2	2.75	8.08	13.54	o
8	8	2	952.82	878.79	31.90	o
9	8	2	75.93	61.58	14.85	o
10	8	2	25.46	49.13	14.63	o
11	8	2	23.44	32.32	12.88	o
12	8	2	80.06	113.99	14.19	o
1	9	2	406.69	424.16	16.29	o
2	9	2	3260.07	2977.64	67.88	o
3	9	2	52.49	56.78	14.63	o
4	9	2	4137.04	3748.84	74.92	o
5	9	2	6.02	7.64	11.35	o
6	9	2	1138.06	1024.06	34.31	o
7	9	2	62.86	43.89	15.94	o
8	9	2	22.18	26.20	12.88	o
9	9	2	29.77	34.94	14.19	o
10	9	2	499.09	497.57	25.34	o
11	9	2	0.25	5.68	11.79	o
12	9	2	315.10	360.14	21.40	o
0	10	2	1976.32	1775.97	46.81	o
1	10	2	0.22	8.97	8.08	o
2	10	2	1008.60	950.63	33.65	o
3	10	2	151.14	152.21	16.38	o
4	10	2	476.83	467.67	25.78	o
5	10	2	51.54	48.70	14.19	o
6	10	2	2674.73	2281.00	56.66	o
7	10	2	8.68	18.12	12.01	o
8	10	2	1840.80	1744.31	45.25	o
9	10	2	9.48	35.16	13.10	o
10	10	2	670.24	617.33	27.52	o
11	10	2	41.74	36.47	12.67	o
12	10	2	5.97	-1.97	10.92	o
1	11	2	234.16	217.43	18.24	o
2	11	2	1866.45	1670.16	45.48	o
3	11	2	27.52	26.86	13.54	o
4	11	2	2300.56	2008.68	52.71	o
5	11	2	1.23	21.62	12.01	o
6	11	2	739.61	687.51	27.75	o
7	11	2	46.94	36.47	13.54	o
8	11	2	23.33	43.02	14.85	o
9	11	2	14.36	17.91	12.66	o
10	11	2	315.98	331.31	21.40	o

11	11	2	0.33	2.62	10.70 o
0	12	2	5416.88	4571.02	91.19 o
1	12	2	37.27	29.09	10.03 o
2	12	2	2418.53	2125.21	52.71 o
3	12	2	38.90	44.98	13.98 o
4	12	2	180.79	152.00	17.47 o
5	12	2	19.34	5.90	13.54 o
6	12	2	173.03	159.42	18.56 o
7	12	2	0.78	-1.31	12.66 o
8	12	2	352.82	356.87	22.71 o
9	12	2	29.60	29.04	13.98 o
10	12	2	12.61	12.23	12.01 o
11	12	2	12.91	10.70	11.14 o
1	13	2	97.62	101.53	10.96 o
2	13	2	826.77	752.66	30.59 o
3	13	2	47.66	45.64	13.10 o
4	13	2	1605.05	1431.96	42.62 o
5	13	2	16.20	21.18	12.45 o
6	13	2	294.89	314.27	20.53 o
7	13	2	11.33	7.86	12.45 o
8	13	2	3.54	17.91	13.54 o
9	13	2	11.79	12.01	11.14 o
10	13	2	191.92	238.91	17.69 o
0	14	2	631.19	619.52	26.43 o
1	14	2	4.66	5.98	8.80 o
2	14	2	178.25	170.34	18.13 o
3	14	2	29.75	24.24	12.66 o
4	14	2	155.40	172.52	17.47 o
5	14	2	15.08	14.63	12.88 o
6	14	2	896.82	893.13	31.02 o
7	14	2	0.73	-8.52	12.66 o
8	14	2	759.22	801.51	28.84 o
9	14	2	8.71	8.52	11.14 o
1	15	2	75.20	69.78	10.65 o
2	15	2	565.55	541.28	26.43 o
3	15	2	3.69	-3.06	11.35 o
4	15	2	614.35	556.15	27.52 o
5	15	2	0.31	-1.97	12.23 o
6	15	2	259.82	262.51	20.09 o
7	15	2	18.21	21.18	12.66 o
8	15	2	8.87	11.57	11.79 o
0	16	2	1316.65	1279.29	39.55 o
1	16	2	1.17	7.41	8.76 o
2	16	2	828.52	796.97	31.02 o
3	16	2	18.54	12.45	12.66 o
4	16	2	53.07	51.75	13.98 o
5	16	2	6.50	19.65	11.35 o
6	16	2	58.02	65.29	13.54 o
7	16	2	0.40	4.59	11.57 o
1	17	2	27.13	31.69	8.64 o
2	17	2	225.55	255.29	18.56 o
3	17	2	11.61	16.38	11.35 o
4	17	2	422.82	485.53	23.81 o
5	17	2	3.18	2.40	11.14 o
6	17	2	95.35	85.16	14.85 o
0	18	2	188.17	221.88	18.13 o
1	18	2	5.21	8.30	7.21 o

2	18	2	26.39	30.13	12.23	o
3	18	2	4.75	-1.97	11.35	o
4	18	2	42.14	38.87	12.67	o
5	18	2	3.18	12.01	10.26	o
1	19	2	16.41	26.72	8.23	o
2	19	2	123.66	143.91	15.50	o
1	0	3	8209.86	11654.71	137.17	o
2	0	3	2088.97	3212.74	72.08	o
3	0	3	578.67	803.33	32.78	o
4	0	3	937.70	1162.96	40.44	o
5	0	3	7056.08	7199.47	135.05	o
6	0	3	638.93	719.69	32.55	o
7	0	3	6985.46	6064.84	112.88	o
8	0	3	4.96	12.23	13.76	o
9	0	3	3387.91	3006.87	66.98	o
10	0	3	65.34	84.94	16.16	o
11	0	3	466.32	410.63	25.12	o
12	0	3	22.03	43.24	15.50	o
13	0	3	30.12	35.81	13.10	o
0	1	3	784.42	1283.90	27.83	o
1	1	3	4686.69	7073.10	61.07	o
2	1	3	465.29	721.66	22.55	o
3	1	3	13800.65	15465.06	170.50	o
4	1	3	109.22	142.30	14.27	o
5	1	3	7456.24	7368.86	182.41	o
6	1	3	563.73	583.36	21.63	o
7	1	3	450.81	497.92	32.22	o
8	1	3	287.75	282.52	15.82	o
9	1	3	681.84	642.05	22.01	o
10	1	3	46.25	32.14	11.03	o
11	1	3	913.60	842.97	23.47	o
12	1	3	11.08	7.30	9.19	o
13	1	3	315.58	326.06	15.42	o
1	2	3	39874.16	36948.80	339.78	o
2	2	3	819.85	1143.20	40.23	o
3	2	3	5464.35	6619.43	121.62	o
4	2	3	2009.78	2403.75	59.97	o
5	2	3	15.45	124.47	18.78	o
6	2	3	214.45	203.99	20.31	o
7	2	3	2302.55	2223.98	53.82	o
8	2	3	2.69	13.32	13.32	o
9	2	3	635.82	581.74	29.05	o
10	2	3	54.14	55.03	16.16	o
11	2	3	24.76	31.88	14.63	o
12	2	3	48.47	42.36	14.41	o
13	2	3	249.50	269.71	20.53	o
0	3	3	1827.31	2672.88	59.56	o
1	3	3	1482.65	2161.84	61.93	o
2	3	3	83.81	136.71	19.00	o
3	3	3	13843.30	14646.96	229.19	o
4	3	3	46.21	62.67	14.63	o
5	3	3	6783.00	6895.67	123.75	o
6	3	3	403.88	351.24	24.90	o
7	3	3	195.41	199.61	19.66	o
8	3	3	397.25	349.69	24.24	o
9	3	3	356.42	325.43	23.59	o
10	3	3	11.17	10.70	13.10	o

11	3	3	1040.83	973.41	34.30	o
12	3	3	2.37	25.11	13.32	o
13	3	3	265.04	296.58	20.09	o
1	4	3	6539.30	7808.34	206.09	o
2	4	3	1019.20	1287.80	40.89	o
3	4	3	117.72	113.56	17.47	o
4	4	3	1031.16	1125.97	35.85	o
5	4	3	4346.67	4407.99	90.33	o
6	4	3	339.76	323.48	23.15	o
7	4	3	6181.29	5375.08	99.39	o
8	4	3	0.18	1.53	12.88	o
9	4	3	2760.17	2351.50	56.00	o
10	4	3	53.26	55.46	15.50	o
11	4	3	344.81	333.50	22.50	o
12	4	3	26.37	33.85	13.76	o
13	4	3	12.26	6.55	13.10	o
0	5	3	315.26	420.29	24.03	o
1	5	3	3625.37	4403.05	61.49	o
2	5	3	500.19	578.98	27.53	o
3	5	3	7937.13	8077.66	145.78	o
4	5	3	81.42	78.62	15.29	o
5	5	3	4899.51	4847.11	92.99	o
6	5	3	437.95	427.48	24.25	o
7	5	3	447.71	395.14	25.12	o
8	5	3	153.98	137.58	18.78	o
9	5	3	663.23	630.24	29.27	o
10	5	3	57.12	69.98	15.07	o
11	5	3	618.37	639.61	27.09	o
12	5	3	14.17	12.01	12.01	o
13	5	3	259.07	257.70	19.66	o
1	6	3	17129.82	15954.85	181.93	o
2	6	3	698.44	753.02	31.03	o
3	6	3	4306.48	4435.19	88.59	o
4	6	3	698.36	721.70	29.06	o
5	6	3	145.90	160.08	18.56	o
6	6	3	275.46	281.52	21.62	o
7	6	3	1064.35	973.55	34.75	o
8	6	3	0.72	-11.57	12.88	o
9	6	3	431.82	444.05	25.34	o
10	6	3	38.69	30.35	15.07	o
11	6	3	5.83	11.35	13.97	o
12	6	3	22.11	13.54	12.01	o
13	6	3	249.05	293.08	20.31	o
0	7	3	766.60	792.82	31.69	o
1	7	3	863.69	1003.15	73.65	o
2	7	3	82.87	103.51	15.94	o
3	7	3	6635.81	6318.59	116.22	o
4	7	3	26.08	26.64	13.10	o
5	7	3	3685.69	3288.00	72.71	o
6	7	3	226.42	185.20	19.00	o
7	7	3	114.97	126.88	15.94	o
8	7	3	235.71	215.99	19.00	o
9	7	3	228.67	233.90	19.00	o
10	7	3	8.63	0.22	12.66	o
11	7	3	660.26	656.42	28.62	o
12	7	3	2.20	-5.02	11.14	o
1	8	3	3149.96	2980.80	48.54	o

2	8	3	281.22	294.64	20.53 o
3	8	3	3.10	6.99	12.66 o
4	8	3	721.12	715.32	29.06 o
5	8	3	1592.84	1555.96	44.38 o
6	8	3	88.23	82.33	15.07 o
7	8	3	3836.72	3255.13	70.94 o
8	8	3	2.23	4.15	12.01 o
9	8	3	1599.47	1464.25	42.84 o
10	8	3	28.47	24.46	12.88 o
11	8	3	166.35	180.38	18.13 o
12	8	3	25.59	22.71	12.66 o
0	9	3	289.72	241.35	20.09 o
1	9	3	912.87	882.93	23.64 o
2	9	3	117.67	103.29	16.16 o
3	9	3	3673.84	3371.77	72.93 o
4	9	3	21.19	28.17	12.88 o
5	9	3	2212.14	2158.04	53.58 o
6	9	3	183.03	160.30	17.25 o
7	9	3	151.90	143.04	17.47 o
8	9	3	109.06	110.93	15.94 o
9	9	3	259.72	233.03	20.09 o
10	9	3	16.17	12.23	13.34 o
11	9	3	414.82	429.40	24.46 o
12	9	3	3.86	-5.68	11.57 o
1	10	3	6102.72	5270.07	75.32 o
2	10	3	300.37	256.41	20.75 o
3	10	3	2010.16	1935.63	47.67 o
4	10	3	216.14	203.10	18.34 o
5	10	3	86.29	85.38	14.85 o
6	10	3	155.39	125.35	17.69 o
7	10	3	379.21	351.64	22.93 o
8	10	3	0.98	5.90	11.79 o
9	10	3	192.47	208.99	18.78 o
10	10	3	21.64	30.13	13.54 o
11	10	3	0.95	4.15	11.35 o
0	11	3	134.51	135.18	15.50 o
1	11	3	562.33	509.45	23.81 o
2	11	3	77.31	55.68	14.63 o
3	11	3	2051.01	1800.38	46.36 o
4	11	3	18.58	9.61	12.45 o
5	11	3	1370.51	1209.29	39.12 o
6	11	3	113.05	98.92	15.72 o
7	11	3	97.29	107.66	16.16 o
8	11	3	68.17	60.05	14.63 o
9	11	3	177.67	195.01	17.47 o
10	11	3	14.22	10.70	11.79 o
11	11	3	255.37	307.27	19.66 o
1	12	3	898.71	790.01	22.25 o
2	12	3	98.74	89.10	16.60 o
3	12	3	4.05	13.97	12.66 o
4	12	3	237.84	222.11	19.44 o
5	12	3	666.48	664.75	27.31 o
6	12	3	40.66	24.24	14.85 o
7	12	3	1523.57	1361.21	42.18 o
8	12	3	0.40	2.84	12.01 o
9	12	3	722.66	648.14	27.52 o
10	12	3	11.04	10.04	12.45 o

0	13	3	145.60	146.31	16.38 o
1	13	3	157.55	145.75	12.34 o
2	13	3	14.90	7.64	12.23 o
3	13	3	1311.89	1259.26	38.90 o
4	13	3	4.50	16.60	12.23 o
5	13	3	786.11	778.39	29.71 o
6	13	3	53.63	44.11	13.54 o
7	13	3	28.02	30.79	13.54 o
8	13	3	61.84	58.96	14.63 o
9	13	3	65.06	99.36	15.07 o
10	13	3	2.05	2.40	10.04 o
1	14	3	2000.04	1833.41	33.47 o
2	14	3	70.89	61.14	13.98 o
3	14	3	568.75	553.30	26.87 o
4	14	3	98.74	74.03	15.29 o
5	14	3	4.63	8.30	11.57 o
6	14	3	34.92	39.52	13.32 o
7	14	3	157.95	165.97	17.47 o
8	14	3	0.07	-6.99	11.57 o
9	14	3	63.28	58.52	13.32 o
0	15	3	26.23	18.34	13.10 o
1	15	3	197.61	200.61	12.89 o
2	15	3	26.85	24.89	13.10 o
3	15	3	572.03	555.91	26.43 o
4	15	3	6.59	3.28	13.32 o
5	15	3	410.58	403.41	22.28 o
6	15	3	41.94	34.28	13.32 o
7	15	3	43.75	62.89	13.54 o
8	15	3	19.11	34.72	11.35 o
1	16	3	193.89	203.50	13.35 o
2	16	3	40.18	37.56	13.32 o
3	16	3	0.63	0.00	11.14 o
4	16	3	46.33	45.20	12.67 o
5	16	3	286.53	308.81	20.31 o
6	16	3	23.82	18.34	12.23 o
7	16	3	436.72	518.29	23.81 o
0	17	3	32.87	41.71	13.54 o
1	17	3	48.11	42.14	9.40 o
2	17	3	5.36	6.99	11.79 o
3	17	3	344.23	426.76	21.18 o
4	17	3	1.87	-3.71	10.92 o
5	17	3	229.17	290.67	19.44 o
6	17	3	15.60	19.22	11.35 o
1	18	3	563.83	699.04	19.07 o
2	18	3	13.65	8.73	11.57 o
3	18	3	126.82	136.92	15.72 o
4	18	3	36.50	33.19	12.67 o
0	19	3	11.12	17.91	10.48 o
0	0	4	28719.57	28891.91	403.75 o
1	0	4	1686.20	2354.56	41.63 o
2	0	4	12194.71	14198.31	233.56 o
3	0	4	1041.69	1200.48	40.88 o
4	0	4	503.97	671.37	31.46 o
5	0	4	727.00	758.44	34.74 o
6	0	4	1177.75	1082.62	39.34 o
7	0	4	94.87	78.61	19.00 o
8	0	4	1287.16	1176.95	41.31 o

9	0	4	304.64	298.56	24.02 o
10	0	4	56.29	66.38	15.94 o
11	0	4	87.76	99.14	17.69 o
12	0	4	137.68	154.83	18.34 o
13	0	4	50.79	73.59	14.41 o
1	1	4	2622.67	3569.04	43.75 o
2	1	4	7864.78	9020.50	221.66 o
3	1	4	510.23	631.53	22.25 o
4	1	4	10420.48	10583.69	156.50 o
5	1	4	351.59	376.87	17.99 o
6	1	4	2536.91	2457.37	59.08 o
7	1	4	483.91	450.32	22.72 o
8	1	4	3.34	3.80	10.64 o
9	1	4	207.54	195.57	14.49 o
10	1	4	653.35	617.25	21.46 o
11	1	4	5.73	10.72	10.02 o
12	1	4	465.97	469.46	18.38 o
13	1	4	29.06	27.84	9.26 o
0	2	4	5260.44	6539.00	121.83 o
1	2	4	21.16	39.94	12.58 o
2	2	4	1515.05	1845.10	50.75 o
3	2	4	2120.34	2562.48	63.26 o
4	2	4	1550.45	1693.22	48.77 o
5	2	4	838.33	919.57	35.40 o
6	2	4	6222.51	5506.92	106.02 o
7	2	4	1.47	-1.97	15.07 o
8	2	4	4463.94	3870.96	81.49 o
9	2	4	45.53	48.26	16.38 o
10	2	4	1163.51	1088.88	36.71 o
11	2	4	222.67	214.24	20.53 o
12	2	4	16.05	17.47	13.32 o
13	2	4	32.97	41.27	14.19 o
1	3	4	2904.07	3538.61	54.78 o
2	3	4	7088.73	7874.20	152.37 o
3	3	4	42.22	77.08	16.38 o
4	3	4	8455.09	8198.38	157.44 o
5	3	4	29.05	11.57	15.29 o
6	3	4	2497.64	2395.96	60.17 o
7	3	4	727.27	632.29	30.37 o
8	3	4	10.16	19.22	15.07 o
9	3	4	169.30	165.32	18.78 o
10	3	4	580.42	523.60	27.74 o
11	3	4	0.04	14.41	12.88 o
12	3	4	417.01	427.87	24.24 o
13	3	4	6.26	13.10	12.01 o
0	4	4	19388.39	18235.22	327.19 o
1	4	4	461.09	595.19	20.16 o
2	4	4	9389.68	9911.46	167.24 o
3	4	4	1150.39	1256.62	41.76 o
4	4	4	354.02	377.67	25.12 o
5	4	4	601.31	610.85	30.15 o
6	4	4	915.60	969.35	34.53 o
7	4	4	24.55	12.23	14.41 o
8	4	4	973.89	909.86	34.09 o
9	4	4	143.52	138.45	17.69 o
10	4	4	56.98	65.73	15.72 o
11	4	4	120.35	127.31	16.60 o

12	4	4	131.72	147.18	17.03 o
13	4	4	34.98	27.95	12.01 o
1	5	4	1346.64	1532.11	34.77 o
2	5	4	4816.62	5021.18	97.00 o
3	5	4	598.15	639.51	29.93 o
4	5	4	7222.63	6782.45	124.40 o
5	5	4	470.38	493.68	26.87 o
6	5	4	1686.76	1563.32	46.13 o
7	5	4	243.27	227.79	20.31 o
8	5	4	0.69	23.15	14.19 o
9	5	4	160.67	134.09	18.34 o
10	5	4	502.59	445.81	25.99 o
11	5	4	12.53	10.04	13.54 o
12	5	4	371.21	421.74	23.15 o
13	5	4	39.19	45.86	11.79 o
0	6	4	3542.61	3355.92	75.17 o
1	6	4	356.26	343.02	27.96 o
2	6	4	741.92	734.43	31.90 o
3	6	4	781.97	737.27	31.90 o
4	6	4	869.99	890.48	33.65 o
5	6	4	468.75	425.96	25.34 o
6	6	4	4003.25	3685.43	77.97 o
7	6	4	18.33	22.71	13.98 o
8	6	4	3170.46	2623.69	62.58 o
9	6	4	122.34	141.73	15.72 o
10	6	4	760.59	722.66	29.71 o
11	6	4	86.69	92.37	14.85 o
12	6	4	18.80	10.70	12.88 o
1	7	4	1340.66	1320.73	29.53 o
2	7	4	3494.41	3465.30	74.48 o
3	7	4	33.59	32.10	13.10 o
4	7	4	4559.96	4042.21	88.11 o
5	7	4	23.00	19.87	13.54 o
6	7	4	1407.08	1259.91	40.44 o
7	7	4	402.37	371.75	23.59 o
8	7	4	5.19	10.70	13.10 o
9	7	4	113.68	100.67	16.60 o
10	7	4	377.77	379.81	23.15 o
11	7	4	0.08	-4.37	11.79 o
12	7	4	279.40	301.16	20.75 o
0	8	4	8251.82	7318.79	125.36 o
1	8	4	19.10	44.60	9.57 o
2	8	4	4655.34	4295.50	87.90 o
3	8	4	794.67	794.24	31.03 o
4	8	4	179.53	172.53	19.00 o
5	8	4	337.45	307.74	21.62 o
6	8	4	442.91	403.65	24.03 o
7	8	4	0.76	3.06	13.32 o
8	8	4	475.34	399.94	24.25 o
9	8	4	22.22	25.11	13.54 o
10	8	4	42.06	63.98	13.98 o
11	8	4	124.14	99.80	15.72 o
12	8	4	95.57	108.31	15.72 o
1	9	4	655.70	609.22	20.16 o
2	9	4	2093.55	1912.92	50.09 o
3	9	4	115.12	135.18	17.03 o
4	9	4	3055.46	2736.96	60.62 o

5	9	4	96.06	126.00	15.94 o
6	9	4	880.88	811.03	31.46 o
7	9	4	193.79	181.92	19.00 o
8	9	4	1.41	12.23	12.45 o
9	9	4	75.14	92.15	15.50 o
10	9	4	267.37	284.78	19.66 o
11	9	4	3.20	18.12	12.45 o
0	10	4	1312.11	1140.10	39.56 o
1	10	4	235.42	230.07	17.47 o
2	10	4	225.83	258.14	19.87 o
3	10	4	250.83	221.02	19.00 o
4	10	4	404.11	349.91	24.03 o
5	10	4	[illegible]	[illegible]	17.25 o
6	10	4	1854.52	1662.64	45.91 o
7	10	4	24.99	22.05	12.66 o
8	10	4	1595.90	1407.62	41.97 o
9	10	4	95.48	97.39	15.50 o
10	10	4	383.89	388.33	21.84 o
11	10	4	33.66	45.42	12.45 o
1	11	4	380.74	358.43	16.06 o
2	11	4	1195.43	1173.79	38.46 o
3	11	4	83.65	75.77	15.29 o
4	11	4	1860.90	1620.37	46.35 o
5	11	4	70.67	54.59	14.85 o
6	11	4	523.49	509.82	26.87 o
7	11	4	87.63	82.11	15.29 o
8	11	4	0.56	-4.37	12.66 o
9	11	4	58.85	75.55	14.19 o
10	11	4	185.87	203.75	17.47 o
11	11	4	1.17	5.02	10.70 o
0	12	4	2947.87	2580.52	58.86 o
1	12	4	11.36	7.16	8.57 o
2	12	4	1668.87	1462.68	44.16 o
3	12	4	255.00	227.13	19.66 o
4	12	4	88.69	83.42	16.38 o
5	12	4	131.00	140.63	16.16 o
6	12	4	151.36	139.33	16.82 o
7	12	4	0.29	7.42	11.14 o
8	12	4	189.79	288.70	18.78 o
9	12	4	12.48	15.72	11.79 o
10	12	4	16.08	30.35	11.35 o
1	13	4	257.91	236.49	14.36 o
2	13	4	707.81	697.97	29.49 o
3	13	4	6.03	6.55	12.23 o
4	13	4	990.38	912.87	32.77 o
5	13	4	4.51	7.21	12.66 o
6	13	4	354.34	373.04	22.28 o
7	13	4	112.80	114.86	16.16 o
8	13	4	1.29	5.46	11.79 o
9	13	4	29.90	41.71	12.66 o
0	14	4	312.36	304.67	21.18 o
1	14	4	30.10	27.19	11.46 o
2	14	4	60.72	59.40	14.41 o
3	14	4	110.98	98.92	15.29 o
4	14	4	163.72	133.43	17.03 o
5	14	4	60.16	65.51	14.19 o
6	14	4	677.30	640.26	27.96 o

7	14	4	2.70	16.38	11.79 o
8	14	4	588.62	640.23	26.65 o
9	14	4	19.53	27.73	11.57 o
1	15	4	101.41	108.77	17.69 o
2	15	4	349.86	411.26	22.71 o
3	15	4	42.28	35.81	13.98 o
4	15	4	590.06	613.15	26.87 o
5	15	4	35.46	38.65	13.76 o
6	15	4	168.31	169.68	17.47 o
7	15	4	27.28	23.80	11.79 o
8	15	4	0.14	-1.09	10.48 o
0	16	4	915.51	944.04	31.68 o
1	16	4	21.81	23.20	8.72 o
2	16	4	477.30	470.91	23.59 o
3	16	4	49.69	41.71	12.45 o
4	16	4	34.73	36.25	12.67 o
5	16	4	36.54	40.83	12.67 o
6	16	4	42.41	41.27	12.45 o
7	16	4	1.46	-1.09	11.35 o
1	17	4	68.45	65.13	10.09 o
2	17	4	192.52	199.38	17.47 o
3	17	4	2.79	3.71	11.14 o
4	17	4	290.28	361.66	21.40 o
5	17	4	2.75	14.41	10.48 o
0	18	4	68.67	78.83	13.76 o
1	18	4	1.36	-6.05	7.18 o
2	18	4	15.67	13.96	11.57 o
3	18	4	39.32	49.35	12.45 o
1	0	5	5450.88	6226.82	86.93 o
2	0	5	1547.72	1723.13	50.53 o
3	0	5	12.43	19.65	17.69 o
4	0	5	1687.49	1732.80	52.71 o
5	0	5	1682.46	1652.98	49.86 o
6	0	5	393.97	426.15	25.99 o
7	0	5	5202.54	4726.87	97.76 o
8	0	5	18.07	1.09	16.38 o
9	0	5	2043.84	1894.39	50.95 o
10	0	5	215.02	220.35	20.53 o
11	0	5	216.47	203.97	19.87 o
12	0	5	95.19	98.48	15.50 o
13	0	5	1.93	16.38	13.32 o
0	1	5	3004.52	3412.25	55.54 o
1	1	5	1135.24	1344.78	22.73 o
2	1	5	1240.27	1467.10	52.91 o
3	1	5	6842.08	6726.05	93.05 o
4	1	5	13.21	27.08	10.04 o
5	1	5	3667.66	3488.49	56.45 o
6	1	5	692.44	681.42	32.12 o
7	1	5	127.68	127.53	13.59 o
8	1	5	514.42	485.38	20.07 o
9	1	5	325.70	304.36	16.29 o
10	1	5	73.51	63.59	11.64 o
11	1	5	698.87	690.19	21.53 o
12	1	5	7.91	7.32	8.96 o
13	1	5	208.12	229.90	13.12 o
1	2	5	15894.25	15019.49	183.96 o
2	2	5	1263.67	1331.80	45.92 o

3	2	5	5300.51	5519.51	109.31 o
4	2	5	1780.90	1737.92	50.30 o
5	2	5	139.44	143.48	20.31 o
6	2	5	337.22	344.01	25.12 o
7	2	5	646.90	613.00	29.71 o
8	2	5	23.84	21.18	15.50 o
9	2	5	340.38	425.46	24.46 o
10	2	5	169.10	167.93	17.91 o
11	2	5	1.06	20.74	14.19 o
12	2	5	113.17	116.39	16.60 o
13	2	5	245.89	254.20	19.22 o
0	3	5	2752.33	2917.17	67.02 o
1	3	5	2216.24	2424.70	44.11 o
2	3	5	1010.34	1112.15	39.35 o
3	3	5	4879.61	4907.20	99.82 o
4	3	5	15.49	26.86	13.76 o
5	3	5	3141.37	2895.37	66.77 o
6	3	5	565.61	527.57	28.84 o
7	3	5	265.97	276.71	22.06 o
8	3	5	511.33	505.67	27.52 o
9	3	5	531.49	500.87	27.74 o
10	3	5	62.55	63.11	16.81 o
11	3	5	472.90	465.23	25.56 o
12	3	5	8.49	6.55	12.23 o
13	3	5	220.69	246.56	18.34 o
1	4	5	3643.27	3648.26	56.95 o
2	4	5	1120.83	1193.98	41.10 o
3	4	5	19.21	66.38	17.03 o
4	4	5	1369.03	1337.94	43.72 o
5	4	5	1893.69	1781.27	49.42 o
6	4	5	305.11	282.40	22.06 o
7	4	5	3784.50	3353.62	70.28 o
8	4	5	16.91	12.23	14.19 o
9	4	5	1766.89	1580.08	45.69 o
10	4	5	167.25	182.78	18.56 o
11	4	5	218.49	224.06	20.53 o
12	4	5	88.21	85.60	16.16 o
0	5	5	1896.25	1966.43	54.91 o
1	5	5	413.65	398.75	18.90 o
2	5	5	859.75	809.66	34.09 o
3	5	5	5134.34	4855.78	97.83 o
4	5	5	7.47	9.83	13.76 o
5	5	5	2643.67	2423.14	59.95 o
6	5	5	521.59	479.48	26.65 o
7	5	5	42.60	46.73	15.72 o
8	5	5	359.20	337.88	23.81 o
9	5	5	160.00	114.43	17.91 o
10	5	5	58.83	68.13	16.60 o
11	5	5	634.33	605.95	27.74 o
12	5	5	5.68	12.45	11.14 o
1	6	5	10054.27	8771.76	112.95 o
2	6	5	804.32	796.04	32.56 o
3	6	5	2245.99	2198.01	57.76 o
4	6	5	1026.71	967.03	35.18 o
5	6	5	2.29	0.22	12.23 o
6	6	5	229.21	190.22	20.09 o
7	6	5	628.65	628.49	28.62 o

8	6	5	13.39	13.98	12.88 o
9	6	5	201.97	209.87	20.31 o
10	6	5	135.40	139.32	18.34 o
11	6	5	7.33	9.83	13.10 o
12	6	5	72.51	65.95	13.76 o
0	7	5	1425.80	1348.48	42.85 o
1	7	5	1060.61	1015.44	25.96 o
2	7	5	528.03	508.56	26.87 o
3	7	5	2728.43	2444.63	59.52 o
4	7	5	8.79	4.37	13.97 o
5	7	5	1765.95	1544.70	45.91 o
6	7	5	332.99	288.74	22.71 o
7	7	5	157.71	153.74	18.34 o
8	7	5	319.41	295.94	21.84 o
9	7	5	327.37	333.50	22.06 o
10	7	5	41.18	54.37	14.19 o
11	7	5	327.16	310.56	21.84 o
12	7	5	5.59	13.32	11.35 o
1	8	5	1396.00	1302.56	29.91 o
2	8	5	501.07	463.76	26.21 o
3	8	5	80.33	79.49	16.81 o
4	8	5	736.96	653.25	29.28 o
5	8	5	1547.50	1319.89	43.06 o
6	8	5	153.93	145.66	18.13 o
7	8	5	1807.64	1619.72	47.00 o
8	8	5	11.57	12.45	13.76 o
9	8	5	1090.62	1004.24	35.18 o
10	8	5	89.27	98.05	15.29 o
11	8	5	176.07	225.37	18.13 o
0	9	5	846.32	779.82	31.90 o
1	9	5	370.93	333.96	16.13 o
2	9	5	371.00	325.01	23.15 o
3	9	5	2007.59	1783.98	48.77 o
4	9	5	3.85	18.34	12.45 o
5	9	5	1238.31	1127.68	36.06 o
6	9	5	241.56	216.86	19.66 o
7	9	5	45.86	57.87	14.63 o
8	9	5	198.68	201.35	19.44 o
9	9	5	145.62	165.75	18.13 o
10	9	5	30.93	17.47	12.01 o
11	9	5	295.99	321.91	21.84 o
1	10	5	4373.07	3763.88	65.28 o
2	10	5	341.34	325.43	22.50 o
3	10	5	839.58	783.49	30.59 o
4	10	5	416.07	344.67	22.50 o
5	10	5	22.02	29.92	13.54 o
6	10	5	108.90	103.29	16.38 o
7	10	5	324.03	340.05	22.06 o
8	10	5	5.96	10.04	12.88 o
9	10	5	97.49	89.53	15.94 o
10	10	5	74.90	79.49	15.50 o
11	10	5	8.67	3.93	10.92 o
0	11	5	498.53	432.72	24.68 o
1	11	5	187.05	159.82	12.97 o
2	11	5	207.69	173.18	19.22 o
3	11	5	1274.41	1114.14	36.28 o
4	11	5	2.99	1.09	13.10 o

5	11	5	742.89	668.71	29.71	o
6	11	5	155.90	173.83	17.47	o
7	11	5	29.96	45.86	14.41	o
8	11	5	134.73	101.98	16.60	o
9	11	5	85.59	92.37	14.85	o
10	11	5	21.76	35.81	12.45	o
1	12	5	442.95	415.55	28.07	o
2	12	5	175.99	144.79	18.13	o
3	12	5	14.50	20.96	13.10	o
4	12	5	277.76	256.40	20.31	o
5	12	5	603.47	564.01	27.52	o
6	12	5	60.37	56.12	14.63	o
7	12	5	811.23	759.60	29.93	o
8	12	5	4.83	-1.31	11.14	o
9	12	5	469.84	530.32	24.68	o
0	13	5	300.03	238.06	19.66	o
1	13	5	229.80	226.41	13.89	o
2	13	5	119.45	100.89	17.03	o
3	13	5	580.53	554.39	25.78	o
4	13	5	1.52	-1.09	11.14	o
5	13	5	427.37	420.45	24.46	o
6	13	5	82.47	67.26	13.76	o
7	13	5	38.81	28.61	12.45	o
8	13	5	86.15	86.69	14.63	o
9	13	5	99.08	104.38	16.38	o
1	14	5	1406.72	1370.41	29.35	o
2	14	5	106.37	120.54	16.16	o
3	14	5	392.04	372.39	23.59	o
4	14	5	143.82	167.06	16.60	o
5	14	5	1.28	9.17	11.14	o
6	14	5	37.92	41.71	13.32	o
7	14	5	80.16	86.26	14.19	o
8	14	5	2.56	2.62	10.70	o
0	15	5	143.18	136.49	17.03	o
1	15	5	38.14	34.14	9.38	o
2	15	5	66.46	64.42	13.76	o
3	15	5	421.78	418.26	23.15	o
4	15	5	0.95	-2.18	12.23	o
5	15	5	254.41	257.26	19.44	o
6	15	5	55.74	54.15	13.54	o
7	15	5	5.68	3.49	10.92	o
1	16	5	139.44	136.28	12.10	o
2	16	5	55.20	43.02	13.32	o
3	16	5	0.63	5.46	11.79	o
4	16	5	80.08	78.18	14.63	o
5	16	5	135.77	160.29	16.60	o
6	16	5	20.30	19.22	12.23	o
0	17	5	86.12	88.00	13.54	o
1	17	5	55.72	62.50	9.57	o
2	17	5	33.59	46.51	12.45	o
3	17	5	177.13	235.85	17.03	o
4	17	5	0.38	2.18	10.70	o
1	18	5	370.00	468.58	15.80	o
0	0	6	12052.35	11242.66	188.24	o
1	0	6	130.97	161.31	32.43	o
2	0	6	5120.43	5027.18	102.47	o
3	0	6	2682.20	2705.64	65.88	o

4	0	6	311.48	347.94	27.08 o
5	0	6	1289.60	1223.62	44.81 o
6	0	6	342.48	300.54	24.24 o
7	0	6	18.85	8.73	15.50 o
8	0	6	636.57	549.40	30.15 o
9	0	6	33.51	35.37	15.07 o
10	0	6	17.78	29.92	13.54 o
11	0	6	244.85	294.39	21.40 o
12	0	6	84.71	80.80	16.38 o
1	1	6	2057.02	2182.99	34.87 o
2	1	6	3016.67	3115.48	60.55 o
3	1	6	87.81	98.24	12.50 o
4	1	6	4557.13	4286.76	77.71 o
5	1	6	312.60	305.82	16.91 o
6	1	6	1188.73	1116.65	27.74 o
7	1	6	889.25	792.85	24.32 o
8	1	6	0.70	36.59	10.88 o
9	1	6	268.49	290.76	27.19 o
10	1	6	319.44	324.68	20.09 o
11	1	6	1.31	0.87	9.42 o
12	1	6	270.43	308.67	21.51 o
0	2	6	1851.21	1855.41	52.94 o
1	2	6	865.19	921.12	25.87 o
2	2	6	618.84	643.87	32.55 o
3	2	6	1676.97	1612.99	50.08 o
4	2	6	750.73	694.16	32.77 o
5	2	6	1143.70	1143.69	39.34 o
6	2	6	3321.85	2848.69	66.76 o
7	2	6	129.35	139.98	19.22 o
8	2	6	2308.48	1948.32	53.14 o
9	2	6	174.91	169.90	19.65 o
10	2	6	738.97	668.48	29.71 o
11	2	6	110.88	111.59	16.60 o
12	2	6	20.72	19.43	13.10 o
1	3	6	1510.90	1460.32	35.97 o
2	3	6	3029.18	2964.20	68.09 o
3	3	6	307.70	313.86	23.59 o
4	3	6	3505.49	3239.88	71.61 o
5	3	6	627.14	600.99	29.71 o
6	3	6	1255.32	1185.90	40.00 o
7	3	6	545.35	483.63	26.87 o
8	3	6	1.59	-7.64	14.41 o
9	3	6	275.23	244.82	21.84 o
10	3	6	332.42	327.38	23.15 o
11	3	6	6.40	5.68	13.32 o
12	3	6	209.77	223.84	19.87 o
0	4	6	8717.30	8250.52	139.31 o
1	4	6	292.09	320.69	16.83 o
2	4	6	4329.55	4137.28	85.70 o
3	4	6	1775.39	1716.22	49.86 o
4	4	6	252.61	243.08	22.71 o
5	4	6	1017.95	1001.72	36.49 o
6	4	6	307.00	327.83	25.12 o
7	4	6	42.15	40.83	15.50 o
8	4	6	446.03	398.18	25.12 o
9	4	6	66.84	50.22	15.07 o
10	4	6	23.03	20.53	15.07 o

11	4	6	155.04	141.51	18.34 o
12	4	6	77.37	89.75	15.29 o
1	5	6	1549.73	1496.85	32.85 o
2	5	6	1915.04	1837.59	51.40 o
3	5	6	11.98	5.24	13.76 o
4	5	6	3493.71	3098.79	68.31 o
5	5	6	115.61	106.79	18.34 o
6	5	6	785.07	683.18	30.59 o
7	5	6	797.56	684.92	31.24 o
8	5	6	0.24	11.35	13.76 o
9	5	6	195.96	163.35	19.44 o
10	5	6	226.62	223.63	20.31 o
11	5	6	0.06	-5.46	12.23 o
12	5	6	235.07	277.79	19.65 o
0	6	6	1401.90	1368.94	44.38 o
1	6	6	189.82	203.14	13.74 o
2	6	6	246.93	249.20	21.62 o
3	6	6	1384.04	1225.22	40.22 o
4	6	6	500.83	494.98	27.96 o
5	6	6	761.45	667.45	30.81 o
6	6	6	2090.87	1911.41	49.86 o
7	6	6	33.07	33.85	14.85 o
8	6	6	1810.13	1701.86	46.78 o
9	6	6	48.12	52.84	14.63 o
10	6	6	467.18	431.81	25.12 o
11	6	6	136.25	144.56	15.94 o
12	6	6	18.39	22.93	12.88 o
1	7	6	849.33	772.93	23.02 o
2	7	6	1669.86	1539.00	45.26 o
3	7	6	161.42	164.01	19.00 o
4	7	6	2019.70	1800.37	49.42 o
5	7	6	346.03	302.94	22.50 o
6	7	6	750.30	690.14	30.37 o
7	7	6	353.16	343.12	23.37 o
8	7	6	0.79	12.23	13.97 o
9	7	6	168.04	165.75	17.69 o
10	7	6	220.69	219.70	19.22 o
11	7	6	4.52	5.90	12.01 o
0	8	6	4019.75	3598.27	77.09 o
1	8	6	356.80	354.34	16.75 o
2	8	6	2521.66	2334.22	58.41 o
3	8	6	703.78	617.39	28.62 o
4	8	6	151.31	139.98	18.13 o
5	8	6	527.97	486.24	26.21 o
6	8	6	190.69	166.63	19.44 o
7	8	6	63.35	51.32	15.50 o
8	8	6	191.16	198.51	18.56 o
9	8	6	92.79	79.92	14.85 o
10	8	6	22.77	35.59	12.01 o
11	8	6	59.00	65.07	14.19 o
1	9	6	622.76	602.23	33.21 o
2	9	6	961.70	859.61	32.99 o
3	9	6	32.47	43.45	14.41 o
4	9	6	1546.53	1420.16	42.84 o
5	9	6	128.63	122.07	16.60 o
6	9	6	451.22	378.09	25.12 o
7	9	6	326.88	312.31	21.40 o

8	9	6	0.33	9.83	13.54 o
9	9	6	124.07	145.66	16.38 o
10	9	6	136.51	137.14	16.38 o
11	9	6	0.48	1.75	11.35 o
0	10	6	595.08	494.57	26.87 o
1	10	6	38.62	34.24	13.32 o
2	10	6	61.56	72.06	14.41 o
3	10	6	671.69	667.60	28.40 o
4	10	6	256.61	231.93	20.53 o
5	10	6	364.59	348.36	22.50 o
6	10	6	981.90	952.62	33.21 o
7	10	6	6.82	0.00	12.66 o
8	10	6	985.76	985.15	33.21 o
9	10	6	12.56	3.06	12.45 o
10	10	6	233.51	242.85	18.56 o
1	11	6	395.98	351.59	16.37 o
2	11	6	586.09	568.17	27.31 o
3	11	6	16.49	24.89	13.54 o
4	11	6	963.35	853.43	33.65 o
5	11	6	62.55	73.81	15.07 o
6	11	6	280.95	299.64	20.97 o
7	11	6	233.24	229.09	19.65 o
8	11	6	0.12	-3.93	11.57 o
9	11	6	69.60	88.00	13.32 o
10	11	6	96.92	119.01	15.07 o
0	12	6	1565.91	1397.15	42.19 o
1	12	6	116.24	111.03	11.26 o
2	12	6	996.24	966.41	34.09 o
3	12	6	286.31	267.10	20.31 o
4	12	6	72.99	49.79	15.72 o
5	12	6	205.77	194.58	19.22 o
6	12	6	70.67	87.35	15.72 o
7	12	6	25.98	23.58	13.54 o
8	12	6	80.48	76.21	14.85 o
9	12	6	36.76	53.72	12.23 o
1	13	6	181.16	160.81	12.66 o
2	13	6	384.20	368.02	22.50 o
3	13	6	36.55	37.12	13.54 o
4	13	6	500.71	487.30	25.99 o
5	13	6	97.46	111.15	15.77 o
6	13	6	203.86	204.84	19.00 o
7	13	6	95.95	82.76	14.41 o
8	13	6	0.22	19.65	10.70 o
0	14	6	148.16	162.25	16.60 o
1	14	6	35.31	31.14	9.64 o
2	14	6	20.27	30.35	13.10 o
3	14	6	189.57	204.19	18.56 o
4	14	6	103.59	114.86	14.63 o
5	14	6	131.59	135.61	16.81 o
6	14	6	388.74	430.48	22.93 o
7	14	6	6.71	7.42	11.14 o
1	15	6	134.68	135.90	11.96 o
2	15	6	174.87	165.10	17.91 o
3	15	6	1.97	3.71	11.35 o
4	15	6	341.52	360.14	21.84 o
5	15	6	13.68	13.32	10.92 o
6	15	6	90.21	97.61	13.54 o

0	16	6	540.76	598.49	26.21 o
1	16	6	13.61	9.95	8.33 o
2	16	6	290.29	372.36	20.75 o
3	16	6	114.16	168.15	15.50 o
4	16	6	26.68	35.81	12.23 o
5	16	6	67.87	82.98	13.10 o
1	17	6	53.70	62.94	8.92 o
2	17	6	111.51	141.29	15.50 o
3	17	6	8.31	17.69	11.14 o
1	0	7	1022.69	1011.95	32.02 o
2	0	7	862.33	872.09	34.74 o
3	0	7	22.60	64.20	18.12 o
4	0	7	1933.74	1841.45	50.73 o
5	0	7	1710.85	1545.74	48.10 o
6	0	7	173.52	210.90	21.40 o
7	0	7	1857.44	1608.46	50.50 o
8	0	7	30.15	19.22	15.07 o
9	0	7	1138.85	1115.94	36.93 o
10	0	7	217.36	214.02	20.53 o
11	0	7	185.82	238.47	19.44 o
12	0	7	185.00	203.75	17.47 o
0	1	7	3185.99	3067.81	71.71 o
1	1	7	652.97	676.50	15.88 o
2	1	7	1173.21	1137.62	27.82 o
3	1	7	2418.37	2305.13	54.81 o
4	1	7	0.43	17.40	15.18 o
5	1	7	1606.25	1462.81	32.77 o
6	1	7	638.02	624.25	19.85 o
7	1	7	134.37	124.03	13.27 o
8	1	7	572.65	532.59	20.00 o
9	1	7	153.52	174.74	15.61 o
10	1	7	69.27	72.88	11.16 o
11	1	7	254.18	294.48	25.88 o
12	1	7	5.83	6.45	8.32 o
1	2	7	6272.31	5937.76	81.50 o
2	2	7	1302.22	1278.54	43.94 o
3	2	7	1328.76	1276.78	42.19 o
4	2	7	1080.17	1050.51	37.81 o
5	2	7	15.43	28.17	14.41 o
6	2	7	380.52	380.48	24.68 o
7	2	7	388.07	383.10	24.90 o
8	2	7	49.53	35.38	15.94 o
9	2	7	106.59	97.39	17.25 o
10	2	7	271.76	242.85	20.75 o
11	2	7	10.43	14.85	12.23 o
12	2	7	109.68	140.63	15.29 o
0	3	7	2090.62	2116.94	54.03 o
1	3	7	287.44	299.51	16.60 o
2	3	7	1403.46	1404.54	42.41 o
3	3	7	2545.10	2422.91	62.14 o
4	3	7	2.36	0.00	13.97 o
5	3	7	1447.60	1383.65	42.19 o
6	3	7	612.89	568.41	29.93 o
7	3	7	70.66	66.17	14.63 o
8	3	7	371.40	352.51	24.68 o
9	3	7	73.74	52.84	16.81 o
10	3	7	112.13	115.52	15.94 o

11	3	7	309.11	381.54	21.62 o
12	3	7	9.75	8.30	12.23 o
1	4	7	864.82	813.92	24.26 o
2	4	7	833.32	790.32	33.87 o
3	4	7	0.78	15.07	13.97 o
4	4	7	1280.37	1175.66	38.69 o
5	4	7	1158.58	1060.34	37.59 o
6	4	7	208.36	233.89	20.97 o
7	4	7	1740.93	1665.12	47.00 o
8	4	7	33.45	41.71	15.94 o
9	4	7	919.41	852.29	33.86 o
10	4	7	201.76	227.12	20.31 o
11	4	7	148.54	171.86	17.69 o
0	5	7	2629.85	2392.67	61.49 o
1	5	7	625.80	631.07	21.37 o
2	5	7	687.44	649.30	30.80 o
3	5	7	1566.65	1384.04	45.91 o
4	5	7	0.09	1.75	14.19 o
5	5	7	1167.00	1095.73	36.28 o
6	5	7	338.06	326.96	23.37 o
7	5	7	132.01	113.56	17.69 o
8	5	7	521.88	472.68	26.43 o
9	5	7	159.82	190.64	18.56 o
10	5	7	35.60	41.05	14.19 o
11	5	7	169.23	193.48	17.25 o
1	6	7	3833.25	3496.59	101.72 o
2	6	7	626.45	534.13	28.40 o
3	6	7	1205.57	1202.24	37.37 o
4	6	7	994.66	918.62	34.09 o
5	6	7	2.17	19.43	14.63 o
6	6	7	153.89	139.54	17.47 o
7	6	7	163.15	137.14	17.69 o
8	6	7	24.05	0.22	14.19 o
9	6	7	89.99	70.53	16.38 o
10	6	7	170.49	184.31	18.78 o
11	6	7	4.68	9.39	11.79 o
0	7	7	1210.10	1081.17	37.37 o
1	7	7	179.52	177.51	17.14 o
2	7	7	794.68	682.10	31.90 o
3	7	7	1457.26	1366.35	42.62 o
4	7	7	1.10	4.37	13.32 o
5	7	7	386.08	790.70	32.34 o
6	7	7	381.67	347.49	23.37 o
7	7	7	45.73	43.45	15.72 o
8	7	7	243.62	259.45	20.09 o
9	7	7	51.20	47.39	15.29 o
10	7	7	72.08	79.05	14.19 o
11	7	7	200.33	241.75	19.22 o
1	8	7	469.79	432.59	17.99 o
2	8	7	572.92	520.12	27.52 o
3	8	7	19.86	17.25	14.19 o
4	8	7	494.21	449.31	26.43 o
5	8	7	492.52	409.55	25.12 o
6	8	7	187.68	159.20	18.56 o
7	8	7	1204.11	1169.52	37.37 o
8	8	7	27.35	39.96	14.41 o
9	8	7	534.94	535.58	26.65 o

10	8	7	144.48	198.94	17.25 o
0	9	7	1068.13	973.06	35.40 o
1	9	7	200.94	187.75	14.13 o
2	9	7	423.04	400.80	24.90 o
3	9	7	872.59	830.68	32.12 o
4	9	7	0.14	-1.75	13.97 o
5	9	7	589.18	596.34	28.83 o
6	9	7	202.55	139.55	19.22 o
7	9	7	52.42	58.52	15.29 o
8	9	7	234.30	295.26	19.65 o
9	9	7	63.26	77.30	15.07 o
10	9	7	32.63	49.35	13.32 o
1	10	7	1738.80	1889.13	82.96 o
2	10	7	233.54	222.98	20.75 o
3	10	7	669.89	614.94	27.96 o
4	10	7	542.30	501.08	26.87 o
5	10	7	3.36	15.50	13.76 o
6	10	7	54.34	62.02	15.07 o
7	10	7	60.58	59.61	14.85 o
8	10	7	11.13	10.70	12.66 o
9	10	7	46.53	54.81	13.54 o
0	11	7	667.00	624.99	29.27 o
1	11	7	145.79	151.72	12.65 o
2	11	7	246.28	235.86	20.97 o
3	11	7	521.61	502.82	26.21 o
4	11	7	0.07	17.47	14.19 o
5	11	7	393.67	369.99	24.03 o
6	11	7	140.45	150.68	17.91 o
7	11	7	36.56	49.79	13.98 o
8	11	7	162.81	181.91	17.91 o
9	11	7	45.76	41.27	12.23 o
1	12	7	156.92	140.18	12.04 o
2	12	7	220.05	205.94	19.00 o
3	12	7	9.82	19.43	11.79 o
4	12	7	205.63	206.59	17.91 o
5	12	7	233.69	269.71	20.09 o
6	12	7	73.88	61.36	14.85 o
7	12	7	513.96	613.33	25.77 o
8	12	7	10.60	17.69	10.70 o
0	13	7	304.35	324.32	21.62 o
1	13	7	39.83	44.94	9.95 o
2	13	7	207.82	200.04	19.00 o
3	13	7	373.98	376.31	23.81 o
4	13	7	0.15	6.99	12.45 o
5	13	7	231.99	215.33	19.65 o
6	13	7	99.31	80.58	14.85 o
7	13	7	12.84	8.73	10.70 o
1	14	7	658.28	677.57	20.23 o
2	14	7	99.25	96.74	15.72 o
3	14	7	211.69	211.18	18.56 o
4	14	7	159.11	158.11	17.25 o
5	14	7	0.83	5.46	11.57 o
6	14	7	30.97	39.52	12.45 o
0	15	7	247.96	254.64	19.87 o
1	15	7	57.78	62.47	9.72 o
2	15	7	70.84	80.14	14.63 o
3	15	7	167.51	217.07	17.47 o

4	15	7	0.03	-1.31	11.14 o
5	15	7	133.90	170.99	16.38 o
1	16	7	38.68	43.89	8.57 o
2	16	7	53.66	58.74	13.98 o
3	16	7	0.60	7.64	10.48 o
0	0	8	3529.72	3301.59	76.41 o
1	0	8	477.53	458.05	47.62 o
2	0	8	3093.65	2895.84	67.63 o
3	0	8	1421.12	1318.29	43.50 o
4	0	8	247.38	274.31	21.84 o
5	0	8	1003.04	899.38	35.40 o
6	0	8	105.73	103.29	17.47 o
7	0	8	79.82	93.24	16.81 o
8	0	8	69.23	63.98	16.16 o
9	0	8	119.49	131.68	17.47 o
10	0	8	32.82	59.61	14.41 o
11	0	8	125.03	130.15	17.03 o
1	1	8	1370.84	1252.17	20.44 o
2	1	8	1006.13	1022.11	25.42 o
3	1	8	122.47	111.23	12.95 o
4	1	8	1209.08	1116.13	27.19 o
5	1	8	354.20	343.45	16.83 o
6	1	8	441.39	434.37	18.14 o
7	1	8	649.72	602.26	23.92 o
8	1	8	5.08	10.79	10.03 o
9	1	8	267.51	264.40	15.11 o
10	1	8	168.87	184.49	12.97 o
11	1	8	3.24	-0.66	8.87 o
0	2	8	1083.53	1024.70	36.71 o
1	2	8	240.33	212.26	14.59 o
2	2	8	75.42	68.13	16.60 o
3	2	8	1625.37	1551.96	46.13 o
4	2	8	240.03	298.76	23.37 o
5	2	8	922.73	821.98	34.30 o
6	2	8	1077.31	974.13	36.71 o
7	2	8	48.41	57.43	14.85 o
8	2	8	1284.07	1225.74	39.55 o
9	2	8	63.43	66.16	15.50 o
10	2	8	278.62	281.07	20.97 o
11	2	8	173.62	197.63	17.91 o
1	3	8	1312.27	1184.57	47.54 o
2	3	8	643.60	690.12	30.58 o
3	3	8	62.17	70.97	15.94 o
4	3	8	1548.74	1435.73	45.90 o
5	3	8	218.23	199.17	19.00 o
6	3	8	235.21	203.10	19.66 o
7	3	8	705.77	675.46	29.93 o
8	3	8	0.46	8.95	12.45 o
9	3	8	214.51	259.22	20.75 o
10	3	8	133.15	176.88	17.47 o
11	3	8	2.53	1.75	12.01 o
0	4	8	3402.25	3107.81	73.77 o
1	4	8	297.86	268.38	21.95 o
2	4	8	2200.96	1953.92	53.15 o
3	4	8	1255.16	1084.24	38.03 o
4	4	8	235.01	214.03	20.97 o
5	4	8	809.25	688.64	30.59 o

6	4	8	58.33	68.35	14.41 o
7	4	8	56.08	63.11	15.50 o
8	4	8	97.01	82.76	16.38 o
9	4	8	80.52	100.01	16.16 o
10	4	8	11.91	24.89	12.88 o
11	4	8	126.79	132.55	14.41 o
1	5	8	949.01	912.93	24.10 o
2	5	8	874.00	879.00	33.87 o
3	5	8	114.58	91.28	18.34 o
4	5	8	701.32	633.10	29.93 o
5	5	8	321.24	292.22	23.37 o
6	5	8	429.72	449.29	24.24 o
7	5	8	449.82	409.10	25.54 o
8	5	8	7.19	0.66	12.23 o
9	5	8	223.68	221.23	19.65 o
10	5	8	146.49	149.15	17.69 o
11	5	8	2.97	5.68	10.48 o
0	6	8	365.63	332.86	23.59 o
1	6	8	247.41	235.52	14.74 o
2	6	8	123.65	126.88	19.00 o
3	6	8	952.93	804.51	33.21 o
4	6	8	204.04	166.85	18.78 o
5	6	8	647.97	613.41	29.27 o
6	6	8	889.16	863.87	32.55 o
7	6	8	46.58	39.31	14.85 o
8	6	8	728.13	710.41	29.49 o
9	6	8	68.03	98.05	15.29 o
10	6	8	284.41	309.68	21.40 o
1	7	8	776.48	719.11	21.61 o
2	7	8	389.97	342.26	23.37 o
3	7	8	40.99	39.96	13.54 o
4	7	8	932.74	816.93	32.77 o
5	7	8	142.38	139.32	17.47 o
6	7	8	155.76	144.13	17.03 o
7	7	8	441.61	420.23	24.46 o
8	7	8	0.70	5.46	13.10 o
9	7	8	145.57	159.41	16.60 o
10	7	8	87.91	102.35	15.07 o
0	8	8	2408.48	2182.92	52.93 o
1	8	8	106.65	93.21	11.97 o
2	8	8	1007.88	912.69	34.96 o
3	8	8	781.51	713.30	31.68 o
4	8	8	167.04	146.97	17.69 o
5	8	8	455.53	470.04	24.68 o
6	8	8	13.29	-10.70	13.54 o
7	8	8	25.05	29.92	13.32 o
8	8	8	105.13	114.86	16.60 o
9	8	8	34.06	53.28	13.54 o
10	8	8	0.78	-13.32	11.57 o
1	9	8	491.06	496.26	18.15 o
2	9	8	363.90	343.99	22.93 o
3	9	8	38.82	23.36	14.41 o
4	9	8	477.06	448.64	24.24 o
5	9	8	135.48	127.09	17.25 o
6	9	8	170.55	152.21	17.69 o
7	9	8	288.36	285.44	20.53 o
8	9	8	1.28	3.93	12.23 o

9	9	8	116.23	152.86	16.38 o
0	10	8	100.29	127.31	16.16 o
1	10	8	135.43	125.15	12.35 o
2	10	8	73.58	82.54	14.63 o
3	10	8	431.27	356.89	23.37 o
4	10	8	114.02	129.93	16.81 o
5	10	8	321.44	328.26	21.62 o
6	10	8	502.69	575.11	26.21 o
7	10	8	27.68	29.70	13.10 o
8	10	8	337.38	345.51	21.62 o
9	10	8	41.98	48.69	12.45 o
1	11	8	316.11	303.86	14.82 o
2	11	8	236.94	233.46	19.22 o
3	11	8	32.37	40.18	13.54 o
4	11	8	294.57	356.20	21.62 o
5	11	8	94.43	104.38	15.50 o
6	11	8	121.68	132.99	15.94 o
7	11	8	174.87	181.47	17.47 o
8	11	8	2.20	15.72	12.01 o
0	12	8	992.04	956.11	34.30 o
1	12	8	49.48	54.72	10.03 o
2	12	8	451.90	463.48	24.90 o
3	12	8	314.26	322.14	21.40 o
4	12	8	73.65	73.81	14.19 o
5	12	8	199.46	212.92	17.69 o
6	12	8	4.80	-5.24	12.23 o
7	12	8	11.75	-0.22	10.92 o
1	13	8	195.21	176.63	12.97 o
2	13	8	103.47	169.02	16.38 o
3	13	8	8.44	3.28	11.14 o
4	13	8	257.99	262.29	19.22 o
5	13	8	41.05	39.52	11.57 o
6	13	8	44.69	50.44	12.88 o
0	14	8	55.27	69.88	14.19 o
1	14	8	35.86	43.39	8.88 o
2	14	8	12.30	12.45	11.57 o
3	14	8	176.39	203.31	17.03 o
4	14	8	40.54	56.99	13.10 o
5	14	8	118.85	151.11	15.72 o
1	15	8	106.64	115.10	10.58 o
2	15	8	93.31	91.72	14.85 o
3	15	8	13.03	20.74	11.57 o
1	0	9	134.52	142.93	13.65 o
2	0	9	986.62	921.01	35.40 o
3	0	9	39.16	29.70	13.54 o
4	0	9	734.37	691.22	31.24 o
5	0	9	553.36	519.88	28.83 o
6	0	9	393.82	378.94	24.46 o
7	0	9	929.98	902.77	33.43 o
8	0	9	32.18	48.91	15.29 o
9	0	9	435.05	458.23	24.46 o
10	0	9	193.97	203.97	18.34 o
0	1	9	1497.25	1312.41	31.14 o
1	1	9	158.21	154.31	9.30 o
2	1	9	795.60	684.56	22.47 o
3	1	9	829.60	791.98	23.10 o
4	1	9	5.18	7.60	9.65 o

5	1	9	587.49	565.07	32.98 o
6	1	9	456.93	437.97	17.84 o
7	1	9	75.58	91.06	11.34 o
8	1	9	362.39	359.03	41.39 o
9	1	9	22.53	13.07	9.76 o
10	1	9	78.47	93.15	10.73 o
1	2	9	1813.29	1688.66	33.93 o
2	2	9	566.55	534.53	28.18 o
3	2	9	571.03	453.70	27.74 o
4	2	9	1284.71	1053.82	39.34 o
5	2	9	2.15	40.18	14.19 o
6	2	9	150.30	158.54	18.34 o
[illegible]	2	9	58.07	72.06	15.29 o
8	2	9	9.73	8.08	13.54 o
9	2	9	36.42	38.65	13.76 o
10	2	9	153.98	165.31	17.69 o
0	3	9	1900.19	1686.85	48.98 o
1	3	9	166.72	165.40	13.34 o
2	3	9	464.71	464.59	25.77 o
3	3	9	704.73	641.18	31.02 o
4	3	9	0.97	-1.53	14.19 o
5	3	9	567.29	527.74	27.52 o
6	3	9	335.43	318.87	23.15 o
7	3	9	67.04	62.67	16.16 o
8	3	9	477.13	457.81	24.68 o
9	3	9	23.68	24.02	13.54 o
10	3	9	33.50	34.72	12.01 o
1	4	9	101.14	98.07	11.95 o
2	4	9	670.88	624.79	30.37 o
3	4	9	31.58	35.59	14.85 o
4	4	9	794.38	762.24	31.68 o
5	4	9	493.12	481.63	25.77 o
6	4	9	235.75	216.42	20.09 o
7	4	9	751.47	748.22	29.93 o
8	4	9	17.01	14.63	13.10 o
9	4	9	393.00	362.78	22.93 o
10	4	9	156.71	180.82	17.25 o
0	5	9	885.37	806.44	31.68 o
1	5	9	108.74	97.82	11.16 o
2	5	9	738.64	637.04	29.93 o
3	5	9	642.18	597.68	28.84 o
4	5	9	6.21	1.31	14.41 o
5	5	9	432.29	405.60	24.46 o
6	5	9	395.74	359.72	24.03 o
7	5	9	59.99	56.12	14.41 o
8	5	9	220.37	228.21	19.22 o
9	5	9	16.50	22.93	13.32 o
10	5	9	86.33	81.67	14.19 o
1	6	9	1265.61	1150.94	26.73 o
2	6	9	536.04	445.61	26.43 o
3	6	9	387.80	364.53	23.15 o
4	6	9	611.46	512.25	28.40 o
5	6	9	4.95	7.42	12.88 o
6	6	9	201.09	158.33	17.47 o
7	6	9	51.54	50.01	13.76 o
8	6	9	17.18	19.00	12.66 o
9	6	9	18.85	27.95	12.66 o

0	7	9	1142.67	1055.67	36.27 o
1	7	9	98.57	92.48	11.66 o
2	7	9	297.41	270.60	21.18 o
3	7	9	448.87	435.09	25.12 o
4	7	9	1.07	29.26	12.88 o
5	7	9	362.94	328.92	22.06 o
6	7	9	218.55	212.49	18.56 o
7	7	9	44.10	55.90	13.32 o
8	7	9	313.38	275.40	20.09 o
9	7	9	15.33	31.23	12.66 o
1	8	9	47.61	47.66	10.47 o
2	8	9	277.13	239.36	20.75 o
3	8	9	20.35	21.40	12.88 o
4	8	9	653.92	622.35	29.27 o
5	8	9	321.54	312.97	20.53 o
6	8	9	76.85	82.32	15.29 o
7	8	9	435.16	450.15	23.15 o
8	8	9	4.55	12.45	12.01 o
9	8	9	265.82	307.71	19.00 o
0	9	9	610.13	618.40	27.74 o
1	9	9	66.23	72.29	10.88 o
2	9	9	304.93	272.78	21.40 o
3	9	9	324.22	322.80	21.40 o
4	9	9	1.09	0.22	11.79 o
5	9	9	246.06	240.67	19.66 o
6	9	9	192.51	199.16	17.47 o
7	9	9	33.32	54.37	12.66 o
8	9	9	163.35	193.48	17.47 o
1	10	9	637.15	618.92	23.70 o
2	10	9	306.18	320.83	20.75 o
3	10	9	201.87	224.94	18.34 o
4	10	9	246.85	259.23	19.66 o
5	10	9	3.83	9.61	11.35 o
6	10	9	131.07	108.53	16.16 o
7	10	9	27.83	25.98	12.01 o
0	11	9	363.96	339.84	21.62 o
1	11	9	37.89	40.04	13.43 o
2	11	9	206.18	220.79	18.78 o
3	11	9	222.20	215.33	17.91 o
4	11	9	2.15	5.02	11.14 o
5	11	9	163.74	152.43	17.47 o
6	11	9	131.07	163.78	16.60 o
7	11	9	22.39	19.43	11.79 o
1	12	9	17.55	17.74	8.89 o
2	12	9	123.15	145.44	15.29 o
3	12	9	12.08	20.74	12.88 o
4	12	9	272.20	295.70	20.97 o
5	12	9	142.09	163.13	16.81 o
6	12	9	39.67	40.83	12.23 o
0	13	9	328.79	329.13	21.40 o
1	13	9	29.11	31.60	9.50 o
2	13	9	86.00	93.90	13.76 o
3	13	9	125.17	153.30	16.16 o
4	13	9	0.06	10.92	10.70 o
5	13	9	106.41	109.62	14.63 o
1	14	9	243.22	258.72	26.53 o
2	14	9	94.62	103.73	13.98 o

3	14	9	83.67	89.53	13.32 o
0	0	10	1920.97	1783.61	48.97 o
1	0	10	207.51	197.33	15.72 o
2	0	10	720.24	738.18	30.15 o
3	0	10	833.98	749.37	31.68 o
4	0	10	208.82	245.25	20.75 o
5	0	10	495.29	485.56	26.43 o
6	0	10	1.74	-9.61	12.66 o
7	0	10	34.80	34.94	12.67 o
8	0	10	50.79	80.58	13.32 o
9	0	10	91.29	126.00	15.94 o
1	1	10	943.58	839.44	16.36 o
2	1	10	191.09	175.96	18.13 o
3	1	10	110.12	103.29	12.50 o
4	1	10	386.94	355.90	16.68 o
5	1	10	161.15	134.41	12.89 o
6	1	10	82.79	83.67	18.45 o
7	1	10	417.60	383.68	16.60 o
8	1	10	0.31	10.48	12.12 o
9	1	10	174.10	202.02	27.95 o
0	2	10	56.71	77.30	14.85 o
1	2	10	151.45	153.19	12.89 o
2	2	10	55.95	66.16	16.16 o
3	2	10	816.85	769.24	31.24 o
4	2	10	115.69	105.69	17.91 o
5	2	10	531.41	478.58	26.43 o
6	2	10	448.75	445.35	24.90 o
7	2	10	16.38	25.33	13.76 o
8	2	10	313.12	314.27	21.84 o
9	2	10	68.02	57.87	13.76 o
1	3	10	895.17	850.22	34.74 o
2	3	10	270.68	266.01	21.84 o
3	3	10	81.08	87.35	14.19 o
4	3	10	200.00	229.96	20.09 o
5	3	10	126.74	145.66	18.56 o
6	3	10	154.37	148.72	17.03 o
7	3	10	382.10	392.04	23.81 o
8	3	10	4.56	9.39	12.01 o
9	3	10	176.46	176.89	17.25 o
0	4	10	1345.38	1202.22	40.65 o
1	4	10	158.25	136.26	12.97 o
2	4	10	746.36	684.44	30.80 o
3	4	10	699.03	669.78	28.18 o
4	4	10	157.62	138.23	17.25 o
5	4	10	434.60	399.05	24.24 o
6	4	10	0.66	2.18	12.45 o
7	4	10	23.18	25.77	14.41 o
8	4	10	23.44	26.86	13.10 o
9	4	10	71.40	69.22	14.19 o
1	5	10	694.24	619.30	20.46 o
2	5	10	106.15	93.68	15.94 o
3	5	10	95.01	108.75	16.81 o
4	5	10	388.09	385.49	23.59 o
5	5	10	137.25	146.97	17.25 o
6	5	10	37.30	36.90	14.63 o
7	5	10	327.82	316.68	22.28 o
8	5	10	0.08	-4.37	10.70 o

9	5	10	130.55	151.33	15.72 o
0	6	10	115.79	121.42	16.16 o
1	6	10	122.28	117.36	11.65 o
2	6	10	5.66	17.03	13.54 o
3	6	10	565.35	530.14	26.21 o
4	6	10	65.92	68.79	14.85 o
5	6	10	352.81	336.12	23.59 o
6	6	10	278.25	316.67	21.62 o
7	6	10	18.73	6.77	12.66 o
8	6	10	309.71	329.34	21.40 o
1	7	10	575.84	543.00	27.85 o
2	7	10	168.14	172.52	17.69 o
3	7	10	52.36	53.94	14.41 o
4	7	10	136.01	161.38	17.91 o
5	7	10	80.77	121.41	14.63 o
6	7	10	95.00	73.37	15.07 o
7	7	10	254.56	247.87	19.87 o
8	7	10	2.33	-0.66	11.35 o
0	8	10	605.59	590.00	28.18 o
1	8	10	79.09	78.77	11.29 o
2	8	10	590.34	559.20	28.18 o
3	8	10	421.14	402.54	23.15 o
4	8	10	83.76	89.09	15.50 o
5	8	10	280.67	304.88	20.53 o
6	8	10	1.40	2.40	11.35 o
7	8	10	9.15	10.48	11.57 o
1	9	10	382.21	384.30	16.04 o
2	9	10	82.77	66.38	13.98 o
3	9	10	45.80	47.17	13.32 o
4	9	10	156.09	177.54	17.25 o
5	9	10	73.02	69.00	14.41 o
6	9	10	41.39	54.81	13.10 o
7	9	10	188.56	228.65	17.25 o
0	10	10	80.77	79.70	14.19 o
1	10	10	69.06	65.60	9.96 o
2	10	10	0.53	-2.18	12.01 o
3	10	10	285.00	262.51	20.75 o
4	10	10	33.23	50.22	12.45 o
5	10	10	177.21	227.33	17.69 o
6	10	10	135.42	165.53	15.72 o
1	11	10	264.68	267.73	13.97 o
2	11	10	51.08	61.80	13.76 o
3	11	10	31.55	38.87	12.45 o
4	11	10	112.45	156.35	15.50 o
5	11	10	44.12	51.32	12.67 o
0	12	10	289.85	302.04	20.53 o
1	12	10	33.65	43.26	8.96 o
2	12	10	254.82	306.62	20.53 o
3	12	10	189.10	186.28	17.25 o
4	12	10	42.39	54.81	11.79 o
1	13	10	161.91	210.09	12.26 o
2	13	10	49.87	79.92	13.10 o
1	0	11	9.16	9.39	9.57 o
2	0	11	344.87	289.17	21.84 o
3	0	11	55.33	32.10	15.50 o
4	0	11	791.81	726.82	31.02 o
5	0	11	149.69	142.38	17.91 o

6	0	11	119.66	134.52	17.47	o
7	0	11	300.33	300.95	21.62	o
8	0	11	0.58	-7.42	12.23	o
0	1	11	801.68	753.87	21.32	o
1	1	11	28.34	31.09	6.65	o
2	1	11	273.40	266.17	15.21	o
3	1	11	188.64	170.83	13.98	o
4	1	11	5.93	14.64	9.65	o
5	1	11	153.26	149.52	12.88	o
6	1	11	261.51	277.66	14.42	o
7	1	11	20.40	19.85	8.85	o
8	1	11	269.31	319.89	32.54	o
1	2	11	521.94	523.56	18.69	o
2	2	11	472.35	499.31	26.87	o
3	2	11	261.44	227.78	20.75	o
4	2	11	498.34	486.21	26.21	o
5	2	11	6.43	15.07	13.10	o
6	2	11	225.90	243.28	19.65	o
7	2	11	2.95	3.28	10.92	o
8	2	11	7.63	10.70	12.23	o
0	3	11	533.81	532.31	27.09	o
1	3	11	52.00	61.37	15.07	o
2	3	11	353.34	323.89	22.50	o
3	3	11	151.90	145.88	18.56	o
4	3	11	11.94	11.14	12.88	o
5	3	11	125.26	135.39	17.47	o
6	3	11	272.60	270.37	20.97	o
7	3	11	34.07	50.00	12.88	o
8	3	11	194.60	226.24	18.78	o
1	4	11	4.85	11.30	9.14	o
2	4	11	339.43	346.17	22.93	o
3	4	11	32.85	37.56	13.76	o
4	4	11	567.36	603.75	26.65	o
5	4	11	154.07	179.29	17.91	o
6	4	11	140.21	143.04	16.38	o
7	4	11	243.61	273.20	20.31	o
8	4	11	2.38	2.62	9.61	o
0	5	11	726.43	698.40	29.05	o
1	5	11	12.22	17.09	8.57	o
2	5	11	169.77	181.26	17.47	o
3	5	11	157.53	162.47	17.91	o
4	5	11	2.50	7.64	11.57	o
5	5	11	128.47	138.67	17.69	o
6	5	11	189.06	213.14	18.34	o
7	5	11	10.08	16.16	11.14	o
1	6	11	405.88	391.11	30.25	o
2	6	11	268.05	264.69	19.44	o
3	6	11	145.86	138.23	17.91	o
4	6	11	474.68	470.47	24.24	o
5	6	11	14.52	7.64	12.66	o
6	6	11	107.19	116.83	14.63	o
7	6	11	3.95	1.09	11.35	o
0	7	11	358.08	364.74	22.06	o
1	7	11	33.84	39.23	9.19	o
2	7	11	220.74	203.97	19.44	o
3	7	11	100.80	110.50	15.50	o
4	7	11	7.42	2.18	11.79	o

5	7	11	83.66	90.19	14.41 o
6	7	11	184.45	203.97	17.47 o
1	8	11	1.17	4.19	8.39 o
2	8	11	253.53	274.08	19.87 o
3	8	11	10.14	18.78	12.23 o
4	8	11	267.96	262.29	20.75 o
5	8	11	124.80	155.48	15.72 o
6	8	11	126.91	135.17	16.81 o
0	9	11	335.12	358.18	21.40 o
1	9	11	12.26	11.31	8.48 o
2	9	11	128.40	120.32	15.94 o
3	9	11	82.09	95.65	14.85 o
4	9	11	2.93	4.15	10.70 o
5	9	11	68.80	96.52	14.19 o
1	10	11	225.16	250.44	13.54 o
2	10	11	125.22	141.94	15.72 o
3	10	11	66.71	86.25	13.76 o
4	10	11	281.36	366.90	20.53 o
0	11	11	233.11	285.65	18.56 o
1	11	11	8.57	10.68	8.84 o
2	11	11	74.35	72.72	13.98 o
0	0	12	288.26	273.21	21.40 o
1	0	12	46.02	50.51	9.38 o
2	0	12	306.06	320.83	21.84 o
3	0	12	441.53	435.30	24.90 o
4	0	12	60.37	64.42	14.85 o
5	0	12	270.43	256.61	20.53 o
6	0	12	2.91	3.00	12.01 o
7	0	12	3.01	10.92	10.26 o
1	1	12	521.62	524.49	12.96 o
2	1	12	47.72	64.48	12.34 o
3	1	12	56.18	50.09	10.09 o
4	1	12	64.75	74.35	14.08 o
5	1	12	56.73	60.24	9.50 o
6	1	12	37.21	40.66	8.80 o
0	2	12	8.09	19.22	13.32 o
1	2	12	116.62	123.22	11.89 o
2	2	12	7.63	6.77	12.66 o
3	2	12	350.54	385.92	21.62 o
4	2	12	41.21	47.82	13.98 o
5	2	12	230.17	233.24	19.22 o
6	2	12	114.33	156.57	16.60 o
1	3	12	442.02	427.65	28.61 o
2	3	12	28.96	38.65	13.32 o
3	3	12	90.76	105.25	15.29 o
4	3	12	92.51	109.84	14.63 o
5	3	12	87.31	86.47	13.76 o
6	3	12	16.94	21.62	13.10 o
0	4	12	295.30	298.55	20.75 o
1	4	12	60.57	62.55	10.16 o
2	4	12	223.56	260.97	19.65 o
3	4	12	347.64	332.41	22.06 o
4	4	12	59.82	54.15	13.98 o
5	4	12	221.04	258.35	18.34 o
6	4	12	3.25	0.87	11.35 o
1	5	12	426.94	467.47	22.06 o
2	5	12	45.62	34.72	12.67 o

3	5	12	28.54	32.75	12.23 o
4	5	12	38.19	28.61	13.32 o
5	5	12	31.10	42.58	12.01 o
0	6	12	0.46	13.10	12.01 o
1	6	12	48.58	56.68	9.57 o
2	6	12	0.65	-3.28	11.79 o
3	6	12	287.64	307.06	20.75 o
4	6	12	39.16	40.62	12.67 o
5	6	12	180.41	230.39	17.03 o
1	7	12	298.21	332.84	14.36 o
2	7	12	20.46	24.46	11.79 o
3	7	12	60.62	66.16	13.54 o
4	7	12	58.94	52.63	13.98 o
0	8	12	231.52	273.86	18.13 o
1	8	12	62.98	58.56	9.63 o
2	8	12	111.42	137.57	15.72 o
3	8	12	192.28	211.83	16.60 o
1	9	12	230.26	271.22	13.67 o
2	9	12	20.17	30.35	12.88 o
1	0	13	3.54	1.10	8.18 o
2	0	13	201.33	237.82	18.34 o
3	0	13	2.74	-2.18	11.14 o
4	0	13	269.80	305.53	19.00 o
0	1	13	320.04	327.45	14.59 o
1	1	13	7.33	19.11	6.97 o
2	1	13	144.33	1 1.49	11.42 o
3	1	13	18.78	14.85	7.86 o
4	1	13	3.79	7.56	7.24 o
1	2	13	179.80	218.38	12.58 o
2	2	13	175.16	173.61	16.60 o
3	2	13	60.76	102.41	13.54 o
4	2	13	297.88	402.72	20.75 o
0	3	13	328.91	398.14	21.84 o
1	3	13	0.10	-1.09	7.56 o
2	3	13	112.44	110.93	15.29 o
3	3	13	28.85	41.93	12.45 o
4	3	13	1.91	0.22	10.70 o
1	4	13	1.53	10.89	8.26 o
2	4	13	164.03	177.76	15.94 o
3	4	13	8.12	12.88	10.70 o
0	5	13	239.46	269.71	18.34 o
1	5	13	13.69	24.02	7.72 o
2	5	13	124.50	140.20	16.16 o
1	6	13	115.19	129.77	10.72 o

REFERENCES

Abe, M. and Uchino, K., *Mat. Res. Bull.*, **1974**, *9*, 147-156.

Amow, G. and Greedan, J. E., *J. Solid State Chem.*, **1996**, *121*, 443-450.

Bacon, G. E., *Neutron Diffraction*, **1955**, Oxford University Press, Oxford.

Bazuev, G. V., Makarova, O. V. and Shveikin, G. P., *Russ. J. Inorg. Chem.*, **1978**, *23*, 800-802.

Bazuev, G. V., Makarova, O. V. and Shveikin, G. P., *Russ. J. Inorg. Chem.*, **1979**, *24*, 772-773.

Bazuev, G. V., Makarova, O. V. and Shveikin, G. P., *Inorg. Mater.*, **1983**, *19*, 92-95.

Bazuev, G. V. and Shveikin, G. P., *Sov. Phys. Solid State*, **1976**, *17*, 2261-2262.

Bazuev, G. V. and Shveikin, G. P., *Inorg. Mater.*, **1986**, *22*, 1185-1189.

Belov, N. V., Neronova, N. N. and Smirnova, T. S., *Soviet Phys. Cryst.*, **1975**, *2*, 311.

Bertaut, E. F., *Magnetism*, **1963**, III, Academic Press, New York and London.

Bertaut, E. F., *Acta Cryst.*, **1968**, *A*, 217-231.

Blatt, F. J., Schroeder, P. A. and Foiles, C. L., *Thermoelectric Power of Metals*, **1976**, Plenum Press, New York.

Bloch, F., *Z. Phys.*, **1929**, *57*, 545.

Bozorth, R. M., Williams, H. J. and Walsh, D. E., *Phys. Rev.*, **1956**, *103*, 572.

Brinkman, W. F. and Rice, T. M., *Phys. Rev. B*, **1970**, *2*, 4302.

Brinkman, W. F. and Rice, T. M., *Phys. Rev. B*, **1970**, *2*, 1324-1338.

Carlin, R. L. and van Duyneveldt, A. J., *Magnetic Properties of Transition Metal*

Compounds, **1977**, Springer-Verlag, New York.

Chaikin, P. M., *Organic Superconductivity*, **1990**, Plenum Press, New York.

Chevalier, B., Etourneau, J., Hagenmuller, P., Quezel, S. and Roosat-Mignod, J., *J. Less Comm. Metals.* **1985**, *111*, 161.

Cox, P. A., *Transition Metal Oxides*, **1992**,27, Clarendon Press, Oxford.

Crandles, D. A., Timusk, T., Garett, J. and Greedan, J. E., *Phys. Rev. B.*, **1994**, *49*, 4299-4302.

Crandles, D. A., Timusk, T., Garett, J. D. and Greedan, J. E., *Physica C*, **1992**, *201*, 407-412.

Davis, E. A. and Mott, N. F., *Phil. Mag.*, **1970**, *22*, 903.

deBoer, J. H. and Verwey, E. J. W., *Proc. Phys. Soc.*, **1937**, *A49*, 59.

Donnay, G., Corliss, L. M., Donnay, J. D. H., Elliot, N. and Hastings, J. M., *Phys. Rev.*, **1958**, *112*, 1917.

Efros, A. L. and Shklovskii, B. I., *J. Phys.*, **1975**, *C8*, L49.

Eylem, C., Gotthard, S. S., Chen, B. H., Eichhorn, B., Peng, J. L., Greene, R., Lourdes, S. R. and Nahm, S., *Chem. Mater.*, **1992**, *4*, 1038-1046.

Eylem, C., Ju, H. L., Eichhorn, B. W. and Greene, R. L., *J. Solid State Chem.*, **1995**, *114*, 164-173.

Fourquet, J. L., Duroy, H. and Crosnier-Lopez, M. P., *J. Solid State Chem.*, **1996**, *127*, 283-294.

Fujimori, A., Hase, I., Nakamura, M., Namatane, H., Fujishima, Y., Tokura, Y., Abbate, M., de Groot, F. M. F., Czyzyk, M. T., Fuggle, J. C., Strebel, O., Lopez , F., Domke, M. and Kaindl, G., *Phys. Rev. B.*, **1992**, *46*, 9841-9844.

Ganguly, P., Parkash, O. and Rao, C. N. R., *Phys. Stat. Sol.(a)*, **1976**, *36*, 669-678.

Goodenough, J. B., *Prog. Sol. State Chem.*, **1971**, *5*, 145-399.

Goodenough, J. B. and Zhou, J. S., *Chem. Mater.*, **1998**, *10*, 2980-2993.

Gopal, E. S. R., *Specific Heats at Low Temperatures*, **1966**, Plenum Press, New York.

Goral, J. P. and Greedan, J. E., *J. Magn. Magn. Mater.*, **1983**, *37*, 315-321.

Greedan, J. E., *J. Magn. Magn. Mater.*, **1984**, *44*, 299-303.

Gutzwiller, M. C., *Phys. Rev. A*, **1965**, 1726.

Hahn, T., *International Table for Crystallography*, **1983**, A, D. Reidel Publishing Company, Holland.

Halpern, O. and Johnson, M. H., *Phys. Rev.*, **1939**, *55;22*, 898;135-50,237,244-5.

Hamilton, W. C., *Acta Cryst.*, **1964**, *18*, 502-510.

Harman, T.C. and Honig, J.M., *Thermoelectric and Thermomagnetic Effects and Applications*, **1967**, McGraw-Hill, New York.

Honig, J. M. and Spalek, J., *Chem. Mater.*, **1998**, *10*, 2910-2929.

Hubbard, J., *Proc. Roy. Soc. (London)*, **1963**, *A276*, 238.

Hubbard, J., *Proc. Roy. Soc. (London)*, **1964**, *A277*, 238.

Imada, M., Fujimori, A. and Tokura, Y., *Rev. Mod. Phys.*, **1998**, *70*, 1039-1263.

Izyumov, Y. A. and Ozerov, R. P., *Magnetic Neutron Diffraction*, **1970**, Plenum Press, New York.

Ju, H. L., Eylem, J. L., Peng, B., Eichorn, B. W. and Greene, R. L., *Phys. Rev. B*, **1994**, *49*, 13335.

Kadowki, K. and Woods, S. B., *Solid State Comm.*, **1986**, *58*, 507.

Katsufuji, T., Taguchi, Y. and Tokura, Y., *Phys. Rev. B.*, **1997**, *56*, 10145-10153.

Kay, H. F. and Bailey, P. C., *Acta Cryst.*, **1957**, *10*, 219-226.

Kirsanov, N. A. and Bazuev, G. V., *Russ. J. Inorg. Chem.*, **1986**, *31*, 1115-1117.

Koehler, W. C. and Wollan, E. O., *J. Phys. Chem. Solids*, **1957**, *2*, 100-106.

Koehler, W. C., Wollan, E. O. and Wilkinson, M. K., *Phys. Rev.*, **1960**, *110*, 58-70.

Kumagai, K., Suzuki, T., Taguchi, Y., Okada, Y., Fujishima, Y. and Tokura, Y., *Phys. Rev. B.*, **1993**, *48*, 7636-7642.

Landau, L. D., *Sov. Phys.-JETP*, **1957**, *5*.

Landau, L. D., *Sov. Phys.-JETP*, **1957**, *3*, 920.

Lee, P. A., Rice, T. M., Serence, L. W., Sham, L. J. and Wilkins, J. W., *Comments Cond. Matt. Phys.*, **1986**, *12*, 98-161.

Lejus, A. and Queyroux, F., *C.R. Acad. SC. Paris*, **1970**, *271*, 56-57.

Lin, C. L., Waliash, A., Crow, J. E., Mihalisin, T. and Schlottmann, P., *Phys. Rev. Lett.*, **1987**, *58*, 1232-1235.

MacEachern, M. J., Dabkowska, H., Garrett, J. D., Amow, G., Gong, W., Liu, G. and Greedan, J. E., *Chem. Mater.*, **1994**, *6*, 2092-2102.

MacLean, D. A. and Greedan, J. E., *Inorg. Chem.*, **1981**, *20*, 1025-1029.

MacLean, D. A., Ng, H. K. and Greedan, J. E., *J. Solid State Chem.*, **1979**, *30*, 35-44.

MacLean, D. A., Seto, K. and Greedan, J. E., *J. Solid State Chem.*, **1981**, *40*, 241-247.

Malik, S. K. and Adroja, D. T., *Phys. Rev.*, **1991**, *B43*, 6277-6279.

Mitchell, R. H. and Chakhmouradian, R., *J. Solid State Chem.*, **1998**, *138*, 307-312.

Miyake, K., Matsuura, T. and Varma, C. M., *Solid State Commun.*, **1989**, *71*, 1149-1153.

Moos, R., Gnudi, A. and Hardtl, K. H., *J. Appl. Phys.*, **1995**, *78*, 5042-5047.

Mott, N. F., *Philos. Mag.*, **1949**, 416-422.

Mott, N. F., *Philos. Mag.*, **1968**, *17*, 1259.

Mott, N. F., *Metal-Insulator Transitions*, **1990**, 2nd Edition, Taylor and Francis, London.

Palsson, G. and Kotliar, G., *Phys. Rev. Lett.*, **1998**, *80*, 4775-4778.

Rietveld, H. M., *J. Appl. Cryst.*, **1969**, *2*, 65.

Rossat-Mignod, J., *Methods of Experimental Physics*, **1987**,23 Part C, Academic Press, New York.

Sarma, D. D., *J. Solid State Chem.*, **1990**, *88*, 45-52.

Schull, C. G. and Smart, J. S., *Phys. Rev.*, **1949**, *76*, 1256.

Sheldrick, G. M., *Siemens SHELXTL, Version 5.03, Siemens Crystallographic Research Systems, Madison, WI*, **1993**.

Srinivasan, G., *Phys. Rev.*, **1971**, *B4*, 2581.

Stewart, G. R., *Rev. Mod. Phys.*, **1984**, *56*, 755-787.

Sunstrom, J. E., Kauzlarich, S. and Klavins, P., *Chem. Mater.*, **1992**, *4*, 346-353.

Sych, A. M., Bilyk, D. I., Klenus, V. G. and Novik, T. V., *Russ. J. Inorg. Chem.*, **1976**, *21*, 1775-1776.

Torrance, J. B. and Lacorre, P., *J. Solid State Chem.*, **1991**, *90*, 168-172.

Turner, C. W. and Greedan, J. E., *J. Magn. Magn. Materials*, **1983**, *36*, 242-248.

van Vleck, J. H., *The Theory of Electric and Magnetic Susceptibilities*, **1932**, Oxford University Press, London.

van der Pauw, L.J., *Philips Res. Repts.*, **1958**, *13(1)*, 1-9.

Varez, A., Garcia-Alvarado, Moran, E. and Alario-Franco, M. A., *J. Solid State Chem.*, **1995**, *118*, 78-83.

West, A. R., *Basic Solid State Chemistry*, **1984**, John Wiley and Sons Ltd., Chichester

Wilson, A. H., *Proc. R. Soc. Lond.*, **1931**, *A133*, 458.

Yoshii, K. and Nakamura, A., *J. Solid State Chem.*, **1997**, *133*, 584-586.

Yoshii, K. and Nakamura, A., *J. Solid State Chem.*, **1998**, *137*, 181-183.

Zaanen, J., Sawatsky, G. A. and Allen, J. W., *Phys. Rev. Lett.*, **1985**, *55*, 418-421.

Zaanen, J., Sawatsky, G. A. and Allen, J. W., *J. Magn. Magn. Matls.*, **1986**, *54-57*, 607-611.